Design and Optimisation of a Hub Drive Electrical Motor for an L2 Class Electrical Vehicle for Sustainable Urban Transport Applications

by

Andreas Joss

UNIVERSITEIT
iYUNIVESITHI
STELLENBOSCH
UNIVERSITY

Thesis presented in partial fulfilment of the requirements for the degree of Master of Engineering in the Faculty of Engineering at Stellenbosch University

Supervisor: Dr. J.M. Strauss
Dr. P.J. Randewijk

December 2018

Declaration

By submitting this thesis electronically, I declare that the entirety of the work contained therein is my own, original work, that I am the sole author thereof (save to the extent explicitly otherwise stated), that reproduction and publication thereof by Stellenbosch University will not infringe any third party rights and that I have not previously in its entirety or in part submitted it for obtaining any qualification.

Date: December 2018

Abstract

Design and Optimisation of a Hub Drive Electrical Motor for an L2 Class Electrical Vehicle for Sustainable Urban Transport Applications

A. Joss

Department of Electrical and Electronic Engineering,

Stellenbosch University,

Private Bag X1, Matieland 7602, South Africa.

Thesis: MEng (E&E)

December 2018

This thesis is a comparative study of the electromagnetic aspects, between the Ironless Double-rotor Radial Flux Permanent Magnet (IDRFPM) machine and the Single Outrunner Rotor Synchronous Permanent Magnet (SORSPM) machine for the application of the Mellowcabs L2 class direct-drive electrical vehicle. The IDRFPM machine is analysed analytically using the subdomain analysis method, and validated using a Finite Element Method (FEM) package. Two conductor types are considered for the SORSPM machine, namely Litz wire and solid copper bars. The SORSPM machine is subsequently analysed using a FEM package. The IDRFPM and SORSPM machines are both optimised for various pole numbers with priority given to efficiency, torque density and torque ripple. The optimisation results conclude that the IDRFPM machine has superior performance with regards to efficiency, power factor and torque ripple. However, the torque density of the IDRFPM machine (2.70 N·m/kg) is much lower than that of the SORSPM machine (7.17 N·m/kg). The IDRFPM machine's low torque density makes it an infeasible choice, as it would increase the vehicle mass significantly, requiring yet a larger IDRFPM machine to provide sufficient hill-climbing capability. A first attempt into a possible method of constructing the SORSPM machine using solid copper bars reveals that the complexity would be too high. The construction complexity, together with unconvincing performance gains of the solid copper bar type, makes the SORSPM machine using Litz wire the preferred candidate for the Mellowcabs vehicle.

Uittreksel

Ontwerp en Optimering van 'n Elektriese Hub-motor vir 'n L2 Klas Elektriese Voertuig vir Volhoubare Stedelike-vervoer Toepassings

A. Joss

Departement Elektries en Elektroniese Ingenieurswese,

Universiteit Stellenbosch,

Privaatsak X1, Matieland 7602, Suid-Afrika.

Tesis: MIng (E&E)

Desember 2018

Hierdie tesis is 'n vergelykende studie in terme van die elektromagnetiese aspekte, tussen die Ysterlose Dubbel-rotor Radiale Vloed Permanente Magneet (YDRVPM) masjien en die Enkel Buite-rotor Sinkroon Permanente Magneet (EBSPM) masjien, vir die toepassing van die Mellowcabs L2-klas direk-aangedrewe elektriese voertuig. Die YDRVPM masjien is analities geanaliseer met behulp van die subdomein analitiese metode en die resultate daarvan is bevestig met 'n Eindige-Element Metode (EEM) sagteware program. Vir die EBSPM masjien, word twee geleier tipes oorweeg, naamlik Litz draad en soliede koperstawe. Die EBSPM masjien is gevolglik met behulp van EEM sagteware geanaliseer. Beide die YDRVPM en EBSPM masjiene is vir verskeie poolnommers geoptimeer, terwyl uitkomstes soos die benuttingsgraad, draaimomentdigtheid en rimpel draaimoment geprioritiseer was. Dit was egter gevind dat die draaimomentdigtheid van die YDRVPM masjien (2.70 N·m/kg) heelwat laer is as dié van die EBSPM masjien (7.17 N·m/kg). Die YDRVPM masjien se teleurstellende draaimomentdigtheid maak die masjien 'n onpraktiese keuse vir die toepassing, omdat dit die voertuig se gewig aansienlik sal vergroot, wat op keer selfs 'n groter YDRVPM masjien sal verg om die nodige draaimoment vir opdraendes te voorsien. 'n Eerste poging, aangaande 'n moontlike metode vir die konstruksie van die EBSPM masjien wat soliede koperstawe benut, wys dat die masjien te ingewikkeld sal wees om te bou. Die soliede koperstaaf opsie se ingewikkelde konstruksie, tesame met die onoortuigende prestasievermoë, het tot gevolg dat, die EBSPM masjien wat Litz draad gebruik, die aanbevole masjien vir die Mellowcabs toepassing is.

Author Publications

Publications for some of the research done in this thesis can be found in:

A. Joss and P.J. Randewijk, "Design of an Ironless Double-Rotor Radial Flux Permanent Magnet machine", *2016 XXIV South African Universities Power and Engineering Conference - SAUPEC 2016*, January 2016.

A. Joss and P.J. Randewijk, "Design of an Ironless Double-Rotor Radial Flux Permanent Magnet machine", *2016 XXII International Conference on Electrical Machines - ICEM 2016*, pp. 1476-1481, September 2016.

Acknowledgements

I would like to express my sincere gratitude to the following people and organisations.

Dr. Peter Jan Randewijk - For his in-depth insight and inputs, especially of the subdomain analysis method.

Dr. Johann Strauss - For guiding me through the second half of this project, with his invaluable insight and strategic advice.

The Centre for Renewable and Sustainable Energy Studies (CRSES) - For their financial support towards this study, a sincere thank you for giving me this opportunity.

The Electrical Machines Lab - For all the advice, camaraderie, and laughter that was shared. I will always remember the wonderful time I had spent there. A special thanks to Stiaan Gerber and Eddy Howard for sharing their indispensable knowledge and advice towards my project.

The friendly Mellowcabs team - For their cooperation, and for making me part of their team.

Gert Oosthuizen - For his friendship and advice, whose project inspired me to embark on this journey.

My dearest friends, who continuously supported and motivated me. There are too many of them to mention here, but they know very well who they are.

My parents, who truly supported me through the toughest times, and always kept believing in me. I will forever be grateful for their unconditional support and love.

My Heavenly Father, who has blessed my work and given me perseverance throughout this journey.

Contents

List of Figures **ix**

List of Tables **xv**

Nomenclature **xvii**

1 Introduction **1**

1.1 Research Background 1
1.2 Powertrain Systems for EVs 4
1.3 Direct-Drive Applications for EVs 4
1.4 Problem Statement 7
1.5 Research Objectives 7
1.6 Thesis Overview 9

2 Performance Specification **10**

2.1 Introduction 10
2.2 Dimension Constraints 11
2.3 Battery System 11
2.4 Vehicle Modelling 12
2.5 Motor Performance Requirement 16
2.6 Conclusion 18

3 Analysis of the IDRFPM Machine **19**

3.1 Introduction 19
3.2 Stator Topology 20
3.3 Rotor Topology 24
3.4 Electromagnetic Analysis 25
3.5 Copper Losses 42
3.6 Other Losses 47

3.7 Total Losses and Efficiency . . . 47
3.8 Equivalent Circuit Model . . . 48
3.9 Total Mass . . . 49

4 Analysis of the SORSPM Machine 50
4.1 Introduction . . . 50
4.2 Stator Topology . . . 50
4.3 Rotor Topology . . . 59
4.4 Electromagnetic Analysis . . . 60
4.5 Copper Losses . . . 66
4.6 Iron Losses . . . 75
4.7 Magnet Losses . . . 76
4.8 Total Losses and Efficiency . . . 82
4.9 Equivalent Circuit Model . . . 83
4.10 Flux Weakening . . . 85
4.11 Torque Ripple . . . 86
4.12 Total Mass . . . 88

5 Optimisation 89
5.1 Introduction . . . 89
5.2 Pole-Slot Selection . . . 89
5.3 Operating Points . . . 91
5.4 Multi-objective Optimisation . . . 92
5.5 Single-objective Optimisation . . . 99
5.6 Design Variables . . . 100
5.7 Overview . . . 102
5.8 Results . . . 106

6 Design Recommendation 126
6.1 Introduction . . . 126
6.2 Design Comparison . . . 126
6.3 Construction Investigation . . . 133
6.4 Design Recommendation . . . 144

7 Conclusions and Recommendations 146
7.1 Conclusions . . . 146
7.2 Recommendations . . . 149

Appendices **151**

A Subdomain Analysis **152**

A.1 Magnetisation 152
A.2 The Maxwell Equations 155
A.3 Magnetic Vector Potential 155
A.4 Subdomain Modelling 156
A.5 Finding the Poisson and Laplace Equations 157
A.6 Magnetisation Distribution Functions of Radial Magnetised Permanent Magnets 159
A.7 Magnetisation Distribution Functions of Azimuthal Magnetised Permanent Magnets 161
A.8 Finding the Format of the General Solution 163
A.9 Finding the Format of the Particular Solution 165
A.10 Boundary Conditions 167
A.11 Solving the Coefficients 172

B Initial Design of the SORSPM Machine **174**

Bibliography **178**

List of Figures

1.1 (a) The Dimoni vehicle placed 2nd at the 2017 European Shell Eco Marathon for the battery-electric class, achieving 729.4 km/kWh. (b) 3D model of the Stellenbosch University Shell Eco Marathon prototype vehicle. 2
1.2 The Mellowcabs prototype vehicle. 2
1.3 (a) Gearbox and differential powertrain. (b) Direct-drive powertrain. Figure is courtesy of Vorster [4]. 3
1.4 (a) The MW Motors Luka EV. (b) The 12.5 kW hub drive with joints for mounting to vehicle chassis. 4
1.5 (a) Hub drive of the Coboc ONE e-bike. (b) Motor placed at bottom bracket of the Scott E-SUB e-bike. 5
1.6 Cut-through of the GEM Motors in-wheel motors. 6
1.7 (a) A two-wheel electric scooter equipped with a 4 kW GEM motor. (b) A three-wheel delivery and last-mile EV equipped with two 4 kW GEM motors. . 6

2.1 The torque components acting against the direct-drive motor for the full vehicle speed range, while the vehicle climbs a 15° incline angle. 14
2.2 Total torque and power delivered by a motor at various angles of inclination. . 14
2.3 Total torque and power delivered by a motor at various angles of inclination, with a power limit of 2 kW on each motor. 15

3.1 The double-rotor radial flux permanent magnet machine, with non-overlapping double-layer concentrated windings. Courtesy of Stegmann [13]. 21
3.2 The stator coil segments which are cast in a mould with epoxy resin as done by Stegmann [13]. 21
3.3 The radial magnetic flux density distribution, of which the second harmonic of the stator $B_{r_{2|AR}}$ and the fundamental component of the rotor $B_{r_{1|PM}}$ is shown by Joss *et al.* [3]. 22

3.4 The IDRFPM machine, exhibiting the quasi-Halbach array and its resulting flux paths. 24
3.5 A linear representation of the different regions of the IDRFPM machine. . . . 28
3.6 The SEMFEM model with mesh, and component sizing according to the IDRFPM prototype in [1]. 36
3.7 Magnetic vector potential with flux lines for the IDRFPM prototype in [1], as obtained with a) SEMFEM and with b) the subdomain analysis method. . . . 37
3.8 Torque comparison of the IDRFPM prototype in [1], using a SEMFEM simulation versus the analytical method which uses (3.29). 37
3.9 Radial flux density distribution of the IDRFPM prototype in [1], with only the permanent magnets active. The flux density distribution is shown for three radii, at the inner airgap $r_n - h_c/2$, at the center of the coil r_n and at the outer airgap $r_n + h_c/2$. 38
3.10 Radial flux density distribution of the IDRFPM prototype in [1], considering only the armature reaction, for a q-axis current density of $J_q = 6.4\,\text{Arms/mm}^2$. The flux density distribution at the center of the stator coil r_n is shown. . . . 38
3.11 The effect of the armature reaction on the total magnetic field of the IDRFPM prototype in [1], for a q-axis current density of $J_q = 4.0\,\text{Arms/mm}^2$. The flux density distribution at the center of the stator coil r_n is shown. 39
3.12 The effect of the armature reaction on the total magnetic field of the IDRFPM prototype in [1], for a q-axis current density of $J_q = 20.0\,\text{Arms/mm}^2$. The flux density distribution at the center of the stator coil r_n is shown. 40
3.13 Eddy currents I_{eddy} induced by external alternating transverse fields. Courtesy of Stegmann [13]. 44
3.14 Per phase equivalent circuit of the IDRFPM motor. 48

4.1 Extract is courtesy of Hanselman [15, p. 97], indicating the stator component names. 52
4.2 Example machine exhibiting rectangular slots, stator holes, and round conductors. 53
4.3 Round Litz wire, displaying various strand numbers and diameters [41]. 54
4.4 (a) Solid copper bars can be cut in a wide variety of dimensions [46]. (b) FR4 sheets can be ordered in different widths and sizes [43]. 55
4.5 Preformed copper hair pins of the Chevrolet Spark EV motor [48]. 56
4.6 Rectangular slots are packed with regular rectangular conductors on the left, or rectangular Litz wire on the right [47]. 56
4.7 Rectangular Litz wire with taped insulation [49]. 57

4.8 Rectangular magnets are used, and are kept in place with the help of small locators. 60
4.9 Starting positions in (a) and (b). Finishing positions in (c) and (d). An initial design (Appendix B) is simulated, with the mesh in (a)(c) and flux density and flux paths shown in (b)(d). 62
4.10 A non-specific motor, which is simulated in a) SEMFEM and in b) ANSYS® Maxwell 63
4.11 Torque benchmark of SEMFEM versus ANSYS® Maxwell, for the non-specific motor. 64
4.12 Radial flux density distribution at the radius in the centre of the airgap for the non-specific motor. The starting position is shown in Figure 4.10, with a q-axis current density of $i_q = 5\,\text{Arms/mm}^2$. Results of both SEMFEM and ANSYS® Maxwell are shown. 65
4.13 Open slots machine with 40 poles and 30 slots, featuring embedded magnets. Specifications are according to Rix [10, p. 78]. 65
4.14 Copper losses and phase resistance versus number of turns per coil for an initial design (Appendix B), using a constant current density. In (a) the series connection resistance is neglected, and in (b) the $q\ell_s$ term is taken into account. 68
4.15 Eddy currents I_w induced by the alternating magnetic field H which is caused by the alternating current I. 69
4.16 The power losses attributed to a case-specific conductor, due to a low frequency (LF), high frequency (HF) and exact (EX) approximations of the skin effect. Extract courtesy of Van den Bossche *et al.* [32]. 70
4.17 Several rectangular conductors surrounded by regions with infinite permeability. The magnetic field strength seen by each conductor is shown on the right. Extract courtesy of Van den Bossche *et al.* [32]. 71
4.18 Points within rectangular conductors (two bars or two turns, per coil) which are sampled during one full electrical period. 73
4.19 Radial and azimuthal flux densities which traverse the rectangular copper bars during a full electrical period, under no-load conditions. Various layers (dashed lines) are averaged and represented by a single solid line. Machine specifications in Appendix B. 74
4.20 Sample point within a magnet. 78
4.21 Magnetic flux density within a magnet and harmonics thereof is shown. The initial design (Appendix B) is simulated for two electrical periods, under no-load conditions. 80

4.22 Magnet losses versus machine speed, with both the no-load and rated current scenarios shown for the initial design (Appendix B). 81
4.23 Per phase equivalent circuit of the SORSPM motor. 83
4.24 Equivalent *dq* models under steady state and balanced three phase conditions, for the SORSPM motor. 84
4.25 The rated torque output of the initial SORSPM design (Appendix B) at base speed (100 rpm), simulated for a full electrical period. 87

5.1 Two numerical solutions 93
5.2 Two numerical solutions 94
5.3 Dimensions to be optimised for the IDRFPM machine. 101
5.4 Dimensions to be optimised for the SORSPM machine. 101
5.5 Execution of an optimisation process using the *optimisation.py* script. 104
5.6 Two numerical solutions 105
5.7 Top-level optimisation work flow. 106
5.8 Performance comparison at 2 kW, 100 rpm, of the IDRFPM machine for various pole numbers utilising round Litz wire. 110
5.9 Performance comparison at 2 kW, 465 rpm, of the IDRFPM machine for various pole numbers utilising round Litz wire. 111
5.10 Input parameter comparison of the IDRFPM machine for various pole numbers, utilising round Litz wire. 112
5.11 Cross-section of the active components, focussed on $\frac{1}{6}^{\text{th}}$ of the IDRFPM machine. Each pole number is shown according to the same scale. The red and dark blue magnets represent the radially magnetised magnets. 113
5.12 Performance comparison at 2 kW, 100 rpm, of the SORSPM machine for various pole numbers utilising round Litz wire. 116
5.13 Performance comparison at 2 kW, 465 rpm, of the SORSPM machine for various pole numbers utilising round Litz wire. 117
5.14 Input parameter comparison of the SORSPM machine for various pole numbers, utilising round Litz wire. 118
5.15 Cross-section of the active components, focussed on $\frac{1}{6}^{\text{th}}$ of the SORSPM machine with Litz wire. Each pole number is shown according to the same scale. 119
5.16 Performance comparison at 2 kW, 100 rpm, of the SORSPM machine for various pole numbers utilising solid copper bars. 122
5.17 Performance comparison at 2 kW, 465 rpm, of the SORSPM machine for various pole numbers utilising solid copper bars. 123

5.18 Input parameter comparison of the SORSPM machine for various pole numbers, utilising solid copper bars. 124
5.19 Cross-section of the active components, focussed on $\frac{1}{6}^{\text{th}}$ of the SORSPM machine with solid copper bars. Each pole number is shown according to the same scale. 125

6.1 Performance comparison of the most appealing design of each machine configuration at 2 kW, 100 rpm. 129
6.2 Performance comparison of the most appealing design of each machine configuration at 2 kW, 465 rpm. 130
6.3 Input parameter comparison of the most appealing design of each machine configuration. 131
6.4 IDRFPM machine, utilising round Litz wire, 16 pole. 132
6.5 SORSPM machine, utilising round Litz wire, 40 pole. 132
6.6 SORSPM machine, utilising solid copper bars, 48 pole. 132
6.7 Copper bars, with end-turn pieces, and a single lamination shown of the machine specified in Appendix B. 134
6.8 Aluminium stator drum of the machine described in Appendix B. 134
6.9 Aluminium stator drum, with FR4 ring, transformer paper and nylon rods. Machine dimensions as described in Appendix B. 136
6.10 Same as Figure 6.9, but with copper bars placed into position. An additional FR4 ring is inserted, which will rest on top of the end-turn pieces. Machine dimensions as described in Appendix B. 136
6.11 Aluminium stator drum, with the lamination stack in place, and a final FR4 ring on top. Machine dimensions as described in Appendix B. 137
6.12 FR4 sheets inserted along with copper bars. Machine dimensions as described in Appendix B. 137
6.13 Majority of stator now assembled, with end-turn pieces, stator cap, shaft and ball bearings in place. Machine dimensions as described in Appendix B. 139
6.14 Stator openings in stator drum, in order to insulate the screw heads from the stator drum and neighbouring screw heads. Machine dimensions as described in Appendix B. 139
6.15 Complete stator assembly, with series connections between coils and three-phase terminals included. Machine dimensions as described in Appendix B. 140
6.16 The external connections could perhaps be realised using flexible braided copper cables, commonly used as earthing conductors in buildings. 140

6.17 Aluminium rotor drum. Machine dimensions as described in Appendix B. . . . 142
6.18 Rotor drum with insulating transformer paper and FR4 ring. Machine dimensions as described in Appendix B. 142
6.19 Complete rotor assembly of the machine in Appendix B. 142
6.20 Complete machine assembly of the machine in Appendix B. 143
6.21 Cross-section view of the complete machine assembly. Machine dimensions as described in Appendix B. 143
6.22 Top view of the stator and rotor. Machine dimensions as described in Appendix B. 144

A.1 A linear representation of the different regions of the RFAPM machine with only the permanent magnets active. 157
A.2 The residual magnetisation distribution of the radially magnetised permanent magnets on the inner and outer rotor (i.e regions II and IV respectively) with respect to ϕ. 160
A.3 The derivative of the residual magnetisation distribution of the radial magnetised permanent magnets on the inner and outer rotor (i.e regions II and IV respectively) with respect to ϕ. 160
A.4 The residual magnetisation distribution of the azimuthal magnetised permanent magnets on the inner rotor (i.e. region II) with respect to ϕ. 161
A.5 The residual magnetisation distribution of the azimuthal magnetised permanent magnets on the outer rotor (i.e. region IV) with respect to ϕ. 162

List of Tables

2.1 Battery management system specifications. 12
2.2 The basic vehicle properties as described by Mellowcabs. 12
2.3 Summary of the constraints and performance required of a single direct-drive motor. 17

3.1 The governing equations for solving the magnetic vector potential in the different regions of the IDRFPM machine when considering only the excitation due to the permanent magnets. 29
3.2 Synchronous inductance results obtained for the IDRFPM prototype in Oosthuizen *et al.* [1] using various approximations. 42
3.3 Measured eddy current losses at 300 rpm [1] 44
3.4 Main materials used in the construction of the IDRFPM machine. 49

4.1 Summary of the various copper conductor types available for the SORSPM machine. 58
4.2 Snippet of parameters from Appendix B of an initial design attempt. 70
4.3 DC and AC resistances of a copper bar from the initial design attempt of Appendix B, at maximum speed. 72
4.4 Eddy current losses within the rectangular copper bars. The SORSPM initial design (Appendix B) is simulated at the top speed of 465 rpm operating point. 75
4.5 Hysteresis losses for the initial SORSPM design (Appendix B) during top speed, using the Steinmetz equation. 76
4.6 Snippet of parameters from the initial design (Appendix B). 79
4.7 Main materials used in the construction of the SORSPM machine. 88

5.1 Various pole-slot combinations under consideration for the IDRPFM machine. 90
5.2 Various pole-slot combinations under consideration for the SORSPM machine. 91
5.3 Ideal values used to scale objective functions. 97
5.4 SORSPM weight values used by the Weighted Sum Method. 98

5.5 IDRFPM weight values used by the Weighted Sum Method. 98
5.6 Boundaries applied to the design variables of the IDRFPM machine. 102
5.7 Boundaries applied to the design variables of the SORSPM machine. 102

6.1 A summary of all the most important advantages of each configuration. 145

A.1 The governing equations for solving the magnetic vector potential in the different regions of the RFAPM machine when employing permanent magnet excitation. 158

B.1 Design parameters of an early attempt of the SORSPM machine utilising solid copper bars. 175
B.2 Performance metrics of an early attempt of the SORSPM machine utilising solid copper bars, at the rated base speed (100 rpm) operating point. 176
B.3 Performance metrics of an early attempt of the SORSPM machine utilising solid copper bars, at the top speed (465 rpm) operating point. 177

Nomenclature

Abbreviations

1D	One Dimensional
2D	Two Dimensional
3D	Three Dimensional
AC	Alternating Current
AR	Armature Reaction
BMS	Battery Management System
CNC	Computer Numerical Control
CPU	Central Processing Unit
DC	Direct Current
EMF	Electromotive Force
EV	Electric Vehicle
FE	Finite Element
FEM	Finite Element Method
FFT	Fast Fourier Transform
GCD	Greatest Common Divisor
IDRFPM	Ironless Double-rotor Radial Flux Permanent Magnet
LCM	Lowest Common Multiple
MMF	Magnetomotive Force
MSE	Modified Steinmetz Equation
MOGA	Multi-Objective Genetic Algorithm
NdFeB	Neodymium-Iron-Boron
NEDC	New European Driving Cycle
PDE	Partial Differential Equation
PM	Permanent Magnet
PMSM	Permanent Magnet Synchronous Machine
RAM	Random Access Memory

RMS	Root Mean Square
RSM	Reluctance Synchronous Machine
SAM	Subdomain Analysis Method
SF	Safety Factor
SMC	Soft Magnetic Composite
SORSPM	Single Outrunner Rotor Synchronous Permanent Magnet
SSD	Solid State Drive
VSD	Variable Speed Drive
WSM	Weighted Sum Method

Constants

π	Pi	[3.141592654]
μ_0	Permeability of free space	[$4\pi\times10^{-7}$ H/m]
ρ_{air}	Density of air at sea level and at 20 °C	[1.225 kg/m^3]
ρ_{T_0}	Resistivity of copper at 20 °C	[1.72×10^{-8} Ω·m]
g	Gravitational acceleration	[9.81 m/s^2]

Roman Symbols

A_{front}	Vehicle frontal area	[m^2]
A_{slot}	Slot area	[m^2]
a	Number of parallel circuits per phase	[unitless]
B_{rem}	Remnant flux density of the permanent magnets	[T]
C_{drag}	Vehicle aerodynamic drag coefficient	[unitless]
C_{rr}	Vehicle rolling resistance coefficient	[unitless]
d	Conductor diameter	[mm]
D_o	Machine outer shell diameter	[mm]
$D_{o(SF)}$	Machine outer shell diameter considering safety factor	[mm]
$D_{o(active)}$	Outer diameter of the active material	[mm]
D_{tyre}	Inflated tyre surface diameter	[mm]
e	Induced voltage per phase	[V]
f_e	Electrical frequency	[Hz]
f_{slots}	Slotting frequency experienced by magnets	[Hz]
F_d	Aerodynamic drag force acting on the vehicle	[N]
F_g	Gravitational force acting on the vehicle	[N]
F_{rr}	Rolling resistance acting against the vehicle	[N]
F_t	Total force acting against the vehicle	[N]

g	Airgap height	[mm]
h_c	Stator coil height	[mm]
h_{mi}	Inner rotor magnet height	[mm]
h_{mo}	Outer rotor magnet height	[mm]
h_s	Stator shoe tip height	[mm]
h_y	Yoke height	[mm]
I_a	RMS phase-a current	[A]
I_p	Peak sinusoidal phase current	[A]
J_q	RMS q-axis current density	[A/mm^2]
J_z	Three-phase current density distribution in the z-direction	[A/m^2]
k_c	Ratio of coil core pitch relative to coil sides	[unitless]
k_f	Copper fill factor	[unitless]
k_h	Stator hole height ratio	[unitless]
k_m	Ratio of relative pitch of radially magnetised magnets	[unitless]
k_q	Number of coils per pole per phase	[unitless]
k_w	General winding factor	[unitless]
$k_{w,pitch}$	Winding pitch factor	[unitless]
$k_{w,slot}$	Winding slot width factor	[unitless]
L	Self inductance	[µH]
L_s	Synchronous inductance	[µH]
m	Harmonic number related to the rotor space distribution	[unitless]
M	Mutual inductance	[µH]
$M_{unloaded}$	Vehicle unloaded mass	[kg]
$M_{payload}$	Vehicle freight mass	[kg]
M_{total}	Vehicle total anticipated mass	[kg]
n	Harmonic number related to the stator space distribution	[unitless]
n_a	Conductor density distribution of the phase a windings	[unitless]
n_p	Number of parallel strands per turn	[unitless]
n_{rpm}	Mechanical speed of a motor	[rpm]
N	Number of turns per coil	[unitless]
N_{active}	Number of active traction wheels	[unitless]
p	Number of rotor pole pairs	[unitless]
P	Number of rotor poles	[unitless]
P_{BMS}	Rated continuous power available from BMS	[kW]
P_{copper}	Phase current losses due to phase winding resistance	[W]
P_{eddy}	Eddy current losses within the copper conductors	[W]

$P_{magnets}$	Eddy current losses within the magnets	[W]
P_{mech}	Rated mechanical output power of a motor	[kW]
P_{rotor}	Rotor iron losses	[W]
P_{stator}	Stator iron losses	[W]
P_{losses}	Total losses of a machine	[W]
q	Number of stator coils per phase	[unitless]
Q	Total number of stator coils of all three phases	[unitless]
r_n	Nominal stator radius	[mm]
r_o	Active material outer radius	[mm]
r_s	Stator teeth radius	[mm]
R_a	Phase winding resistance	[Ω]
v_{car}	Vehicle speed	[km/h]
v_r	Stator surface speed	[m/s]
V_a	Phase voltage at motor terminals	[V]
V_{cu}	Slot copper volume	[m^3]
w_s	Stator shoe tip width	[mm]

Other Symbols

ℓ	Active machine stack length	[mm]
ℓ_e	Length of a single end-turn	[mm]
ℓ_s	Length of external connection between each series-connected coil	[mm]
ℓ_{total}	Total length of all the conductors which make up a phase winding	[mm]

Greek Symbols

α	Vehicle incline angle	[°]
δ	Penetration depth	[mm]
Δ	Half the coil side-width pitch of the stator coils	[rad]
η	Efficiency of a motor	[%]
η_{VSD}	Efficiency of a non-specific VSD	[%]
θ_s	Stator shoe taper angle	[°]
λ	Flux-linkage of a single turn	[Wb]
λ_a	Flux-linkage of the entire phase-a circuit	[Wb–turns]
Λ	Total flux-linkage per phase	[Wb–turns]
μ_r	Relative magnetic permeability	[unitless]
ρ	Resistivity of copper	[Ω·m]
$\tau_{density}$	Torque density	[N·m/kg]

τ_{mech}	Mechanical torque developed	[N·m]
$\tau_{q,res}$	Resultant coil pitch angle of a phase	[rad]
τ_{ripple}	Torque ripple	[%]
τ_t	Slot pitch	[rad]
χ_m	Magnetic susceptibility	[unitless]
ω_e	Electrical angular frequency	[rad/s]
ω_{mech}	Mechanical rotation speed	[rad/s]

Vectors

$\vec{\mathbf{A}}$	Magnetic vector potential	[V·s·m^{-1}]
$\vec{\mathbf{B}}$	Magnetic flux density	[T]
$\vec{\mathbf{f}}(\vec{\mathbf{x}})$	Optimisation objective function	[ ]
$\vec{\mathbf{H}}$	Magnetic field intensity	[A/m]
$\vec{\mathbf{J}}_f$	Free current density	[A/m]
$\vec{\mathbf{M}}$	Magnetisation of a magnetised material	[A/m]
$\vec{\mathbf{M}}_\mathbf{0}$	Residual magnetisation of a magnetised material	[A/m]
$\vec{\mathbf{x}}$	Optimisation design space vector	[ ]

Accents or Attributes

$\vec{\mathbf{A}}$	Vector field
$\hat{\mathrm{A}}$	Amplitude

Subscripts

AR	A quantity which is only due to the effect of the Armature Reaction
PM	A quantity which is only due to the effect of the Permanent Magnets
AC	A quantity which takes into account both AC and DC components
DC	A quantity which only considers the DC component
$1\|2\|\ldots$	Relates to a specific harmonic component, with "1" being the fundamental
$a\|b\|c$	Relates to phase a, b, or c components
$d\|q$	Relates to dq quantities from the dq-model
$r\|\phi\|z$	Relates to a specific cylindrical coordinate component
$gen\|part$	Relates to either a general or particular solution of a PDE

Superscripts

$I\|II\|\ldots$	A quantity relating to a specific region within the subdomain model

Chapter 1

Introduction

1.1 Research Background

Electric vehicles (EVs) have long been an interesting point of discussion, but only the last couple of years it has received widespread renewed interest. The renewed interest is due to both increased environmental awareness and significant advancements in batteries, power electronics and the implementation of control systems. Other than the usual course of improved technology, the most profound impact to date has arguably been made by the ambitious inventor, engineer and business mandate Elon Musk. Under his leadership and firm conviction, the EV has had a revival, proving that EVs could be just as or even more desirable than conventional internal combustion engine sports cars. At the same time, other car makers such as BMW, Nissan, Toyota and Volkswagen has seen modest growth in EV sales. However in developing countries such as South Africa, the ownership and access to electric vehicles is generally still unreachable for the majority of the public, for both private and public transportation use. This is largely attributed to a still relatively high cost-of-ownership and lack of infrastructure for EVs.

The Shell Eco Marathon, a reputable competition held yearly, is a well-known initiative to help promote and illustrate the latest innovations in achieving energy efficient vehicles. The competitors consist of university student teams from across the globe. The competition thus serves as an ideal platform to test new ideas and research, and gives credibility to the performance results that were achieved. To this end, a team representing Stellenbosch University was formed to showcase some of the latest research projects of the university. One of the projects that was to be tested, is a prototype of an Ironless Double-rotor Radial Flux Permanent Magnet (IDRFPM) machine researched by Oosthuizen *et al.* [1].

Unfortunately, the university's participation never realised, and a new application and case study for the IDRFPM machine had to be found. Figure 1.1a shows an example of an battery-electric vehicle at the 2017 European Shell Eco Marathon. The Stellenbosch University prototype model is shown in Figure 1.1b.

(a)

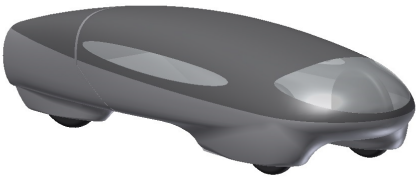

(b)

Figure 1.1: (a) The Dimoni vehicle placed 2nd at the 2017 European Shell Eco Marathon for the battery-electric class, achieving 729.4 km/kWh. (b) 3D model of the Stellenbosch University Shell Eco Marathon prototype vehicle.

Mellowcabs is a South African start-up company based in Stellenbosch. The company seeks to provide an affordable and environment-friendly short-distance taxi service within the urban areas of Cape Town and other towns in the Western Cape - with the aim to expand to European countries shortly after. The European Commission wishes to achieve a zero-emission level for European cities and town centres in the future, with some European countries already vowing to stop the sale of internal combustion engine vehicles by 2030. Mellowcabs aims to capitalise on this zero-emission policy, and therefore the vehicle needs to adhere to a certain vehicle class specification. Since the Mellowcabs vehicle is envisioned to be a three-wheeled vehicle, similar in the form of a "tuk-tuk" taxi, the company decided to pursue the L2 class specification. Figure 1.2 shows the Mellowcabs prototype vehicle.

Figure 1.2: The Mellowcabs prototype vehicle.

The preliminary Mellowcabs vehicle prototype makes use of a powertrain very similar to that of an electric golf cart. This powertrain includes a 5 kW electric motor (limited to 4 kW), single gear and differential, and the traction wheels. The preliminary design of the vehicle did not include any formal investigation into various powertrain solutions. It is therefore believed that other solutions could be more suitable, especially as efficiency, weight and torque density will be vital to increase the vehicle range. An investigation into other viable solutions is thus warranted.

During the same time period in which Mellowcabs was designing and building vehicle prototypes, this Master's project was originally focussed only on the electromagnetic design and optimisation of the IDRFPM machine. Because this project was a continuation of the work done by Oosthuizen *et al.* [1], the application for this project was initially assumed to be for the prototype vehicle which was to represent Stellenbosch University in the Shell Eco Marathon competition. This project focus was also evident in two subsequent articles by Joss *et al.* [2] [3]. Since the university decided to forgo the competition, it was decided to evaluate the IDRFPM machine for the application of the Mellowcabs vehicle. Furthermore, it was also recommended to compare the proposed IDRFPM machine, with a more conventional synchronous permanent magnet machine, dubbed in this project as the Single Outrunner Rotor Synchronous Permanent Magnet (SORSPM) machine. This project therefore became a comparative study between the IDRFPM and SORPSM machine, for the application of the Mellowcabs vehicle. Due to the objectives of the Mellowcabs company, the L2 class specification was extended to this project.

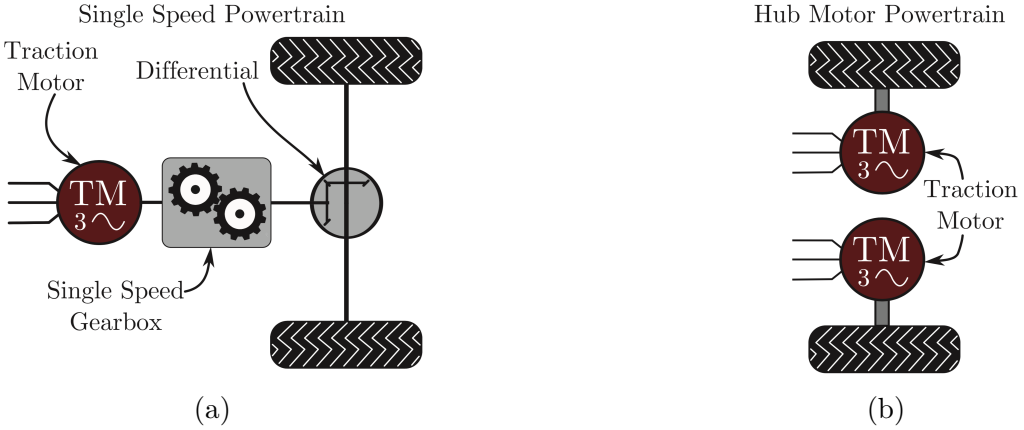

Figure 1.3: (a) Gearbox and differential powertrain. (b) Direct-drive powertrain. Figure is courtesy of Vorster [4].

1.2 Powertrain Systems for EVs

Figure 1.3 shows the two main powertrain configurations used for electric vehicles. The existing Mellowcabs powertrain is that of Figure 1.3a. Since the IDRFPM machine is essentially an outrunner machine, and because this project follows on the work done by Oosthuizen *et al.* [1], the scope of this project will be for outrunner machines to be used in a direct-drive (hub drive) powertrain configuration. This project will thus focus on the powertrain shown in Figure 1.3b.

1.3 Direct-Drive Applications for EVs

The concept of the in-wheel hub drive has been tested since the late 19th century, of which arguably, the most well-known example in that time was the Lohner Porsche in 1897. Despite the long history of the in-wheel hub drive, and all the research focus it has enjoyed, present-day real-world production EVs using hub drives are still yet to be seen. Generally speaking, production EVs, mostly use a single gear transmission, such as all the Tesla models, Chevy Spark EV, Nissan Leaf, the entire Volkswagen EV range, and the BMW i3. There is however one start-up company, named MW Motors, which is set to start production in 2018 of their first EV prototype, called the Luka EV. If successful, the Luka EV will become the first company to sell production vehicles propelled solely by in-wheel hub motors. The EV is a light-weight M1 class vehicle and has four brushless (Direct Current) DC hub motors, each rated 12.5 kW. It has an unloaded mass of 815 kg and is equipped with a 110 V, 200 Ah, 21.9 kWh battery. The Luka EV and its hub drive is shown in Figure 1.4.

(a) (b)

Figure 1.4: (a) The MW Motors Luka EV. (b) The 12.5 kW hub drive with joints for mounting to vehicle chassis.

The hub drive is however common in the electric bike (e-bike) industry. E-bikes are either propelled by hub drives, or motors mounted near the bottom bracket of the bike. Both these configurations overwhelmingly use permanent magnet synchronous machines (PMSMs), as they offer high efficiency and good torque density. Depending on the specific country's laws, e-bikes are generally limited to a nominal power output of 250 W, and a cruise limit of 25 km/h. The system voltage is usually 36 V, and the battery capacity is typically in the range of 7 Ah to 10 Ah. Figure 1.5a shows an e-bike which uses a PMSM hub drive at the rear wheel, and Figure 1.5b shows a mid-drive powertrain using an off-the-shelf Bosch product. Both these drives can deliver a maximum traction torque of 40 N·m. The e-bike market is growing rapidly, and in 2017 the US market grew 25 % from the previous year. It is estimated that in 2017 about 34 million e-bikes were sold worldwide [5].

(a) (b)

Figure 1.5: (a) Hub drive of the Coboc ONE e-bike. (b) Motor placed at bottom bracket of the Scott E-SUB e-bike.

Another interesting and exciting in-wheel hub drive development, is that of GEM Motors, a start-up company backed by European Union funding. Their aim is to provide off-the-shelf and custom solutions to light-weight vehicle manufacturers. These light-weight vehicles include scooters, motorbikes, three-wheel vehicles and small four-wheel vehicles. As of mid 2018, the company has started production of their 4 kW and 6 kW in-wheel motors, with the 2 kW versions following soon. It is planned to produce about 100000 units within the next five years [6]. From Figure 1.6, it seems that the company is using an outer rotor radial flux permanent magnet structure, with non-overlapping stator coils. The 4 kW version, has an operating voltage between 48 V and 75 V, and an active motor mass of 11.5 kg. The motor is air-cooled and can be fitted with a minimum tyre rim size of R13. Furthermore, it has a nominal torque output of 145 N·m, and a peak torque of 180 N·m

which can be sustained for 20 seconds. This means the claimed nominal torque density of the active components is a very impressive 12.61 N·m/kg. Interestingly, the 4 kW version is specifically aimed at the L1e (two-wheel vehicle) category, of which the power and speed limit is identical to the L2 (three-wheel vehicle) category. Of course, for the two-wheel EV, the 4 kW in-wheel drive will be mounted only at the rear wheel, as shown in Figure 1.7a. In Figure 1.7b, the three-wheel EV is equipped with two 4 kW hub drives. It is believed that this vehicle is therefore an L5 class vehicle, as the L5 category does not have the 4 kW power limit as the L2 category has.

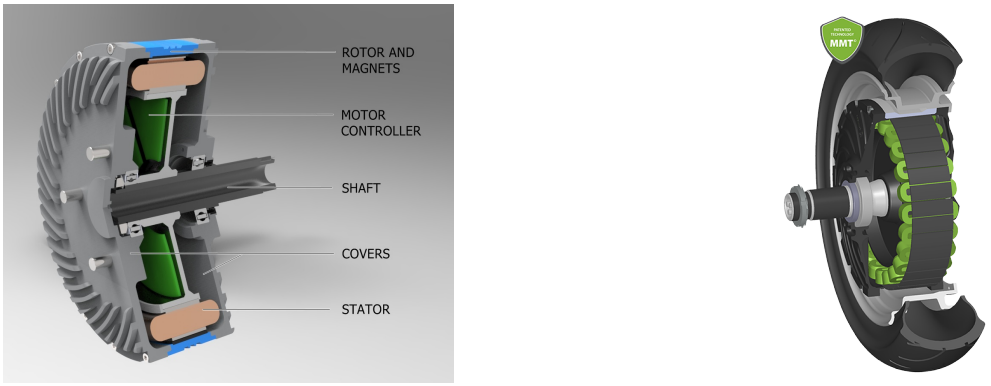

(a) (b)

Figure 1.6: Cut-through of the GEM Motors in-wheel motors.

(a) (b)

Figure 1.7: (a) A two-wheel electric scooter equipped with a 4 kW GEM motor. (b) A three-wheel delivery and last-mile EV equipped with two 4 kW GEM motors.

1.4 Problem Statement

- In a preceding project Oosthuizen *et al.* [1], the IDRFPM machine was developed for an extremely light-weight prototype vehicle to be entered in the Shell Eco Marathon competition. The performance and dimensions of the IDRFPM machine has however not yet been optimised for any given application. Also, the optimised performance and dimensions of the IDRFPM machine has not been compared side-by-side with a more conventional synchronous permanent magnet machine. If such a comparison could be done, the strengths and weaknesses of the IDRFPM machine will be better understood, and in the future, more suitable applications can be selected for the IDRFPM machine.

- In the aforementioned project, the direct-drive powertrain was designed for a maximum angle of inclination of 6°, with a total vehicle mass of 85 kg and a cruising speed of 27 km/h. Therefore, it can be argued that the IDRFPM machine is yet to be evaluated for a more demanding application. As was the case with the Shell Eco Marathon vehicle, the Mellowcabs company requires an energy efficient and light-weight powertrain solution. However for the Mellowcabs vehicle, the design anticipates a maximum elevation angle of 15°, a maximum total mass of 500 kg and a maximum cruising speed of 50 km/h. Therefore the Mellowcabs vehicle, creates a more challenging platform for the IDRFPM machine to be compared with a conventional machine.

- Depending on the outcome of the machine comparison, a design recommendation has to be made for the Mellowcabs L2 class vehicle. The recommendation should consider the performance priorities of the vehicle, and also the manufacturability of the competing machines.

1.5 Research Objectives

1.5.1 Project Scope

As discussed in Section 1.1, this project is a comparative study, comparing the suitability of the two machine topologies - the IDRFPM machine and the SORSPM machine, for the application of the L2 class Mellowcabs vehicle. Since this project follows on the work done in Oosthuizen *et al.* [1] and because the powertrain efficiency is a high priority, only hub drive (not in-hub drive, but still direct-drive) powertrain configurations are considered in

this project. The scope of this study is further limited to the electromagnetic aspects of the machines. Therefore, the dimensions and parameters of both machine topologies will be optimised and compared with regards to the electromagnetic performance, and not the mechanical strength and heat transfer capabilities. Furthermore, the study will only focus on the performance of the machines itself, and will exclude specifics about the control strategy implemented by a variable speed drive (VSD).

1.5.2 Objectives and Approach

The main purpose of this study is to determine the suitability of the IDRFPM machine for a light vehicle application. To this end, the IDRFPM is analysed analytically and optimised for the Mellowcabs L2 class vehicle. In order to determine the relative suitability of the IDRFPM machine, the machine is compared with a more conventional machine - in this project dubbed as the SORSPM machine. Therefore the SORSPM machine is also analysed, albeit with the help of a (two dimensional) 2D (Finite Element Method) FEM package, and subsequently optimised for the vehicle requirements.

The research objectives are summarised as:

- Determine the performance and dimension requirements of a direct-drive powertrain for the Mellowcabs L2 class vehicle.
- Analyse, design and optimise the IDRFPM machine.
- Analyse, design and optimise the SORSPM machine.
- Derive conclusions and general observations about both the IDRFPM and SORSPM machines. Compare the machine topologies, and propose the most suitable candidate for the vehicle.

1.6 Thesis Overview

Chapter 2: The design specifications for the direct-drive motor are determined.

Chapter 3: The IDRFPM machine is analysed and design choices are discussed.

Chapter 4: The SORSPM machine is analysed and design choices are discussed.

Chapter 5: The optimisation strategy and implementation thereof is discussed. The optimisation results of each machine type are shown and interpreted.

Chapter 6: The performance and dimensions of the various machine topologies are compared against each other. A practical investigation into a construction method is done, after which a conclusion of the most suitable machine is made.

Chapter 7: Conclusions reached during this project, and recommendations for future work are discussed.

Chapter 2

Performance Specification

2.1 Introduction

Mellowcabs aims to address the need for short-range urban transport and delivery, while appealing to environmentally conscious and tech-savvy cities and civilians. It intends to cover the "last mile" in congested urban areas, which is often costly and difficult for large trucks and delivery vehicles to reach. As such, the vehicle would never have to travel on highways, which means that the performance requirement can be limited to fairly low speeds.

The company also wishes to expand its operations in other countries in the near future, with European countries high on its priority list. Its recent partnership agreement with Uber (South Africa, Sweden and India) serves as part of this expansion plan. Other confirmed partnerships include Bubblepost in Belgium, Happymoov in France, the City of Antwerpen in Belgium, and DHL in South Africa. This necessitates Mellowcabs to design a vehicle which is road legal in most countries. Consequently it has to comply with EU (European Union) and UN (United Nations) standards, according to a specific vehicle classification. Mellowcabs has decided to design the vehicle within the L2 class standard. In short, the L2 classification describes a three-wheeled vehicle with an engine cylinder capacity not greater than $50\,\mathrm{cm}^3$, or a power output not greater than $4\,\mathrm{kW}$ whichever method for propulsion is used [7]. It also stipulates that the vehicle design speed may not exceed $50\,\mathrm{km/h}$.

In this chapter, a basic vehicle force model will be used to determine the performance requirement of the powertrain.

2.2 Dimension Constraints

The tyre size to be used for the Mellowcabs vehicle is 165/65 R14. The surface diameter of the inflated tyre is approximately 570 mm. The vehicle has a relatively low ground clearance of 135 mm. Since this project focusses on a direct-drive topology, a lower ground clearance allows for a greater machine diameter. The overall machine outer diameter is therefore constrained by,

$$\begin{aligned} D_o &= 570 - (2 \times 135) \text{ mm} \\ &= 300 \text{ mm} . \end{aligned} \tag{2.1}$$

A safety factor (SF) is added, which compensates for slightly deflated tyres. This outer diameter includes the motor drum in which the active material is placed.

$$\begin{aligned} D_{o(SF)} &= 300 - 10 \text{ mm} \\ &= 290 \text{ mm} \end{aligned} \tag{2.2}$$

An assumption is made that the outer drum shell will have walls with a thickness of 10 mm. The remaining diameter can be used for the active area of the motor. The active material outer diameter thus has a maximum diameter of

$$\begin{aligned} D_{o(active)} &= 290 - (2 \times 10) \text{ mm} \\ &= 270 \text{ mm} . \end{aligned} \tag{2.3}$$

In this project, no specific constraint is specified for the overall machine length (in the axial direction) or active stack length, but the general objective will be to keep it as short as possible.

2.3 Battery System

The battery management system (BMS) and battery pack for the Mellowcabs vehicle was designed by Horn [8] in a concurrent Master's project. The limitations imposed by the BMS will play a huge role in the design of the motor. The specifications of concern are shown in Table 2.1. The Mellowcabs team has decided to implement a 48 V voltage limit for the entire electrical system as to avoid a potential shock hazard during the manufacture and maintenance of the vehicle. The 48 V BMS results in a fixed DC-bus which the VSD will use as a source.

Parameter	Value	Unit
Energy capacity	9.6	kWh
Rated output	5	kW
DC bus voltage	48	V
Nominal discharge current	104	A
Peak discharge current	500	A

Table 2.1: Battery management system specifications.

2.4 Vehicle Modelling

A publication by Schaltz [9] was used as a guideline to determine a basic model for the vehicle. The required performance will be determined by factors such as the design incline angle, air drag resistance and the rolling resistance. Table 2.2 shows the outline specifications of the Mellowcabs vehicle.

Parameter	Variable	Value	Unit
Unloaded mass	$M_{unloaded}$	200	kg
Maximum payload	$M_{payload}$	300	kg
Tyre surface diameter	D_{tyre}	570	mm
Top vehicle speed	v_{car}	50	km/h
Maximum (continuous) incline angle	α	15	$^\circ$
Front Area	A_{front}	2.04	m^2
Drag Coefficient	C_{drag}	0.5	
Rolling Resistance Coefficient	C_{rr}	0.015	
Number of driven wheels	N_{active}	2	

Table 2.2: The basic vehicle properties as described by Mellowcabs.

The unloaded mass, $M_{unloaded}$, includes the mass of the existing golf cart powertrain. This powertrain includes a 5 kW electric motor (limited to 4 kW) weighing 35 kg, single gear, differential, axle and drum brakes (combined weight of another 35 kg), and the traction wheels. This means the complete powertrain package weighs in at a total of 70 kg. Throughout this project, the performance requirement will be based on the maximum total mass, $M_{total} = 500$ kg.

The aerodynamic drag force acting on the vehicle, as described by Schaltz [9], is

$$F_d = \frac{1}{2}\rho_{air} C_{drag} A_{front} v_{car}^2 \ , \tag{2.4}$$

where ρ_{air} the air density is assumed to be $1.225\,\mathrm{kg/m^3}$. The extra load caused by oncoming wind is ignored for this study. The gravitational force acting on the vehicle is calculated by

$$F_g = M_{total} \mathrm{g} \sin(\alpha) \ , \tag{2.5}$$

where g represents the gravitational acceleration ($9.81\,\mathrm{m/s^2}$) constant. The rolling resistance can be approximated by

$$F_{rr} = M_{total} \mathrm{g} \cos(\alpha) C_{rr} \ . \tag{2.6}$$

The total force which the drive system has to overcome in order to gain vehicle speed, is the sum of 2.4, 2.5 and 2.7. This is referred to as the traction force of the vehicle,

$$F_t = F_d + F_g + F_{rr} \ . \tag{2.7}$$

Since a direct-drive configuration is used, the gear ratio G is one. Figure 2.1 shows all the aforementioned torque components which the motor has to match to maintain a constant speed. The bottom x-axis indicates the vehicle speed values, while the top x-axis indicates the corresponding motor revolution speed. It is important to note that the graph assumes that two direct-drive motors are installed, one motor placed at each rear wheel, as was shown in Figure 1.3b. Therefore Figure 2.1 shows the torque components and power required by one of the two installed motors. The dashed line represents the output power required by one motor to the road surface, which uses the right-hand-side y-axis to display the required power.

All the graphs assume the maximum vehicle mass of 500 kg. It is important to realise that these vehicle modelling calculations provide for a powertrain mass of 70 kg. Thus for the dual motor configuration of this project, the maximum mass per motor in is intended to be less than 35 kg, but preferably as small as possible. Needless to say, a powertrain mass which exceeds the 70 kg figure, will increase the torque requirements derived in this section. For this reason, this project will prioritise the maximisation of the torque density, or the minimisation of the total mass of potential powertrains. Furthermore, since the vehicle will be driven by two motors, each motor will be limited to 2 kW due to the L2 class restriction.

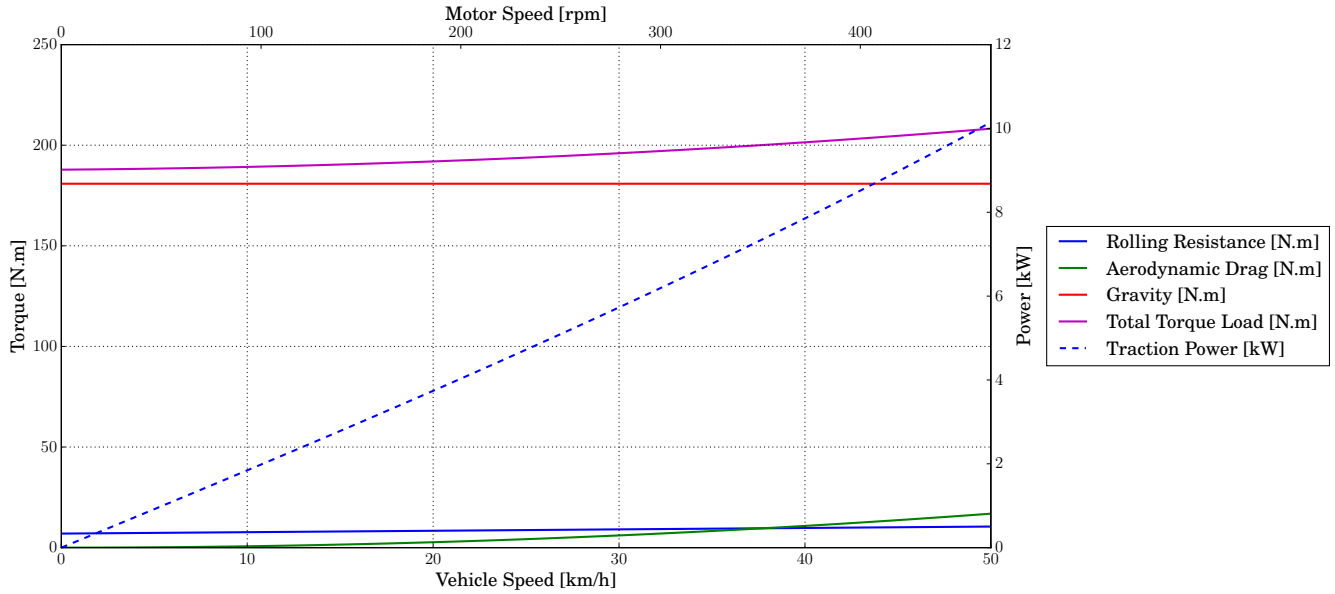

Figure 2.1: The torque components acting against the direct-drive motor for the full vehicle speed range, while the vehicle climbs a 15° incline angle.

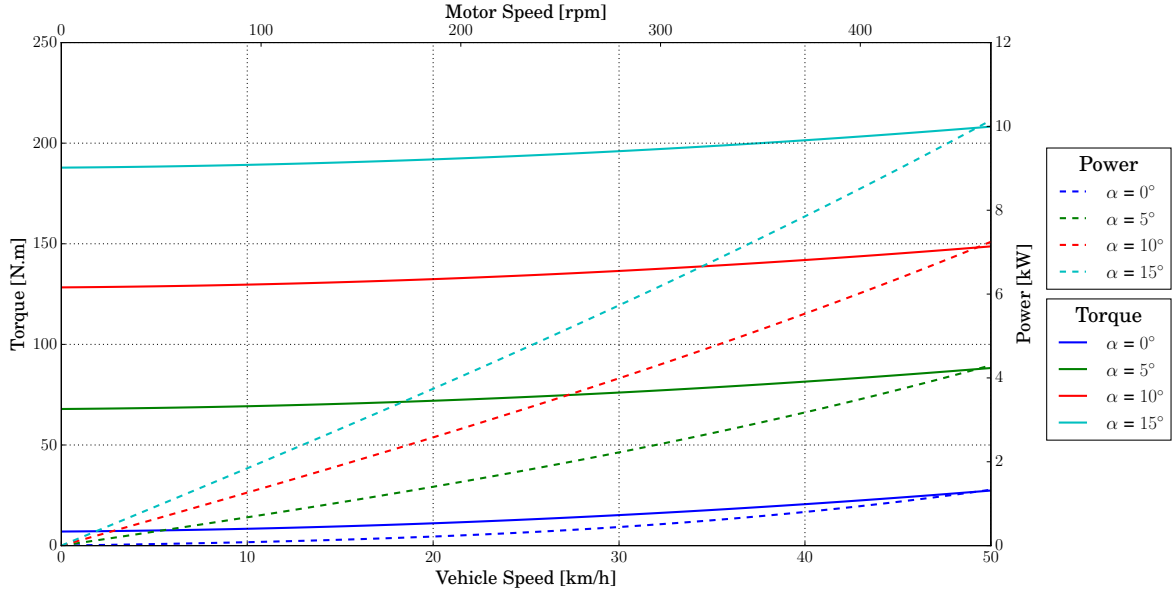

Figure 2.2: Total torque and power delivered by a motor at various angles of inclination.

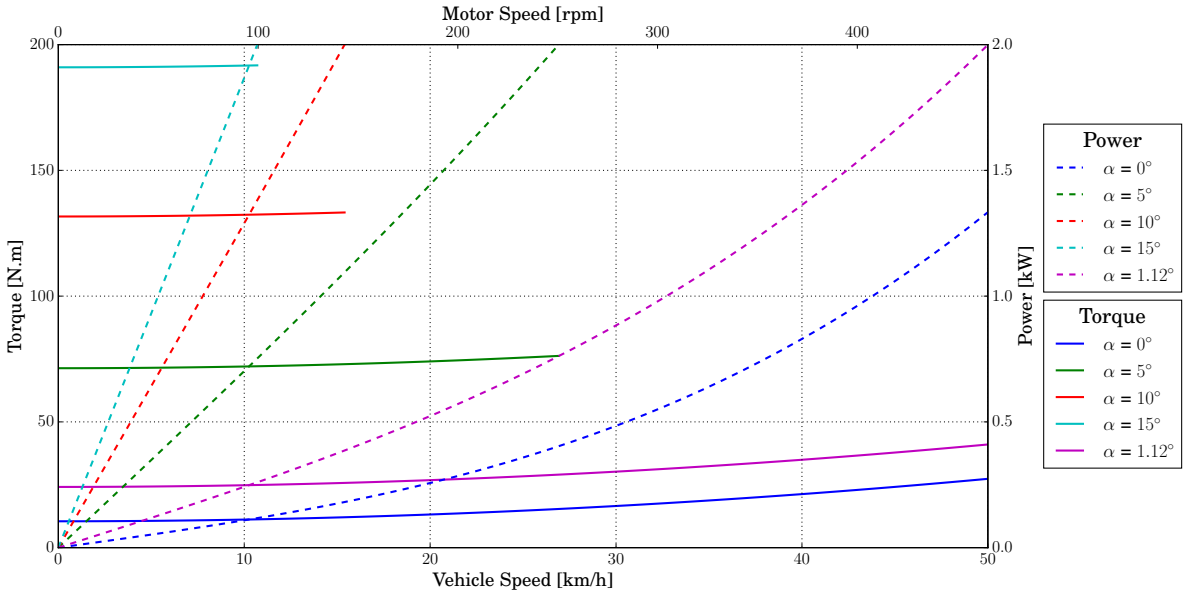

Figure 2.3: Total torque and power delivered by a motor at various angles of inclination, with a power limit of 2 kW on each motor.

Figure 2.2 shows the torque-power curves required by a motor, for various inclination angles and if the L2 power limit is ignored. For this project, the design is carried out with the intention that the maximum speed can only be reached when the incline angle is close to zero or negative. This is because a positive angle of inclination requires a powertrain with considerably larger torque and power output (as seen in Figure 2.2), which renders the L2 specification unachievable. Figure 2.3 highlights the fact the L2 restriction is very quickly reached when positive slopes are encountered. As a result, the maximum slope at which the top speed can still be achieved is 1.12°.

The rated torque can be selected from an operating point at a fairly low speed. The reason being that in urban areas, steep slopes are normally short lived (such as underground parking areas) and can probably be avoided all together, thus the vehicle will not have to travel "high" speeds when a slope is encountered. Naturally there are exceptions to this assumption, but Mellowcabs has decided to limit the vehicles' use to low sloped areas. A speed greater than 0 km/h should be selected to design the rated torque, since the drive system should deliver excess torque in order to gain speed from standstill. In other words, the aforementioned figures only show the torque that is required to maintain a constant speed at a given vehicle speed and incline angle. For this project the rated torque is derived from the requirement to maintain 10 km/h during a 15° slope, which is roughly the point at which the 2 kW limit is achieved. From Figure 2.3, this relates to 191 N·m with a motor

speed of 100 rpm. Notice that in Figure 2.3, the constant torque region is much smaller than the constant power region. The constant torque region is only 100 rpm wide, while the constant power region ranges from 100 rpm to 465 rpm, which is thus 365 rpm wide.

2.5 Motor Performance Requirement

No explicit values for the desired motor power factor and efficiency are requested by Mellowcabs. The efficiency of a non-specific VSD is assumed as $\eta_{VSD} = 0.9$. If the rated output of two motors are to be achieved, the minimum requirement for a motor's rated efficiency can be deduced from Table 2.1 as,

$$\begin{aligned} \eta &= \frac{2 \times P_{mech}}{P_{BMS} \times \eta_{VSD}} \times 100 \\ &= \frac{2 \times 2.0}{5.0 \times 0.9} \times 100 \\ &= 89\,\% \ . \end{aligned} \tag{2.8}$$

In machine design literature, it is common practise to specify a copper loss allowance as done by Rix [10] and Potgieter [11], or alternatively decide on a fixed rated current density as done by Randewijk [12], Stegmann [13] and Martínez [14, p. 49]. Depending on which of these values are fixed by the designer, an optimisation procedure is usually implemented in such a way that the unspecified input is maintained within a certain limit. Generally the purpose is to ensure the amount of heat generated by potential designs are kept within feasible limits, depending on the cooling mechanism as discussed by Rix [10], Potgieter [11], Hanselman [15, p. 96] and Pyrhönen *et al.* [16, p. 294]. The current densities that seem acceptable for various cooling methods vary among literature sources. Roughly speaking, literature suggests that RMS current densities higher than $8\,\mathrm{A/mm^2}$ might require water cooling as discussed in Vorster [4], Rix [10], Groenewald [17] and Pyrhönen *et al.* [16, p. 294]. Values between $4\,\mathrm{A/mm^2}$ and $8\,\mathrm{A/mm^2}$ require forced air cooling as stated by Cote *et al.* [18], Kimiabeigi *et al.* [19], Hendershot [20], Karnavas *et al.* [21] and Pyrhönen *et al.* [16, p. 294], and values lower than $4\,\mathrm{A/mm^2}$ allow for free convection according to Xiao-hai *et al.* [22] and Pyrhönen *et al.* [16, p. 294].

A rated copper loss value at base speed is chosen, so that the rated efficiency of 89 % can be achieved. It is assumed that at base speed, all other loss components will be very small (1 %), so that 10 % of the losses can be assigned to the copper losses. Thus, a rated copper loss value of 200 W per motor is assumed. Throughout the project, machines will be operated such that the copper losses are equal or less than 200 W, depending on the

requirement of the operating point. The current density will not specifically be controlled, but only designs which result in rated root mean square (RMS) current densities less than $4\,\mathrm{A/mm^2}$ will be accepted. The designs in this project will thus exhibit a relatively low copper loss component which subsequently allows for natural cooling. This is intentional, so that the focus of the analysis and design can remain on the electromagnetic aspects instead of the mechanical (cooling) aspects. Perhaps most importantly as mentioned by Deshpande *et al.* [23], direct-drive hub motors necessitate fully enclosed machines for the machine to be sealed and to prevent water and dirt to enter. Consequently this increases the difficulty of implementing external cooling.

Finally, since this a low voltage, high current electrical system, it is especially important to design a machine with high efficiency and a high power factor. This will allow the external wiring to have a smaller diameter, and keep the overall conduction losses at a minimum. Although the reactive power is supplied by the VSD, it is still preferential to have a high power factor machine. A higher power factor results in a smaller current magnitude, and thus the machine will have less heat to dissipate. This also helps to achieve the vision of a naturally-cooled machine. Furthermore, a low power factor motor increases the apparent power requirement of the VSD, thus a higher rated VSD will be needed. As a result of the aforementioned reasons, a fairly high rated power factor of 0.9 is chosen as a relaxed requirement. Table 2.3 summarises the required performance of a single direct-drive motor.

Parameter	Value	Unit
Active Outer Diameter	≤ 270	mm
Rated Power	≥ 2.0	kW
Rated Torque	≥ 191	N·m
Rated Efficiency	≥ 0.89	p.u.
Rated Power Factor	≥ 0.90	p.u.
Peak Voltage (Line-Line)	≤ 48	V
Rated RMS Current Density	≤ 4	$\mathrm{A/mm^2}$
Rated Copper Losses	200	W
Base (Rated) Speed	100	rpm
Top Speed	465	rpm
Mass	≤ 35	kg

Table 2.3: Summary of the constraints and performance required of a single direct-drive motor.

2.6 Conclusion

The basic requirements and constraints for the design of the electric motor were obtained. The most challenging and significant constraints arise from the L2 specification, namely the maximum total power output of 4 kW, and the 48 V restriction as was decided by Mellowcabs. It is already evident that these constraints, coupled together with the expected payload and slopes up to 15°, compose a demanding challenge.

Chapter 3

Analysis of the IDRFPM Machine

3.1 Introduction

In the project done by Oosthuizen *et al.* [1], an IDRFPM in-hub (in-wheel motor) drive was developed for a Shell Eco Marathon compition vehicle, which was intended to represent Stellenbosch University at the event. For this competition, the focus is usually aimed at achieving an extremely efficient and light-weight vehicle, where cost and practicality is not so much of an importance. The project by Oosthuizen *et al.* [1], the focus leaned more towards attaining a structurally viable in-hub drive machine, while optimisation of the electromagnetic aspects was not within the project scope.

As this project follows on the work done by Oosthuizen *et al.* [1], the stator and rotor topology considered in this chapter will be identical to the working prototype of Oosthuizen *et al.* [1]. Therefore, a brief summary of the stator and rotor topology will ensue, after which the focus will shift towards the electromagnetic aspects of the machine. The electromagnetic analysis in this chapter will mostly rely on the use of the subdomain analysis method. The derivations of the subdomain analysis are summarised in this chapter; the expanded derivation can be found in Appendix A. Finally, the loss calculations are also discussed, as well as the efficiency and total mass calculations.

3.2 Stator Topology

3.2.1 Overview

The investigation of the IDRFPM machine in this project is a continuation of the work done by Stegmann *et al.* [24], Randewijk *et al.* [25], Randewijk [12], Oosthuizen *et al.* [26] and Oosthuizen *et al.* [1]. Therefore the machine will also make use the non-overlapping double-layer concentrated winding topology. It is concluded by Kamper *et al.* [27] and Stegmann *et al.* [24], that for non-overlapping windings, the best pole-slot ratio is when the number of coils (slots) per pole per phase is $k_q = \frac{1}{2}$. The ratio $k_q = \frac{1}{2}$ will thus be implemented for this project. As a result the 2^{nd} harmonic (working harmonic) of the stator flux distribution, instead of the fundamental component, will interact with the fundamental harmonic of the rotor flux distribution. This means that the machine inherently has fewer stator coils for a given pole number, compared to conventional synchronous machines. This is favourable with regards to construction of the machine, as fewer components are needed for the stator. However, the undesired consequence is a fairly low fundamental winding factor of $k_{w_1} = 0.866$, where conventional synchronous machines achieve a winding factor k_{w_1} between 0.9 and 1.0.

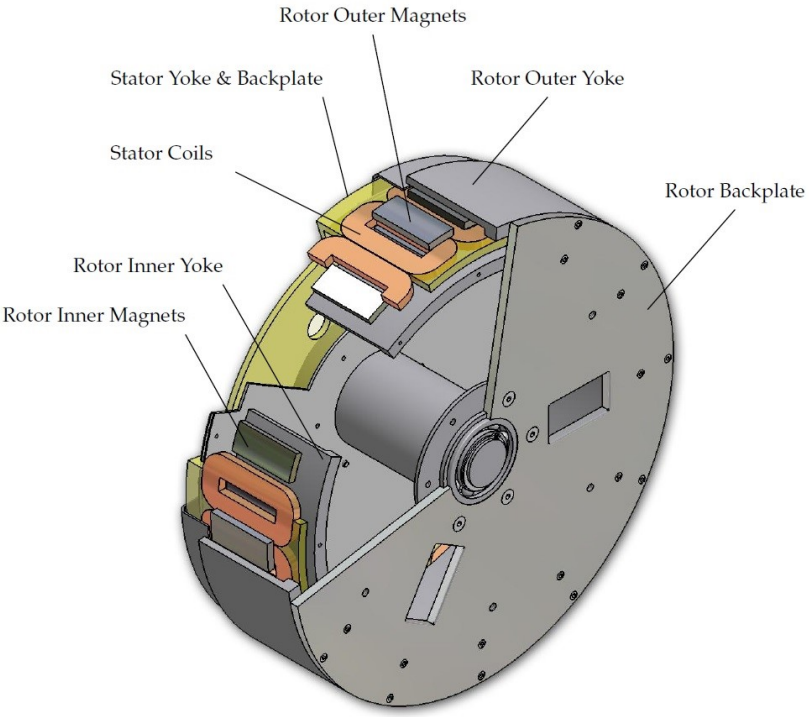

Figure 3.1: The double-rotor radial flux permanent magnet machine, with non-overlapping double-layer concentrated windings. Courtesy of Stegmann [13].

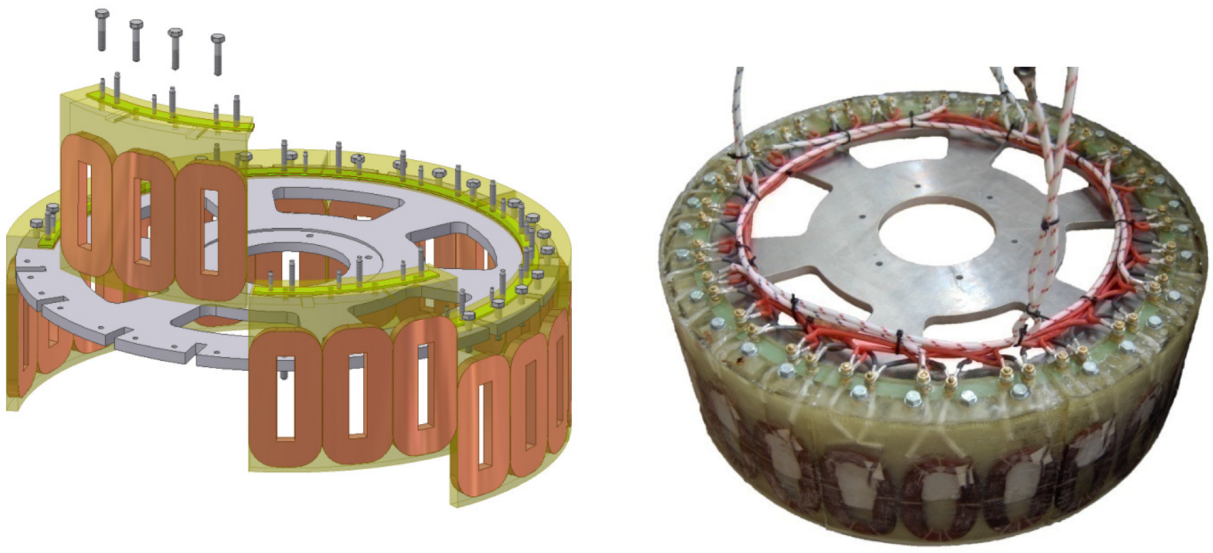

Figure 3.2: The stator coil segments which are cast in a mould with epoxy resin as done by Stegmann [13].

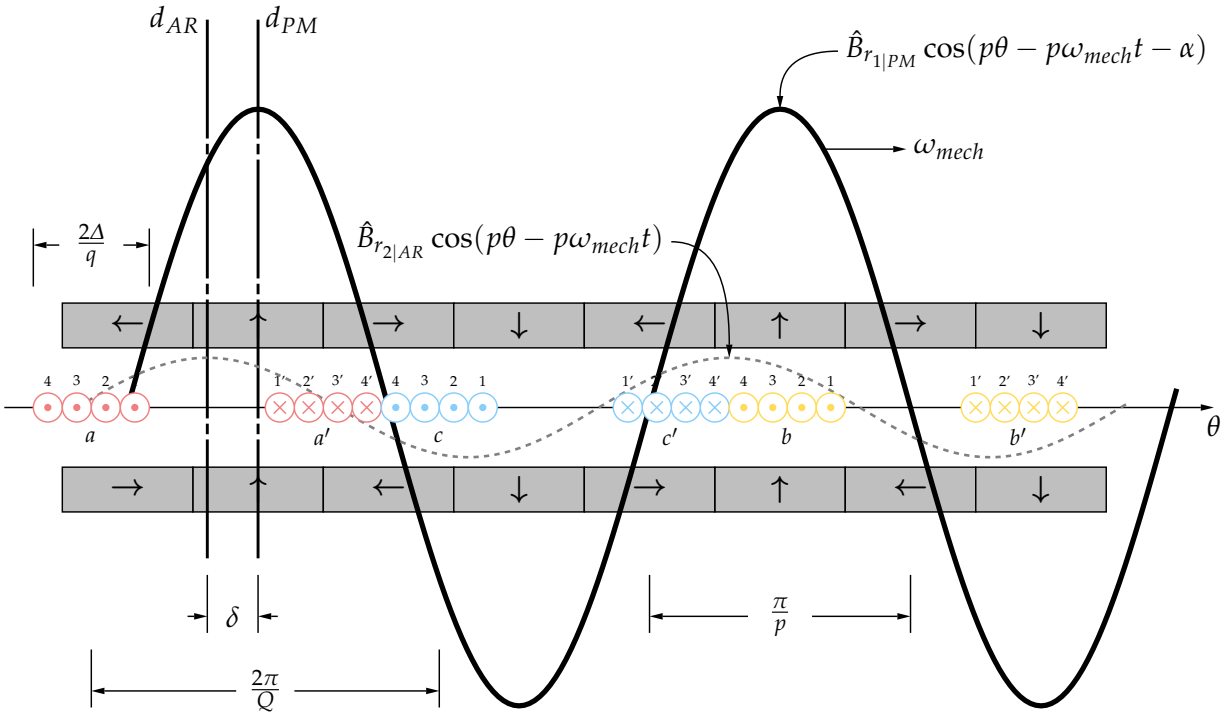

Figure 3.3: The radial magnetic flux density distribution, of which the second harmonic of the stator $B_{r_{2|AR}}$ and the fundamental component of the rotor $B_{r_{1|PM}}$ is shown by Joss *et al.* [3].

The non-overlapping double-layer concentrated windings can be seen in Figure 3.1. The double-layer characteristic implies that the coil sides of two neighbouring phase coils are flush against each other, as can be seen Figure 3.1. The non-overlapping coil structure allows for the coils to be preformed. Also, the coils can be grouped into segments, which was done by Stegmann [13] and Oosthuizen *et al.* [1]. The segments are manufactured one at a time using a mould into which the coils and epoxy resin are inserted. This makes the machine more modular and easier to build. The segments are fitted together as shown in Figure 3.2. In Figure 3.3, the radial magnetic flux density distribution for both the stator and rotor is shown. The fundamental rotor flux density distribution component, $B_{r_{1|PM}}$, interacts with the 2^{nd} harmonic of the stator flux density distribution $B_{r_{2|AR}}$.

3.2.2 Winding Conductors

For the IDRFPM machine, only round Litz wires are considered for the design optimisation since by Oosthuizen *et al.* [1] it is concluded that the eddy current losses are too severe if regular round conductors are employed. As Oosthuizen *et al.* [1] noted, the use of Litz wire reduces the overall slot fill factor slightly as compared to regular round wire. A fill factor of 0.47 is assumed in this project, which is the factor achieved in the prototype built by Oosthuizen *et al.* [1] utilising Litz wire. This conductor type is also considered in the design of the SORSPM machine in Chapter 4. Figure 4.3 shows the strands of typical Litz wire.

3.2.3 Stator Connections

In this project, all the phase coil circuits are to be connected in series. The same design choice is also made by Oosthuizen *et al.* [1] in which a prototype for the IDRFPM machine was constructed. The voltage at the phase terminals is then the vector sum of each coil's back-Electromotive force (back-EMF). The reasoning behind this decision is that circulating currents can occur if the circuits are connected in parallel. This is usually due to manufacturing tolerances, which causes coils to generate a back-EMF which is slightly out of phase and different in magnitude than one another. These circulating currents add to the copper losses and are of no benefit for the normal machine operation.

Given the low voltage limit as discussed in Section 2.3, the series connected coil circuits, a relatively wide operating speed, coupled with the inability to adequately perform flux weakening as discussed by Oosthuizen *et al.* [1, pp. 19-20], it is expected for designs to feature a very low number of turns, such as 4 or 5 turns per coil. Naturally, this low

number of turns will make the initial projected fill factor even more unreachable. That is to say, large round conductors will leave significant open spaces in a slot. Furthermore, fewer turns per coil usually means that a greater current magnitude will be required to achieve the same torque output. Consequently, the conductor diameter will need to be increased, which means the achievable bending radius of the conductors will increase, making it harder to form the coils. With this in mind, the IDRFPM designs in this project will be accepted as practical only if the number of turns per coil are equal or greater than 4. To lighten this problem, it is decided to implement a delta (Δ) connection, so that the phase voltage is allowed a factor $\sqrt{3}$ greater than in the case of a star (Y) connection, which might then allow more turns per coil.

It is worth noting that with a delta connection, the possibility of circulating currents are yet again introduced. The currents are caused by triplen harmonics (harmonics which are multiples of three) in the back-EMFs. The triplen harmonic back-EMFs add together and cause currents with triplen harmonic frequencies to flow in the delta loop. The triplen harmonics are present in machines which generate a non-sinusoidal back-EMF as explained by Hanselman [15, p. 200]. The I^2R losses attributed to the circulating currents are neglected in this study.

3.3 Rotor Topology

As the name suggests, the IDRFPM machine has an inner and an outer rotor. Both rotors contain radially and tangentially magnetised magnets arranged in a quasi-Halbach array. The goal of the quasi-Halbach array is similiar to that of iron yokes; to strengthen the magnetic field distribution within the airgap, while minimising the flux outside of the machine. It is already concluded by Oosthuizen *et al.* [1] that the best electromagnetic performance is achieved when the radially magnetised magnets and the tangentially magnetised magnets are placed equally far from the center of the machine. Figure 3.4 shows the quasi-Halbach array, where the radially magnetised magnets are indicated in blue and red, and the tangentially magnetised magnets are indicated in turquoise and yellow. The magnetisation direction of the magnets are also indicated in Figure 3.3. Since the rotor yokes are ironless, they are electromagnetically considered as air as can be seen in Figure 3.4.

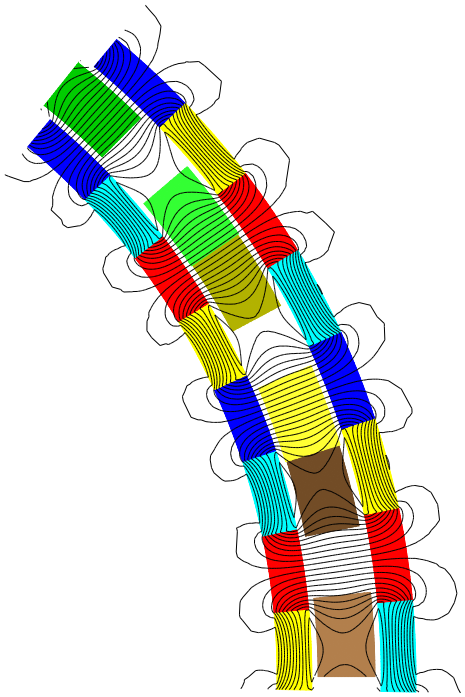

Figure 3.4: The IDRFPM machine, exhibiting the quasi-Halbach array and its resulting flux paths.

3.4 Electromagnetic Analysis

3.4.1 Introduction

The analysis of the IDRFPM machine in this project will mostly rely on a 2D analytical analysis, which makes use of the subdomain analysis method. A 2D Finite Element (FE) simulation will also be done, but for the purpose of validating the subdomain analysis. The 2D FEM package used is an in-house package called SEMFEM developed by Gerber [28].

The subdomain analysis presented in this section will be a summary of the work done in Appendix A. The subdomain analysis of the IDRFPM machine is also summarised in an article by Joss *et al.* [3] for the ICEM conference.

Due to the symmetry of the IDFRPM machine, it is only necessary to analyse a symmetrical section as shown in Figure 3.4. This is true for both the analytical subdomain analysis and the FE analysis, and naturally the aim is to reduce computation time. The number of symmetrical sections can be calculated by the greatest common divisor (GCD) of the number of poles and the number of slots in the machine.

3.4.2 FE Analysis

The SEMFEM model is shown in Figures 3.4 and 3.6. The model is drawn and simulation settings are defined using a Python^{TM} script which uses the Python^{TM} bindings made available by SEMFEM. The simulation is a time-stepped simulation for a full electrical period, with the starting position as shown in Figure 3.4. The rotor yokes and coil centres are represented as air as they will consist of non-magnetic materials. It is important to include the rotor yokes, even though they are air-like, since some of the magnetic flux will exist in this region, as can be seen in Figure 3.4. The mesh density is assigned highest in the regions where large variations in magnetic flux density values can be expected. For the IDRFPM machine, this means all the regions except the ironless rotor yokes as shown in Figure 3.6. The small flux density in the rotor yokes is evident from Figure 3.4 as the flux lines are less dense in the rotor yokes. Recall that the quasi-Halbach array strengthens the magnetic field inside the machine, while reducing the magnetic field on the outside.

3.4.3 Analytical Analysis

3.4.3.1 Introduction

The analytical analysis in this project is a continuation of the work done by Randewijk [12]. A subdomain model by Randewijk *et al.* [25][12], is successfully implemented and good coherence with FEM results are achieved. According to the work flow by Randewijk [12], the subdomain analysis due to the permanent magnets and due to the stator's armature reaction is done separately. The rotor field's analysis in this project differs from the work done by Randewijk [12] in that a quasi-Halbach magnet array is introduced and ironless yokes are implemented. For the armature reaction by Randewijk [12], the analysis for three different winding configurations is done. The last winding configuration investigated by Randewijk [12], dubbed as the "Type II" configuration, is exactly the winding configuration considered in this project - that is, the non-overlapping double-layer concentrated winding topology. This means that the deductions made for the armature reaction can be used "as is" for this project. For this reason, the formulation of the subdomain analysis for the armature reaction will be omitted in this thesis, and the reader is thus referred to Randewijk [12].

It is believed that the IDRFPM machine presents an ideal application for the subdomain analysis method. This is due to the fact that the subdomain analysis assumes a linear B-H relationship for all regions in the machine. In most machines, the aforementioned is almost never the case due to iron saturation. Naturally for the IDRFPM machine, there exists

no iron to be saturated. The copper windings and aluminium yokes all exhibit air-like magnetic permeabilities, implying that a linear B-H relationship will exist. Additionally, since the machine does not have any iron, the armature reaction is assumed to be negligible to the total magnetic field, and the reluctance component is non-existent. Consequently the magnets experience almost no alternating magnetic flux. The result is that the magnet B-H operating point is almost constant (and thus linear). All of the aforementioned suggests that the subdomain analysis of the IDRFPM machine is a near-exact electromagnetic solution. Furthermore, it is determined by Joss *et al.* [3] that the use of the subdomain analysis method leads to huge speed improvements for the optimisation process. For these reasons the subdomain analysis method is the preferred analysis method for the IDRFPM machine in this project.

In this section, a summary of the subdomain modelling due to the permanent magnets will be presented. The complete modelling is discussed in Appendix A. The analysis will be discussed in this order:

- Subdomain Modelling
- Back-EMF Calculation
- Torque Calculation

3.4.3.2 Subdomain Modelling

The overall strategy for the subdomain analysis method, is to divide the machine into regions of uniform magnetic permeabilities, and to find solutions of the magnetic fields for each of those regions. The equations which govern the magnetic field within each region, are known as Maxwell's Equations (Section A.2). These equations can be combined so that the magnetic field within each region is represented by a partial differential equation (PDE) in terms of the magnetic vector potential $\vec{\mathbf{A}}$. The goal then becomes to solve each region's PDE in terms of $\vec{\mathbf{A}}$. Once $\vec{\mathbf{A}}$ is obtained, the solutions for $\vec{\mathbf{H}}$ and $\vec{\mathbf{B}}$ can also be deduced. When $\vec{\mathbf{B}}$ and $\vec{\mathbf{H}}$ are known, these quantities are then used to determine the flux linkage, back-EMF and torque of the machine.

Due to the machine's periodicity, the magnetic vector potential $\vec{\mathbf{A}}$ can be represented as a Fourier series expansion. The Fourier coefficients are revealed using the boundary conditions between each region. In turn, the boundary conditions can be described in terms of $\vec{\mathbf{A}}$, $\vec{\mathbf{B}}$ and $\vec{\mathbf{H}}$.

The magnetic vector potential, sometimes also referred to as an auxiliary variable, is related to the magnetic flux density by,

$$\vec{\mathbf{B}} = \boldsymbol{\nabla} \times \vec{\mathbf{A}} \ . \tag{3.1}$$

The relationship between $\vec{\mathbf{B}}$, $\vec{\mathbf{H}}$ and the magnetisation of a magnetised material $\vec{\mathbf{M}}$ is,

$$\vec{\mathbf{B}} = \mu_0 \vec{\mathbf{H}} + \mu_0 \chi_m \vec{\mathbf{H}} + \mu_0 \vec{\mathbf{M}}_0 \ , \tag{3.2}$$

where χ_m denotes the magnetic susceptibility and $\vec{\mathbf{M}}_0$ denotes the residual magnetisation. Equation (3.2) is subsequently substituted into Ampère's law (A.16) resulting in the PDE,

$$\boldsymbol{\nabla}^2 \vec{\mathbf{A}} = -\mu_0 (\boldsymbol{\nabla} \times \vec{\mathbf{M}}_0) - \mu_0 \mu_r \vec{\mathbf{J}}_f \ , \tag{3.3}$$

where $\vec{\mathbf{J}}_f$ denotes the free current density. Cylindrical coordinates (r, ϕ, z) are utilised in this subdomain analysis. By realising that $\vec{\mathbf{A}}$ is only a function of r and ϕ and that only a component in the z-direction exists, the left-hand-side of (3.3) becomes,

$$\boldsymbol{\nabla}^2 \vec{\mathbf{A}} = \frac{\partial^2 A_z}{\partial r^2} + \frac{1}{r}\frac{\partial A_z}{\partial r} + \frac{1}{r^2}\frac{\partial^2 A_z}{\partial \phi^2} \ . \tag{3.4}$$

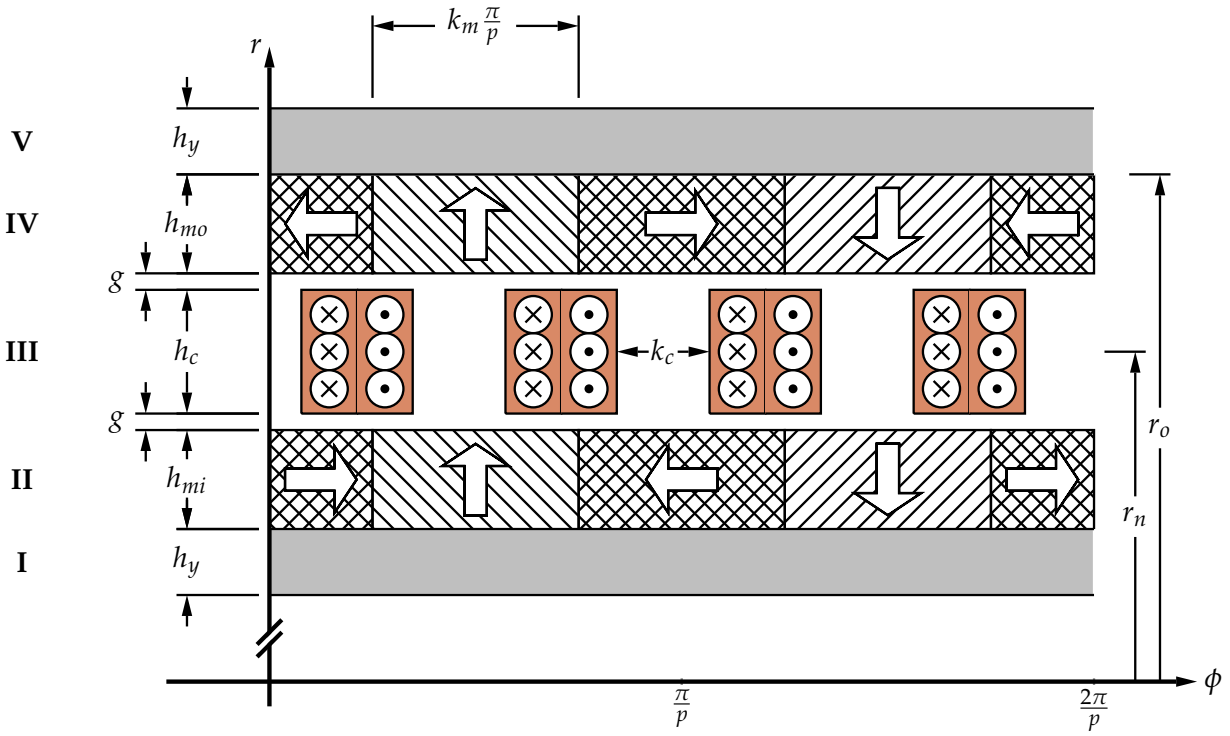

Figure 3.5: A linear representation of the different regions of the IDRFPM machine.

To realise uniform regions, the machine is divided into ring regions as is done by Randewijk [12]. This is illustrated in Figure 3.5 where the roman numbering denotes a specific region name, and h_{mo} and h_{mi} denote the outer and inner magnet widths respectively. The variable k_m describes the relative width from 0 to 1 of the radially magnetised magnets against the width of the tangentially magnetised magnets. For example, $k_m = 1$ would result in the radially magnetised magnets occupying all the space within the rotors, leaving no space for tangentially magnetised magnets. The variable k_c describes the coil core width from 0 to 1, relative to the coil side width. For example, $k_c = 0$ would cause the coil sides, that is the copper area, to take all the space within the stator. Finally, Table 3.1 concludes all the aforementioned considerations.

Table 3.1: The governing equations for solving the magnetic vector potential in the different regions of the IDRFPM machine when considering only the excitation due to the permanent magnets.

Region	Description	μ_r	Governing equation
V	Rotor yoke	μ_{yo}	$\boldsymbol{\nabla}^2\vec{\mathbf{A}} = 0$
IV	Magnets	1	$\boldsymbol{\nabla}^2\vec{\mathbf{A}} = -\mu_0(\boldsymbol{\nabla} \times \vec{\mathbf{M}}_0)$
III	Stator	1	$\boldsymbol{\nabla}^2\vec{\mathbf{A}} = 0$
II	Magnets	1	$\boldsymbol{\nabla}^2\vec{\mathbf{A}} = -\mu_0(\boldsymbol{\nabla} \times \vec{\mathbf{M}}_0)$
I	Rotor yoke	μ_{yi}	$\boldsymbol{\nabla}^2\vec{\mathbf{A}} = 0$

From Table 3.1 it is clear that $(\boldsymbol{\nabla} \times \vec{\mathbf{M}}_0)$ needs to be determined. In this project it is envisioned that the radially and azimuthally (tangentially) excited magnets are of equal magnetic strength. By realising that, in cylindrical coordinates (r, ϕ, z), only radially and azimuthally excited magnets are present, and that for those regions the magnetisation is not a function of r, the governing equation in Region II and IV reduces to,

$$\boldsymbol{\nabla} \times \vec{\mathbf{M}}_0 = \frac{1}{r}\left[M_{0|\phi} - \frac{\partial M_{0|r}}{\partial \phi}\right]\vec{\mathbf{a}}_z \ . \tag{3.5}$$

Thus, from (3.5), it is necessary to determine $M^{II}_{0|\phi}$, $M^{IV}_{0|\phi}$, $\frac{\partial M^{II}_{0|r}}{\partial \phi}$ and $\frac{\partial M^{IV}_{0|r}}{\partial \phi}$. Due to the periodic nature of the magnet arrangements, these functions and their derivatives can be found using Fourier series expansions. As an example, the resultant governing equation for region II will be,

$$\boldsymbol{\nabla}^2\vec{\mathbf{A}} = \frac{4B_{rem}}{\pi r}\sum_{m=1,3,5,\ldots}^{\infty}\left[\frac{mp\cos(mp\beta) - \sin(mp\beta)}{m}\right]\cos(mp\phi) \ , \tag{3.6}$$

where p denotes the number of pole pairs, m the space distribution harmonic number as a result of the rotor periodicity, and with

$$\beta = \left(\frac{1-k_m}{2}\right)\frac{\pi}{p} \ . \tag{3.7}$$

From Table 3.1 it is evident that Regions I, III and V are governed by homogeneous PDEs (specifically Laplace equations), while Regions II and IV are governed by non-homogeneous PDEs (specifically Poisson equations). Therefore, the latter regions will have both general and particular solutions, and the homogeneous PDEs will only have general solutions. The general solution

$$A_{z,gen}(r,\phi) = \sum_{m=1,3,5,\ldots}^{\infty}(C_m r^{mp} + D_m r^{-mp})\cos(mp\phi) \ , \tag{3.8}$$

is successfully implemented by Zhu [29], Zhu *et al.* [30] and Randewijk [12] and is therefore also used in this study. In general when trying to solve Poisson equations, an intuitive guess of the shape of the particular solution is done. Previous subdomain analysis studies on electrical machines with both radial and azimuthal magnetised magnets, such as by Randewijk [12] and Zhu *et al.* [30], successfully use the particular solution,

$$A_{z,part}(r,\phi) = \sum_{m=1,3,5,\ldots}^{\infty} G_m^{II,IV}\, r\cos(mp\phi) \ . \tag{3.9}$$

As an example, the value of the Fourier coefficient G_m^{II} can immediately be determined by substituting (3.9) into (3.6) while also using (3.4). The result is,

$$G_{m|PM}^{II} = \frac{4B_{rem}}{\pi m}\left(\frac{mp\cos(mp\beta) - \sin(mp\beta)}{1-(mp)^2}\right) \ . \tag{3.10}$$

The following boundary condition, at the outskirts of the model is assumed,

$$A_z^{I,V} = 0 \quad . \tag{3.11}$$

Then for each boundary between each region, the following boundary conditions hold (the superscript notation uses the boundaries between Region III and IV as an example),

$$B_r^{III} = B_r^{IV} \qquad \text{and} \tag{3.12}$$

$$H_\phi^{III} = H_\phi^{IV} \quad . \tag{3.13}$$

All the boundary conditions are used to set up simultaneous equations in order to solve for each region the Fourier coefficients of (3.8) and (3.9). With the coefficients now known,

the magnetic vector potential $\vec{\mathbf{A}}$ is known, but more importantly, the flux density $\vec{\mathbf{B}}$ can be determined from (3.1). For example, the radial flux density distribution in the airgap (the airgap being the entire stator region) is described as,

$$\begin{aligned} &B_r^{III}(r,\phi) \\ &= -\sum_{m=1,3,5,\ldots}^{\infty} mp(C_m^{III} r^{mp-1} + D_m^{III} r^{-mp-1}) \sin(mp\phi) \ . \end{aligned} \tag{3.14}$$

3.4.3.3 Back-EMF Calculation

The back-EMF can be determined from Faraday's law,

$$e(t) = \frac{\lambda(t)}{dt} \ . \tag{3.15}$$

The flux-linkage for a single turn can be calculated form the magnetic vector potential as follows,

$$\hat{\lambda}_1(r,\phi) = \int_S \boldsymbol{\nabla} \times \vec{\mathbf{A}} \cdot d\vec{\mathbf{s}} \ . \tag{3.16}$$

Using Stoke's Integral Theorem, the integral of (3.16) can be written into a line integral form. The line integral results in,

$$\hat{\lambda}_1(r,\phi) = 2\ell A_z(r,\phi) \ . \tag{3.17}$$

where ℓ denotes the active conductor length. Assuming perfectly symmetrical phase windings, the total flux-linkage for any phase (in peak value) can be calculated as follows,

$$\hat{\Lambda}_{a,b,c} = \frac{q}{a} \int_{-\frac{1}{2}\tau_{q,res}}^{\frac{1}{2}\tau_{q,res}} n_a(\phi)\hat{\lambda}_1(r,\phi)d\phi \ . \tag{3.18}$$

where a denotes the number of parallel circuits per phase (assumed 1 throughout this project), q the number of coils per phase, $\tau_{q,res}$ the resultant coil pitch angle,

$$\tau_{q,res} = \frac{2\pi}{q} \ . \tag{3.19}$$

The conductor density distribution for phase a of the non-overlapping concentrated coils as used by Randewijk [12], is described as,

$$n_a(\phi) = -\frac{2qN}{\pi} \sum_{n=1}^{\infty} k_{w,n} \sin(nq\phi) \ , \tag{3.20}$$

with the winding factor,

$$k_{w,n} = k_{w,pitch,n} \cdot k_{w,slot,n} \tag{3.21}$$

$$= \sin\big(n(\tfrac{\pi}{3} - \Delta)\big) \cdot \frac{\sin(n\Delta)}{n\Delta} \ , \tag{3.22}$$

where Δ is half the coil-side width angle of the stator coils in radians, and n the space distribution harmonic number due to the stator configuration. The coil-side width in terms of Δ is shown in Figure 3.3. If we assume that A_z in the stator region is everywhere the same as in the centre, i.e. at $r{=}r_n$ so that A_z is no longer a function of r in Region III, the flux-linkage can then be calculated using (3.17), (3.18), (3.20) and the result of $A_z(r_n, \phi)$ from the subdomain analysis (3.8), then the total peak flux-linkage for any given phase is

$$\hat{\Lambda}_{a,b,c} = \frac{2q\ell}{a} \int_{-\frac{1}{2}\tau_{q,res}}^{\frac{1}{2}\tau_{q,res}} n_a(\phi) A_z(r_n, \phi)\, d\phi \ . \tag{3.23}$$

In (3.23), two periodic functions, $n_a(\phi)$ and $A_z(r_n, \phi)$, are multiplied and integrated. The space distribution harmonic number of $n_{a(\phi)}$, denoted by n, originates from the number of coils per phase q. The space distribution harmonic number of $A_z(r_n, \phi)$, denoted by m, originates from the number of rotor pole pairs p. For this non-overlapping coil configuration, we have $p = 2q$ (or otherwise stated, $k_q = q/p = 1/2$), thus the rotor fundamental frequency will be twice the stator fundamental frequency. The integral of (3.23) evaluates to zero except for when the two components have space harmonics with equal frequencies. This is depicted in Figure 3.3, which shows the fundamental space harmonic of the radial magnetic flux density distribution caused by the magnets, denoted by $B_{r_{1|PM}}$, which interacts with the second space harmonic of the radial magnetic flux density distribution caused by the stator coils, $B_{r_{2|AR}}$.

Therefore, the only non-zero components of (3.23) is when $n = 2m$. Thus (3.23) reduces to,

$$\hat{\Lambda}_{a,b,c} = \frac{2q\ell N}{a\pi} k_{w,n=2m} (C_m^{III} r_n^p + D_m^{III} r_n^{-p}) \ . \tag{3.24}$$

Notice in (3.24), that only the Fourier coefficients in the stator are required, as only the stator fields are required in order to determine the stator flux linkage. Furthermore, a constant mechanical speed of ω_{mech} can be assumed, which will be the angular frequency of the time-variant version of (3.24). If only the fundamental space component is considered, then we have $m = 1$ so that $n = 2$. The back-EMF for each phase will be the derivative of the aforementioned time-variant flux linkage, resulting in the fundamental component of

the a phase induced voltage,

$$e_a = \hat{E}_{a,b,c} \sin\left(p\omega_{mech}t\right) \ , \tag{3.25}$$

with

$$\hat{E}_{a,b,c} \approx -\frac{2q\omega_{mech}\ell N}{a\pi} k_{w,n=2m}(C_m^{III} r_n^p + D_m^{III} r_n^{-p}) \ . \tag{3.26}$$

It is important to note the assumption made regarding the flux-linkage and back-EMF calculation, that is, that the radial flux density distribution is constant throughout the entire stator radius $r_n - h_c/2$ to $r_n + h_c/2$. This is implied through the assumption that A_z in the stator region is everywhere the same as in the centre, i.e. at $r{=}r_n$. It is also the approach followed by Randewijk [12], of which satisfactory results are obtained.

3.4.3.4 Torque Calculation

The induced torque can be calculated analytically using the exact Lorentz method as derived by Randewijk [12, pp. 26-31]. This is done by integrating the volumetric torque density distribution within the entire stator region. The integral is described by,

$$\tau_{mech} = \ell \int_{r_n-\frac{h_c}{2}}^{r_n+\frac{h_c}{2}} \int_0^{2\pi} r^2 J_z B_r \, d\phi \, dr \ , \tag{3.27}$$

where J_z is the three-phase current density distribution caused by the double-layer non-overlapping winding configuration derived by Randewijk [12, pp. 106–113] as

$$J_z = \begin{cases} -\frac{3qI_pN}{ar_nh_c\pi} \sum\limits_{n=1}^{\infty} k_{w,n} \sin(nq\phi + p\omega_{mech}t) & \text{for } n = 3k-1, k \in \mathbb{N}_1 \\ -\frac{3qI_pN}{ar_nh_c\pi} \sum\limits_{n=2}^{\infty} k_{w,n} \sin(nq\phi - p\omega_{mech}t) & \text{for } n = 3k-2, k \in \mathbb{N}_1 \ . \end{cases} \tag{3.28}$$

Notice that from (3.28), that for the $3k-1$ space harmonics, when $k = 1$; the second (and working) space harmonic is rotating in the counter clockwise direction. The fundamental frequency component ($3k-2$ with $k = 1$), is rotating in the clockwise direction. The space harmonics rotating in the direction opposite to the working harmonic is actually unwanted, as they can produce torque in the opposite direction. Furthermore, it is also evident that space harmonics which are multiples of 3 (commonly known as triplet or triplen harmonics) do not exist. This is true in three-phase machines if a balanced three-phase supply is injected into the machine.

When equation (3.27) is evaluated, keeping in mind $n{=}2m$, the solution becomes

$$\tau_{mech} = -\frac{3q\ell NI_p}{ar_n h_c} \sum_{m=1,5,7,\ldots}^{\infty} k_{w,n=2m} R_m S_m \tag{3.29}$$

with

$$R_m = \int_{r_n-\frac{h_c}{2}}^{r_n+\frac{h_c}{2}} r^2 \cdot \frac{mp(C_m^{III} r^{mp} + D_m^{III} r^{-mp})}{r}\, dr \tag{3.30}$$

$$= mp \left[\frac{C_m^{III} r^{mp+2}}{mp+2} - \frac{D_m^{III} r^{-mp+2}}{mp-2} \right]_{r_n-\frac{h_c}{2}}^{r_n+\frac{h_c}{2}} \tag{3.31}$$

and

$$S_m = \begin{cases} \cos\big((m{-}1)p\omega_{mech}t\big) & \text{for } m{=}6k{+}1,\ k \in \mathbb{N}_0 \\ \sin\big((m{+}1)p\omega_{mech}t\big) & \text{for } m{=}6k{-}1,\ k \in \mathbb{N}_1 \end{cases} \tag{3.32}$$

Consider again Figure 3.3. Equations (3.31) and (3.32) are derived by Randewijk [12], with the assumption that the magnetic axis of the stator, d_{AR}, is controlled (with field orientated control) such that it is $\delta = 90°$ [electrical] apart from the magnetic axis of the rotor, d_{PM}. Or alternatively stated, the stator magnetic axis is always placed on the q-axis of the rotor magnetic field, which is achieved by injecting a purely q-axis current into the machine.

It is insightful to recognise that with (3.32), only a DC component, and harmonics which are multiples of 6 will exist in the developed torque. This is a direct result of the space harmonics of the rotor ($m = 1, 3, 5, 7, 9, 11, \ldots$) which interact with the space harmonics present in the three-phase current density distribution ($n = 1, 2, 4, 5, 7, 8, 10, 11, \ldots$). Thus only the space harmonics ($m = 1, 5, 7, 11, 13, \ldots$) are interacting, and will be plugged into (3.32), which results in time-domain harmonics which are multiples of 6 (other than the DC component itself).

3.4.4 Analysis Validation

The results from the FE analysis and the subdomain analysis are compared in order to validate the solutions presented in this project. It is shown by Joss *et al.* [3], that the results of the FE analysis and subdomain analysis of the IDRFPM machine are in good agreement. It is also shown that by using the methods in separate independent optimisation procedures, that the resulting pareto curves and solutions are almost identical.

The analysis validation presented in this section makes use of the design parameters of the prototype constructed by Oosthuizen *et al.* [1]. By doing so, the FE results and subdomain analysis results are compared to each other, but also verified with the results measured by Oosthuizen *et al.* [1]. Additionally, a commercial FE package called ANSYS® Maxwell, is employed by Oosthuizen *et al.* [1] to verify the said results. The results presented here can thus also be compared with the ANSYS® Maxwell results, effectively serving as a third verification.

The SEMFEM model, with the dimensions according to the parameters of Oosthuizen *et al.* [1] is shown in Figure 3.6. The magnetic vector potential and the flux lines are compared in Figure 3.7, for when only the magnets are active.

In Figure 3.8 the developed torque for a full electrical period is compared for when a q-axis current is injected, using the maximum current density of 6.4 Arms/mm^2 as specified by Oosthuizen *et al.* [1, p. 35]. As can be seen, the torque curves are in good agreement, and is directly comparable with the ANSYS® Maxwell graph of Oosthuizen *et al.* [1, p. 38]. The torque which is calculated from the subdomain analysis results is done using (3.29). By inspection it is evident that a minute torque ripple is present, and furthermore, the ripple is mostly attributed to a 6$^{\text{th}}$ order harmonic component as expected from the discussion in Section 3.4.3.4. The ripple content also agrees with the analysis results of Randewijk [12, pp. 112-113] for the "Type II" configuration.

The comparison of the magnetic fields, will however be done for two separate cases. Firstly, the magnetic fields will be benchmarked for when only the permanent magnets are active, thus when no stator currents are present. Secondly, the magnetic fields will be compared for when only the armature reaction is present, meaning the magnets are effectively "switched off". The magnetic fields are compared in this manner, because the subdomain analysis does not compute the total resultant magnetic field within the machine due both the magnets and armature reaction being active at the same time. This is also the approach used by Randewijk [12]. Thus in Figure 3.9, the radial flux density distribution is compared for when only the magnets are active, and in Figure 3.10 only the armature reaction is active. The aforementioned q-axis current is injected in the case of Figure 3.10. As can be seen from both figures, the results are in good agreement.

For the results presented in this validation, the analytical analysis script took 0.61 seconds to compute, whereas the SEMFEM simulation took 16 minutes and 20 seconds to complete. The long simulation time is due to the high mesh density and high number of steps (521) required to achieve the accuracy presented in this validation. These times were

achieved on an Intel® Core™ i7-6700K processor clocked at 4.2 GHz, with 32GB RAM installed. The operating system used is 64-bit openSUSE 13.2.

The analytical script used in this validation, will be used with the same configuration settings during the optimisation in Chapter 5. The magnetic fields are computed up to the 19^{th} order harmonic component, and 181 time samples will be evaluated for the torque function. To summarise,

- 10 harmonics with only the permanent magnets enabled ($m = 1, 3, 5, 7, 9, \ldots, 17, 19$)
- 19 harmonics with only the armature reaction enabled ($n = 1, 2, 3, 4, 5, \ldots, 17, 19$)
- 181 time stamps for the full electrical period (used only for torque evaluation (3.29)).

Perhaps a more subtle detail, is that although only certain stator space harmonics (such as $n = 1, 5, 7, 11, 13, \ldots$) are required in order to determine the torque in Section 3.4.3.4, all the other "in-between" harmonics are indeed necessary to determine the magnetic field produced by the armature reaction. This magnetic field is then used to determine the synchronous inductance of the machine, as discussed in Section 3.4.6.

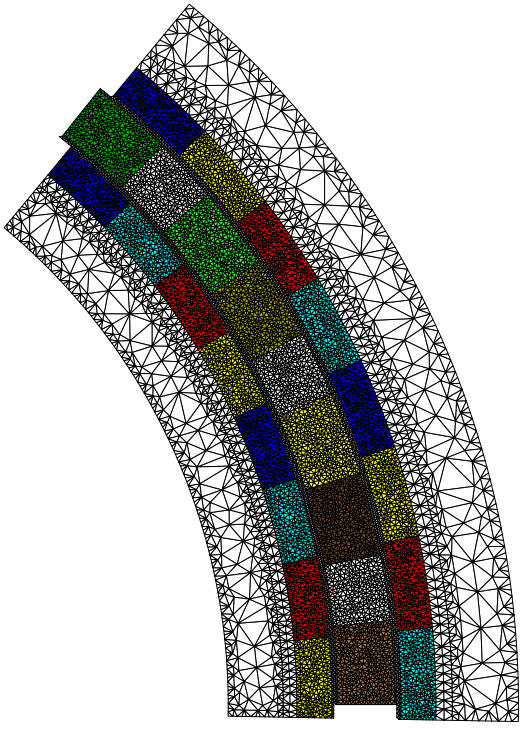

Figure 3.6: The SEMFEM model with mesh, and component sizing according to the IDRFPM prototype in [1].

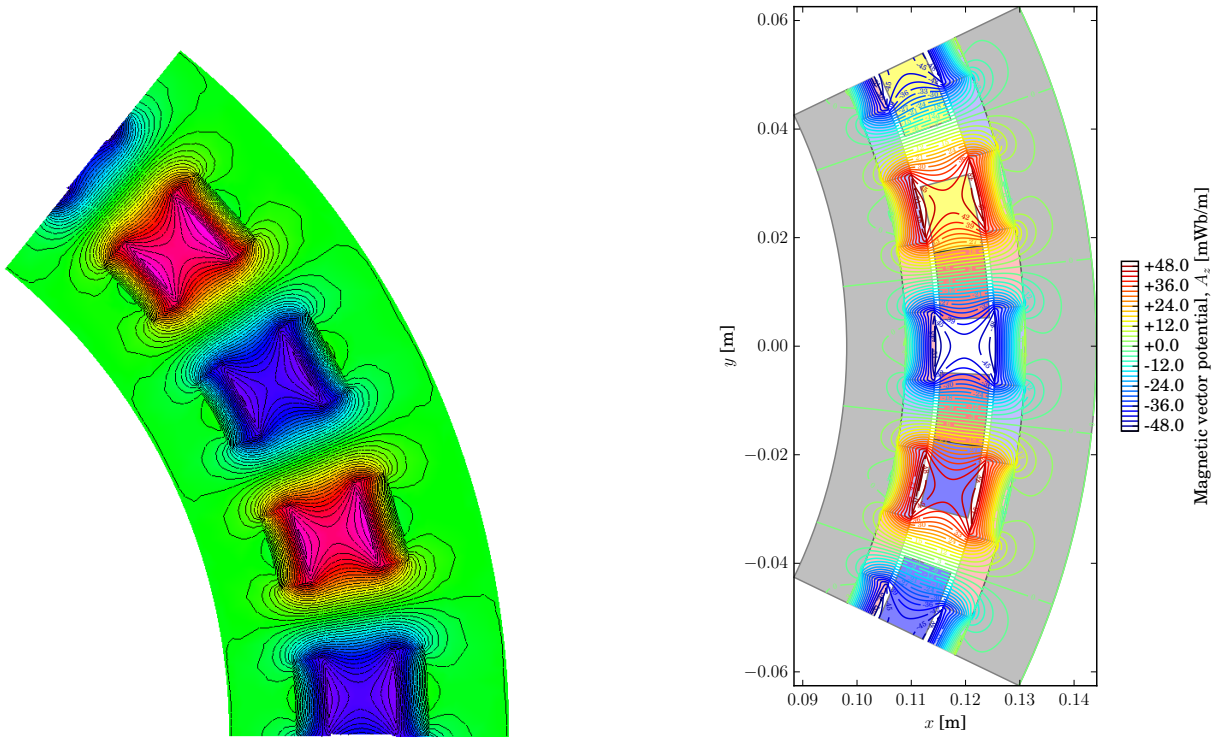

(a) (b)

Figure 3.7: Magnetic vector potential with flux lines for the IDRFPM prototype in [1], as obtained with a) SEMFEM and with b) the subdomain analysis method.

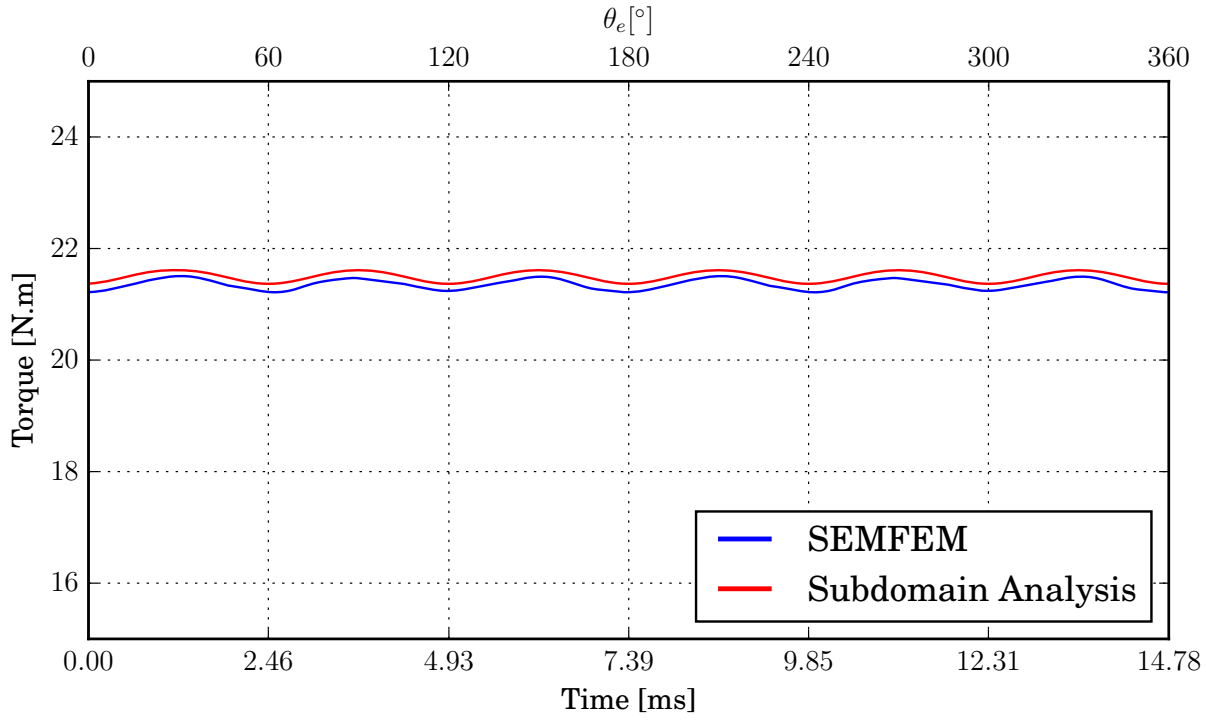

Figure 3.8: Torque comparison of the IDRFPM prototype in [1], using a SEMFEM simulation versus the analytical method which uses (3.29).

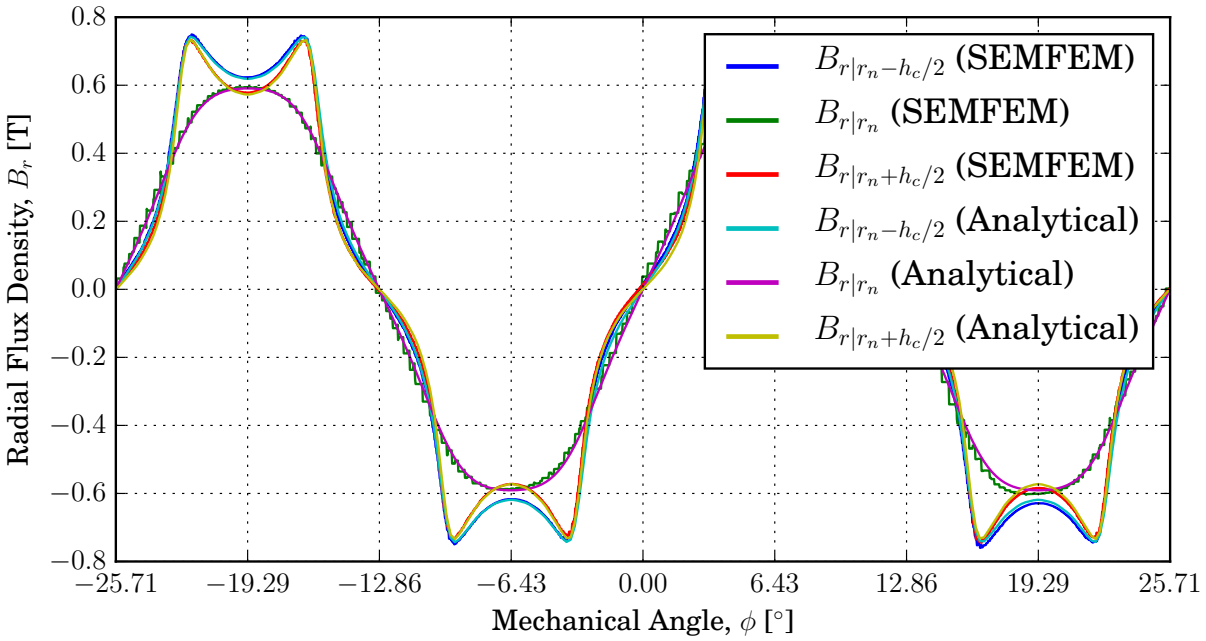

Figure 3.9: Radial flux density distribution of the IDRFPM prototype in [1], with only the permanent magnets active. The flux density distribution is shown for three radii, at the inner airgap $r_n - h_c/2$, at the center of the coil r_n and at the outer airgap $r_n + h_c/2$.

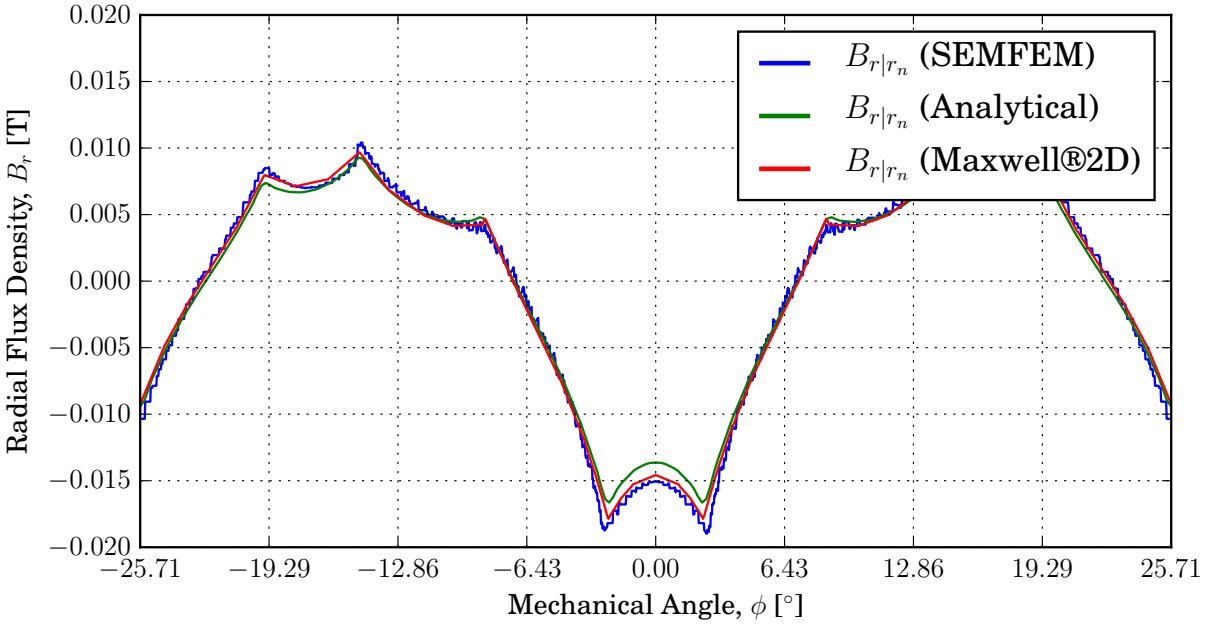

Figure 3.10: Radial flux density distribution of the IDRFPM prototype in [1], considering only the armature reaction, for a q-axis current density of $J_q = 6.4\,\mathrm{Arms/mm^2}$. The flux density distribution at the center of the stator coil r_n is shown.

3.4.5 Armature Reaction

In this section, it will be emphasised the small role the armature reaction plays in the total magnetic field of the IDRFPM machine. In Figures 3.11 and 3.12, the armature reaction is simulated using SEMFEM for a q-axis current density of $J_q = 4.0\,\text{Arms/mm}^2$ and $J_q = 20.0\,\text{Arms/mm}^2$ respectively. The total or resultant magnetic field is indicated as "All". The simulation for $J_q = 4.0\,\text{Arms/mm}^2$ represents the upper limit deemed feasible for this project, as was stated in Table 2.3. The simulation for $J_q = 20.0\,\text{Arms/mm}^2$, represents an unrealistically large current density value. From both figures, it is clear that even an unrealistically large current will not have a noticeable effect on the total magnetic field. Or otherwise put, the magnetic field due to the permanent magnets can be assumed to be the resultant magnetic field. This illustrates that for the IDRFPM machine, flux-weakening will not be a viable option as is the conclusion made by Oosthuizen *et al.* [1, pp. 19-20]. It also shows that, for the subdomain analysis presented in this project, it is not necessary to obtain a total resultant magnetic field. Therefore, the magnetic field due to the permanent magnets is sufficient to analyse the overall machine performance. It is however still important to compute the armature reaction separately, as this will be used to approximate the stator inductance as discussed in the following section.

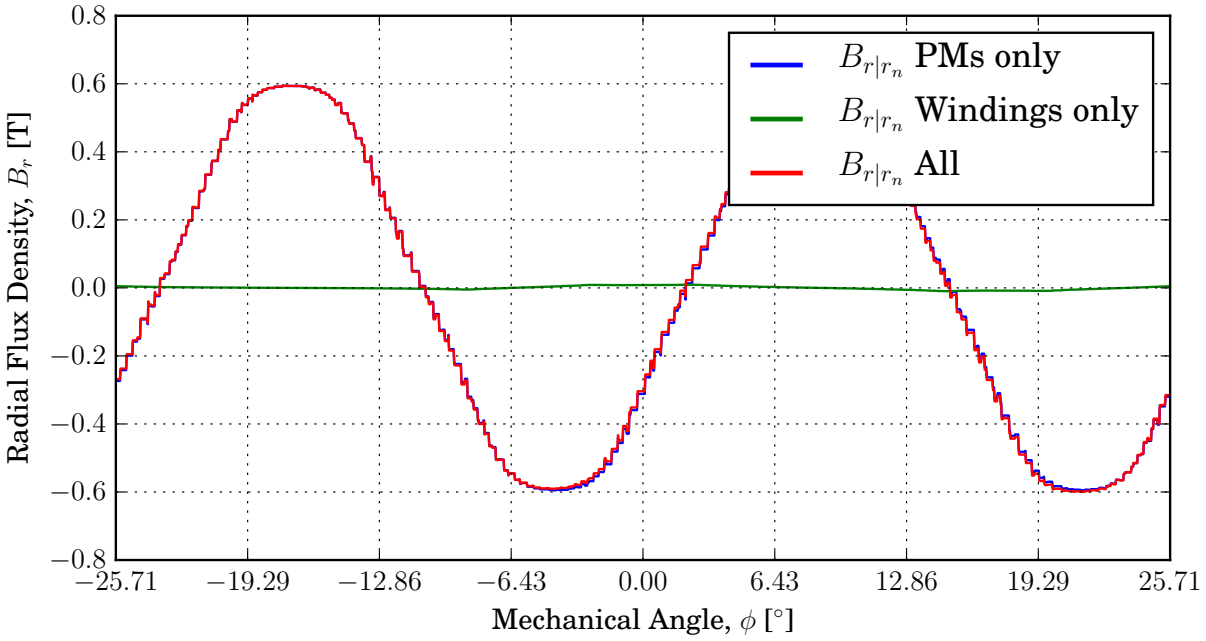

Figure 3.11: The effect of the armature reaction on the total magnetic field of the IDRFPM prototype in [1], for a q-axis current density of $J_q = 4.0\,\text{Arms/mm}^2$. The flux density distribution at the center of the stator coil r_n is shown.

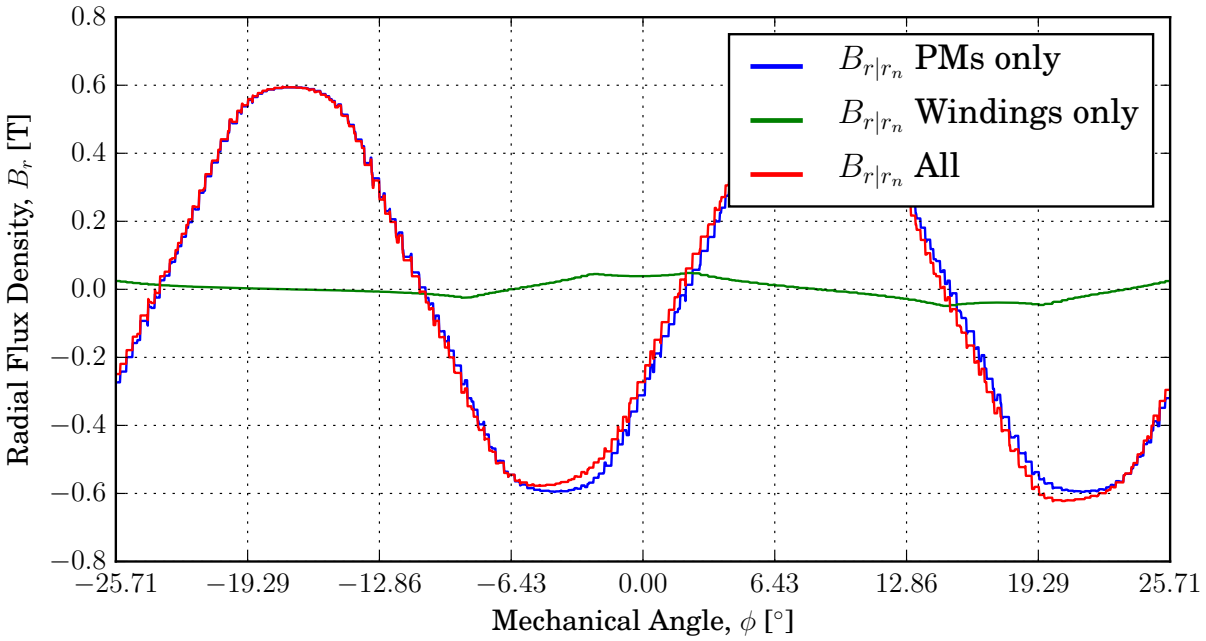

Figure 3.12: The effect of the armature reaction on the total magnetic field of the IDRFPM prototype in [1], for a q-axis current density of $J_q = 20.0\,\text{Arms/mm}^2$. The flux density distribution at the center of the stator coil r_n is shown.

3.4.6 Inductance Calculation

The value of the stator inductance is required in order to complete the equivalent circuit model in Section 3.8. As observed by Oosthuizen *et al.* [1], the inductance value is expected to be inherently low for the ironless machine. This also correlates with the weak armature reaction observed in Figures 3.11 and 3.12.

In this section, the results for the inductance of the various analysis methods will be compared in order to gain confidence of the overall result. As stated in the beginning of this chapter, the optimisation procedure for the IDRFPM machine in Chapter 5 will make use of the subdomain analysis method. Therefore, the inductance value determined using the subdomain analysis script needs to be validated with the other simulation methods. It should be noted that, in this project, the end-turn effect on the inductance value is ignored.

The inductance matrix,

$$\begin{bmatrix} \lambda_{a|AR} \\ \lambda_{b|AR} \\ \lambda_{c|AR} \end{bmatrix} = \begin{bmatrix} L_{aa} & L_{ab} & L_{ac} \\ L_{ba} & L_{bb} & L_{bc} \\ L_{ca} & L_{cb} & L_{cc} \end{bmatrix} \begin{bmatrix} i_a \\ i_b \\ i_c \end{bmatrix} \tag{3.33}$$

describes the general relationship between the phase currents and flux-linkages of each phase. The subscript AR denotes the flux linkage due to the armature reaction only, thus

with the magnets "switched off". In this project, the machines are assumed to be perfectly symmetrical, therefore the mutual inductances will all be equal, and all the self-inductances will also be equal, so that the mutual inductance is

$$M = L_{ab} = L_{ac} = L_{ba} = L_{bc} = L_{ca} = L_{cb} \tag{3.34}$$

and the self-inductance is

$$L = L_{aa} = L_{bb} = L_{cc} \ . \tag{3.35}$$

For a balanced three-phase current supply, the currents sum to zero,

$$i_a + i_b + i_c = 0 \tag{3.36}$$

which allows (3.33) to be simplified as

$$\begin{bmatrix} \lambda_{a|AR} \\ \lambda_{b|AR} \\ \lambda_{c|AR} \end{bmatrix} = \begin{bmatrix} L-M & 0 & 0 \\ 0 & L-M & 0 \\ 0 & 0 & L-M \end{bmatrix} \begin{bmatrix} i_a \\ i_b \\ i_c \end{bmatrix} \tag{3.37}$$

where $L-M$ is known as the synchronous inductance,

$$L_s = L-M \ . \tag{3.38}$$

Finally, by using (3.37) and (3.38), and when sinusoidal currents and flux-linkages are assumed, the synchronous inductance can be estimated by

$$L_s = \frac{\hat{\Lambda}_{a|AR}}{I_p} \ , \tag{3.39}$$

where $\hat{\Lambda}_{a|AR}$ and I_p is the peak flux-linkage due to the armature reaction and the peak phase current respectively.

For the IDRFPM prototype of Oosthuizen *et al.* [1], in ANSYS® Maxwell, the mutual inductance is reported as $M = -13.38$ μH, and the self-inductance $L = 55.42$ μH so that with (3.38), the synchronous inductance is $L_s = 68.80$ μH. This result is shown in Table 3.2.

For the results shown in Table 3.2 which use (3.39), only the armature reaction is activated in the analysis. It can be seen that all the results are in good agreement with each other. As the subdomain analysis is the method to be used for the optimisation procedure in Chapter 5, the inductance value calculated with this analysis can be trusted.

	Synchronous Inductance L_s [μH]		
Equation	SEMFEM	Analytical	ANSYS® Maxwell
(3.39)	68.78	68.39	68.82
(3.38)			68.80

Table 3.2: Synchronous inductance results obtained for the IDRFPM prototype in Oosthuizen *et al.* [1] using various approximations.

3.5 Copper Losses

3.5.1 Introduction

The copper losses in this section will focus on the use of round conductors, as opposed to the use of solid rectangular copper bars in Chapter 4.

In this project, the copper losses are split into two components, that which is caused by the phase resistance namely the phase current losses, and then that which is caused by the eddy current losses within the conductors. In literature, the phase current losses is more commonly known as copper losses, however this term is rather confusing since it does not include all the copper losses. If the eddy current losses is neglected, then of course the term does make sense.

3.5.2 Phase Current Losses

The phase current losses describe the losses due to phase resistance experienced by the current injected into the machine. From the per phase model, these losses for all three phases are determined by

$$P_{copper} = 3I_a^2 R_a \ , \tag{3.40}$$

where a denotes the per phase quantities.

To calculate these losses, the phase resistance must first be determined. Recall that this project only utilises series connected circuits. The DC resistance of a phase winding is described by

$$R_{a|DC} = \frac{\rho \ell_{total}}{A_{slot} k_f} \tag{3.41}$$

where A_{slot} is the slot area, k_f the copper fill factor, and ℓ_{total} the total length of all the conductors which make up a phase winding. The actual cross-section area which consists of copper is described by the $A_{slot}k_f$ term. Only the DC resistance is considered here, as

it can be shown that the skin depth in this application is much greater than the diameter of typical Litz wire.

Throughout the design of the machine, the copper temperature is assumed to be $T = 75\ ^{\circ}\text{C}$, which is a design choice for the maximum operating temperature. The copper resistivity is obtained by the well known linear approximation as discussed by Hanselman [15, p. 91],

$$\begin{aligned} \rho &= \rho_{T_0}[1 + \alpha(T - T_0)] \\ &= 2.09 \times 10^{-8}\ \Omega\cdot\text{m} \end{aligned} \tag{3.42}$$

where $\rho_{T_0} = 1.72 \times 10^{-8}\ \Omega\cdot\text{m}$ at $T_0 = 20\ ^{\circ}\text{C}$ and $\alpha = 0.0039\ ^{\circ}\text{C}^{-1}$.

The total length of a phase circuit is determined by the number of coils q connected in series, the number of turns per coil N, and the length of a single turn. Thus the total length of a phase circuit is,

$$\ell_{total} = 2qN(\ell + \ell_e) + q\ell_s \tag{3.43}$$

where ℓ is the active stack length of the machine, and ℓ_e is the length of a single end-turn. The end-turn length is approximated by the arc length distance of the incoming and outgoing conductors of a turn. The length of the series connection between each coil of a particular phase is accounted for by ℓ_s. Since (3.43) is substituted into (3.41), the assumption is made that the series connections use the same conductor diameter as the stator windings. Notice that the term $q\ell_s$ is not proportional to the number of turns N. The $q\ell_s$ term is important, because it is a prominent term when the number of turns are low. The significance hereof is discussed in detail in Section 4.5.2.

3.5.3 Eddy Current Losses

In Chapter 4, a distinction is made between eddy currents caused by the skin and proximity effect, as opposed to the eddy currents caused by transverse fields due to the rotor field. However for the IDRFPM machine, only small round conductors are considered, and it is therefore assumed that the skin and proximity effects will be negligible. Thus only eddy currents due to the transverse fields caused by the magnets are considered for the IDRFPM machine.

The purpose of this section, is to show that eddy current losses can be quite considerable for the IDRFPM machine, but can easily be avoided if Litz wire is utilised. Moreover, the

analysis technique presented here, will be the basis for the eddy loss calculation of the SORSPM machine in Section 4.5.3.2.

The coil windings of the IDRFPM machine are situated in an airgap between the inner and outer rotor. The magnets in these rotors create 2D magnetic fields which are transverse to the windings. As the rotors rotate, the coil windings cut the magnetic field set-up by the rotors, inducing a voltage on the winding terminals, but unfortunately also eddy currents within the winding themselves. Figure 3.13 illustrates these transverse fields, which induce eddy currents within a conductor.

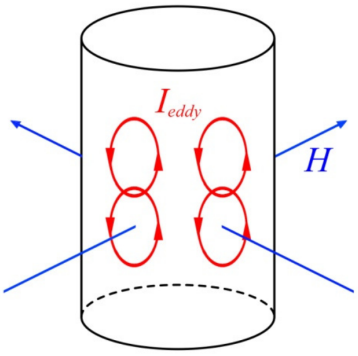

Figure 3.13: Eddy currents I_{eddy} induced by external alternating transverse fields. Courtesy of Stegmann [13].

It is common practice to use Litz wire to reduce the magnitude of the eddy currents. Litz wire consists of fine parallel strands which are insulated from each other. These strands are usually twisted or bunched so that each strand might take all possible positions through out the length of the conductor, as explained by Wang *et al.* [31] and Van den Bossche *et al.* [32]. The aforementioned twisting is done to prevent eddy currents between the parallel strands. The prototype by Oosthuizen *et al.* [1] was initially constructed using 1.6 mm before it was realized that the eddy current losses are too significant. Consequently, a new stator was constructed which makes use of Litz wire. The specific Litz wire used, consists of 70 parallel strands, and a single strand has a diameter of 0.2 mm. The measured eddy current results for both the old and new stator, are shown in Table 3.3.

Conductor Diameter [mm]	Parallel Strands	Eddy Current Losses [W]
1.6	1	31
0.2	70	1

Table 3.3: Measured eddy current losses at 300 rpm [1]

In literature, a variety of methods exist to analytically or numerically (or the combination thereof) determine the eddy current losses, most of which are aimed at the design of inductors and transformers as with Van den Bossche *et al.* [32]. According to Van den Bossche *et al.* [33], the choice on the method largely depends on the desired accuracy, computational expense and complexity.

The approach by Van den Bossche *et al.* [32], is to categorize a particular situation according to a set of applicable analytic derivations. The methods are categorized according to low frequency, high frequency and wide frequency problems. The penetration depth is calculated in order to determine the appropriate method. The penetration depth is approximated by,

$$\delta = \sqrt{\frac{2\rho}{\omega_{e_{1|PM}} \mu_r \mu_0}} \tag{3.44}$$

where $\omega_{e_{1|PM}}$ is the magnetic field's angular frequency experienced by the conductor, due to the permanent magnets. Here $\mu_r = 1$ is assumed as copper's permeability is almost equal to that of free space. The copper resistivity ρ is obtained by (3.42).

According to Van den Bossche *et al.* [32], it is considered a low frequency situation when

$$d \leq 1.6\delta \tag{3.45}$$

is satisfied. The conductor diameter is denoted by d. In a low frequency situation, the assumption is made that the eddy currents induced within the windings do not noticably change the applied magnetic field inside the conductor as discussed by Van den Bossche *et al.* [33] and Wang *et al.* [31]. If this is not the case, then the eddy current induced magnetic field would also need to be taken into account. The conductors of the IDRFPM machine are assumed to be small enough so that the low frequency approximations which follow can be used.

Traditionally, the eddy current losses in windings are calculated using a classic equation derived by Carter [34]. The limitations are that it assumes only a one-dimensional (thus only in the radial direction) pure sinusoidal flux component. The classic approximation to the eddy current losses is described as

$$P_{eddy} = N\, Q\, n_p \left(\frac{\pi \ell d^4 \hat{B}_{r_1}^2 \omega_{e_{1|PM}}^2}{16\rho} \right) , \tag{3.46}$$

where N is the number of turns per coil per phase, Q is the total (including all three phases) number of stator coils, n_p is the number of parallel strands per turn, ℓ is the

axial length of the conductor, d is the conductor diameter, $\hat{B}_{r1}$ is the peak value of the fundamental field density component in the radial direction, $\omega_{e_{1|PM}}$ is the fundamental rotor electrical angular frequency and ρ is the resistivity of copper.

A more accurate method is suggested by Wang *et al.* [31]. The method makes use of the classic equation (3.46), and extends its use to accommodate for both radial and tangential flux components and does not assume pure sinusoidal flux components. According to Van den Bossche *et al.* [32], the superposition of the losses due to the radial and tangential fields is valid since the respective fields and induced eddy currents are orthogonal. The extra information of the field density is then obtained by a 2D FEM simulation and subsequently using the Fast Fourier Transform. This method is therefore known as the hybrid method. Furthermore, it provides for different values of flux densities to be used depending on the position of the particular winding layer. This is important because the flux densities are fairly higher closer to the magnets and from (3.46) the eddy losses are proportional to B^2. The eddy current losses calculated using the hybrid method is described as

$$P_{eddy} = N\ Q\ n_p \left(\frac{\pi \ell d^4}{16\rho}\right) \sum_{j=1}^{l} n_j \ \sum_{i=1}^{n} (i\omega_{e_{1|PM}})^2 \ \left(\hat{B}_{r_{ij}}^2 + \hat{B}_{\phi_{ij}}^2\right) \tag{3.47}$$

where i denotes the harmonic number, j is the layer number, footprint r represents the radial component and footprint ϕ denotes the azimuthal component. The number of conductors in a specific layer is denoted by n_j. The reader is encouraged to study the article by Wang *et al.* [31] for a more elaborative explanation on the hybrid method.

The hybrid method is implemented in the analytical script, and the results are found to be in good agreement with the measured results of Table 3.3. The classical approximation is also used by Oosthuizen *et al.* [1, pp. 33-35], and as expected, the results are slightly lower than in Table 3.3 since the loss contributions of all the other harmonic components are neglected. Therefore, it is concluded that the approach of (3.47) is satisfactory, and the same approach can be applied for the SORSPM machine in Section 4.5.3.2. Lastly, as a consequence of the results shown in Table 3.3, it is decided that all IDRFPM machine designs considered in this project are envisioned to utilise Litz wire. Furthermore, because the eddy losses are minute when Litz wire is used, the eddy losses can be omitted from the total loss calculation.

3.6 Other Losses

Usually, the total electromagnetic losses for synchronous PM machines include copper losses, iron losses and magnet losses. It is worth mentioning that any mechanical or friction losses are neglected in this study.

From the results shown in Section 3.5.3, it is concluded that the copper losses due to eddy currents can be ignored if Litz wire is utilised.

As the IDRFPM machine is completely ironless, the iron losses is omitted. Even if, for instance, aluminium rotor yokes are employed, the eddy current losses in the aluminium is expected to be negligible. This can be attributed to the IDRFPM machine's inherently low armature reaction field, which in turn, is due to the large effective airgap between the inner and outer rotor. Furthermore, it is envisioned for the IDFRPM machine to be cooled by means of natural convection. For this reason, the machine is excited with a fairly low current density to avoid excessive heat loss. This also contributes to a weak armature reaction field.

In Section 4.7, it is discussed that magnet losses are mainly as a result of stator MMF space harmonics due to the winding distribution, stator slotting, and finally, time-harmonics present in the stator magnetomotive force (MMF) due to non-sinusoidal currents originating from the VSD, as discussed by Wang *et al.* [35] and Huynh *et al.* [36]. In this project, perfect sinusoidal currents are assumed, as according to Wang *et al.* [35] and Wu *et al.* [37], the effects of non-sinusoidal currents are difficult to take into account. Since the IDRFPM machine does not exhibit varying reluctance due to stator slotting, and with the armature reaction being weak in general, the magnet losses are neglected.

In conclusion, the IDRFPM machine is a fairly simple machine to analyse, as many of the traditional loss sources can be ignored.

3.7 Total Losses and Efficiency

In conclusion of Section 3.5 and 3.6, the only losses remaining is that due to the phase winding resistance. Thus,

$$P_{losses} = P_{copper} \ , \tag{3.48}$$

where P_{copper} is obtained by using Equations (3.40) to (3.43). The efficiency at any operating point is calculated as,

$$\begin{aligned} \eta &= \frac{P_{out}}{P_{in}} \\ &= \frac{P_{mech}}{P_{mech} + P_{losses}} \ . \end{aligned} \tag{3.49}$$

The mechanical output power is P_{mech} is determined by

$$P_{mech} = \frac{n_{rpm}\pi}{30}\tau_{mech} \ , \tag{3.50}$$

where n_{rpm} is the mechanical speed in revolutions per minute (rpm) and τ_{mech} is the time average of the torque computed with (3.29).

3.8 Equivalent Circuit Model

The standard per phase equivalent circuit for a synchronous permanent magnet machine is shown in Figure 3.14. The equivalent circuit model is used in conjunction with the sub-domain analysis results to determine the voltage and current characteristics of the motor. Thus, the back-EMF is obtained with (3.25), the synchronous inductance is obtained with (3.39), and the phase resistance with (3.41). The phase current I_a is known beforehand as this is the sinusoidal current injected into the machine. Since all the values of the circuit parameters are known, the phase voltage at the terminals of the motor, V_a can be determined. When V_a is known, the number of turns per coil can be determined, as well as the overall efficiency of the machine.

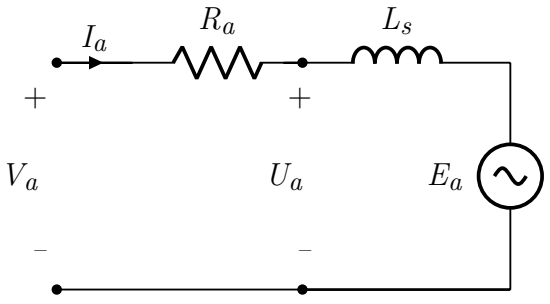

Figure 3.14: Per phase equivalent circuit of the IDRFPM motor.

3.9 Total Mass

The total mass considered for the IDRFPM machine will consist of the copper mass, a coil block mass, magnet mass and also a mass related to an aluminium drum thickness. The aluminium mass is added, to better represent a realistic mass of such a machine within a Mellowcabs vehicle. As mentioned in Section 2.2, an outer drum wall thickness of 10 mm is assumed. The outer drum will accommodate the outer rotor magnets. Also, an inner drum wall thickness of 10 mm is assumed. The inner drum will accommodate the inner rotor magnets. In the prototype of Oosthuizen *et al.* [1], Tufnol® blocks are used to help build the coils. This mass, although quite small, is also added to the total mass. The following mass densities are used for the total mass calculation:

Copper	$8954\,\mathrm{kg/m^3}$
Neodymium Magnets	$7500\,\mathrm{kg/m^3}$
Aluminium	$2700\,\mathrm{kg/m^3}$
Tufnol®	$1360\,\mathrm{kg/m^3}$

Table 3.4: Main materials used in the construction of the IDRFPM machine.

Chapter 4

Analysis of the SORSPM Machine

4.1 Introduction

From Chapter 3 it is clear that the machine for the Mellowcabs vehicle should have high torque, low speed and low voltage properties. Further requirements such as a relative high efficiency and a high power factor are also important. Consequently, a surface-mounted radial-flux PM synchronous machine with a single outrunner rotor is selected as a viable candidate for this application.

In this chapter, the different stator and rotor topologies are described. The analysis is done using 2D FEM software, of which two different packages are tested. Various losses are accounted for by means of analytical approximations, aided by simulation output data.

4.2 Stator Topology

4.2.1 Overview

As with the IDRFPM machine of Chapter 3, the concentrated double-layer non-overlapping windings are also selected for this machine. The experience and familiarity gained from Chapter 3 does play a part in motivating this decision, but even more so all the attractive traits it has. Generally speaking, low speed and high torque PM machines benefit from a fairly high pole count. This is usually true for all machines if frequency dependant losses

are ignored, according to Krause *et al.* [38, p. 609]. Depending on the slots-per-pole-per-phase ratio, a high pole count usually means a relatively high slot count too. In the pursuit of making construction as simple as possible, the aforementioned winding topology helps to keep the number of stator coils a minimum.

Another decision is to connect all the coil circuits in series. The result is that the total flux-linkage and back-EMF of each phase is simply the vector sum of each individual coil's flux linkage and back-EMF. If the phase coils are connected in parallel, circulating currents can flow between these parallel circuits because of a difference in back-EMF quantities as explained by Hanselman [15, p. 101]. These circulating currents contribute to the conduction losses without any benefit to the developed torque. To eliminate circulating currents, the voltage on the terminals of each parallel coil would need to be equal in magnitude and in phase, so that their instantaneous values are identical. This is very hard to achieve, especially when constructing prototypes, because a slight deviation of the symmetry in the machine due to manufacturing tolerances will cause circulating currents to flow in parallel connected coils. For these reasons, parallel connected coils are avoided for this project.

Other than for the IDRFPM machine, here it is more practical to utilise iron laminations for the stator yoke, stator shoes and rotor yoke. With the IDRFPM machine, it is not feasible to have iron laminations in the stator, as the stator is not supported from the outer or inner hubs of the machine. Because the SORSPM machine only has one rotor, the iron laminations help to reduce the reluctance of the flux paths. The reintroduction of iron is accompanied by many consequences, some beneficial and some undesired:

- increased flux density in the machine, resulting in an increased torque density
- iron losses are introduced, which now need to be accounted for
- a reluctance torque component is introduced, which causes greater torque ripple
- increased stator synchronous inductance, which results in better flux weakening capability
- iron saturation is introduced, which causes a non-linear relationship between the stator current and the torque produced
- the magnetic paths now exists mainly in the iron, which leads to decreased flux in the windings and subsequently less eddy losses in the windings, and thus opens the opportunity to use conductors with a larger surface area

Two variations of the stator teeth shapes are considered, that is those with open slots and the other with rectangular slots.

4.2.2 Open Slots

The rectangular teeth causes the slots to have wide openings. In literature, this topology is commonly known as "open slots", as referred to by Meier [39, p. 81], Rix [10, p. 52] and Van Wijk [40, p. 27]. This term might be confusing when the actual "slot openings" are discussed. The "slot openings" can either be "open" or "semi-closed", and describe the opening between two shoes, at the tip of the stator teeth as shown in Figure 4.1. The open slots topology can be seen in Figures 4.10 and 4.13.

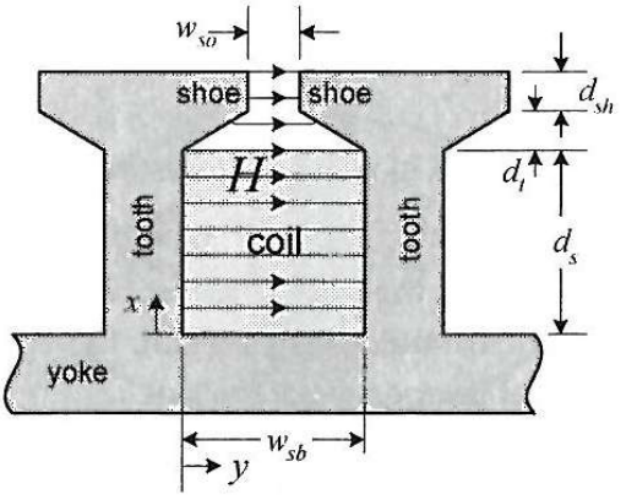

Figure 4.1: Extract is courtesy of Hanselman [15, p. 97], indicating the stator component names.

An advantage of this shape is that preformed coils can be shifted on the stator teeth, which simplifies the manufacture of the machine. The open slots allow for various types of conductors to be used, round or rectangular. A machine with this topology, also for a direct-drive vehicle application is investigated by Rix [10]. It is expected that the torque ripple for such designs would increase, as stated by Meier [39, p. 80]. This is as a result of the greater reluctance torque component caused by the wide stator slot openings. Furthermore according to Meier [39, p. 80], the overall airgap flux density is also less for open slot designs, compared to rectangular slots.

Although the open slot structure is mentioned here, in this project, the focus will remain on the rectangular slot topology discussed in Section 4.2.3. It is shown by Rix [10] that

the rectangular slot topology is superior to the open slot topology regarding the power efficiency. The open slots is indeed simulated in both SEMFEM (using the same script as all the other SORSPM designs) and compared against an ANSYS® Maxwell simulation in order to confirm the overall correctness of the SEMFEM script used for the SORSPM machine. This is further discussed in Section 4.4.3.

4.2.3 Rectangular Slots

The stator teeth have an outward taper as shown in Figure 4.2. This makes it impossible to slide preformed coils into the slots. One of the advantages of this topology is that rectangular coil slots are introduced, which allows for rectangular conductors and thus a higher fill factor. The use of rectangular conductors is shown in Figures 4.9a and 4.9c. This stator topology is also investigated by Rix [10], albeit using round conductors. A prototype is built by Rix [10] using removable stator teeth so that the coils can be wound before the stator teeth are fitted.

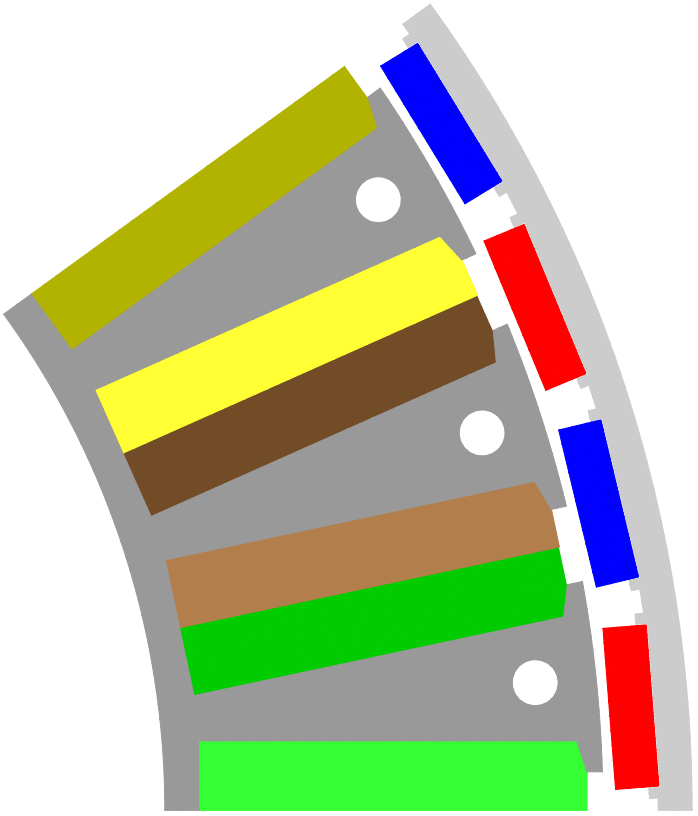

Figure 4.2: Example machine exhibiting rectangular slots, stator holes, and round conductors.

For this topology it is envisioned for the conductors to be inserted or wound manually and directly onto the the stator teeth. Usually this would be very labour intensive, but perhaps due to the unique low voltage limitation of this project, the number of turns is expected to be very low (less than 5 turns per coil). The conductors can either be inserted radially, given a wide enough slot opening, or the conductors can be inserted axially which subsequently allows any slot opening width (which will be referred to as semi-closed slots). It is expected that the rectangular slot structure will exhibit less torque ripple, and less eddy current losses in the copper windings, and less eddy current losses in the magnets, compared to the open slots structure. This is due to a smaller reluctance variation from the rotor to the stator.

As seen from Figure 4.2, a hole within the tooth is introduced. This has two functions. Firstly, non-magnetic and non-conductive rods (such as nylon rods) can be used to help compress the lamination stack. This way, the stack is compressed not only at the yoke, but is also supported more towards the end of the teeth. Secondly, it reduces the overall mass, without any detrimental effects towards the machine's performance given that the holes are appropriately positioned. It is envisioned for the hole to accommodate an M4 rod, so the hole is made 4.2 mm in diameter to provide for an overall construction tolerance.

4.2.4 Winding Conductors

4.2.4.1 Circular Litz Copper Wires

This option is the same conductors envisioned for the IDRFPM machine in Chapter 3. A fill factor of 0.47 is assumed, which is achieved in the prototype built by Oosthuizen *et al.* [1]. The effective fill factor is less than when normal round wire is used, but the advantage is of course reduced eddy current losses in the windings. The round Litz wire is inserted radially, while being wound at the same time. Figure 4.3 shows typical round Litz wire, where each strand is insulated with film.

Figure 4.3: Round Litz wire, displaying various strand numbers and diameters [41].

4.2.4.2 Solid Rectangular Copper Bars

A novel alternative is considered, where solid copper bars are inserted from one axial end. The bars are insulated from each other by means of precut FR4 boards. FR4 consists of woven fibreglass held together by epoxy resin, and is commonly used for the insulation layer between printed circuit boards. Sheets of various thicknesses are available. It seems that 0.5 mm to 5 mm thicknesses are commonly available from suppliers [42] [43] [44] [45]. A 0.8 mm board thickness is assumed for this project, as it is expected to have sufficient insulation and mechanical strength. The simulation models and drawings in this project, will however accommodate for a 0.9 mm gap along each copper bar side, so that sufficient construction tolerance is achieved. Furthermore, in this project, the copper bars will be utilised so that 2 turns per coil are formed. From experience, this number is found to be ideal for the constraints of this project. Examples of solid copper bars and off-the-shelf FR4 sheets are shown in Figure 4.4. This conductor type is investigated extensively in this project. The performance viability thereof and a proposed construction approach is discussed in Chapter 6.

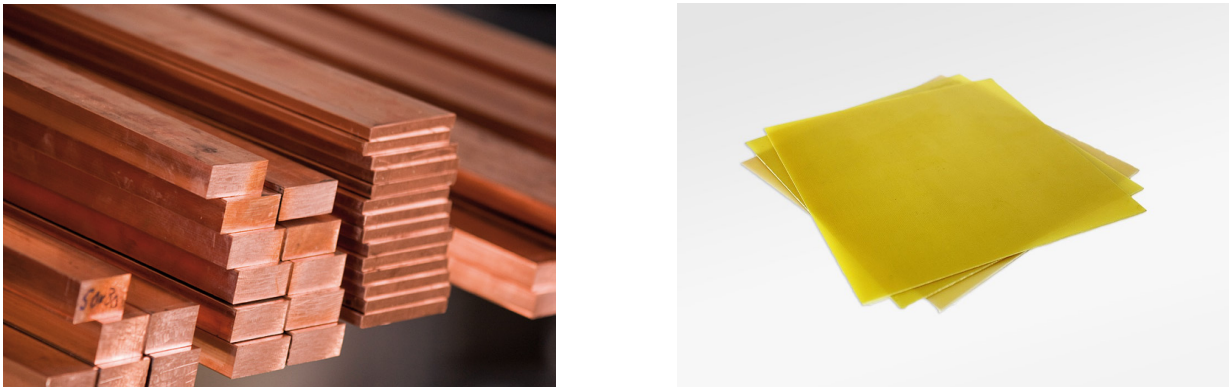

(a) (b)

Figure 4.4: (a) Solid copper bars can be cut in a wide variety of dimensions [46]. (b) FR4 sheets can be ordered in different widths and sizes [43].

4.2.4.3 Enamelled Rectangular Copper Wires

The rectangular copper wires could consist of “hair pins” which are preformed in a press. The hair pins are pushed into place from one axial end. The end turns on the other side are then welded or soldered together. Such hair pins are shown in Figure 4.5. The advantage is the ability to allow semi-closed slots. Notice that Figure 4.5 shows hair pins which are formed for an overlapping topology, whereas in this project the hair pins should be preformed for a non-overlapping structure. Alternatively, the rectangular wires can be wound directly on the stator stack, with the slot openings wide enough for the wires to

be inserted radially. It is envisioned that the turns are stacked in the radial direction, as shown in Figure 4.6. An effective slot fill factor of 0.85 is possible [47].

Figure 4.5: Preformed copper hair pins of the Chevrolet Spark EV motor [48].

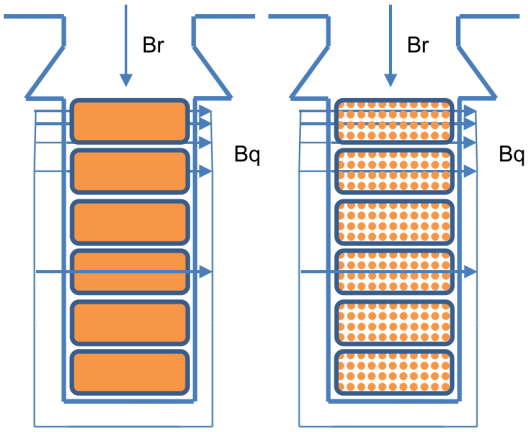

Figure 4.6: Rectangular slots are packed with regular rectangular conductors on the left, or rectangular Litz wire on the right [47].

4.2.4.4 Rectangular Litz Copper Wires

The last option considered for the rectangular slots, is that of rectangular Litz wire. Various insulation options are available from manufacturers such as Von Roll [49]. The insulation made of typical Nomex aramide paper (also known as transformer paper) is deemed the most suitable for the SORSPM machine, see Figure 4.7. This is because it is one of the insulation options which offers the most flexibility and the highest fill factor. The mechanical flexibility is an important requirement due to the relative small size and high number of slots encountered in this project. These conductors could be wound directly on the stator stack, and stacked radially as shown in Figure 4.6.

According to the product brochure [49], cross-sections from 1 to 500 mm^2, and width to height ratios ranging from 1.25 : 1 to 4 : 1 are available. A slot fill factor of 0.65 can be achieved [47].

Figure 4.7: Rectangular Litz wire with taped insulation [49].

4.2.4.5 Stator Connections

As already mentioned, the decision is made that all windings will be connected in series. This is to prevent circulating currents between parallel circuits, which causes torque pulsations and extra losses according to Hanselman [15, pp. 100-101]. This also makes the prototype construction more forgiving, as slight offsets between windings, or slight magnet placement offsets, could otherwise cause significant current flow between the parallel circuits.

It is expected that the conductor types which exhibit low fill factors, will result in machines which are longer in the axial direction in order to produce the required torque. In turn, this will increase the flux linkage of each turn, and thus increase the back-EMF. With the low voltage limit as discussed in Section 2.3, this could result in designs with a very low number of turns; such as 3 or 4 turns per coil. Naturally, this low number of turns will make the initial projected fill factor even more unreachable. That is to say, large round conductors will leave significant open spaces in a slot. Furthermore, fewer turns per coil usually means that a greater current magnitude will be required to achieve the same torque output. Consequently, the conductor diameter will need to be increased, which means the achievable bending radius of the conductors will increase, making it harder to form the coils. With this in mind, for coils consisting of wires, in this project only designs with a number of turns equal or greater than 4 will be accepted as practical.

Due to the aforementioned reasoning, it is decided to choose a delta (Δ) connection for the conductors with low fill factors. The phase voltage is thereby allowed a factor $\sqrt{3}$ greater than in the case of a star (Y) connection. This will allow a higher number of turns for the windings, and also a better fill factor.

It is worth noting that with a delta connection, the possibility of circulating currents are yet again introduced. The currents are caused by triplen harmonics (harmonics which are multiples of three) in the back-EMFs. The triplen harmonic back-EMFs add together and cause currents with triplen harmonic frequencies to flow in the delta loop. The triplen harmonics are present in machines which generate a non-sinusoidal back-EMF, as explained by Hanselman [15, p. 200]. This will be the case for many of the designs considered in this study, as the back-EMFs will not be perfectly sinusoidal. Naturally, these circulating currents cause extra I^2R losses which are neglected in this study, but it remains a concern for the comparison of the various machine topologies.

4.2.4.6 Summary

This section serves as a review of some of the different conductor options available for the SORSPM machine. Table 4.1 shows a summary of the various conductor types and the manner in which they could be implemented. In this project, open slots refer to slots which are wide enough for the conductors to be inserted radially, while semi-closed slots refer to slots which could be designed (optimised) in any manner, be it open, semi-closed or completely closed. This can be done since the conductors are inserted axially. The number of turns per coil is denoted by N.

Of the four conductor types presented in this section, only two of them are investigated in the optimisation procedure in Chapter 5, namely the circular Litz wires and the solid rectangular bars. From these two conductor types, a conclusion is made in Chapter 6 for the most promising conductor type for the SORSPM machine.

			Slot opening		
Rectangular slot conductors	N	Fill factor	Open	Semi-closed	Connection
Circular Litz wires	≥ 4	0.47	✓	✓	Δ
Solid rectangular bars	2	0.65		✓	Y
Enamelled rectangular wires	≥ 4	0.85	✓	✓	Y
Rectangular Litz wires	≥ 4	0.65	✓		Δ

Table 4.1: Summary of the various copper conductor types available for the SORSPM machine.

4.3 Rotor Topology

The decision to have an outrunner rotor stems from three motives. Firstly, this project is a comparative study between the IDRFPM machine and another synchronous PM machine alternative. Therefore, to be able to make a fair comparison, the alternative machine also needs to have an outrunner rotor. Secondly, for a PM synchronous machine, the rotor inherently requires less space than the stator. This means that with the rotor on the outside, the airgap diameter is larger, resulting in a greater developed torque compared to an inrunner rotor machine with an identical machine outer diameter. This is even more so for higher pole machines; the magnets become smaller, which results in less flux density (and less saturation) and as a reward the rotor iron yoke thickness can be decreased, as explained by Mi *et al.* [50] and Hendershot [51]. Of course there is an upper limit for the number of poles at which no benefit is gained. Thirdly, although this project focusses on a direct-drive application and not specifically an in-hub application, the intention is to leave the option open for future in-hub developments for the Mellowcabs vehicle.

Another benefit of this outrunner configuration is that the surface-mounted magnets are more rugged when placed on the inside of an outrunner rotor as opposed to the outside of an inrunner rotor. This is because the centrifugal forces actually help to hold the magnets against the surface on which they are mounted. For this reason, together with the low speed application of the motor, the magnets can simply be glued on the surface as opposed to using non-magnetic screws, of which the latter was recommended by Oosthuizen *et al.* [1, p. 96] and Groenewald [17, p. 30].

In the preceding arguments, it is already mentioned that surface-mounted magnets are envisioned for the SORSPM machine. Surface-mounted magnets have an advantage when the cooling of the machine relies mainly on natural air circulation. The magnets act as small fans, which help to dissipate magnet losses and stator losses according to Groenewald [17, p. 29]. Since this project focusses on the electromagnetic aspects of the machines, the use of surface-mounted magnets will help to avoid investigation into the cooling aspects of the machine. As a final motivation, surface-mounted magnets usually produce less flux leakage, as more flux can cross the airgap in order to develop torque. However, surface-mounted magnet designs are more susceptible to eddy losses as compared to interior magnet topologies as explained by Rix [10, p. 62]. The magnet loss analysis is further discussed in Section 4.7.

A comparison is made by Stegmann [13, p. 31], between various grades of magnets, regarding the cost and performance trade-offs when used in a radial-flux PM machine. It

concludes that it is overall more worthwhile to make use of high grade neodymium-iron-boron (NdFeB) magnets. Therefore, this project will utilise NdFeB N48 magnets, with N52 being the highest available grade, and N48 the second highest.

Figure 4.8 shows rectangular shaped magnets which are surfaced mounted. Rectangular magnets are chosen as they are deemed slightly easier to place, while the performance impact is thought to be negligible. Since the magnets are rectangular, the magnetisation is also changed so to that the magnetic fields are normal to the flat surface, instead of a radial magnetisation. A close look at Figure 4.8 will reveal that small air-like gaps (0.15 mm) are inserted between the magnets and the rotor yoke surface, as well as between the magnets and the locators. The purpose hereof is to provide a manufacturing tolerance, and to provide space for the glue to occupy. This will of course slightly decrease the magnetic flux density produced by the rotor.

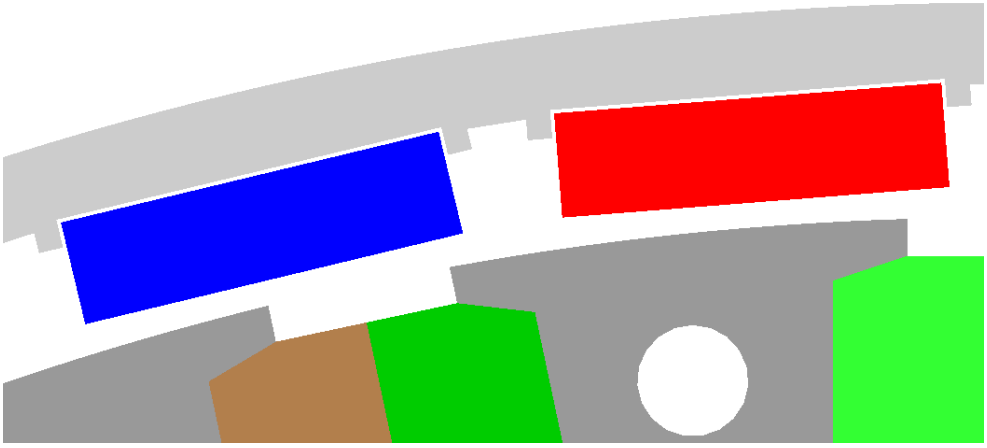

Figure 4.8: Rectangular magnets are used, and are kept in place with the help of small locators.

4.4 Electromagnetic Analysis

4.4.1 Introduction

The machine topologies presented in this chapter are analysed using the same in-house 2D FEM package, SEMFEM, which is also used in Chapter 3. The open slots topology is additionally simulated using a commercial FE package, named ANSYS® Maxwell. This is done in order to serve as validation for the simulation results in general. In this project, both packages are interfaced by using scripts programmed in the Python™ programming

language. The optimisation process in Chapter 5 will only make use of SEMFEM, as the simulation time in SEMFEM is significantly faster.

In Chapter 3, an analytical method is used to validate the 2D FE simulations. The application of the subdomain method for the IDRFPM machine results in an exact solution, since the harmonics normally caused by the saturation of iron is no longer present. But for the SORSPM machine, iron is used and therefore these unpredictable harmonics will exist. Although insightful analytical derivations are done by Rix [10], the purpose of these derivations were to aid the optimisation process, as opposed to being an exact representation of the machine. Furthermore, the decision to follow a pure FE approach allows for quick experimentation of various design types, without having to derive complex mathematical solutions.

4.4.2 Simulation Methodology

As with the IDRFPM machine, a symmetrical section of the machine can be simulated. This is shown in Figure 4.9. However, for the SORSPM machine, a full time-stepped simulation is necessary due to the iron present in the machine. With the IDRFPM machine, it is possible to simulate only a single step and subsequently use dq quantities to determine the induced voltage and developed torque. But for the SORSPM machine, additional performance outputs need to be assessed. These additional performance outputs, such as eddy losses in the copper windings, iron losses, magnet losses and torque ripple, can only be determined if a full electrical period is simulated. All of the aforementioned aspects could be avoided for the analysis of the IDRFPM machine. It is thus evident that the simulation and analysis of the SORSPM machine will require significantly more effort than the IDRFPM machine.

The final step in the symmetrical simulation of the SORSPM machine is shown in Figure 4.9d. It is interesting to see that the flux density and flux lines look almost identical to that of Figure 4.9b, which simply confirms that the simulated segment is indeed periodic and symmetrical. The number of steps between the start and end positions as well as the mesh density, can be altered to suit the required accuracy of the analysis.

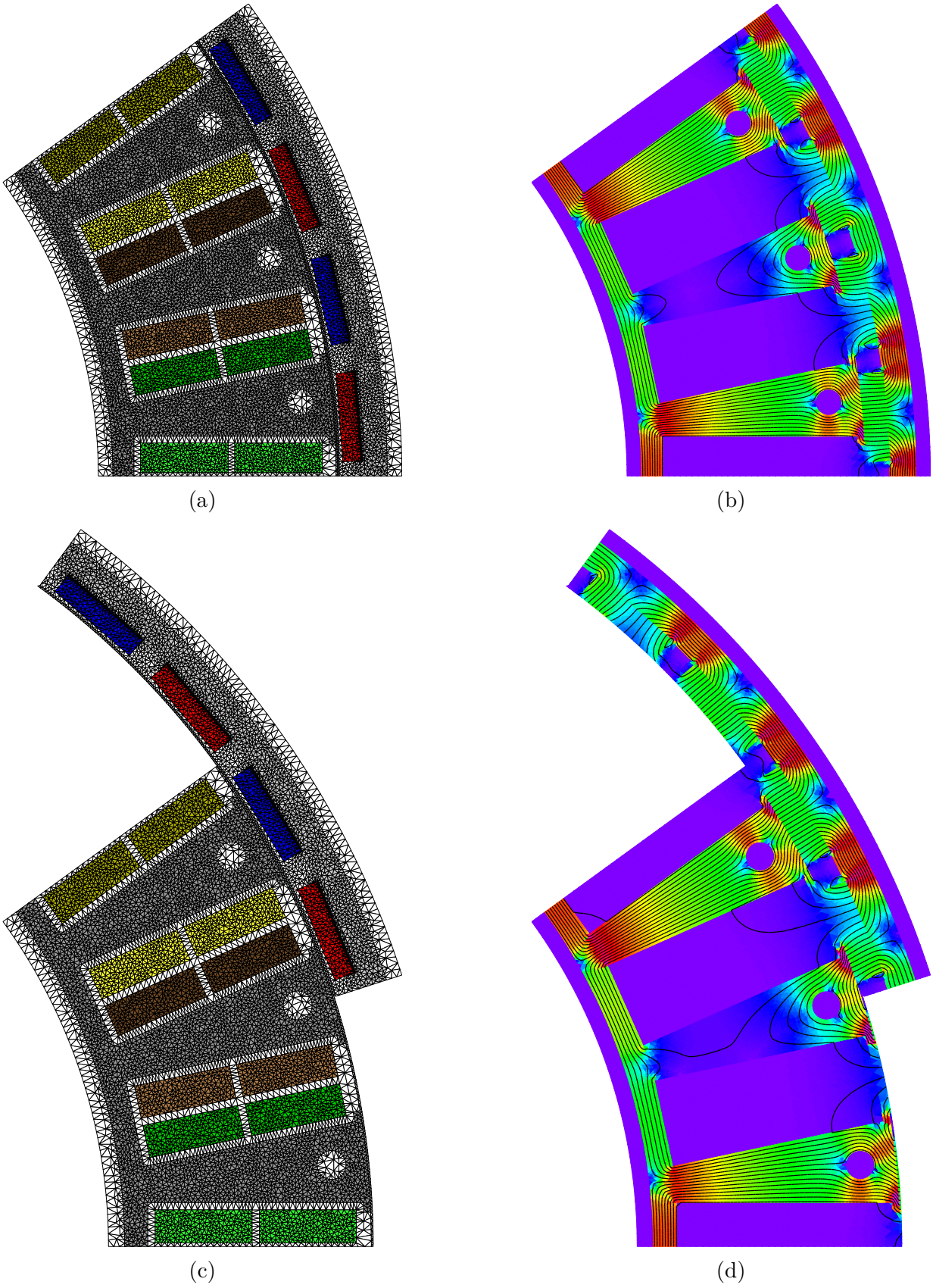

(a) (b)

(c) (d)

Figure 4.9: Starting positions in (a) and (b). Finishing positions in (c) and (d). An initial design (Appendix B) is simulated, with the mesh in (a)(c) and flux density and flux paths shown in (b)(d).

4.4.3 Simulation Validation

In order to validate the SEMFEM simulations for the SORSPM machine, an identical machine is benchmarked between the SEMFEM package and the commercial ANSYS® Maxwell package. Furthermore, a SEMFEM simulation is also benchmarked against a specific machine topology and dimension set which is designed and built by Rix [10, p. 78]. This way, all three sources validate each other, and the SEMFEM simulation script can be used with high confidence in the successive sections of this project.

Figure 4.10 shows both the SEMFEM and ANSYS® Maxwell models of a 40 pole and 30 slot machine. The dimensions of this machine are not of particular importance, as it is not optimised or sized for this specific direct-drive application. It is however important that for the exact same dimension inputs and current densities, an almost identical performance is achieved. To this end, the torque output for a full electrical period is compared in Figure 4.11. Furthermore, the radial flux density in the airgap is compared in Figure 4.12. Other quantities such as the phase flux linkages and the induced voltages also compare well.

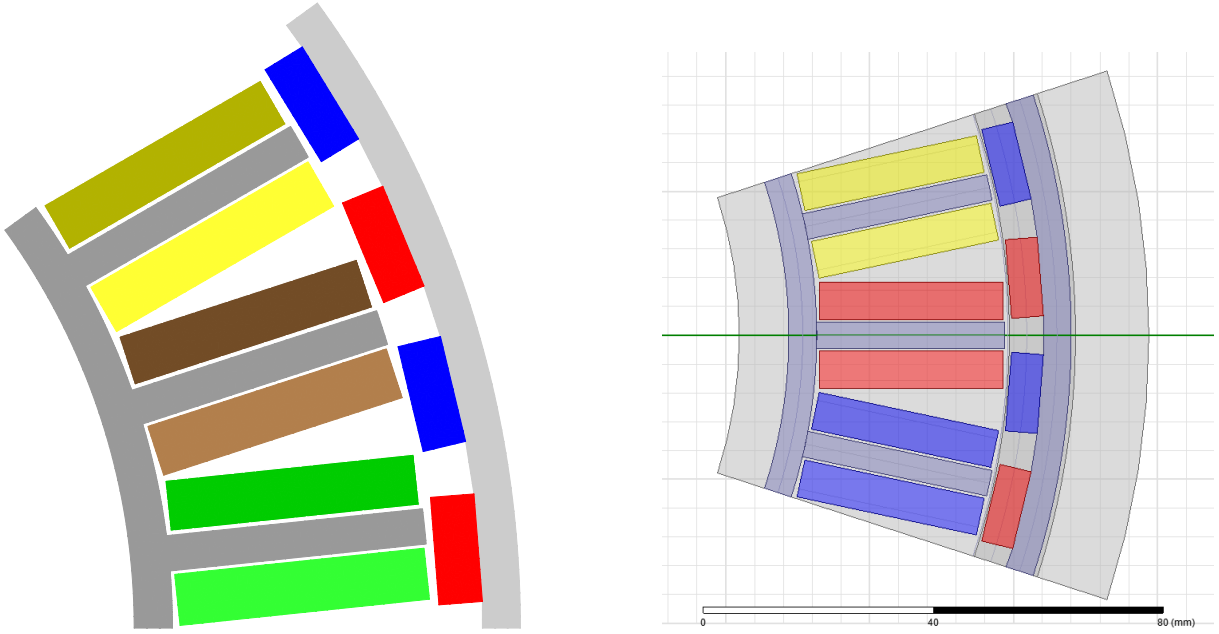

(a) (b)

Figure 4.10: A non-specific motor, which is simulated in a) SEMFEM and in b) ANSYS® Maxwell

The torque output is very similar for both simulation scripts. This was not originally the case, as it was found that a 0.95 stacking factor was used in the ANSYS® script. When the stacking factor is changed to unity, the torque curves become near identical. Additionally,

the mesh density and number of steps play a very important role in the "correctness" of the curves. It is found that a fairly high number of steps and fine mesh is needed to achieve the pleasing results presented here. For this benchmark, both simulations are configured to use 521 steps with a very fine mesh. The mesh quality in the airgap is found to be one of the most influential factors in achieving a "noise free" torque and radial flux distribution curve. The noisiness is dramatically decreased when an auxiliary arc is drawn within the airgap in the case of the ANSYS® simulation. A similar improvement is achieved for the SEMFEM simulation if the airgap is divided into three equally spaced airgaps. The ANSYS® Maxwell simulation made use of 91218 mesh triangles, and took 3 hours and 47 minutes to complete. The SEMFEM simulation made use of 35733 mesh triangles and took 8 minutes and 21 seconds to complete. The disparity in simulation time is in part attributed to the fact that a single-core license for the ANSYS® package is used, while SEMFEM utilises all the processing cores (a CPU with 8 core threads was used in this benchmark) during a simulation. A more elaborate discussion in the differences between the analysis techniques and computation times of ANSYS® Maxwell and SEMFEM is presented by Gerber *et al.* [52].

It is noteworthy, that by inspection, the torque in Figure 4.11, has a significant 6^{th} order harmonic component. This is as expected from the discussion in Section 3.4.3.4.

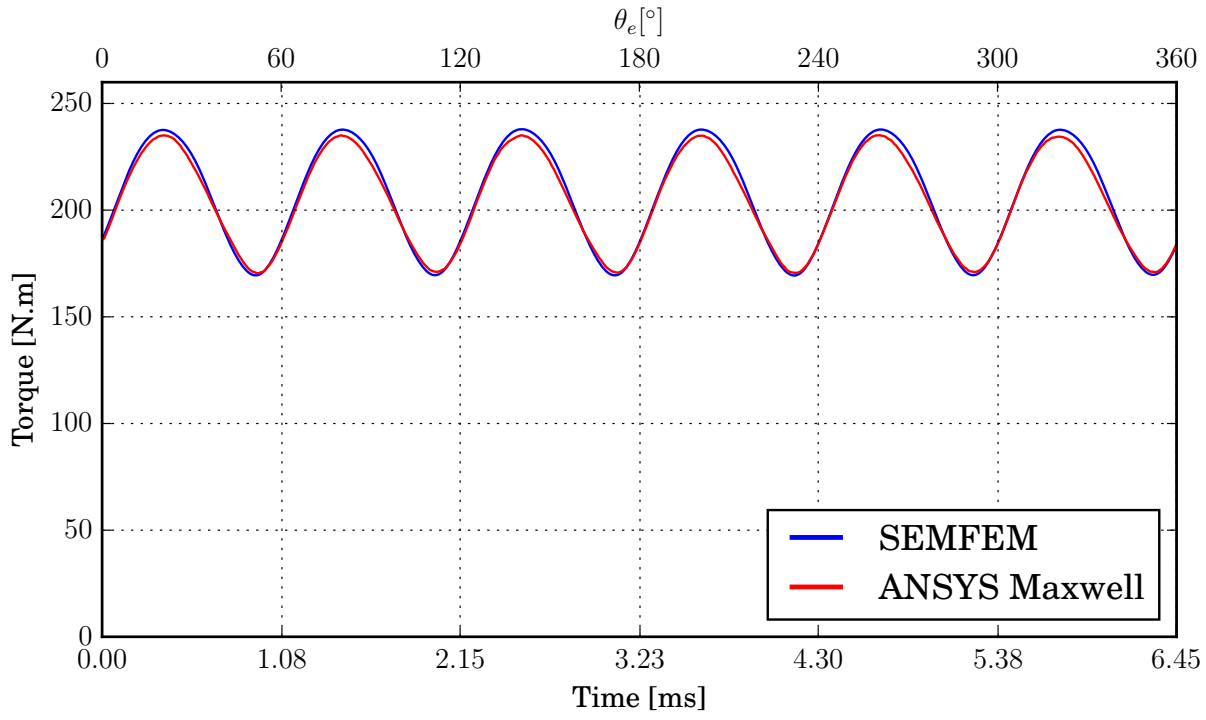

Figure 4.11: Torque benchmark of SEMFEM versus ANSYS® Maxwell, for the non-specific motor.

The prototype of Rix [10, p. 78] uses open slots with embedded magnets. This is illustrated by the SEMFEM model in Figure 4.13. The torque output, voltage, mass and phase resistance are all found to be very similar to that which is reported by Rix [10, p. 78].

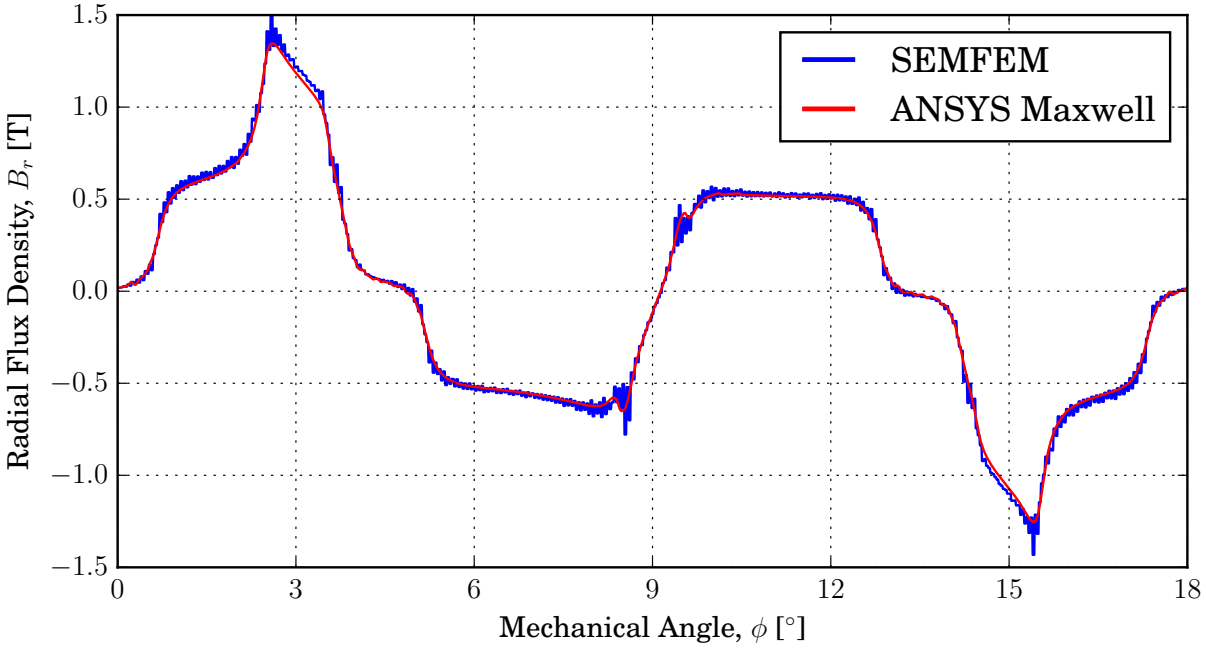

Figure 4.12: Radial flux density distribution at the radius in the centre of the airgap for the non-specific motor. The starting position is shown in Figure 4.10, with a q-axis current density of $i_q = 5\,\text{Arms/mm}^2$. Results of both SEMFEM and ANSYS® Maxwell are shown.

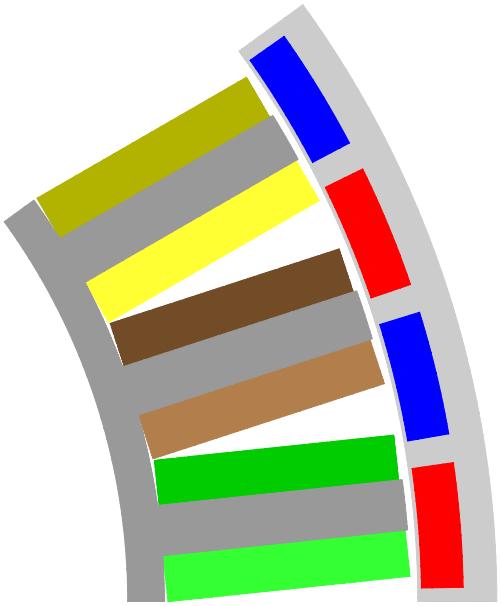

Figure 4.13: Open slots machine with 40 poles and 30 slots, featuring embedded magnets. Specifications are according to Rix [10, p. 78].

4.5 Copper Losses

4.5.1 Introduction

The copper losses in this section will focus on the use of solid rectangular copper bars, as opposed to the use of round wires in Chapter 3. Nevertheless, the use of round wires are also investigated for the SORSPM machine, and the performance trade-offs are presented in Chapter 6.

In this project, the copper losses are split into two components, that which is caused by the phase resistance namely the phase current losses, and then that which is caused by the eddy current losses within the conductors. In literature, the phase current losses is more commonly known as copper losses, however this term is rather confusing since it does not include all the copper losses. If the eddy current losses is neglected, then of course the term does make sense.

4.5.2 Phase Current Losses

The phase current losses describe the losses due to phase resistance experienced by the current injected into the machine. From the per phase model, these losses for all three phases are determined by

$$P_{copper} = 3I_a^2 R_a \ , \tag{4.1}$$

where a denotes the per phase quantities.

To calculate these losses, the phase resistance must first be determined. Although the SEMFEM package can determine a rough resistance value, it is more appropriate for the designer to calculate the resistance and the subsequent phase current losses manually. Recall that this project only utilises series connected circuits. The DC resistance of a phase winding is described by

$$R_{a|DC} = \frac{\rho \ell_{total}}{A_{slot} k_f} \tag{4.2}$$

where A_{slot} is the slot area, k_f the copper fill factor, and ℓ_{total} the total length of all the conductors which make up a phase winding. The actual area which consists of copper is described by the $A_{slot}k_f$ term. Throughout the design of the machine, the copper temperature is assumed to be $T = 75$ °C, which is the intended maximum operating temperature of a prototype. The copper resistivity ρ is obtained by the well known linear approximation,

as discussed by Hanselman [15, p. 91],

$$\begin{aligned}\rho &= \rho_{T_0}[1+\alpha(T-T_0)] \\ &= 2.09\times10^{-8}\ \Omega\cdot\text{m}\end{aligned} \tag{4.3}$$

where $\rho_{T_0} = 1.72\times10^{-8}\ \Omega\cdot\text{m}$ at $T_0 = 20\ ^\circ\text{C}$ and $\alpha = 0.0039\ ^\circ\text{C}^{-1}$.

The total length of a phase circuit is determined by the number of coils q connected in series, the number of turns per coil N, and the length of a single turn. Thus the total length of a phase circuit is,

$$\ell_{total} = 2qN(\ell+\ell_e)+q\ell_s \tag{4.4}$$

where ℓ is the active stack length of the machine, and ℓ_e is the length of a single end-turn. The end-turn length is approximated by the arc length distance of the incoming and outgoing conductors of a turn. The length of the series connection between each coil of a particular phase is accounted for by ℓ_s. Since (4.4) is substituted into (4.2), the assumption is made that the series connections use the same conductor diameter as the stator coil turns. Notice that the term $q\ell_s$ is not proportional to the number of turns N.

It is shown by Pyrhönen *et al.* [16, p. 459], Hanselman [15, p. 106] and Martínez [14, p. 52] that if only the resistance of the windings are considered, then the per phase copper losses are independent of the number of turns and can be determined by,

$$P_{copper} = \rho q V_{cu} J^2\ , \tag{4.5}$$

where V_{cu} is the copper volume in the slot, q the number of slots per phase, and J the current density.

However since the $q\ell_s$ term is introduced, (4.5) cannot be derived. Figure 4.14a shows the copper losses when the $q\ell_s$ term is ignored, and Figure 4.14b takes the effect of $q\ell_s$ into account. The current density, copper area ($A_{slot}k_f$) and thus the copper volume (V_{cu}) within the active length, are all kept constant for this illustration, and are used in both figures. Notice how significant the loss increase is when the number of turns are low. This is important because the designs presented in this project will most likely implement a low number of turns. Also notice that at 20 turns, the copper losses settle at a slightly higher value, 202.5 W, instead of the intended 200 W. Therefore in this project, the $q\ell_s$ term will be accounted for by substituting (4.4) into (4.2).

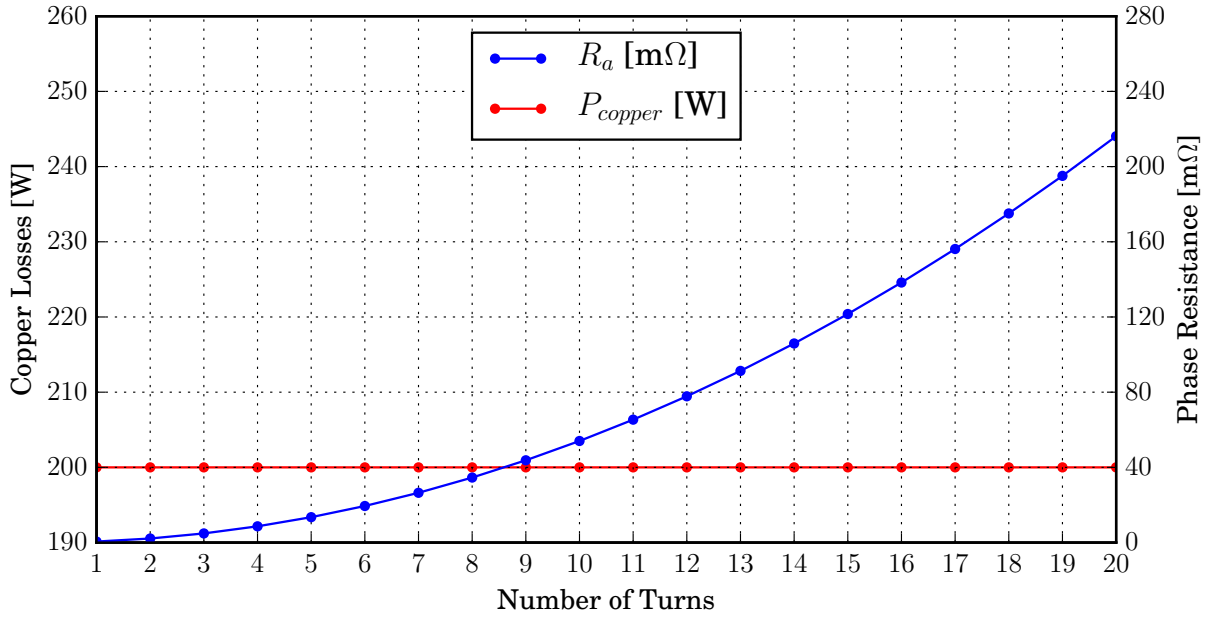

(a)

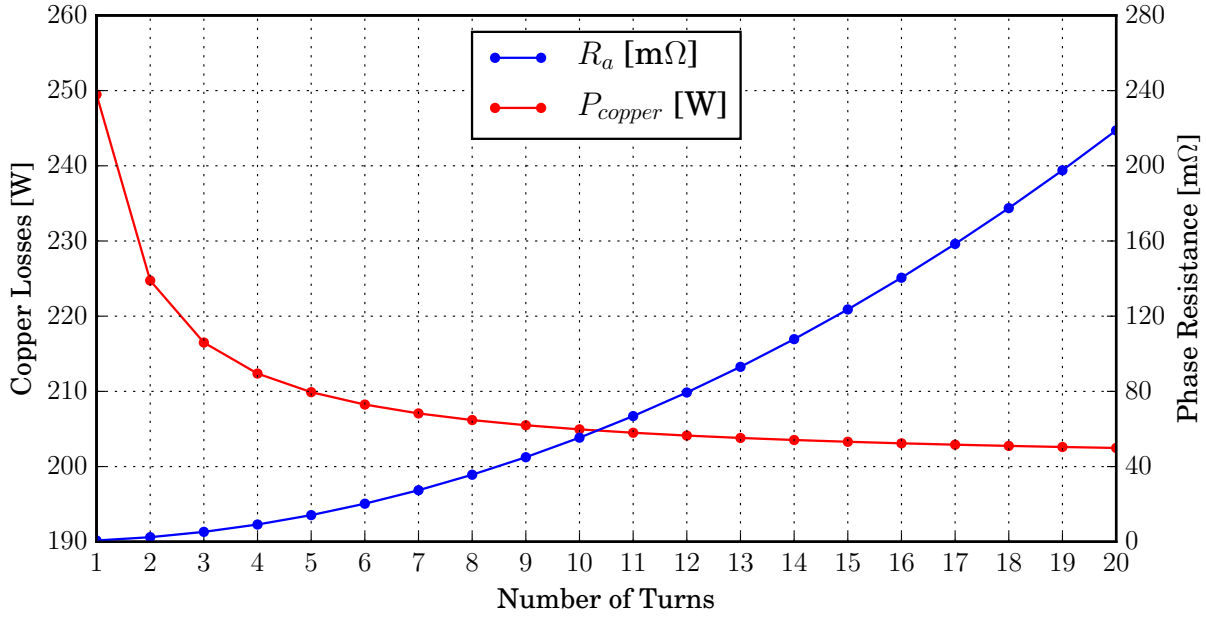

(b)

Figure 4.14: Copper losses and phase resistance versus number of turns per coil for an initial design (Appendix B), using a constant current density. In (a) the series connection resistance is neglected, and in (b) the $q\ell_s$ term is taken into account.

4.5.3 Eddy Current Losses

4.5.3.1 Skin Effect and Proximity Effect

When AC current is flowing through a conductor, it produces an alternating magnetic field within the conductor itself. In turn, the alternating magnetic field induces a voltage which

causes eddy currents to flow. The induced eddy currents exist in such a manner that it opposes the original AC current near the center of the conductor, while it superposes with the AC current towards the outer radius of the conductor. The result is that the current density is higher towards the surface and decreases exponentially towards the center. The effect therefore causes the conductor to have a higher effective resistance than when conducting a DC current.

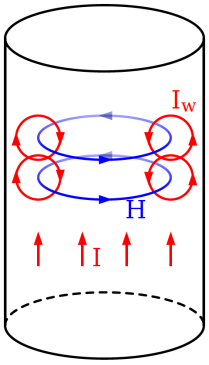

Figure 4.15: Eddy currents I_w induced by the alternating magnetic field H which is caused by the alternating current I.

If the relatively small diameter copper wires are substituted with larger rectangular copper bars, then the skin effect can start to play a modest role. A very thorough study by Van den Bossche *et al.* [32] is done for losses of various conductor shapes under a variety of circumstances. The analytical approximations are categorized according to low frequency, high frequency and wide frequency problems. The penetration depth is used as an indicator to the appropriate approximation. The penetration depth is described by,

$$\delta = \sqrt{\frac{2\rho}{\omega_{e_{1|AR}} \mu_r \mu_0}} \tag{4.6}$$

where $\omega_{e_{1|AR}}$ is the magnetic field's angular frequency present within the conductor, due to the phase current, thus the angular frequency of the injected sinusoidal phase current. Here $\mu_r = 1$ is assumed as copper's permeability is almost equal to that of free space.

According to Van den Bossche *et al.* [32], a low frequency approximation is suitable when

$$d \leq 1.6\delta \tag{4.7}$$

is satisfied. The conductor diameter, or the largest dimension of the conductor, is denoted by d. In a low frequency approximation, or also known as a first order approximation, the assumption is made that the induced eddy currents do not noticably change the orignal

magnetic field inside the conductor, as discussed by Murgatroyd [53], Namjoshi *et al.* [54], Van den Bossche *et al.* [33] and Wang *et al.* [31]. This is the easiest route of determining the eddy current losses (due to the skin effect), if this is not the case then the eddy current induced magnetic field would also need to be taken into account. It is emphasised by Van den Bossche *et al.* [32] that if the problem qualifies for the low frequency approximation, it does not imply that the eddy current losses will be small.

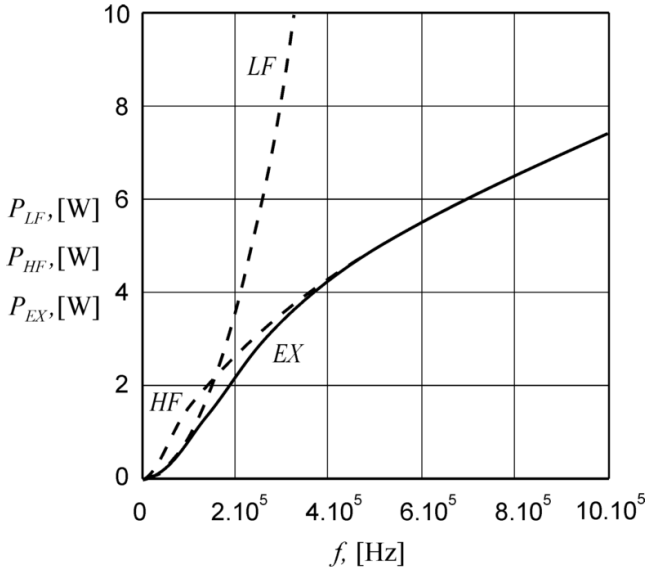

Figure 4.16: The power losses attributed to a case-specific conductor, due to a low frequency (LF), high frequency (HF) and exact (EX) approximations of the skin effect. Extract courtesy of Van den Bossche *et al.* [32].

Copper bar width (a)	5.08 mm
Copper bar height (b)	15.46 mm
Active stack length (ℓ)	100 mm
Maximum speed	465 rpm
Poles	40
Electrical frequency	155 Hz
Copper skin depth	5.84 mm

Table 4.2: Snippet of parameters from Appendix B of an initial design attempt.

Consider Table 4.2, a snippet of the parameters from an initial machine design. The complete parameters are given in Appendix B. The longest side of the rectangular copper bar conductor is 15.463 mm, which is 2.65 times the penetration depth. Although this ratio is greater than (4.7), the approximation will produce a slightly higher equivalent resistance than an exact approximation. The increase will only become prominent on a logarithmic

scale as shown in Figure 4.16, which far exceeds the frequency range that is investigated in this project. Nevertheless, the slightly overcompensated result can easily be justified by the fact that proximity losses are not taken into account. Therefore, this low frequency approximation is used throughout the design process, with the idea that it considers the proximity losses to some extent.

Rectangular Conductors

As illustrated by Figure 4.17, this approximation describes the resistance of several rectangular conductors within a slot, all carrying an identical current. The slot exists in an infinite permeability material, resembling that of iron. Of course this is not a perfect representation of the concentrated double-layer SORSPM conductor and slot configuration, but it is certainly more acceptable than implementing a pure DC resistance for the loss calculations.

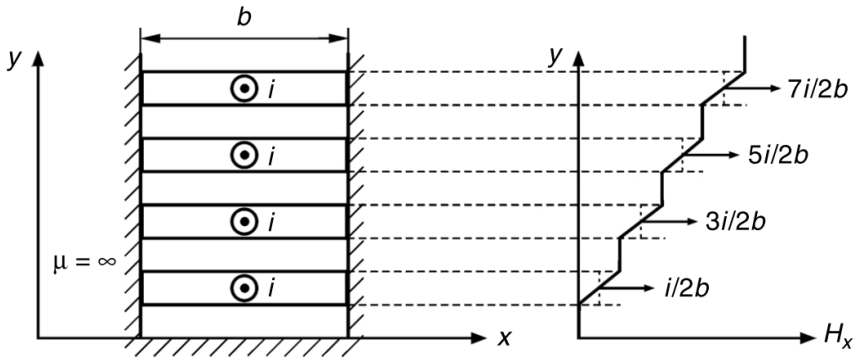

Figure 4.17: Several rectangular conductors surrounded by regions with infinite permeability. The magnetic field strength seen by each conductor is shown on the right. Extract courtesy of Van den Bossche *et al.* [32].

Notice that in Figure 4.17 the strength of the transverse fields due to each conductor is depicted on the right. This means each conductor is exposed to a transverse field caused by all the other current-carrying conductors. The transverse field is alternating, since the current source is also alternating. These alternating transverse fields, also cause eddy currents to flow in neighbouring conductors. As with the skin effect, this again causes an increase in the effective resistance of a conductor. This is known as the proximity effect. The proximity effect is simply the skin effect, but applied towards closely grouped conductors.

It is shown by Van den Bossche *et al.* [32] that the increased AC resistance of a particular conductor due the proximity effect, becomes increasingly significant when more current-

carrying conductors are present. Therefore in this design, where a very small number of turns (bars) are used, the transverse fields due to the proximity effect are ignored in the particular approximation that is used here.

The AC resistance which replaces the use of (4.2), is the superposition of the DC resistance and the resistance due to the skin effect. The low frequency solution is adequately approximated by the first and third term of a Taylor expansion as,

$$R_{a|AC} = \frac{\rho \ell_{total}}{ab}\left(1 + \frac{a^4 \omega^2_{e_{1|AR}} \mu_r^2 \mu_0^2}{720\rho^2}\right) \tag{4.8}$$

where a is the shorter side and b the longer side of the rectangular conductor.

Considering again the parameters from Table 4.2, the DC and AC resistances of a single copper bar are computed as shown in Table 4.3. The AC resistance amounts to a 27.1 % increase compared to the DC resistance.

DC Resistance	26.6 µΩ
AC Resistance	33.8 µΩ

Table 4.3: DC and AC resistances of a copper bar from the initial design attempt of Appendix B, at maximum speed.

Circular Conductors

For the circular conductors, the diameter is very small compared to the skin depth, so the AC resistance becomes negligible and thus only the DC resistance is used in the loss analysis.

4.5.3.2 Transverse Fields

As discussed in Section 3.5.3, the transverse fields (other than that caused by the skin effect and proximity effect) are produced by the magnetic fields due to the magnets. As the rotor rotates around the stator, the magnetic fields of the poles cut through the conductors in the stator. These moving magnetic fields appear to be alternating from the conductor's perspective and subsequently, alternating currents (eddy currents) are induced within the conductors.

In the IDRFPM machine, the magnets' fields are uniformly spread in the stator since there is no iron in the stator to attract the magnetic fields. With the SORSPM topology, the magnetic path now favours the iron teeth, which means the magnetic flux density is lower in the windings compared to a similar sized IDRFPM machine.

For rectangular conductors experiencing transverse fields, a low frequency approximation is presented by Carter [34] and Murgatroyd [53]. The transverse field should be directed perpendicular to the conductor axis and parallel to a pair of faces. The assumption is made that the incoming field is spatially uniform. The losses experienced by such a conductor are described as,

$$P_{eddy} = \frac{1}{24\rho}\omega_{e_{1|PM}}^2 B_{r_{1|PM}}^2 ab^3\ell \tag{4.9}$$

where $B_{r_{1|PM}}$ is the RMS value of a perfect sinusoidal alternating field in the radial direction, caused by the rotor magnets. This alternating field has a fundamental electrical angular frequency of $\omega_{e_{1|PM}}$. It is interesting to note the similarities between (3.46) and (4.9), with (3.46) being the approximation for round conductors.

A method to represent conductors of various shapes with an equivalent radius is presented by Namjoshi *et al.* [54]. The equivalent radius is derived from the moment of inertia of the conductor cross section, and allows certain symmetrical shapes, such as a rectangular conductor, to use classic approximations based on circular conductors. Using the method of Namjoshi *et al.* [54] delivers

$$P_{eddy} = \frac{1}{2}\frac{1}{\delta^3}\left[(2a)^3\left(\frac{b}{3(a+b)}\right)\right]\frac{H_{r_{1|PM}}^2\rho}{\delta}(a+b)4\ell \ , \tag{4.10}$$

which after some simplification actually deduces to the same result as (4.9), given that by Namjoshi *et al.* [54] the rectangle sides are described by $2a$ and $2b$, instead of just a and b.

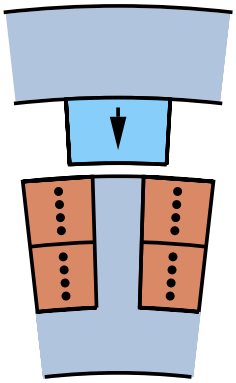

Figure 4.18: Points within rectangular conductors (two bars or two turns, per coil) which are sampled during one full electrical period.

Since the incoming transverse fields are not spatially uniform, and does not have a single sinusoidal component, (4.9) is modified in a similar manner as was done with (3.46) and (3.47) for round conductors. As depicted in Figure 4.18, the flux density is obtained at

several layers (sampled as a single point in each layer) within each rectangular conductor. This allows the eddy current losses to be determined for each bar (conductor) separately. The flux densities are obtained at multiple steps during a full electrical period. The magnitudes and harmonic components thereof, are found to be equal for each phase over a full electrical period. Thus only a single coil winding needs to be analysed. Figure 4.19 shows the radial and azimuthal flux density values found in each rectangular bar, for a two-bar (two-turn) per coil configuration. The values of the layers are averaged into a single radial and azimuthal component, and then a Fast Fourier Transform (FFT) is used to determine the RMS value of each harmonic component. The number of layers to be sampled should be chosen, keeping in mind the FE resolution (mesh density) inside the conductor area. The modified equation of (4.9) is described as,

$$P_{eddy} = \frac{ab^3\ell}{24\rho} \sum_{i=1}^{n} (i\omega e_{1|PM})^2 \left(B_{r_i}^2 + B_{\phi_i}^2\right) \tag{4.11}$$

where i denotes the harmonic number, and P_{eddy} just the losses for a single copper bar in a specific layer.

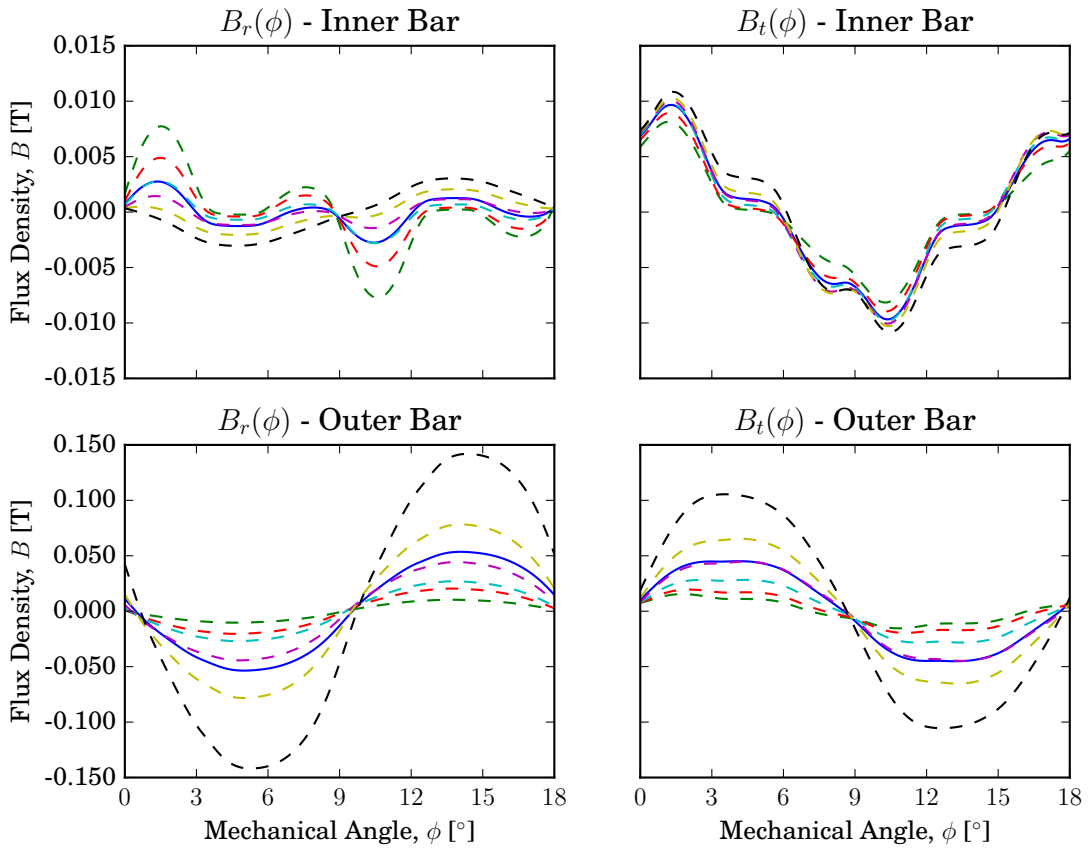

Figure 4.19: Radial and azimuthal flux densities which traverse the rectangular copper bars during a full electrical period, under no-load conditions. Various layers (dashed lines) are averaged and represented by a single solid line. Machine specifications in Appendix B.

Finally, if only two bars per coil is implemented, all the losses within the copper are summarised as

$$P_{copper|TOTAL} = 3I_a^2 R_{a|AC} + 2Q(P_{eddy|inner} + P_{eddy|outer}) \ , \tag{4.12}$$

where $P_{eddy|inner}$ and $P_{eddy|outer}$ denote the losses for a single inner and outer bar respectively. Table 4.4 shows the per bar losses, as well as the total losses for all the bars in the entire machine. Note that the losses are tabulated for the operating point at top speed, which is a worst case scenario for the eddy current losses. As expected, the losses are greatest for the outer bars, which is closest to the rotor, since it experiences the highest change in magnetic flux density (Figure 4.19) due to the movement of the rotor poles. It is noteworthy to see that the scale in Figure 4.19 for the flux density on the outer bar is 10 times greater than the scale of the inner bar.

	Per Bar [W]	Total [W]
$P_{eddy\|inner}$	0.18	10.58
$P_{eddy\|outer}$	2.87	172.29
$P_{eddy\|total}$		182.87

Table 4.4: Eddy current losses within the rectangular copper bars. The SORSPM initial design (Appendix B) is simulated at the top speed of 465 rpm operating point.

4.6 Iron Losses

Iron losses are caused by an alternating magnetic field density within the iron, and are typically represented by two components, an eddy current loss component and a hysteresis loss component. However, Reinert *et al.* [55] points out that this does not mean that the physical effects can also be separated into two independent effects.

For the design of the SORSPM, a very basic approach is used to determine the iron losses. It is assumed that iron laminations are utilised, so that eddy current losses can be neglected. The remaining iron losses can thus be accounted for by the hysteresis losses. The hysteresis losses exist due to the energy required to continuously change the magnetic field density within the iron. The hysteresis losses are automatically determined by SEMFEM, which makes use of a time-domain implementation of the well-known Steinmetz equation,

$$P_{hysteresis} = C_m f^{\alpha} B^{\beta} \tag{4.13}$$

where $P_{hysteresis}$ is the losses per volume, and C_m, α and β are coefficients which can usually be obtained by curve fitting the losses versus flux density graphs supplied by the material manufacturer. The SEMFEM default assumes $C_m = 2 \times 10^{-4}$, $\alpha = 2$ and $\beta = 2.5$. By using the in-built core loss function of SEMFEM, additional complexity and computation of the iron losses are avoided. Specifically, the process to sample magnetic flux densities at various points within the SEMFEM simulation is computationally expensive. This decision translates into swift optimisation iterations, to be discussed in Chapter 5.

It is well known that the emperical Steinmetz solution has many shortcomings. A more in-depth study of the iron losses could involve the implementation of the Modified Steinmetz Equation (MSE) discussed by Reinert *et al.* [55], or other approaches such as those proposed by Chen *et al.* [56], Soulard [57] and Ionel *et al.* [58].

As an example, the iron losses in the rotor and stator, as determined by SEMFEM for the initial SORSPM design (Appendix B) is shown in Table 4.5. As can be seen, the stator losses are far higher than the rotor losses. This is mostly due to the changing magnetic fields seen by the stator, caused by the moving rotor poles, and also to a lesser degree, the alternating magnetic fields caused by the alternating phase currents in the stator. The magnetic field in the rotor is much more constant, as the main source of alternating fields are derived from the varying reluctance of the flux paths due to relative movement of the rotor with the stator teeth.

P_{rotor}	15.11 W
P_{stator}	194.94 W

Table 4.5: Hysteresis losses for the initial SORSPM design (Appendix B) during top speed, using the Steinmetz equation.

4.7 Magnet Losses

4.7.1 Introduction

Eddy current losses exist in the magnets of synchrnonous PM machines. These eddy losses in the magnets, are commonly known as magnet losses. In literature, the magnet losses are attributed to three main causes as discussed by Wang *et al.* [35], Polinder *et al.* [59], Toda *et al.* [60], Fang *et al.* [61] and Huynh *et al.* [36]. Firstly, the varying reluctance caused by the rotor's movement relative to the stator teeth (commonly known as stator slotting). Secondly, some winding distributions, such as a non-overlapping topology, produce signifi-

cant stator MMF space harmonics which move at different speeds and directions than that of the rotor magnets. Lastly, non-sinusoidal excitation currents produce time harmonic MMF components, which also cause additional eddy current losses within the magnets. The latter is caused by the switching of the power electronics in VSDs. In this project a pure sinusoidal excitation current is assumed, which is reasonable when line inductors are installed.

The main concern of the magnet losses according to Wills *et al.* [62] and Wu *et al.* [37], are that the magnets can build up excessive heat causing irreversible demagnetisation. Additionally, according to Huynh *et al.* [36], it is more difficult to extract the heat produced in the rotor than heat produced in the stator.

Methods to alleviate the magnet losses include smaller stator openings, employing a retaining ring for the magnets, a larger airgap, and segmentation of the magnets as discussed by Wills *et al.* [62].

All of the above measures can be avoided, if a rough estimation can prove that the magnet losses are not severe for the application in this project. Furthermore, the optimisation process can make use of a rough magnet loss estimate in order to avoid designs with excessive magnet losses.

The difficulty in determining accurate magnet losses, as well as the difficulty of implementing such approximations, are well known according to Wu *et al.* [37]. This is due to the fact that many analytical derivations are either too complicated or too simple, and usually ignore some of the key aspects involved in producing magnet losses. Wu *et al.* [37] states that the simulation of eddy currents using 2D or 3D FEM can be accurate, but is usually too slow to include in an optimisation process.

4.7.2 Methodology

With inspiration from Rix [10], a similar and simple approach is used to approximate the eddy losses within the magnets. The magnet's flux density is analysed using a time-stepped 2D FE simulation, and then inserted into an analytical power loss calculation. Two distinct analytical formulas are implemented and compared so that better confidence in the results is obtained. These two approaches are discussed in Section 4.7.3 and 4.7.4 respectively.

The flux density within the magnet is obtained using a 2D FE simulation. The magnet is only sampled at a single point, as shown in Figure 4.20. The assumption here is that each region of a particular magnet experiences roughly the same alternating flux density.

This can be explained by the fact that each region within the magnet experiences the same reluctance space distribution as the rotor moves relative to the stator. In the case of the copper conductors of Section 4.5.3.2, several sample points are needed because each sample point is further from the flux path produced by the magnets. The magnet loss calculation presented here will focus on the losses due to stator slotting, since the armature reaction is fairly weak for a naturally cooled machine and sinusoidal excitation currents are assumed.

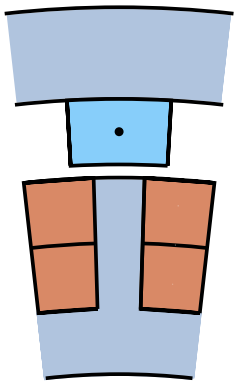

Figure 4.20: Sample point within a magnet.

Many articles concerning magnet loss calculation, categorise the eddy current losses according to resistance limited (low frequency) or skin limited (high frequency) problems, as discussed by Fang *et al.* [61] and Wang *et al.* [63]. Both analytical approximations presented here assume resistance limited eddy current losses. A quick check is done to see if this assumption is valid and if the magnet skin depth adheres to (4.6),

$$\delta_{PM} = \sqrt{\frac{2\rho_{PM}}{2\pi f_{slots}\mu_r\mu_0}} \tag{4.14}$$

where the electrical resistivity of N48 neodymium iron boron (NdFeB) magnets is obtained from a manufacturer datasheet [64] as $\rho_{PM} = 1.5$ µΩ/m, and the relative permeability $\mu_r = 1.05$. The conductivity of the magnets is therefore about 1% of the conductivity of pure copper. It is assumed that the glue used to attach the magnets to the rotor surface will isolate the magnets from the rotor structure, so that eddy currents originating in the magnets are limited to the magnets alone. Since this magnet loss calculation will focus on the losses caused by the stator slots, the frequency at which magnets "experience" the stator slots is defined as,

$$f_{slots} = \frac{n_{rpm}Q}{60} \tag{4.15}$$

where n_{rpm} is the machine speed in rpm and Q the total number of slots. It is instructive to see that the fundamental slot frequency f_{slots} is the 3$^{\text{rd}}$ harmonic shown in Figure 4.21. The parameters of interest of the initial design (Appendix B) is shown in Table 4.6. The slot frequency, and subsequently the skin depth can then be calculated as $\delta_{PM} = 39.45\,\text{mm}$, which satisfies the requirement of (4.7) for a low frequency approximation.

Magnet width (b_{PM})	15.16 mm
Magnet height (h_{PM})	3.15 mm
Active stack length (ℓ)	100 mm
Maximum speed	465 rpm
Poles	40
Slots	30
Electrical frequency	155 Hz

Table 4.6: Snippet of parameters from the initial design (Appendix B).

4.7.3 Method 1

The magnets are seen as rectangular conductors which experience alternating transverse fields. The approximation is based on the discussion of the eddy losses of rectangular copper conductors in Section 4.5.3.2. The analytical equation used here, is similar to the equation used by Rix [10] and Polinder *et al.* [59], but differs in that both the width and the height of the magnet are considered.

Figure 4.21 shows the magnetic flux density within a magnet, during open circuit operation. Notice that, other than in Figure 4.9 and 4.19, here the machine is rotated two electrical periods instead of one. This is done so that Figure 4.21 is periodic and perhaps more intuitive to the reader. Therefore during this new simulation period, a magnet experiences the passing by of three stator slots. This is evident from the dominant 3$^{\text{rd}}$ harmonic shown in Figure 4.21.

The magnetic flux density harmonics, in both the radial and tangential directions, are substituted into (4.11) keeping in mind the aforementioned magnet resistivity and slot frequency values. The results thereof are plotted for the entire speed operating range in Figure 4.22, and labelled as “Method 1”. Both the open circuit and rated current scenarios are shown. The values seem on par considering the magnet losses determined for a machine reported by Cote *et al.* [18], with a similar topology, size and performance.

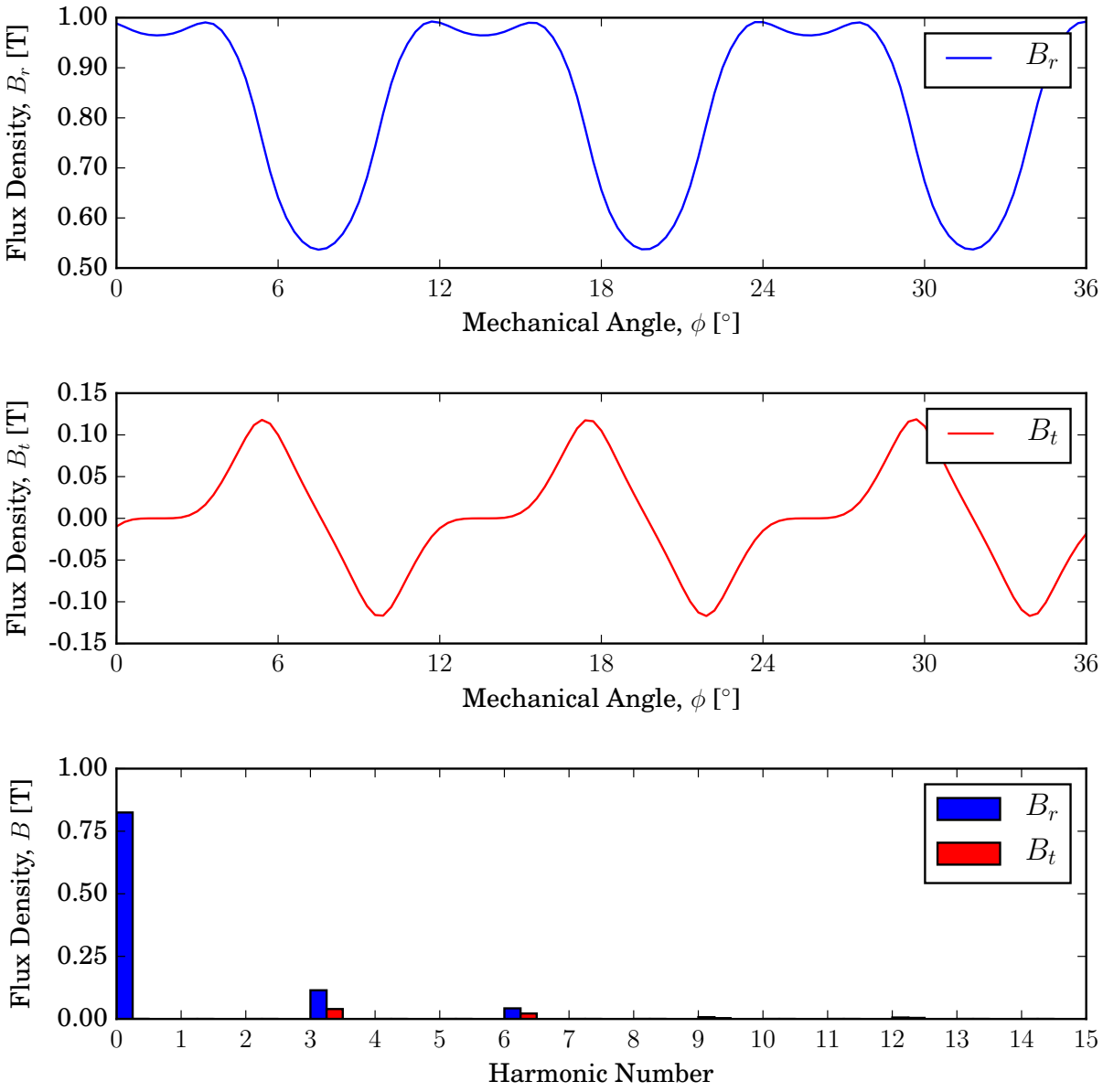

Figure 4.21: Magnetic flux density within a magnet and harmonics thereof is shown. The initial design (Appendix B) is simulated for two electrical periods, under no-load conditions.

4.7.4 Method 2

This method is presented by Markovic *et al.* [65] and discussed by Fang *et al.* [61], and uses an analytical expression to describe the open circuit magnet losses due to stator slotting. The analytical expression only makes use of the magnitude of the radial flux density $\hat{B}_r$. In this section, the radial flux density within the magnet is obtained from the FE simulation when the magnet and a stator tooth are perfectly aligned. As an alternative, the radial flux density of a one-dimensional (1D) analytical approximation is also used for comparison.

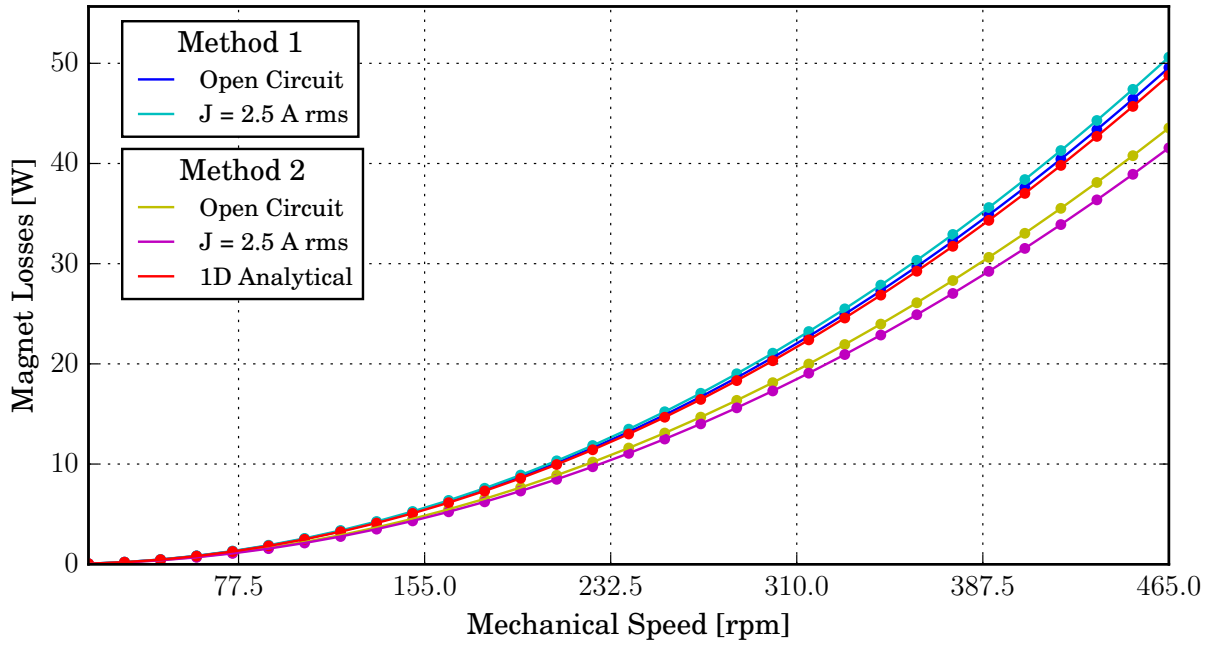

Figure 4.22: Magnet losses versus machine speed, with both the no-load and rated current scenarios shown for the initial design (Appendix B).

The results using the FE simulated flux density is represented by "Open Circuit" and "$J = 2.5\,\text{Arms}$" under the "Method 2" title in Figure 4.22. The results obtained by using the open circuit 1D analytical flux density in the magnet, as described by Zhu *et al.* [66] and Fang *et al.* [61], is represented by "1D Analytical". The total losses in all the magnets are determined by,

$$P_{magnets} = \frac{p\ell h_{PM}\hat{B}_r^2 v_r^2 b_{PM}}{\rho_{PM}} \sum_{i=1} K_i^2 \left[1 - \left(\frac{\tau_t}{\pi i b_{PM}} \sin\left(\frac{\pi i b_{PM}}{\tau_t}\right)\right)\right] \tag{4.16}$$

where p is number of pole pairs, ℓ the stack length, h_{PM} the magnet height, b_{PM} the magnet width, v_r the stator surface speed, τ_t the slot pitch. The summation is a Fourier series of a modulation function describing the stator surface. The coefficient is described as,

$$K_i = \beta \frac{4}{\pi i} \sin\left(\frac{1.6\pi i b_0}{\tau_t}\right) \left[0.5 + \frac{(ib_0/\tau_t)^2}{0.7815 - 2(ib_0/\tau_t)^2}\right] \tag{4.17}$$

where β is defined as,

$$\beta = \frac{1}{2}\left[1 - \frac{1}{\sqrt{1 + (b_0 g/2)}}\right] . \tag{4.18}$$

The slot-opening width is denoted by b_0 and the airgap with g. The stator surface speed relative to the rotor is,

$$v_r = \omega_{mech} r_s , \tag{4.19}$$

where ω_{mech} is the rotor angular speed, and r_s the stator teeth radius. The slot pitch is determined by,

$$\tau_t = \frac{2\pi}{Q} . \tag{4.20}$$

4.7.5 Conclusion

The results of the methods tested are in good agreement. The computation of "Method 2" is significantly faster than "Method 1", since "Method 1" requires an FFT to be performed. Furthermore, Figure 4.22 shows that the results obtained by the 1D analytical flux calculation is also in good agreement. The use of the analytical flux value increases the magnet loss calculation speed even further, since the flux density in the magnet does not have to be sampled in the simulation. For this reason, "Method 2" with the 1D analytical flux calculation, is selected for the magnet loss calculation in the optimisation procedure of Chapter 5. It is interesting to see that the rated current operation did not noticeably increase the magnet losses. This can be attributed to the relatively weak effect that the armature reaction has at the centre of the magnet.

4.8 Total Losses and Efficiency

The losses of the preceding sections are simply added to obtain the total losses. As mentioned in Chapter 3, any mechanical or friction losses are neglected in this study. For the machines implementing solid copper bars the total losses are described as,

$$P_{losses} = P_{copper} + P_{eddy} + P_{iron} + P_{magnets} , \tag{4.21}$$

where $P_{copper} + P_{eddy}$ account for the total copper losses. For machines utilising Litz wire, the eddy losses within the copper P_{eddy} are omitted. The efficiency at any operating point

is calculated as,

$$\begin{aligned}\eta &= \frac{P_{out}}{P_{in}} \\ &= \frac{P_{mech}}{P_{mech} + P_{losses}} \ .\end{aligned} \tag{4.22}$$

The mechanical output power is P_{mech} is determined by

$$P_{mech} = \frac{n_{rpm}\pi}{30}\tau_{mech} \ , \tag{4.23}$$

where n_{rpm} is the mechanical speed in revolutions per minute (rpm) and τ_{mech} is determined by (4.26). The torque derived from (4.26) is used since the result is more accurate as opposed to the averaging of instantaneous torque values. This is especially true when a small number of steps are simulated, which will be the case during the optimisation procedure in Chapter 5.

4.9 Equivalent Circuit Model

The standard per phase equivalent circuit for a synchronous permanent magnet machine is shown in Figure 4.23. The SEMFEM package does not directly consider the phase resistance R_a as mentioned in Section 4.5.2. The phase voltage reported by SEMFEM is indicated as U_a. The user can implement its own resistance calculation, and determine the phase voltage at terminals V_a.

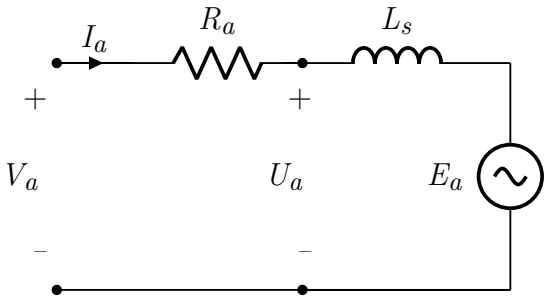

Figure 4.23: Per phase equivalent circuit of the SORSPM motor.

The three phase *abc* stator quantities of Figure 4.23 can be transformed into a *dq* model by using the Park transformation as explained by Umans [67, pp. 664-670]. The purpose is to work with quantities (flux linkages, inductances, currents and voltages) which are not time dependant during steady state conditions. The *dq* model makes use of a rotating reference frame, which has a quadrature axis (q-axis) and a direct axis (d-axis), and which

is always perpendicular to one another. The reference frame rotates at the speed of the electrical frequency ω_e. The d-axis is always aligned with the rotor field, and thus the fictitious d-axis stator flux linkage includes, λ_{PM}, the flux linkage due to the permanent magnets. For a balanced three phase system, the dq models can be described as shown in Figure 4.24. The phase resistance R_a is now called R_s according to the dq naming convention, and in general the subscript s is the shorthand for synchronous.

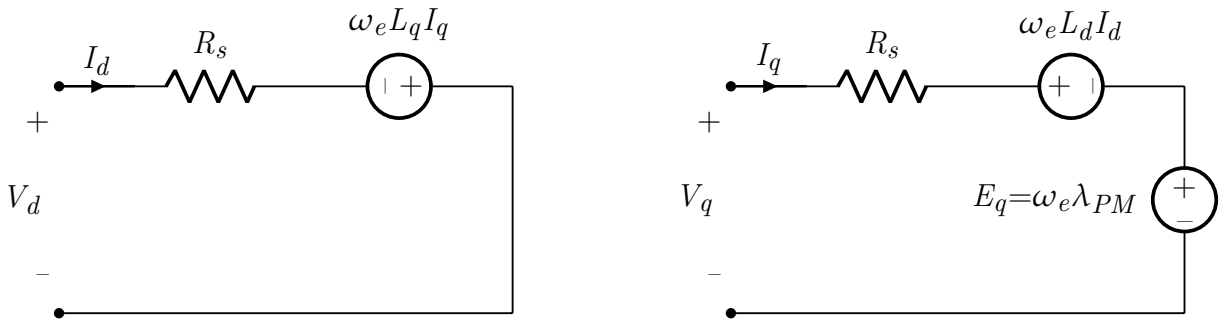

(a) d-axis (b) q-axis

Figure 4.24: Equivalent dq models under steady state and balanced three phase conditions, for the SORSPM motor.

The stator inductances are denoted by L_d and L_q, and are related to the dq flux linkages by

$$\lambda_d = L_d I_d + \lambda_{PM} \tag{4.24}$$

$$\lambda_q = L_q I_q \ . \tag{4.25}$$

The mechanical torque can be determined from the foregoing dq quantities by

$$\tau_{mech} = \frac{3}{2} p(\lambda_d I_q - \lambda_q I_d) \ , \tag{4.26}$$

where p is the number of pole pairs. In this project it is assumed that the machine's saliency is negligible, so that $L_q = L_d = L_s$ where L_s is known as the synchronous inductance. By substituting (4.24) and (4.25) into (4.26) with non-saliency in mind, the torque expression becomes

$$\tau_{mech} = \frac{3}{2} p \lambda_{PM} I_q \ . \tag{4.27}$$

Equation (4.27) shows that for permanent magnet synchronous machines under vector control, the desired torque is specified using a single control current I_q.

The d-axis terminal voltage V_d and the q-axis terminal voltage V_q are related to the RMS per phase terminal voltage by

$$V_a = \sqrt{\frac{V_d^2 + V_q^2}{2}} \ , \tag{4.28}$$

and the d-axis current I_d and the q-axis current I_q are related to the RMS injected phase current

$$I_a = \sqrt{\frac{I_d^2 + I_q^2}{2}} \ . \tag{4.29}$$

4.10 Flux Weakening

Unlike the IDRFPM machine, the SORSPM exhibits a stronger armature reaction due to the iron teeth. The armature reaction is the effect on the magnetic field distribution due to the stator phase currents. The original magnetic field set up by the rotor poles can thus be altered by the armature reaction.

With a flux weakening regime, the purpose is to reduce the back-EMF in the stator coils. The armature reaction is set up in such a way that it weakens the original magnetic field produced by the magnets. In terms of the dq reference system, a negative i_d current is injected in order to reduce the d-axis flux linkage in (4.24). Subsequently the q-axis voltage is reduced, and thereby the overall phase voltage V_a of (4.28) is reduced. Ideally in the case of a surface PM synchronous machine with non-saliency, the flux weakening does not affect the developed torque given that i_q is kept constant, as can be deduced from (4.27).

In this project, flux weakening is employed for the SORSPM machine when the motor is operating near top speed, at which the back-EMF exceeds the VSD voltage. This is done as long as the phase current loss P_{copper} allowance of 200 W is not exceeded. If the terminal voltage at top speed is above the voltage limit, and the P_{copper} allowance is already spent, then the number of turns is reduced until both the voltage limit and P_{copper} allowance is adhered to. The challenge will be to find the trade-off between the number of turns which seems feasible for manufacture, while adhering to the voltage limit, and while keeping the P_{copper} losses a minimum. This selection and optimisation process is further discussed in Chapter 5.

4.11 Torque Ripple

According to Martínez [14, p. 39], the torque ripple is caused by various sources:

- a varying reluctance path, also known as the reluctance torque component or cogging torque, as discussed by Meier [39, p. 33], Martínez [14, p. 68] and Hanselman [15, p. 7]
- the chosen winding topology develops significant space harmonics which are moving at different speeds and opposing directions than that of the rotor poles as discussed by Randewijk [12, p. 105]
- time harmonics due to imperfect sinusoidal currents injected into the machine by the VSD
- manufacturing imperfections, discussed by Gerber *et al.* [68]

In this project, the latter three causes are not dealt with, however a low torque ripple is pursued by choosing a suitable pole-slot combination, and by means of optimal selection of the machine dimensions - which minimises the reluctance torque component. This is addressed in Chapter 5.

The harmonic content of the developed torque is determined by simulating various steps (positions) of the machine, with the assumption that the machine is operated under a maximum torque regime. In other words, for each step, the stator magnetic axis is always aligned perpendicular to the rotor magnetic axis (only q-axis current is injected), thereby developing a maximum instantaneous torque value. The torque ripple is calculated by the difference in the minimum and maximum torque at a given operating point, and then described as a percentage of the average torque at that operating point,

$$\tau_{ripple} = \frac{\tau_{max} - \tau_{min}}{\tau_{average}} \times 100 \ . \tag{4.30}$$

Values which adequately represent the minimum and maximum torque can be achieved if an ample number of steps are sampled during an electrical period, else one could miss the peaks of the “true” minimums and maximums. The well-known Nyquist criteria dictates that the torque ripple should be sampled at least twice, preferably higher, than the frequency of the highest harmonic which is of practical interest.

Generally, without prior knowledge to the harmonic content of the developed torque, it would be wise to select a fairly large prime number as the number of steps (samples) to

evaluate, such as 31, 73 or 97. This avoids accidental loss of the most significant torque ripple harmonics.

As previously discussed in Chapter 3, the designs considered in this project, all implement double-layer non-overlapping coils, with a coils per pole (per phase) ratio of $k_q = \frac{1}{2}$. Due to this configuration, the developed torque will exhibit harmonics in multiples of 6. This is also evident from the analytical analysis of Chapter 3, where the Lorentz method is used to determine the torque. This agrees with the work done by Randewijk [12, p. 113]. From simulation experience of the SORSPM machine configurations presented in this chapter, it is observed that the machine exhibits a dominant 6^{th} harmonic, and a less pronounced 12^{th} harmonic. The method to determine the torque ripple presented here, will thus only focus on the 6^{th} harmonic component. The aim here is to determine the ripple, without simulating an excessive number of time-steps, thereby reducing optimisation time.

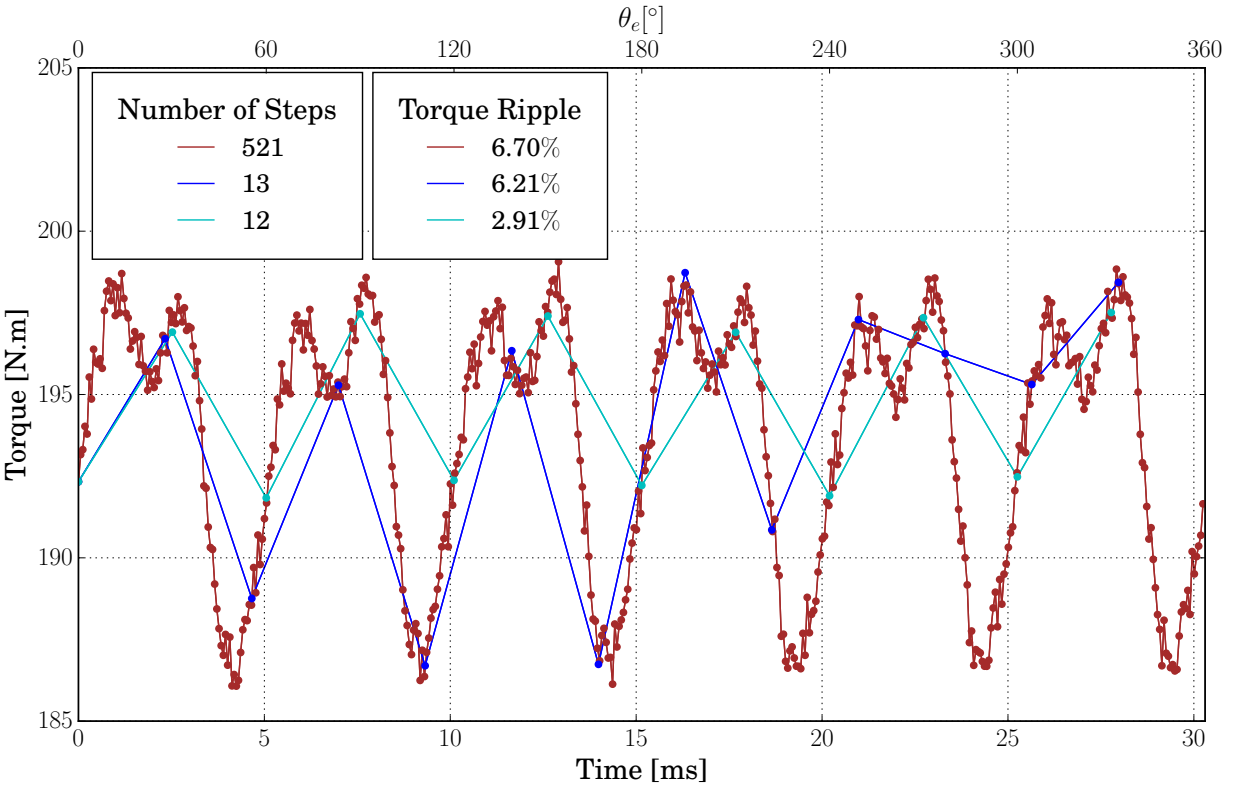

Figure 4.25: The rated torque output of the initial SORSPM design (Appendix B) at base speed (100 rpm), simulated for a full electrical period.

Figure 4.25 indicates the pitfall when the number of steps is chosen as a multiple of 6, in this case 12. All the important peaks are lost in the sampling process, since the samples are repeatedly obtained at the same positions on the curve of the 6^{th} harmonic. Using a

prime number, such as 13, which is greater than the Nyquist criteria, results in an adequate torque ripple calculation. Notice that when 13 steps are simulated ($\tau_{ripple} = 6.21\,\%$), the torque ripple result is much closer to the "true" torque ripple when 521 steps are simulated ($\tau_{ripple} = 6.70\,\%$), as compared to when only 12 steps are simulated ($\tau_{ripple} = 2.91\,\%$).

Another important aspect to keep in mind is that SEMFEM automatically assigns a step to be simulated to each available core of the computer. In this case, the package is used on an 8-core processor. This means, the simulation time is roughly doubled when 9 steps are simulated as compared to 8 steps. And furthermore, the time it takes to simulate 9 steps or 16 steps is roughly the same. With the intent to use a prime number, and with SEMFEM's multiprocessing in mind, a step number of 13 is implemented. This allows minimum and maximum peaks to be detected sufficiently and increases the efficiency of the optimisation process.

4.12 Total Mass

The total mass considered for the SORSPM machine will consist of the iron mass, copper mass, magnet mass and also a mass related to an aluminium drum thickness. The aluminium mass is added, to better represent a realistic mass of such a machine within a Mellowcabs vehicle. As mentioned in Section 2.2, an outer drum wall thickness of 10 mm is assumed. The outer drum will accommodate the rotor yoke laminations. Also, an inner drum wall thickness of 10 mm is assumed. The inner drum will accommodate the stator yoke laminations. The following mass densities are used for the total mass calculation:

Steel Laminations	$7600\,\mathrm{kg/m^3}$
Copper	$8954\,\mathrm{kg/m^3}$
Neodymium Magnets	$7500\,\mathrm{kg/m^3}$
Aluminium	$2700\,\mathrm{kg/m^3}$

Table 4.7: Main materials used in the construction of the SORSPM machine.

Chapter 5

Optimisation

5.1 Introduction

In this chapter, the procedure to obtain optimum machine parameters is discussed. The goal is to optimise the machines in order to achieve the objectives stated in Table 2.3. In the next chapter, the optimal designs for each machine topology is compared in order to determine the most suitable candidate for the Mellowcabs application.

5.2 Pole-Slot Selection

In literature, the winding factor, the lowest common multiple (LCM) and the greatest common divisor (GCD) of the pole and slot combination are used as general guidelines for desirable combinations, as discussed by Skaar *et al.* [69], Meier [39], Rix [10, p. 56], Martínez [14, p. 41] and Van Wijk [40, pp. 38-39]. Recall that this project focuses on a number of coils (slots) per pole (per phase) of $k_q = \frac{1}{2}$ for a non-overlapping double-layer concentrated coil structure. This is due to the findings by Kamper *et al.* [27] and Stegmann *et al.* [24], that for non-overlapping windings, the best pole-slot ratio is when $k_q = \frac{1}{2}$. This means the fundamental winding factor is fixed at $k_{w_1} = 0.866$. As a result this topology allows a specific set of pole-slot combinations, some of which are shown in Table 5.1 and 5.2.

Generally, a low LCM value describes a machine which is more prone to exhibit high torque ripple. The GCD value describes the symmetrical periodicity of the machine, so that for a 40 pole and 30 slot machine, the machine can be divided into 10 symmetrical portions. This is also seen in Section 4.4.2, where the simulated section includes 4 poles

and 3 slots, of a 40 pole and 30 slot machine. It is generally desired to design a machine with a high LCM value and a low GCD value, as long as the GCD is greater than unity. The latter is important to avoid unbalanced magnetic pull within the machine as stated by Skaar *et al.* [69], Meier [39, p. 32] and Martínez [14, p. 42].

In this optimisation procedure, a range of pole numbers will be optimised independently in order to find a good performance trade-off. The IDRFPM and SORSPM machine will both be optimised, each with their own range of pole numbers. Table 5.1 shows the pole numbers considered for the IDRFPM machine, and Table 5.2 shows the pole numbers considered for the SORSPM machine. The pole numbers in consideration for each machine differ, as it will become clear from Section 5.8 that the optimal designs are situated in these respective pole ranges. The pole-slot range considered is therefore selected by studying the tendency of the results, which means the range is readjusted if the desirable designs seem to fall outside this range.

As can be seen from Table 5.2, the designs for the SORSPM machine in this project will focus on fairly large pole numbers. Inherently, higher pole numbers use smaller magnets, and thus a smaller rotor yoke is needed for the flux return path according to Lovatt *et al.* [70]. Thus, according to Mi *et al.* [50] and Meier [39, p. 53], a higher pole number usually leads to a reduction in overall mass. Furthermore Lovatt *et al.* [70] states that, a higher pole number is also accompanied by a higher slot number and as a result, is usually accompanied by an increase in stator losses and eddy current losses in the windings. Naturally, a high pole number increases the manufacturing complexity, as this means more magnets need to be placed and more windings need to be wound and inserted. All these factors will compete against each other, and the performance trade-offs will be optimised in this chapter.

Poles	Slots (Coils)	GCD	LCM	Working Harmonic Frequency (100 rpm)
12	9	3	36	10.00 Hz
16	12	4	48	13.33 Hz
20	15	5	60	16.67 Hz
24	18	6	72	20.00 Hz
28	21	7	84	23.33 Hz
32	24	8	96	26.67 Hz
36	27	9	108	30.00 Hz
40	30	10	120	33.33 Hz

Table 5.1: Various pole-slot combinations under consideration for the IDRPFM machine.

Poles	Slots (Coils)	GCD	LCM	Working Harmonic Frequency (100 rpm)
32	24	8	96	26.67 Hz
36	27	9	108	30.00 Hz
40	30	10	120	33.33 Hz
44	33	11	132	36.67 Hz
48	36	12	144	40.00 Hz
52	39	13	156	43.33 Hz
56	42	14	168	46.67 Hz
60	45	15	180	50.00 Hz

Table 5.2: Various pole-slot combinations under consideration for the SORSPM machine.

5.3 Operating Points

It is evident from Chapter 2, Figure 2.3, that the motors (a motor at each rear wheel) will need to operate at both constant torque and constant power regions. The performance specification summarised in Table 2.3 will determine the main operating points of concern in this chapter. From Table 2.3, the motor will need to deliver a constant 191 N·m torque from 0 rpm to 100 rpm. Thereafter, a constant power from 100 rpm to 465 rpm is required.

The rated torque-power versus speed curves for the initial design (Appendix B) are shown in Figure 5.1a. Notice that the curves satisfy the aforementioned specification requirements, and that it mimics the curves of Figure 2.3. The area shaded in green indicates the constant torque operating region. Recall that the initial design utilises solid copper bars, which results in 2 turns per coil for a machine with 40 poles and 30 slots.

Some designs, which utilise a higher number of turns, will require flux weakening in order to keep the terminal voltage below the 48 V limit. The rated torque-power versus speed curve of a design using 5 turns per coil with 40 poles and 30 slots, is shown in Figure 5.2a. The area shaded in red indicates where flux weakening is implemented.

Throughout the rated torque and rated power operation, the copper losses P_{copper} due to the phase currents (discussed in Section 4.5.2) is sustained at or below 200 W. When the machine is operating at rated torque, then the copper losses are set at the rated 200 W. When the machine is operating in the constant power region, then the copper losses will be at or below 200 W.

It was initially attempted to optimise the machines at both base speed (100 rpm) and at top speed (465 rpm). However the optimisation procedure discussed in Sections 5.4 and 5.5 struggled to converge and to deliver satisfactory results. It is thought that the objectives

of both operating points are competing strongly against each other. For this reason only the operating point at base speed is optimised, and then the performance at top speed is studied as a result of this optimisation.

5.4 Multi-objective Optimisation

5.4.1 Introduction

The goal of this optimisation is to produce designs which are optimal with regard to three objectives, namely efficiency (η), torque density ($\tau_{density}$) and torque ripple (τ_{ripple}). Recall that from Section 2.4, the mass due to the motors is not accounted for in the vehicle modelling calculations. Thus the machine mass has to be as low as possible, so that it does not increase the initial torque requirement too significantly. Therefore the torque density will be optimised to be as high as possible. For the IDRFPM machine, the torque ripple is extremely low due to a non-existent reluctance component. Additionally for the IDRFPM machine, the efficiency is actually fixed if the output power is constant, since the only losses are the copper losses which of course is kept constant. For these reasons the efficiency and torque ripple objectives are omitted for the IDRFPM machine. The other performance traits are studied afterwards as a result of the optimisation.

During the course of this project, a post graduate subject "Advanced Design 814" from the Mechanical Department was completed in order to better understand and utilise optimisation procedures as a whole. A book by Snyman [71] was covered during the course, and it was used as a general guide for the optimisation of the machines in this project.

The IDRFPM machine was initially optimised and presented in a SAUPEC paper by Joss *et al.* [2] and an ICEM paper by Joss *et al.* [3]. The approach followed in these papers are different from the method which is used in this thesis. In essence, the initial approach involved optimising for a wide range of objective weight combinations, thereby not defining any specific priorities beforehand. This proved to be very insightful, as the solutions can be plotted on a 3D scatter plot (since three weight objectives were varied). The 3D scatter plot then resembles the Pareto front, a surface of solutions which are all optimal for a given trade-off between objectives. The designer, or decision-maker, is then equipped with an intuitive spectrum of solutions to choose from. This is advantageous, since it is usually hard to express the desired performance trade-offs prior to attempting an optimisation procedure. Despite all these benefits, this approach is found to be very time consuming when the function evaluator is slow as is the case for the SORSPM machine.

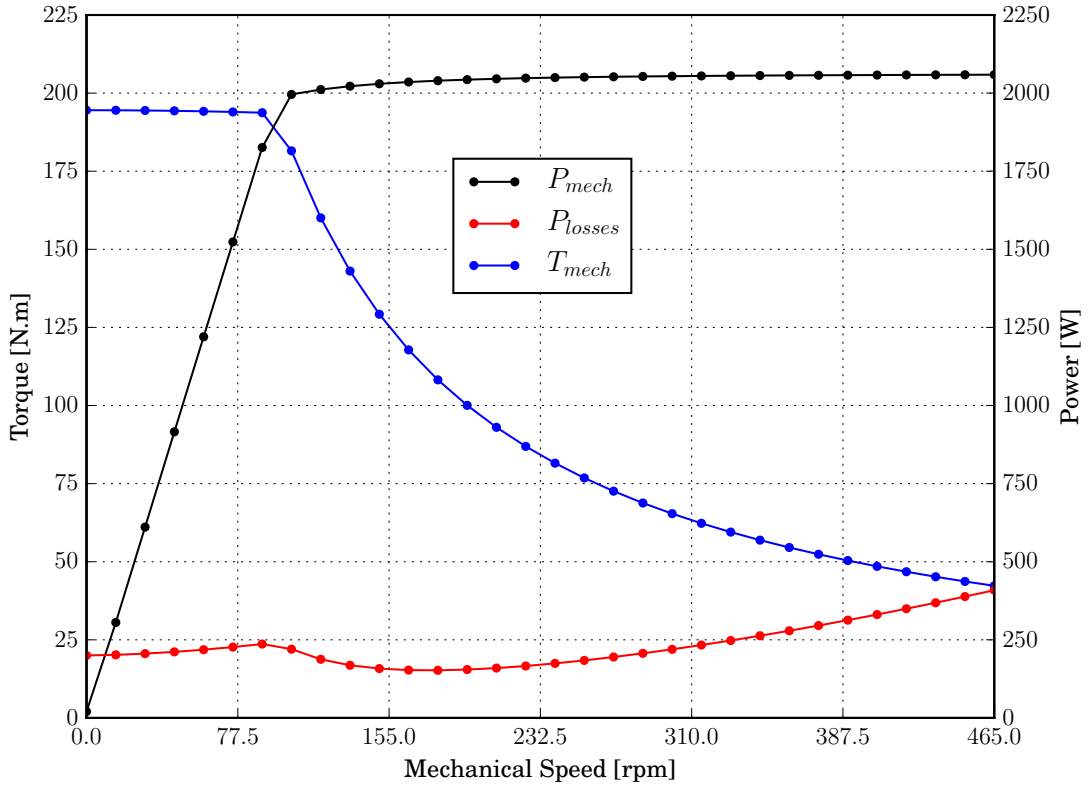

(a)

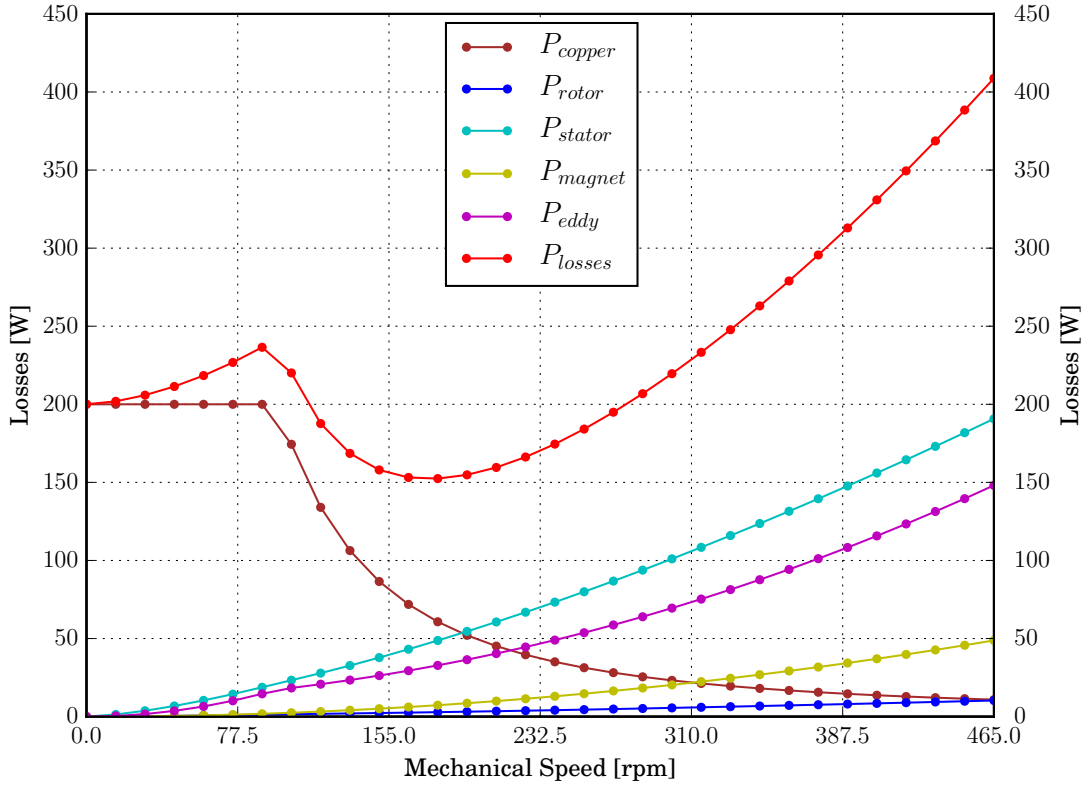

(b)

Figure 5.1: Solid copper bars used. (a) Power versus torque curves with the copper losses at a maximum threshold of $P_{copper} = 200\,\mathrm{W}$. Constant torque and flux weakening regions are shaded in green and red respectively. (b) As for (a) but all the loss components shown, with the total losses denoted by P_{losses}. Machine specifications as in Appendix B.

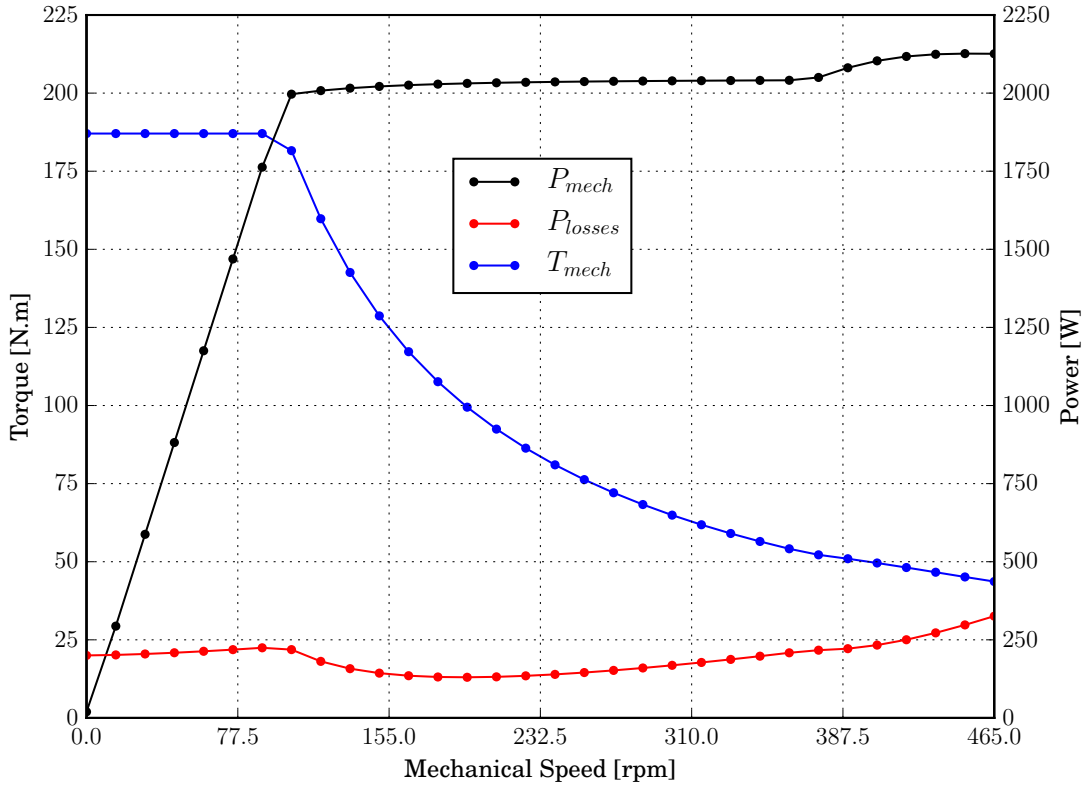

(a)

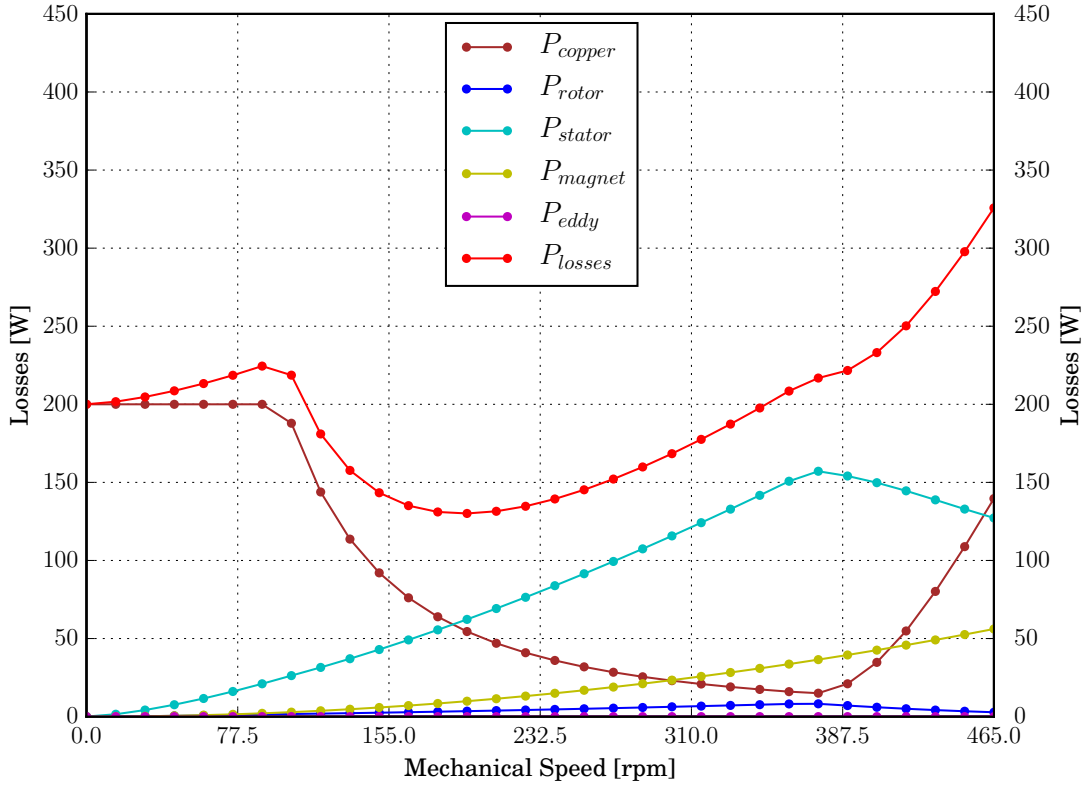

(b)

Figure 5.2: Round or rectangular wires used. (a) Power versus torque curves with the copper losses at a maximum threshold of $P_{copper} = 200\,\mathrm{W}$. Constant torque and flux weakening regions are shaded in green and red respectively. (b) As for (a) but all the loss components shown, with the total losses denoted by P_{losses}. Machine specifications as in Appendix B.

This was not a problem with the IDRFPM machine, as the subdomain analysis method is executed extremely fast. For the IDRFPM machine, it was even possible to use a 2D SEMFEM simulation for the function evaluator (also discussed by Joss *et al.* [3]), since all the required performance outputs could be deduced from a single step simulation. The SORSPM simulation is significantly slower due to the fact that many of the loss calculations (and also the torque ripple calculation) depend on simulation data from a full electrical period.

It is good to keep in mind that, for optimisation problems in general, it is possible for similar solutions in the objective space, $\vec{\mathbf{f}}(\vec{\mathbf{x}})$, to correspond with completely different solutions in the design space, $\vec{\mathbf{x}}$. This means for some optimisation problems, there could be many designs (which in a physical sense all look different) but which all exhibit a similar output performance. Therefore the solutions presented in this chapter are not necessarily (but probably are) the only solutions available for the specific output performance required.

5.4.2 Methodology

In general, for any multi-objective function, it is desired to optimise a vector of objective functions,

$$\underset{\text{subject to constraints}}{\text{Minimise}} \quad \vec{\mathbf{f}}(\vec{\mathbf{x}}) = [f_1(\vec{\mathbf{x}}), f_2(\vec{\mathbf{x}}), ..., f_k(\vec{\mathbf{x}})]^T \ . \tag{5.1}$$

For the SORSPM machine, the vector of multi-objective functions is chosen as,

$$\underset{\text{subject to constraints}}{\text{Minimise}} \quad \vec{\mathbf{f}}(\vec{\mathbf{x}}) = [f_\eta(\vec{\mathbf{x}}), f_{\tau_{density}}(\vec{\mathbf{x}}), f_{\tau_{ripple}}(\vec{\mathbf{x}})]^T \ , \tag{5.2}$$

where $\vec{\mathbf{x}}$ is the design-space vector containing all the machine's dimensions that need to be optimised. For the reasons mentioned in Section 5.4.1, the optimisation of the IDRFPM machine will actually focus only on one objective, thus the objective function is described as,

$$\underset{\text{subject to constraints}}{\text{Minimise}} \quad \vec{\mathbf{f}}(\vec{\mathbf{x}}) = f_{\tau_{density}}(\vec{\mathbf{x}}) \ . \tag{5.3}$$

The torque density referred to in this project, is a mass torque density (N·m/kg), that is to say, not a volumetric torque density (N·m/m^3). The mass used to determine the torque density, is a total mass, as stated in Sections 3.9 and 4.12.

A wide variety of multi-objective optimisation techniques are available, for example the Lexicographic Method, Bounded Objective Function Method, Normal Boundary Intersection Method, Normal Constraint Method, scalarisation (weighted) methods, and the

Multi-objective Genetic Algorithm (MOGA) [72] [73] [74]. All the methods except for the last mentioned method, reduce the multi-objective optimisation problem to single-objective optimisation subproblems (of which the weighted methods reduce the problem within a single step, and the other methods require sequential steps of single-objective solving or extra constraints to reduce the problem to a final single-objective problem). In contrast, MOGA can solve multi-objective problems directly and is also not gradient dependant, but is according to Marler *et al.* [72] more complex to program.

No single method is best for all circumstances ("no free lunch"), therefore the method to be selected depends solely on the personal preferences and problem insight of the decision-maker as explained by Marler *et al.* [72] and Oliveira *et al.* [73]. In this project, the Weighted Sum Method (WSM) is used due to the ease of implementation and relative acceptable results. In spite of these advantages, much literature exists explaining the pitfalls of using this method. The first pitfall is that this method is unable to capture Pareto optimal points situated on non-convex portions of the Pareto optimal curve. The second pitfall according to Marler *et al.* [75] is that the method does not produce an even distribution of points on the Pareto curve when using consistent change in weights. An adapted WSM method is presented by Kim [76] which determines uniformly-spaced Pareto optimal solutions, however this also adds more programming complexity and was avoided for this reason. The regular WSM is described as

$$f(\vec{\mathbf{x}}) = \sum_{k=1}^{n} w_k f_k(\vec{\mathbf{x}}) \ , \tag{5.4}$$

where the weights (which can be selected otherwise) are chosen in this project such that

$$\sum_{k=1}^{n} w_k = 1 \ . \tag{5.5}$$

In the case of the SORSPM machine, the multi-objective function (5.2) is then scalarised into the form of

$$f(\vec{\mathbf{x}}) = -w_1\eta(\vec{\mathbf{x}}) - w_2\tau_{density}(\vec{\mathbf{x}}) + w_3\tau_{ripple}(\vec{\mathbf{x}}) + w_4 P_{mech}(\vec{\mathbf{x}}) \ , \tag{5.6}$$

where the weights w_1, w_2, w_3 and w_4 are selected according to the preferences of the designer. Notice that some of the terms are subtracted while others are added, this is because some objectives are to be minimised while others are maximised. As a whole, the function (5.6) is minimised. The reason for the $w_4 P_{mech}(\vec{\mathbf{x}})$ term will soon become clear. It is important to realise that by using the WSM, the vector of multi-objective functions is

simplified into a single scalar value, and is now technically a single-objective optimisation problem.

Similarly, the objective function for the IDRFPM machine is in the form of,

$$f(\vec{\mathbf{x}}) = -w_2\tau_{density}(\vec{\mathbf{x}}) + w_4 P_{mech}(\vec{\mathbf{x}}) \ . \tag{5.7}$$

It is discussed by Marler *et al.* [75] that it can be difficult to distinguish between setting weights to compensate for differences in objective function magnitudes as opposed to setting weights in order to indicate the relative importance of an objective. For this reason, it is advised to transform each objective function so that they all have similar magnitudes. Many different approaches exist to transform an objective function. One of the simplest transformations, is to divide the objective function by its ideal desired value as explained by Marler *et al.* [72]. The ideal value of each objective function can be obtained either by optimising only for the specific objective function or it can be determined by engineering intuition. The transformation

$$f_i^{\text{trans}}(\vec{\mathbf{x}}) = \frac{f(\vec{\mathbf{x}})}{|f_i^{\text{ideal}}(\vec{\mathbf{x}})|} \ , \tag{5.8}$$

is used in this project. The ideal values in Table 5.3 are selected using intuition and experience.

Efficiency	η	89	%
Torque Density	$\tau_{density}$	7	N·m/kg
Torque Ripple	τ_{ripple}	10	%
Mechanical Power	P_{mech}	2	kW

Table 5.3: Ideal values used to scale objective functions.

Now that the objective functions are transformed into per unit values, the weights can be set knowing that the weights will now better represent the objective function priorities rather than compensating for disparities between objective function magnitudes. Different weight combinations were tested, and for the SORSPM optimisation problem it was found that the weights in Table 5.4 delivered the most satisfactory results.

η	w_1	0.1
$\tau_{density}$	w_2	0.2
τ_{ripple}	w_3	0.1
P_{mech}	w_4	0.6

Table 5.4: SORSPM weight values used by the Weighted Sum Method.

Similarly, for the IDRFPM machine the weights in Table 5.5 were found to deliver the most satisfactory results.

$\tau_{density}$	w_2	0.5
P_{mech}	w_4	0.5

Table 5.5: IDRFPM weight values used by the Weighted Sum Method.

It is common practice to add penalty functions to the existing objective function in order to demand certain performance outputs. In this project, all feasible designs should have a mechanical output power of $P_{min} = 2\,\text{kW}$ or higher. The penalty function

$$\sigma = \begin{cases} (P_{min} - P_{mech})^2 & , P_{mech} < P_{min} \\ 0 & , P_{mech} \geq P_{min} \end{cases} \tag{5.9}$$

is employed to demotivate designs with inadequate power outputs. Note that before (5.9) is added to (5.6) and (5.7), the penalty function should also be normalised with (5.8) by using the ideal P_{ideal} power of 2 kW. While the penalty function does penalise designs with a power output below the desired value, it does not motivate designs with a power output greater than 2 kW to be as close to 2 kW as possible. The penalty function could be modified to do this, by describing it as

$$\sigma = \begin{cases} (P_{min} - P_{mech})^2 & , \text{for all } P_{mech} \end{cases} \tag{5.10}$$

however this was found to be slightly too aggressive. For this reason, the $w_4 P_{mech}(\vec{\mathbf{x}})$ term is added to the objective function as seen in (5.6) and (5.7). The P_{mech} objective is thus minimised, while penalising designs using (5.9) which deliver less than 2 kW. This specific configuration did perform well, however other alternative configurations could also work well or even better. An alternative approach could for example implement independent weights for the piece-wise defined function, such as

$$\sigma = \begin{cases} \kappa_1 (P_{min} - P_{mech})^2 & , P_{mech} < P_{min} \\ \kappa_2 (P_{min} - P_{mech})^2 & , P_{mech} \geq P_{min} \end{cases} \tag{5.11}$$

where κ_1 and κ_2 could be defined individually.

5.5 Single-objective Optimisation

In the preceding section, the optimisation problem is reduced from a multi-objective problem to a single-objective problem. This section will discuss the approach for optimising the single-objective optimisation problem.

The initial optimisation approach by Joss *et al.* [2] and Joss *et al.* [3], made use of an open-source Python-based package "pyOpt" [77]. In this project, another open-source optimisation package "NLopt" [78] is used since its community and developers seem more active. It also has a Python interface available which made the existing scripts of this project easy to adapt.

In the NLopt package, both global and local optimisation procedures are available. The purpose of a global optimisation is to find a global optimum for a particular problem. This means that the algorithm will try to explore the design space $\vec{\mathbf{x}}$ over the entire feasible design space. This is done so that convergence into a local minimum is avoided. It is thus hoped that a global optimisation will explore all the local minima and subsequently determine the global minima from these local minima. The global optimisation algorithms in NLopt do not require a starting point, but upper and lower bounds for the design space $\vec{\mathbf{x}}$ are required.

For the global optimisation, a few of the algorithms available were tested for the application of this project. It is found that the algorithm named "DIRECT", by Jones *et al.* [79], performs most satisfactory. Again, it is noteworthy that no algorithm is superior in all circumstances, and thus suitability will depend on the problem at hand. The DIRECT (DIviding RECTangles) algorithm divides the design space $\vec{\mathbf{x}}$ into increasingly smaller hyperrectangles. This is done so that the entire design space can be explored efficiently.

After a global optimisation is completed, it is a good idea to fine tune the result using a local optimisation algorithm. The result from the global optimum is thus used as a starting point for the local optimisation. Again, many of the available local optimisation algorithms were tested, and it is found for this situation that the "SBPLX" algorithim by Rowan [80]

performs best. The SBPLX (Subplex) procedure is a local derivative-free algorithm based on the more well-known Nelder-Mead algorithm.

5.6 Design Variables

The two topologies, IDRFPM and SORSPM, each has its own unique parameters which need to be optimised. Figure 5.3 and Figure 5.4 indicate the optimisation dimensions for the IDRFPM and SORSPM respectively. In order to make future prototypes easy to construct and comparable, the airgap g is fixed at 1 mm. Notice that Figure 5.3 omits the inner and outer yokes, as they are assumed ironless and thus will not affect the electromagnetic performance. However, as mentioned in Section 3.9 and 4.12, an aluminium drum mass within the active length is taken into account for both machines. This is implemented so that the machine optimisation more accurately considers the realistic mass consequences due to the active area's inner and outer radii.

The design space for the IDRFPM machine is described by,

$$\vec{\mathbf{x}} = [\ell, r_o, h_{mo}, h_c, h_{mi}, k_m, k_c, P]^T \ . \tag{5.12}$$

where the number of poles P is optimised a posteriori by comparing all the optimisation results for each P value. The ratio of the radially magnetised magnet width, in relation to the magnet pitch is given by k_m. The width ratio of the tangentially magnetised magnets is thus $1 - k_m$. The optimisation therefore does not cater for open spaces between the magnets. The inner radius r_i was not constrained, but studied as a result of all the other dimensions. The design variables were given the boundaries stated in Table 5.6. These boundaries were used for both the global and local optimisation of the IDRFPM machine. The boundaries were determined through experience and practical considerations.

The design space for the SORSPM machine is described by,

$$\vec{\mathbf{x}} = [\ell, r_o, h_{yo}, h_m, h_s, h_c, h_{yi}, k_h, k_m, k_c, w_s, \theta_s, P]^T \ . \tag{5.13}$$

Again, k_m is a ratio of the magnet width, in relation to the magnet pitch. The inner radius r_i was not constrained, but studied as a result of all the other dimensions. The design variables were given the boundaries stated in Table 5.7. As with the IDRFPM machine, these boundaries were used for both the global and local optimisation of the SORSPM machine. The boundaries were determined trough experience and practical considerations.

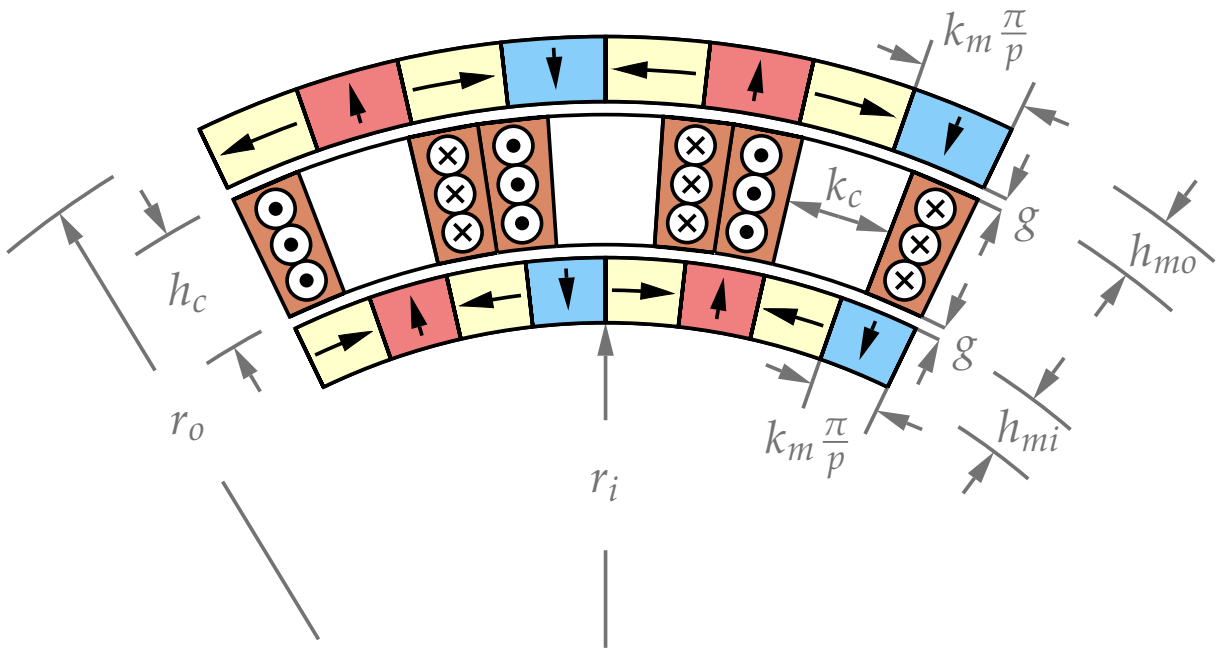

Figure 5.3: Dimensions to be optimised for the IDRFPM machine.

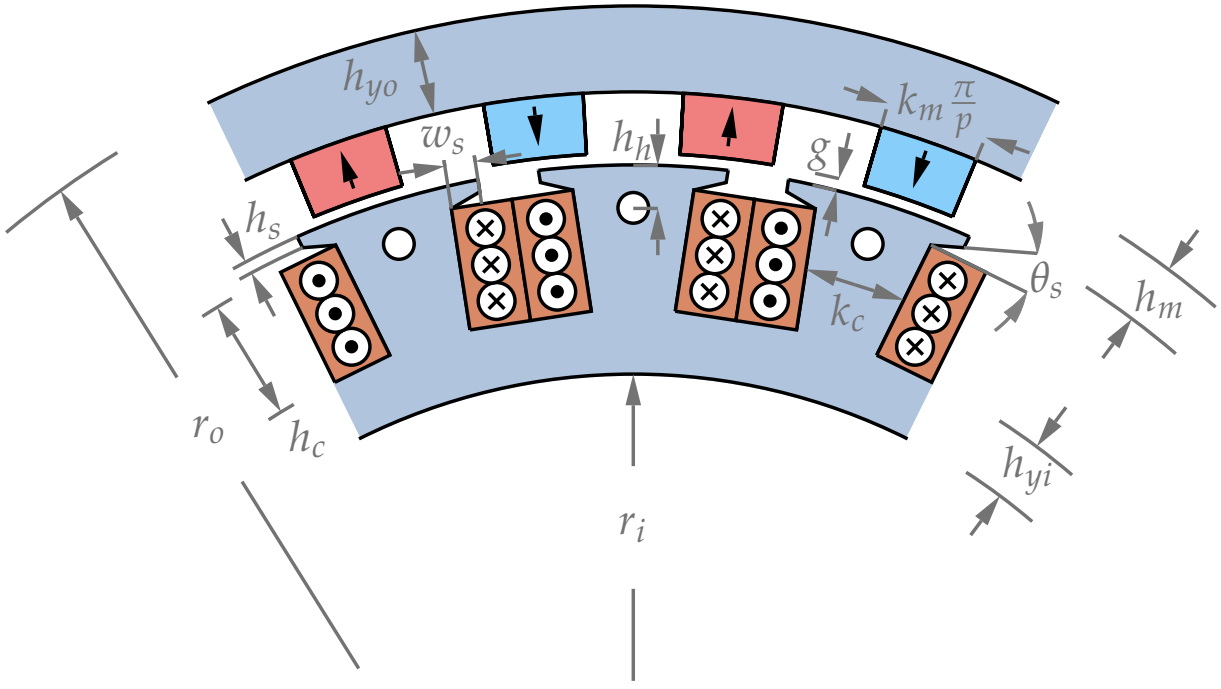

Figure 5.4: Dimensions to be optimised for the SORSPM machine.

Variable		Lower Bound	Upper Bound	Unit
Active length	ℓ	200	400	mm
Outer radius	r_o	100	135	mm
Outer rotor magnet height	h_{mo}	5	35	mm
Coil height	h_c	4	30	mm
Inner rotor magnet height	h_{mi}	5	35	mm
Magnet pitch ratio	k_m	0.3	0.9	p.u.
Coil pitch ratio	k_c	0.1	0.4	p.u.
Number of poles	P	12	40	poles

Table 5.6: Boundaries applied to the design variables of the IDRFPM machine.

Variable		Lower Bound	Upper Bound	Unit
Stack length	ℓ	30	150	mm
Outer radius	r_o	100	135	mm
Rotor yoke height	h_{yo}	3	10	mm
Magnet height	h_m	3	10	mm
Shoe tip height	h_s	0	4	mm
Slot height	h_c	20	45	mm
Stator yoke height	h_{yi}	3	10	mm
Hole height ratio	k_h	0	1	p.u.
Magnet pitch ratio	k_m	0.5	0.9	p.u.
Slot pitch ratio	k_c	0.1	0.4	p.u.
Shoe tip width	w_s	0	12	mm
Shoe taper angle	θ_s	0	80	°
Number of poles	P	32	60	poles

Table 5.7: Boundaries applied to the design variables of the SORSPM machine.

5.7 Overview

In this section, the execution of the overall optimisation process is discussed. As previously mentioned, the scripts to perform the optimisation is scripted in Python. The *optimisation.py* script is the top-level script which makes use of the function evaluator scripts. The function evaluator script either consists of the *SORSPM_semfem.py* script, or the subdomain analysis script for the IDRFPM machine, *idrfpm.py*. The scripts store and exchange machine data with the use of the open-source SQLite3 package which is callable within Python. The use of SQLite vastly improves flexibility, robustness and user-friendliness of the scripts as opposed to using a text file (csv or txt files) based storage system. The

SQLite database can also be viewed, created and edited externally by using an open-source browser called "DB Browser for SQLite". The browser proved to be a huge benefit for this project, as results and inputs are stored in a very intuitive and descriptive manner, requiring minimal effort and maintenance from the user. The data is easily sorted and filtered, even while new results are being added, which gives quick insight into the optimisation progress. As the name suggests, SQLite is similar to other SQL based platforms, but is simplified in one great aspect in that it does not rely on a client-server environment. This means the SQLite functionality is extremely easy to use and virtually no configuration is needed when creating a database. Furthermore, during the duration of this project it was found that the read and write speeds are noticeably faster as opposed to using text files as a storage medium.

Figure 5.5 shows the procedure used to execute an optimisation process, regardless of the optimisation algorithm used. The optimisation procedure is started by executing the *optimisation.py* script. The *optimisation.py* script is configured to use a specific optimisation algorithm prior to execution (such as a global or local optimisation technique).

The **setup.db** database holds all the boundary limits, starting solution (if applicable) and the specific pole-slot combination to be used. As mentioned before, the starting solution is only used when a local optimisation is selected.

The **optimise.db** database records every optimisation iteration's input parameters and output performance in two separate tables. The two tables are shown in Figure 5.6 using the "DB Browser for SQLite" application. As can be seen from Figure 5.6, the input parameters to be optimised are gradually perturbed by the optimisation technique after each iteration. New iterations (counted as "primary_key") are added to the input table in **optimise.db** by the *optimisation.py* script, and in turn the function evaluator script reads the latest value in the input table and produces an output which is added to the output table within the **optimise.db** database. The *optimisation.py* script then reads this output and determines the objective function value according to Section 5.4. If this objective function value is a new best value, then the input and output value of that iteration is added to the **best.db** database. The last entry added to **best.db** is of course the overall best value achieved during the entire optimisation.

For the termination conditions of both the global and local optimisations, the objective function $f(\vec{\mathbf{x}})$ convergence tolerance was set at 10^{-6} and the design space $\vec{\mathbf{x}}$ tolerance was also set at 10^{-6}.

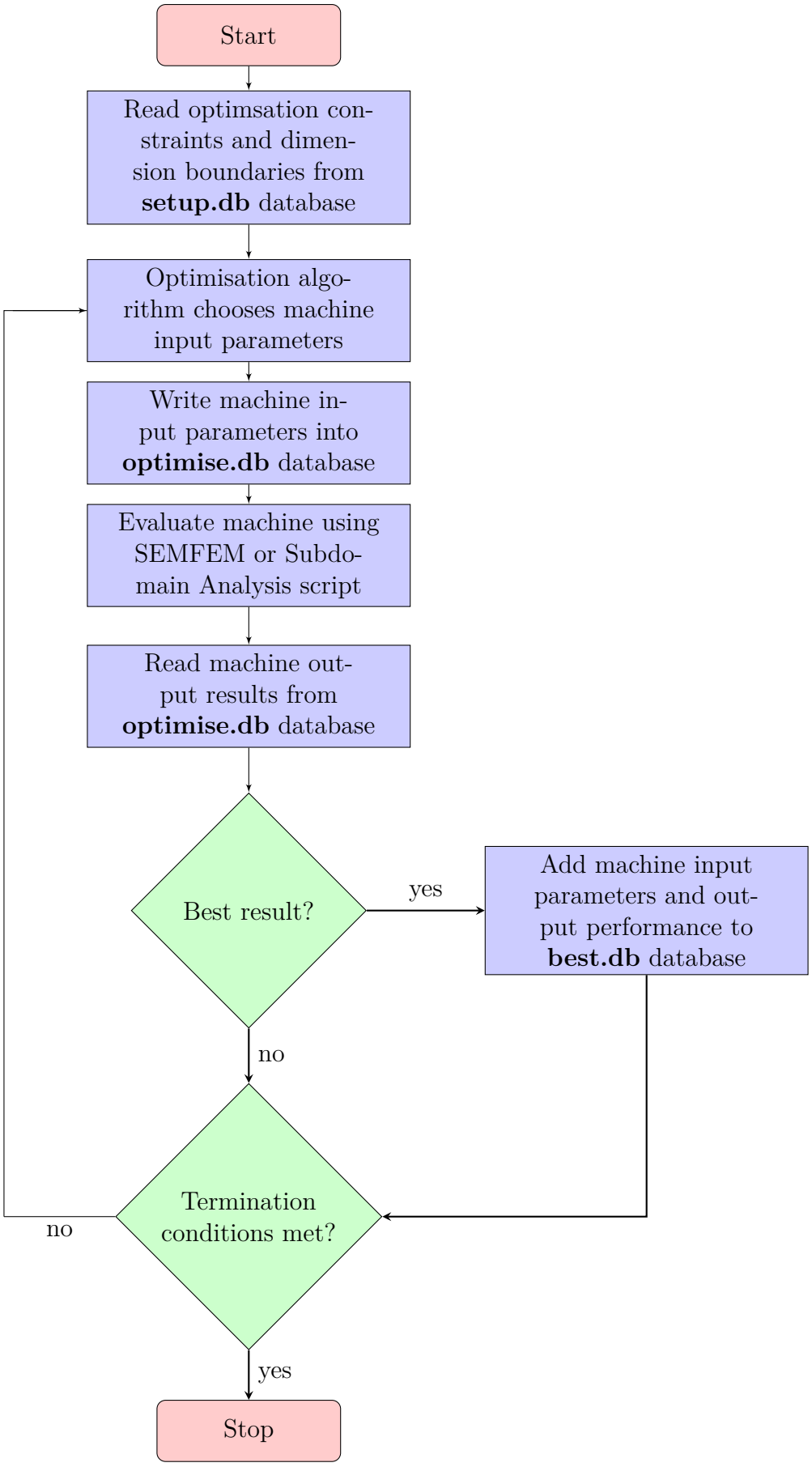

Figure 5.5: Execution of an optimisation process using the *optimisation.py* script.

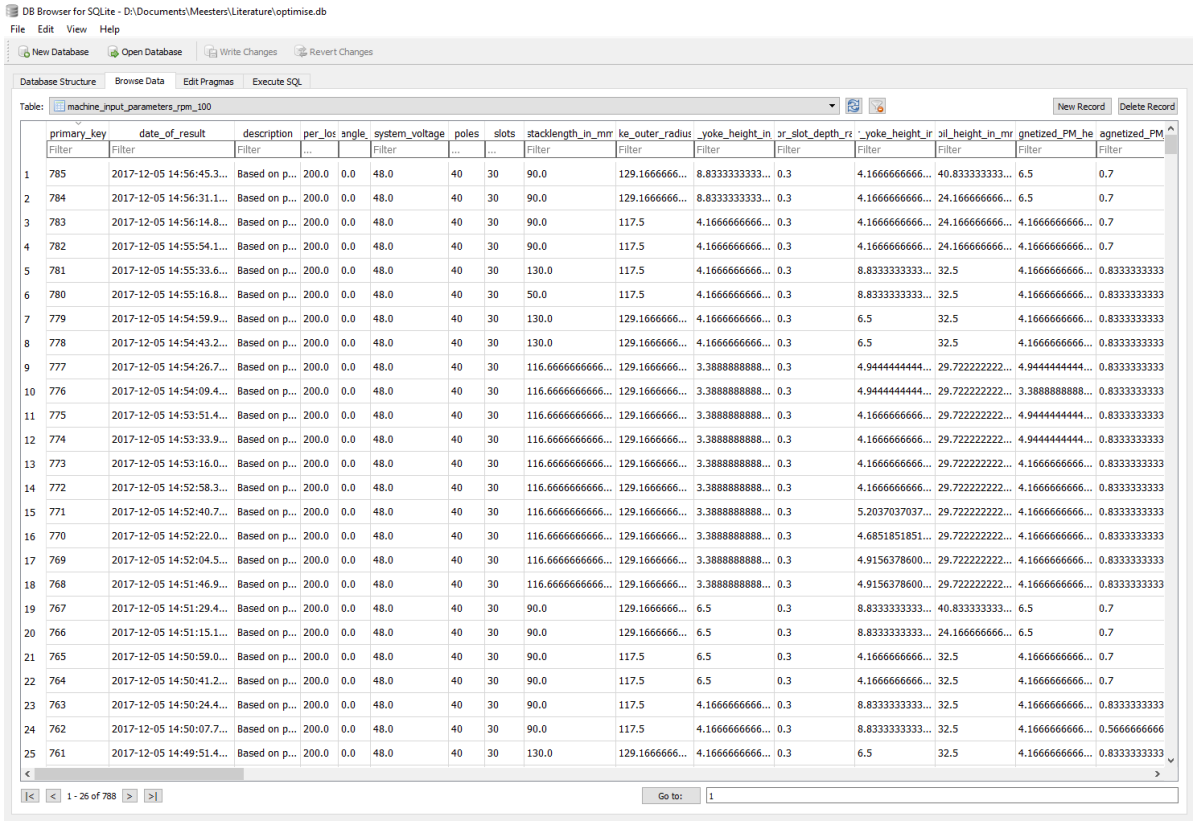

(a)

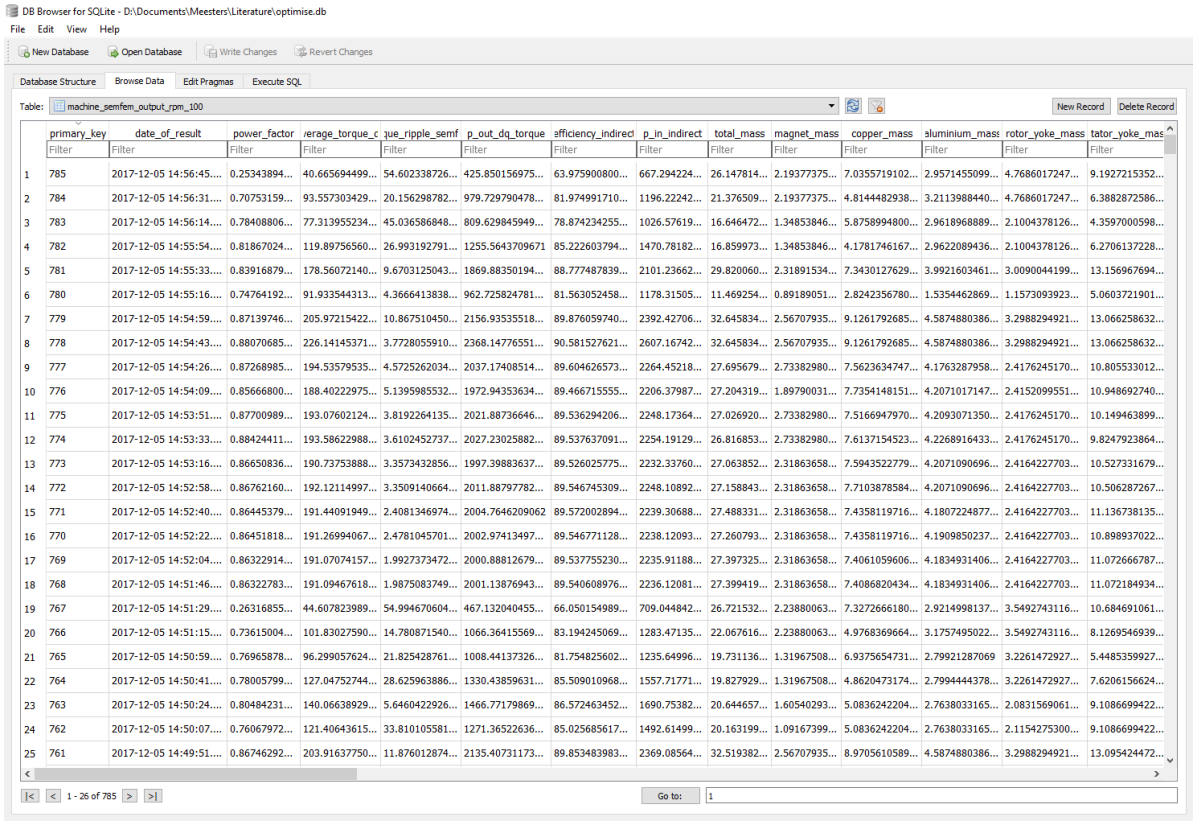

(b)

Figure 5.6: Tables of **optimise.db** shown using "DB Browser for SQLite". The tables shown are the (a) machine input parameters and (b) output performance.

A flow diagram is illustrated in Figure 5.7 which describes the work flow followed to achieve a final optimisation result for a given machine topology and pole-slot combination. Both the global and local optimisation makes use of the *optimisation.py* script as described by Figure 5.5. The best solution provided by the global optimisation is used as a starting solution for the local optimisation. The process described by Figure 5.7 is repeated for each pole-slot combination listed in Table 5.1 or 5.2.

Figure 5.7: Top-level optimisation work flow.

As an example, for the SORSPM machine, a global optimisation procedure using a SEMFEM simulation with 31 steps, convergence was reached after about 600-900 function evaluations in which 4-6 hours elapsed. A function evaluation usually took about 30-40 seconds. The next step, involving the local optimisation, the SEMFEM simulation was adjusted to use 127 steps and with a finer mesh. The local optimisation typically executed about 500-700 function evaluations after which 11-15 hours elapsed. In this case a function evaluation took about 1 minute and 15 seconds. This process was repeated for each pole-slot combination listed in Table 5.2 for a given topology. Therefore each pole-slot combination is treated as a completely separate optimisation problem. The aforementioned time durations were achieved using a computer equipped with an Intel® Core™ i7-6700K processor clocked at 4.2 GHz, with 32GB RAM and a 256GB SSD. The entire optimisation procedure was hosted by the 64-bit openSUSE™ 13.2 operating system. It was found that by using an SSD as a storage medium for the simulation environment, the speed was noticeably increased since each function evaluation writes simulation files typically in excess of 500MB.

5.8 Results

5.8.1 Introduction

The results of the optimisation are presented in the form of bar plots. In Figure 5.8, the performance of optimised IDRFPM machines utilising round Litz wire are shown. Each pole combination is indicated in a different colour. Recall that the pole combinations are optimised independently from each other. The bar plots are scaled according to a value

shown just below the label of the performance metric. For example, the torque density is scaled according to a torque density of 7 N·m/kg, and is measured along the per unit y-axis. The actual values of the performance is shown in blue font on top of each bar.

For each topology, such as the IDRFPM machine with round Litz wire, or the SORSPM machine with round Litz wire, or the SORSPM machine with solid bars (2 turns per coil), the bar plots are shown for the following:

- Performance at the 2 kW, 100 rpm (rated torque, rated power) operating point.
- Performance at the 2 kW, 465 rpm (top speed, rated power) operating point.
- Optimised machine parameters

Recall that the designs are optimised for the 2 kW, 100 rpm operating point, and then the performance at 2 kW, 465 rpm is observed as a result. The optimisation is refined to such an extent, that the power output is 2000 W up to the second decimal, thus 2000.00 W.

The cross-section of the active components, optimised for each pole number, is shown in Figures 5.11, 5.15 and 5.19. Each figure represents $\frac{1}{6}^{\text{th}}$ of the machine, and the figure for each pole number is shown according to the same scale.

5.8.2 IDRFPM machine utilising round Litz wires

The IDRFPM machine is optimised for the rated torque, rated power operating point, and the performance of this operating point is shown in Figure 5.8. It is evident that the torque density reaches a peak for the 24 and 28 pole machines, where pole numbers smaller and greater than the aforementioned, exhibit smaller torque densities. The torque densities range just below 3 N·m/kg, which in this project also include non-active material such as aluminium and Tufnol, and are in agreement with the relatively low torque density reported by Oosthuizen *et al.* [1, p. 76] as 2.79 N·m/kg. As per the optimisation strategy, the copper losses are maintained at 200 W, while the output power is optimised very accurately to 2 kW. The other losses, as discussed in Section 3.6, are assumed negligible, and are thus all indicated as 0 W. Consequently, the efficiency will remain constant at 90.91 % for every design. The power factor is always very close to unity, because only q-axis currents are injected and the synchronous inductance is very small. The total mass is a minimum for the 24 and 28 pole machines, which of course takes shape of the inverse of the torque density. Glancing at the magnet mass, it is clear that the total mass is mostly attributed to the magnet mass. The Tufnol mass (used for the coil blocks) decreases as the number of poles increases, and is actually minute relative to the other materials. The torque ripple, is as expected, very small for the IDRFPM machine and is thus mostly irrelevant when comparing machines optimised at different pole numbers.

Figure 5.9 is quite similar to Figure 5.8, as it represents the same optimised designs shown in Figure 5.8, but evaluated at the rated power, top speed operating point. For this operating point, the torque required is much lower than in Figure 5.8, and the copper losses are much smaller due to the smaller current required by the machine. This naturally results in a much lower torque density and current density. For the same reasons, the efficiency is much better than in Figure 5.8 due to the smaller I^2R copper loss component. The power factor remains close to unity, as flux weakening is not implemented for the IDRFPM machine. The number of turns per coil are chosen such that the top speed voltage does not exceed the inverter voltage feeding from the 48 V supply.

Figure 5.10 shows the parameters that were optimised to achieve the performance in Figure 5.8 and 5.9. The coil height (h_c) decreases as the number of poles increase, while the coil pitch ratio (k_c) remains constant. This causes the overall cross-section area of the copper to decrease, which correlates with the decrease in copper mass shown in the previous figures, as well as with the increase in current density (due to the decrease in cross-section area of the copper). The number of turns allowed per coil decreases as the number of poles

increases. This is due to the general increase in back-EMF with the increase of poles, and therefore the number of turns has to decrease. The outer radius (r_o) was always optimised to the maximum limit of $r_o = 135\,\text{mm}$ and is therefore not shown in Figure 5.10. However, the active region height is decreasing as the number of poles increases. This means that the inner radius of the active material is increasing, therefore the inner aluminium yoke radius is also increasing. This results in an increase in the aluminium mass as can be seen in Figure 5.8 and 5.9. Interestingly, the inner magnet height (h_{mi}) is always greater than the outer magnet height (h_{mo}), and both these heights decrease as the pole number increases. Furthermore, the radially magnetised magnet pitch ratio (k_m) increases with the number of poles, as can be seen in Figure 5.11. For the higher pole numbers, the tangentially magnetised magnets tends to have the same width as the radially magnetised magnets ($k_m \approx 0.5$).

The increasing stack length (ℓ) along with the increase in the number of poles, is more difficult to explain. An increase in the number of poles, is accompanied by an increase in the number of coils, and thus an increase in the number of end-turns. Therefore if the stack length were to remain constant, the electrical resistance due to the end-turns would increase relative to the resistance of the copper in the active stack length. This means a smaller portion of the 200 W copper loss budget will contribute to torque development, and consequently the desired rated torque value is harder to achieve. To ensure that a larger portion of the copper losses will contribute to torque development, the stack length is increased by the optimisation algorithm, given if that is the most optimal manner, considering the constraints and objectives, to increase the torque.

If a preferred machine has to be selected, while neglecting the construction difficulty posed by a very low turns per coil number, the 24 pole machine seems the most appealing as it promises a high torque density compared to the other pole numbers. Naturally, it exhibits a low stack length and magnet mass relative to the other pole numbers. However the turns per coil is only 2, which might make the coil construction completely impractical as discussed in Section 3.2.3. With this in mind, the 16 pole machine with 4 turns per coil seems to be a better option. The 16 pole design, and all the other pole numbers, satisfy the efficiency requirement of 89 % at rated (base) speed. To conclude, the 16 pole design is chosen as the preferred candidate in this category.

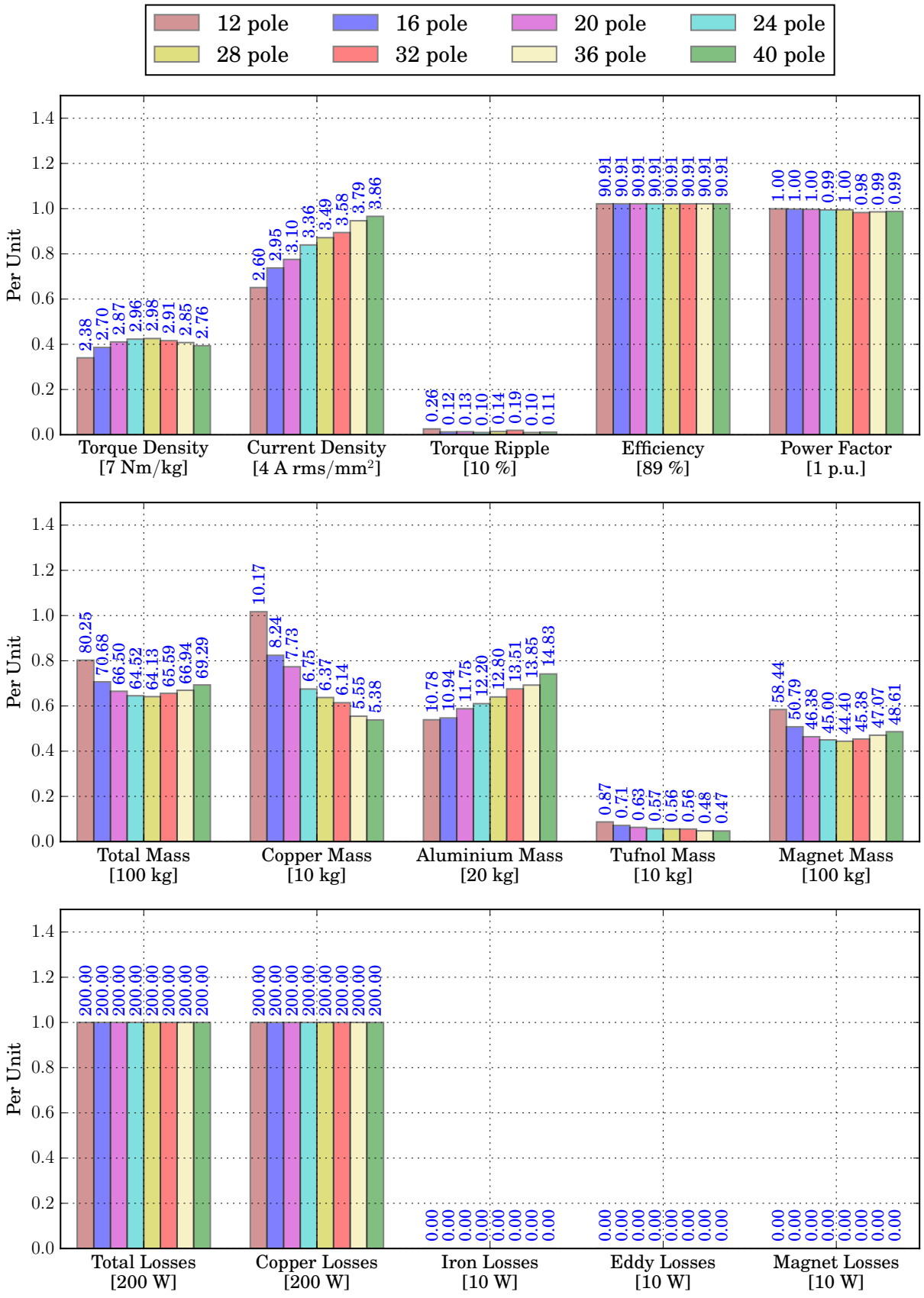

Figure 5.8: Performance comparison at 2 kW, 100 rpm, of the IDRFPM machine for various pole numbers utilising round Litz wire.

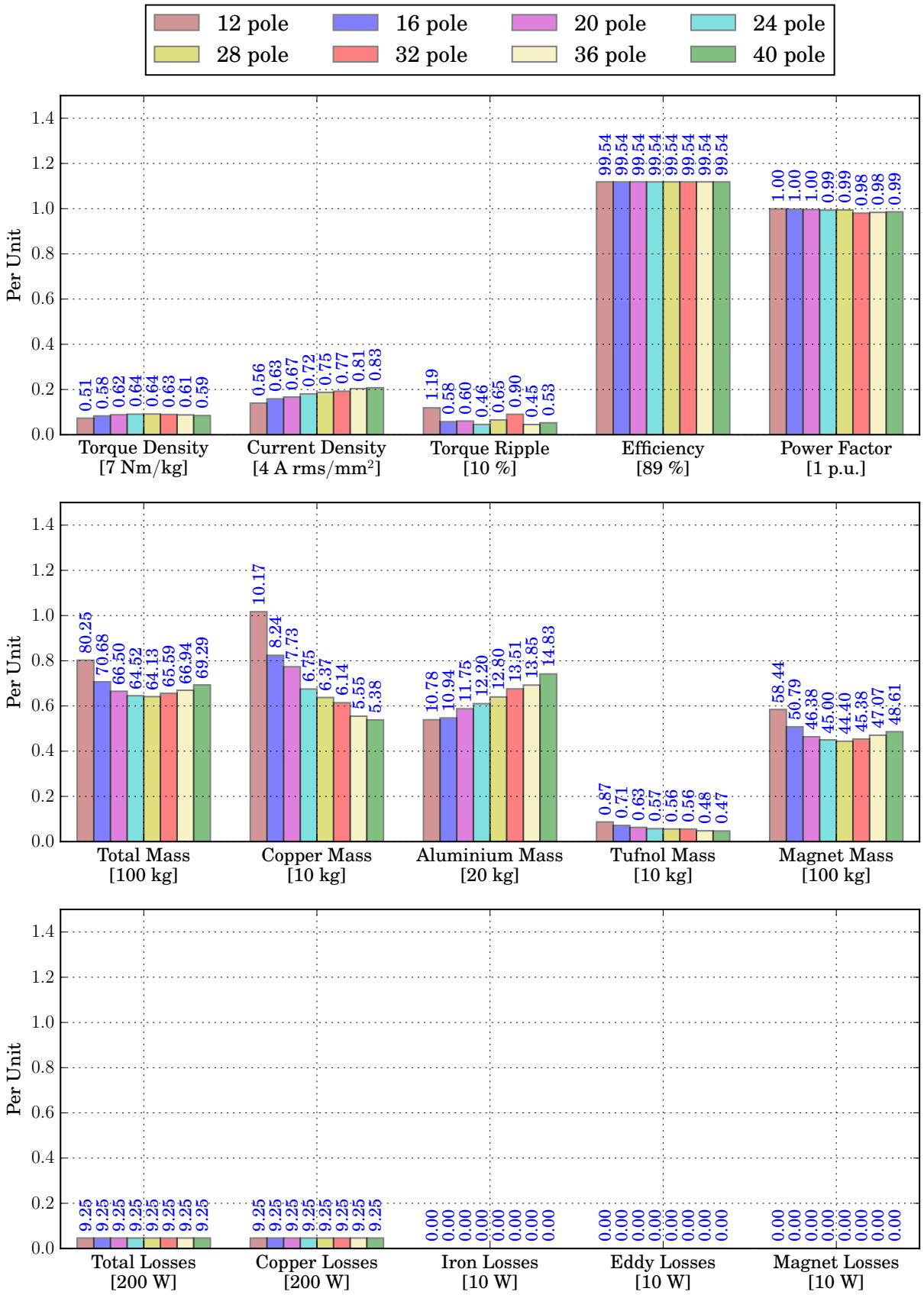

Figure 5.9: Performance comparison at 2 kW, 465 rpm, of the IDRFPM machine for various pole numbers utilising round Litz wire.

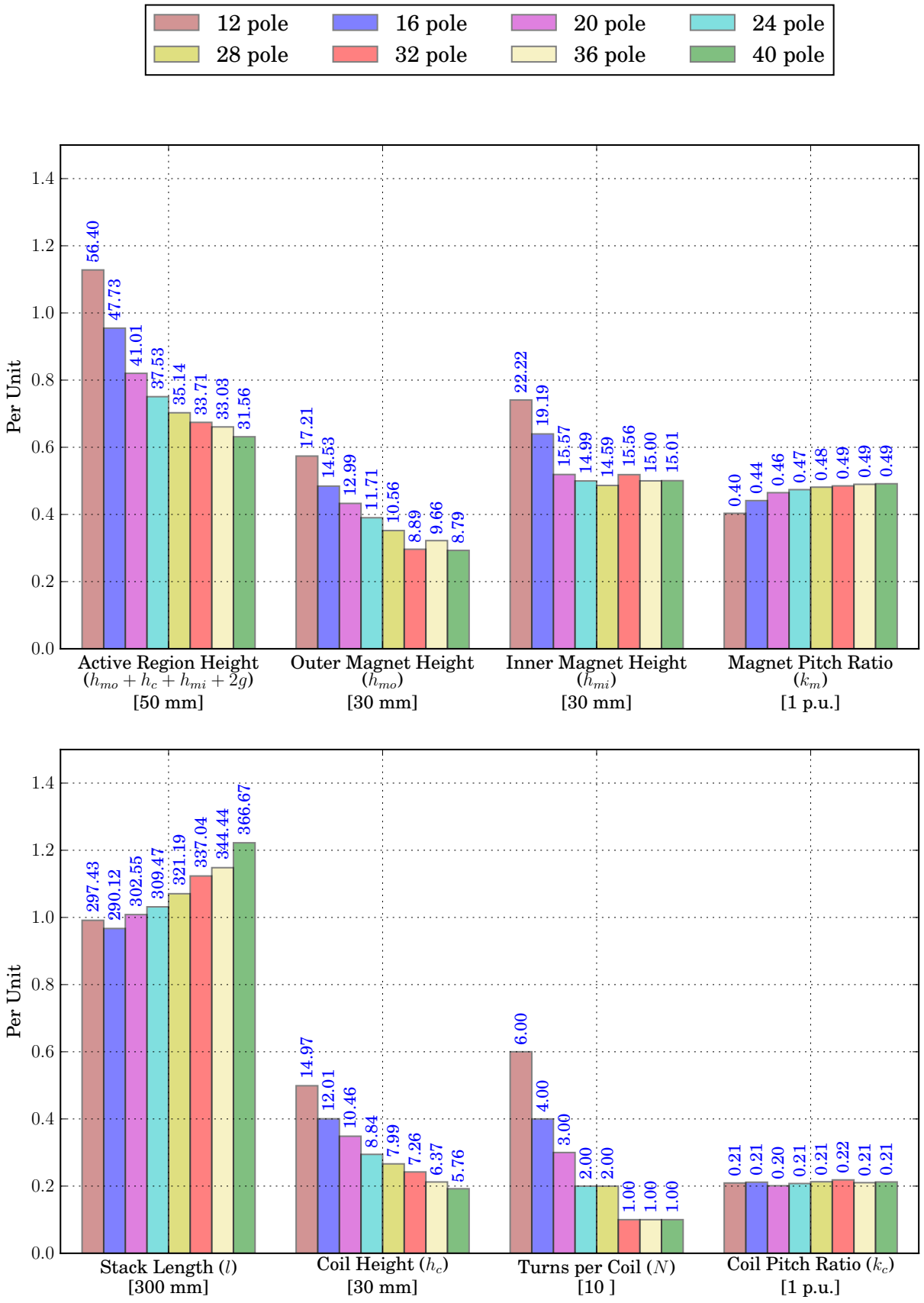

Figure 5.10: Input parameter comparison of the IDRFPM machine for various pole numbers, utilising round Litz wire.

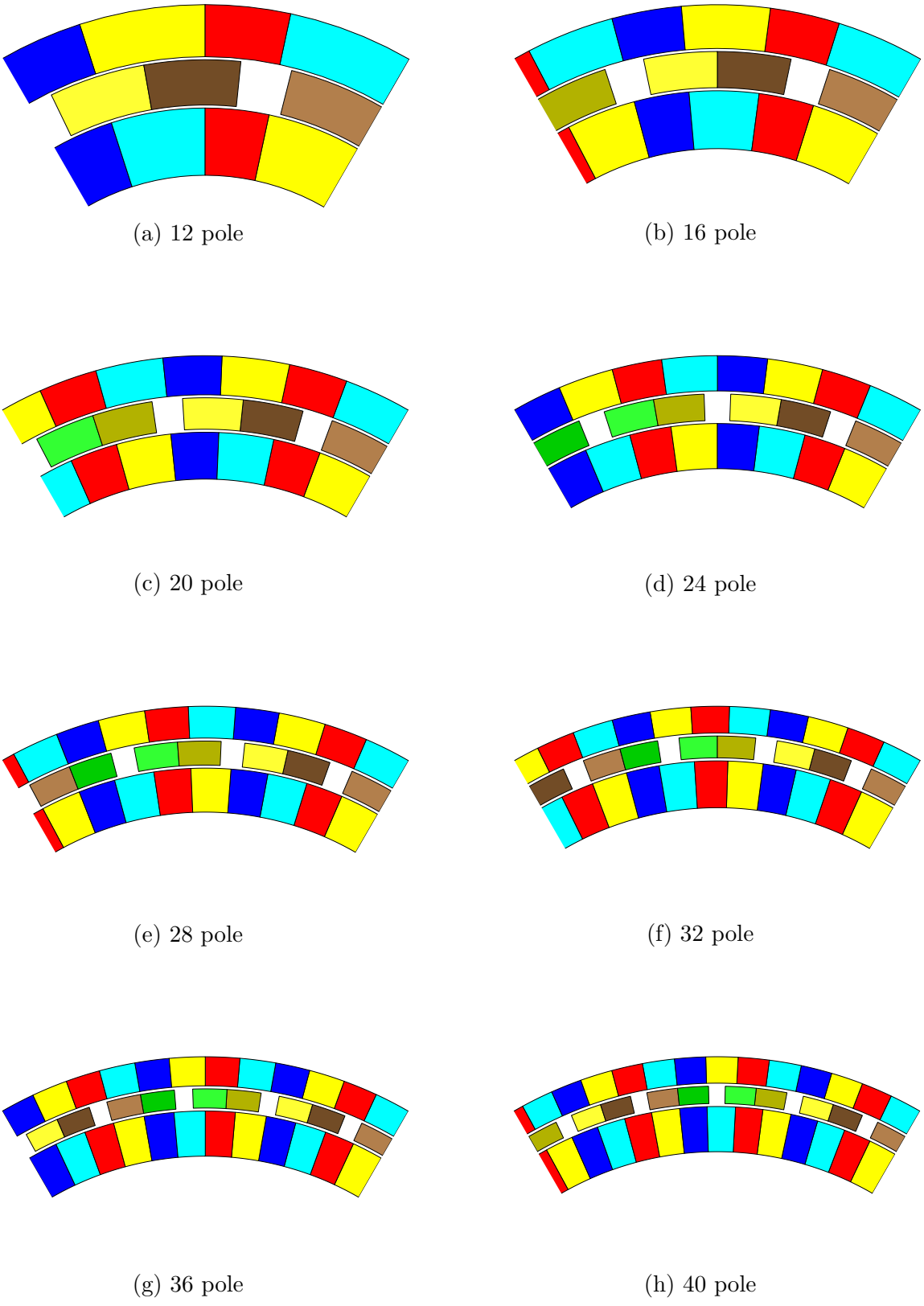

(a) 12 pole

(b) 16 pole

(c) 20 pole

(d) 24 pole

(e) 28 pole

(f) 32 pole

(g) 36 pole

(h) 40 pole

Figure 5.11: Cross-section of the active components, focussed on $\frac{1}{6}^{\text{th}}$ of the IDRFPM machine. Each pole number is shown according to the same scale. The red and dark blue magnets represent the radially magnetised magnets.

5.8.3 SORSPM machine utilising round Litz wires

The performance results for the various pole numbers, at the rated torque and rated power operating point is shown in 5.12. As can be seen from Figure 5.12, the torque density increases with the number of poles and then starts to flatten out at pole numbers larger than 40. While the torque density increases with the number of poles, the efficiency experiences a slight decrease, which can also be deduced from the gradual increase in the total losses. As expected for a synchronous permanent magnet machine, the rotor iron losses are very small. The magnet losses are also very small at this point since the speed is much lower than the top speed. As per the optimising strategy, the copper losses are all kept at 200 W. It is interesting to see that the copper mass and stator iron mass remain fairly constant over the range of pole numbers, while the rotor mass and magnet mass decrease. This confirms the overall tendency for a higher pole number to require less rotor iron. It is also shown that the torque ripple, although very low, experiences a great reduction when opting for pole numbers higher than 36. This confirms that a design with a lower LCM value is more susceptible to torque ripple.

In Figure 5.13, the machine is operated at top speed and rated power. Naturally this means the developed torque is much lower than at the previous operating point, which can be seen from the torque densities ranging around 1.5 N·m/kg to 1.7 N·m/kg. At first glance the bar plots of Figure 5.13 might seem disorientating. It is important to realise that for this topology, the number of turns are calculated according to the flux weakening capability of the machine. The flux weakening capability is constrained by the copper losses allowed in the windings. Thus the maximum number of turns is pursued, as long as the copper losses remain below 200 W and the voltage limit is adhered to. Consider for example the 40 pole design in Figure 5.13, which has a copper loss component of 29.2 W. According to Figure 5.14, this design has 4 turns per coil. Now consider the 44 pole design, which of course has a greater back-EMF (due to the increased number of poles). The 44 pole design, can also make use of 4 turns per coil, but at a much larger copper loss component of 191.14 W attributed to the necessary flux weakening. The 48 pole design would require too much flux weakening, and thus only 3 turns per coil are implemented at which flux weakening can be avoided completely. It is insightful to see that the designs which depend greatly on flux weakening, such as the 36 pole, 44 pole and 60 pole designs, that their stator iron losses are noticeably smaller than the other designs. This can be explained in that stator losses are mostly attributed to the alternating flux caused by the rotor poles, where the rotor field is effectively reduced by flux weakening. The power factor is also reduced for the designs which make use of flux weakening, since the i_d current does not

contribute to real mechanical power (Equation 4.27). Finally, it is important to notice that some of the losses of Figure 5.13 are shown in larger scales than in Figure 5.12. Of special interest is the stator iron losses and the magnet losses, which are vastly greater than at the 100 rpm operating point. This is of course attributed to the increased frequency of the alternating flux within the stator caused by the rotor, and the increased slotting frequency experienced by the magnets.

Figure 5.14 shows all the dimensions which were optimised, and the physical implication thereof can be seen in Figure 5.15. It can be observed that the rotor yoke height (h_{yo}), stator yoke height (h_{yi}) and magnet height (h_m) gradually decrease as the pole number increases, while the slot height (h_c) remains more or less constant. It is interesting to see that the (h_{yo}, h_{yi}, h_m) dimensions all reach the 3 mm thickness minimum at the higher pole numbers. The placement of the hole in the stator teeth (h_h), is placed closer to the stator tooth tip (stator shoe) as the pole number is increased. This makes sense, as a higher pole number means a higher slot number, which means the stator teeth widths become smaller, and the flux path becomes bottlenecked where the stator tooth meets the stator yoke. Thus in order to avoid an additional barrier for the flux path, the hole is placed closer to the stator tooth tip where the flux path is not bottlenecked. Another observation is that the shoe tip width (w_s) is decreased when the number of poles is increased, which makes sense as the stator teeth are closer to one another. Furthermore, it is interesting to see that the magnet pitch ratio (k_m) and slot pitch ratio (k_c) remain almost constant regardless of the pole number. The designer can thus consider to make these two variables constant, and exclude them from future optimisations in order to obtain optimal results with less computational effort.

As can be seen from Figure 5.12, all the designs satisfy the minimum efficiency requirement at rated (base) speed of 89 %. Taking into account that the torque density gain for machines with 40 poles and higher is minimal, the 40 pole machine seems like a good compromise between torque density and efficiency at both operating points. The torque ripple is satisfactory, and the number of turns per coil is 4 which satisfies the turns per coil strategy discussed in Section 4.2.4.5. The 44 pole design also satisfies these constraints, but the power factor at top speed is much worse at 0.32 compared to that of the 40 pole design at 0.62. Both power factors are relatively low because of the flux weakening strategy implemented. Furthermore, the torque ripple of the 44 pole design at top speed is 22.24 % while the 40 pole design is at 8.40 %. Considering all the aforementioned, the 40 pole design is chosen as the preferred candidate in this category.

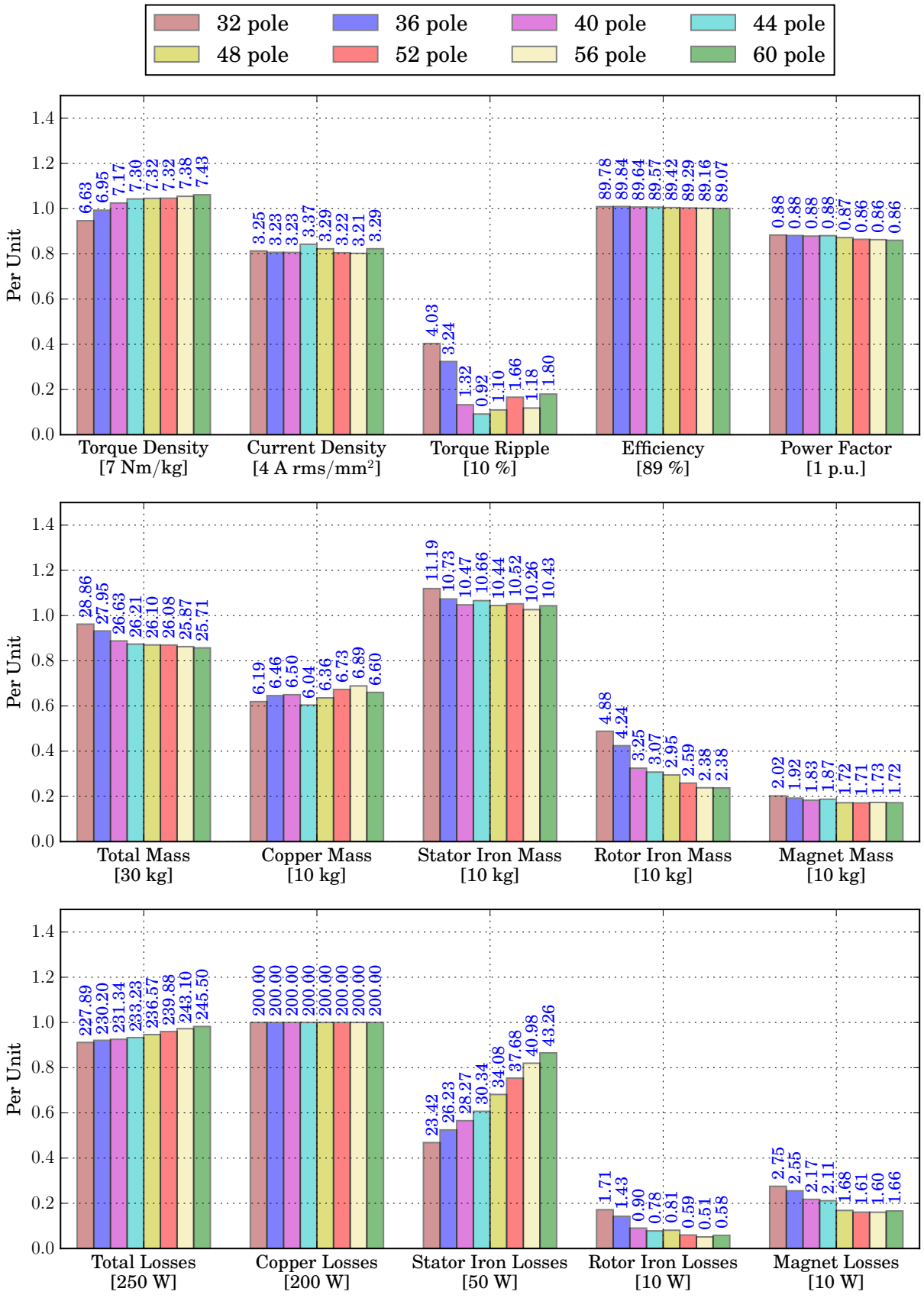

Figure 5.12: Performance comparison at 2 kW, 100 rpm, of the SORSPM machine for various pole numbers utilising round Litz wire.

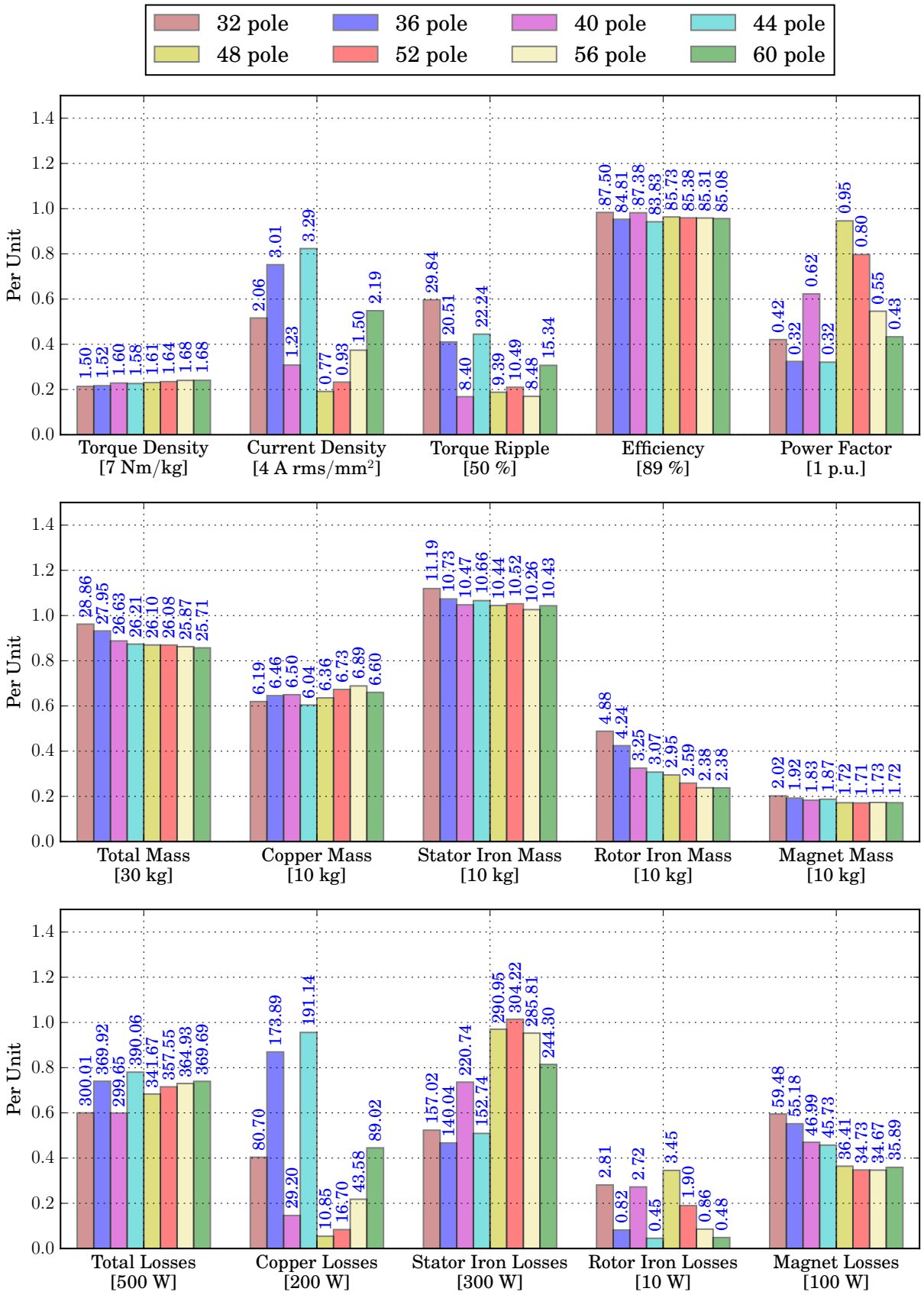

Figure 5.13: Performance comparison at 2 kW, 465 rpm, of the SORSPM machine for various pole numbers utilising round Litz wire.

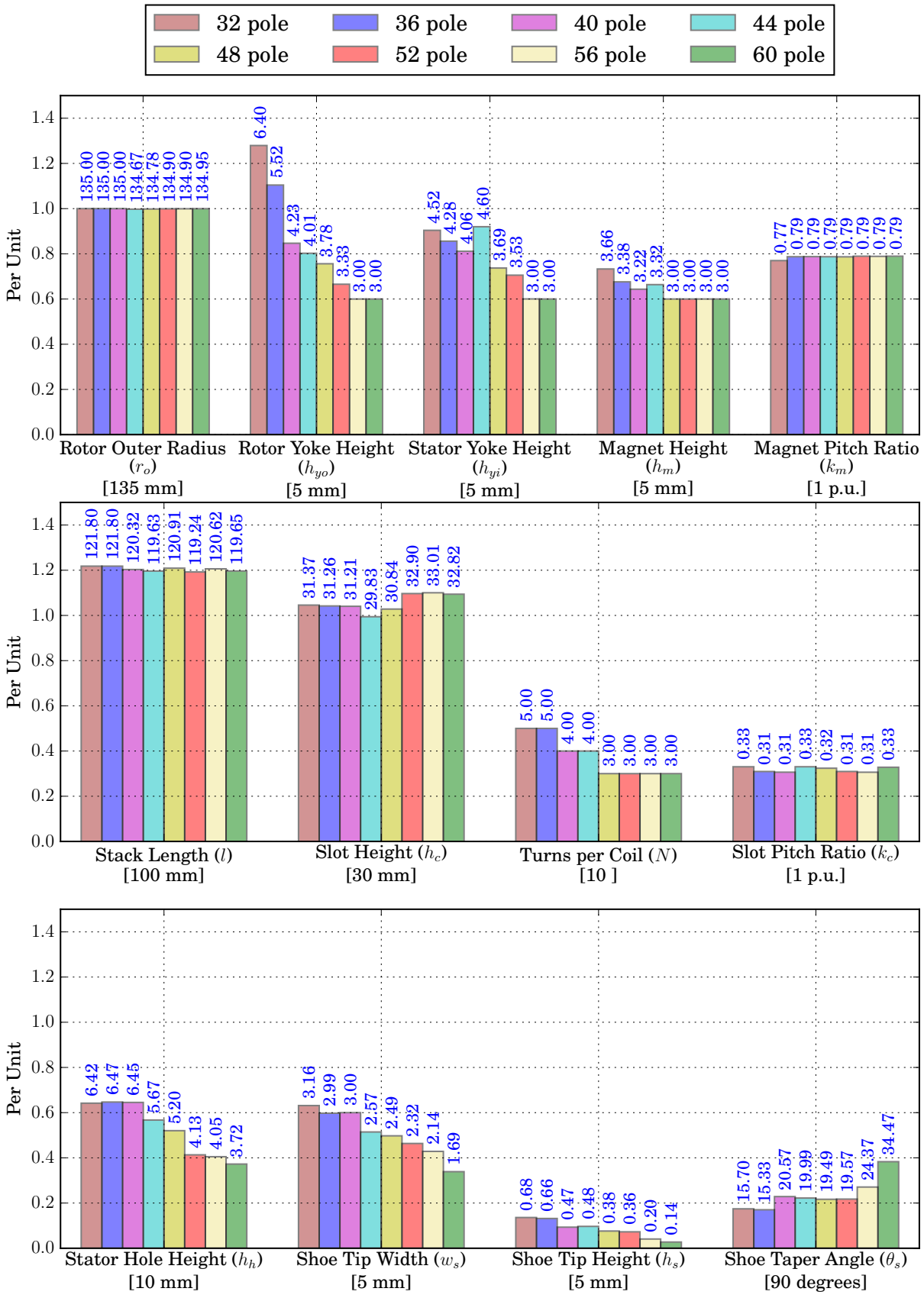

Figure 5.14: Input parameter comparison of the SORSPM machine for various pole numbers, utilising round Litz wire.

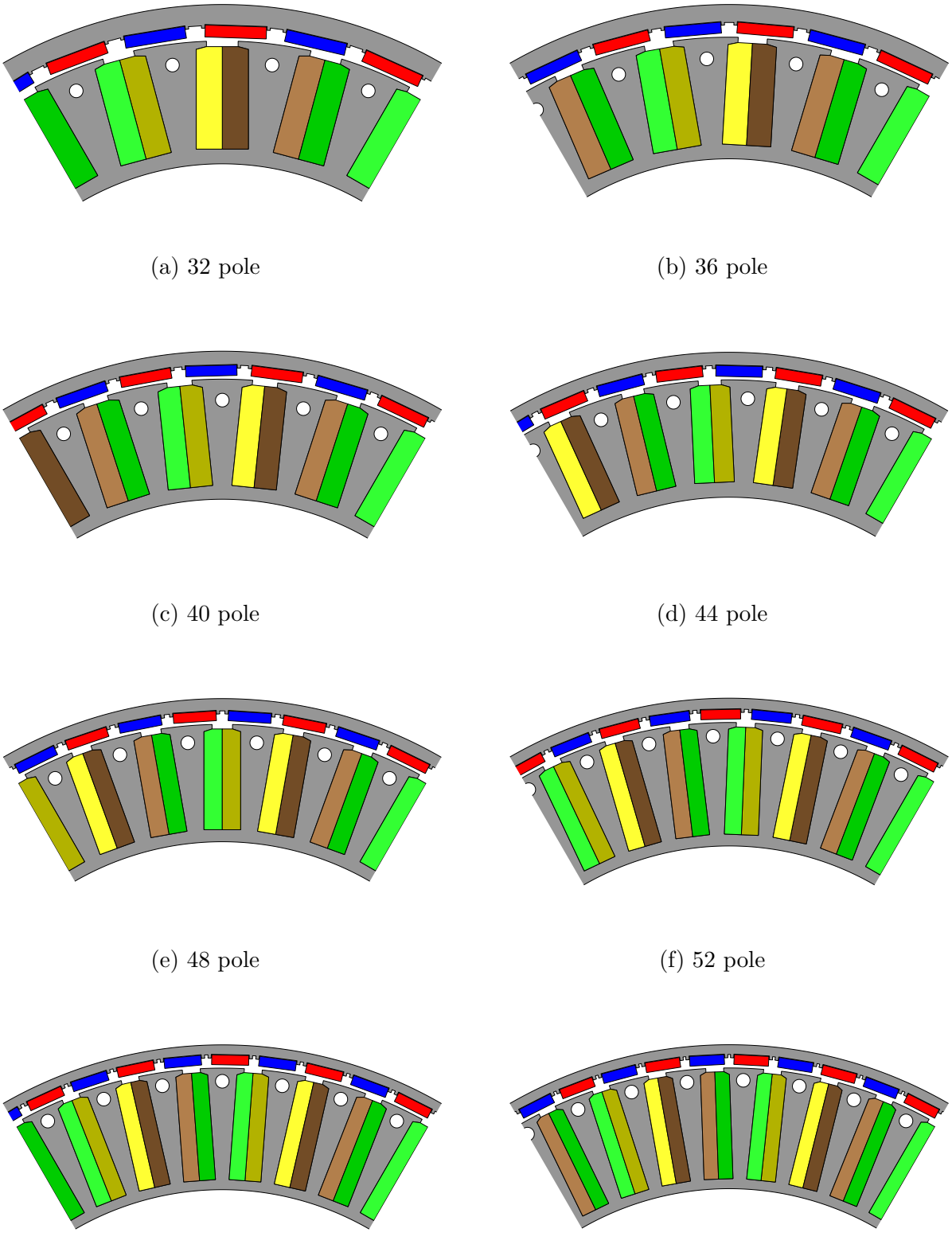

(a) 32 pole

(b) 36 pole

(c) 40 pole

(d) 44 pole

(e) 48 pole

(f) 52 pole

(g) 56 pole

(h) 60 pole

Figure 5.15: Cross-section of the active components, focussed on $\frac{1}{6}^{\text{th}}$ of the SORSPM machine with Litz wire. Each pole number is shown according to the same scale.

5.8.4 SORSPM machine utilising solid copper bars

For the solid copper bar configuration, the number of turns per coil is kept at two ($N = 2$). This means there are two bars per coil side, as depicted in Figure 4.9a and 4.9c.

In Figure 5.16, the performance at the rated torque and rated power operating point is shown. It is again apparent that the torque density increases with the number of poles. Other than the round Litz wire variant, the torque density growth starts to flatten out at a much higher pole number of 56. As was seen with the round Litz wire variant, the efficiency decreases slightly with an increase in the number of poles. In Figure 5.16, the rotor iron losses is omitted since the losses were always below 3 W, and consequently the more significant eddy current losses within the bar conductors can be shown instead. The eddy current losses initially decrease as the pole number increases, and then again starts to increase for the pole numbers larger than 40. This can be explained by the much larger copper mass (and thus a larger cross-section area for the eddy currents to exist) when the pole numbers are less than 40. For the designs with pole numbers larger than 40, the copper mass is reduced very slightly, so the benefit of a smaller cross-section area is easily outweighed by the increased frequency of the alternating flux due to the increased number of rotor poles. The reader is reminded that the total mass also includes an aluminium yoke mass as discussed in Section 4.12. The aluminium mass is not indicated in Figures 5.16 and 5.17.

The top speed and rated power performance is shown in Figure 5.17. For this solid copper bar topology, flux weakening is also implemented if necessary. This is evident from the copper losses, which for the pole numbers 32 to 44, are all very consistent and below 11 W. From 48 poles and onwards, the back-EMF becomes too large and flux weakening is required, hence the gradual increase in copper losses. The increase in copper losses is also visible from the increase in current density. Once again, the power factor and efficiency is deteriorated when flux weakening is activated. It is however interesting to see that the stator iron losses and magnet losses decrease once flux weakening is implemented. As previously mentioned, the reason being that the alternating flux caused by the rotor field (which is being weakened) is the primary contributor to the aforementioned losses. Another interesting observation is that the eddy current losses within the copper bars are relatively small for the pole numbers which are not making use of flux weakening. This highlights two features of this specific topology. Firstly, the low eddy current losses during top speed in the case of a non flux weakening environment, shows that the copper bars are well protected against the alternating flux caused by the rotor field. This is due to the stator

shoe structure, which guides the flux path away from the copper bars. Secondly, it shows that the sudden increase in eddy current losses when flux weakening is implemented, is due to the alternating flux created by the stator conductors themselves (proximity effect). The latter effect is very hard to avoid in a double layer structure as there are many neighbouring conductors. Figure 5.17 also shows that in general the torque ripple becomes noticeably smaller as the pole number increases.

The trends in the dimensions, shown in Figures 5.18 and 5.19, are very much the same as for the SORSPM machine utilising round Litz wires, with minor exceptions. Firstly, the turns per coil in Figure 5.14 (which is constant at 2 turns for the solid bars topology) is replaced with a fill factor. The fill factor is calculated as a result of the insulation used for the copper bars. The gap for the insulation is kept constant at 0.9 mm as explained in Section 4.2.4.2 (although the insulation itself is 0.8 mm thick). This causes the copper area to decrease relative to the slot area when the slot area is decreased (the slot area becomes smaller as the number of slots increases) and therefore the fill factor decreases. It is interesting that the decreasing fill factor is still outweighed by the other benefits of a higher pole number. Another exception is that of the shoe tip height (h_s) and the stator shoe taper angle (θ_s), which is much larger than the topology utilising round Litz wire. The reason for this is that efficiency is one of the objectives that were optimised. The increased (h_s) and (θ_s) values help to create larger flux "funnels" which guide the flux path away from the copper bars thereby avoiding excessive eddy current losses. Interestingly, the outer radius (r_o) for this design did not follow the same optimisation trend as the previous two topologies. It seems that a trade-off between the stack length and outer radius is more prominent for this topology. The outer radius tends to increase with the pole count, while the stack length remains constant or decreases. By comparing the values in Figure 5.18 with the boundaries specified in Table 5.7, it is good to see that the optimal designs are found well within the boundary limits.

Overall, the last two pole numbers, 56 and 60, appear the most attractive if only torque density and torque ripple is prioritised. The downside of these high pole count machines is that efficiency and power factor are sacrificed when operating at top speed, rated power. The design with the highest torque density which adheres to the 89 % efficiency constraint, is the 48 pole machine. It has an acceptable power factor at top speed. Unfortunately none of the machines in this category reach the rated (base) speed power factor goal of 0.9. The 48 pole design is nevertheless relatively close to the goal, with a power factor of 0.85 at the base speed operating point. Considering all the aforementioned, the 48 pole design is chosen as the preferred candidate in this category.

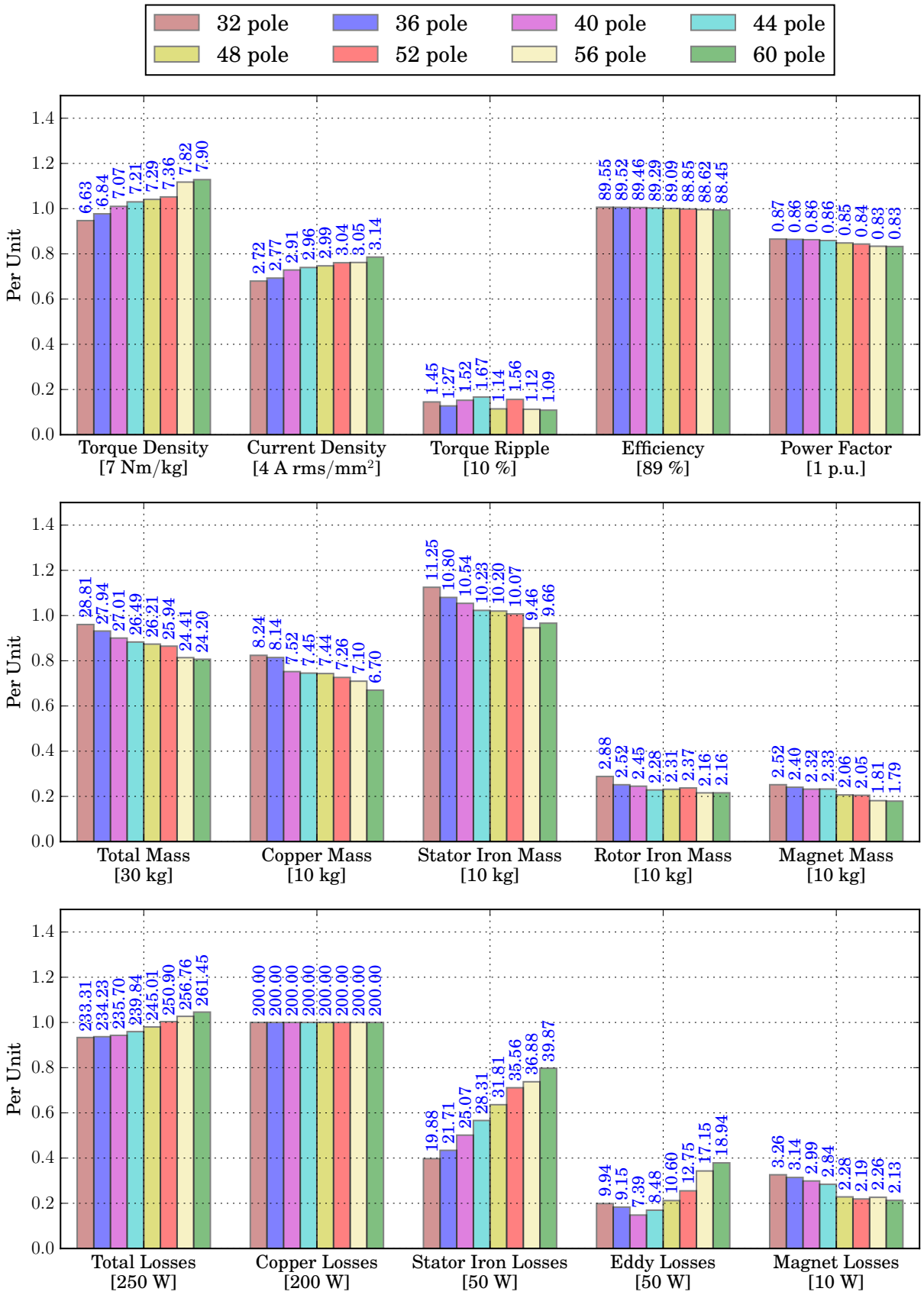

Figure 5.16: Performance comparison at 2 kW, 100 rpm, of the SORSPM machine for various pole numbers utilising solid copper bars.

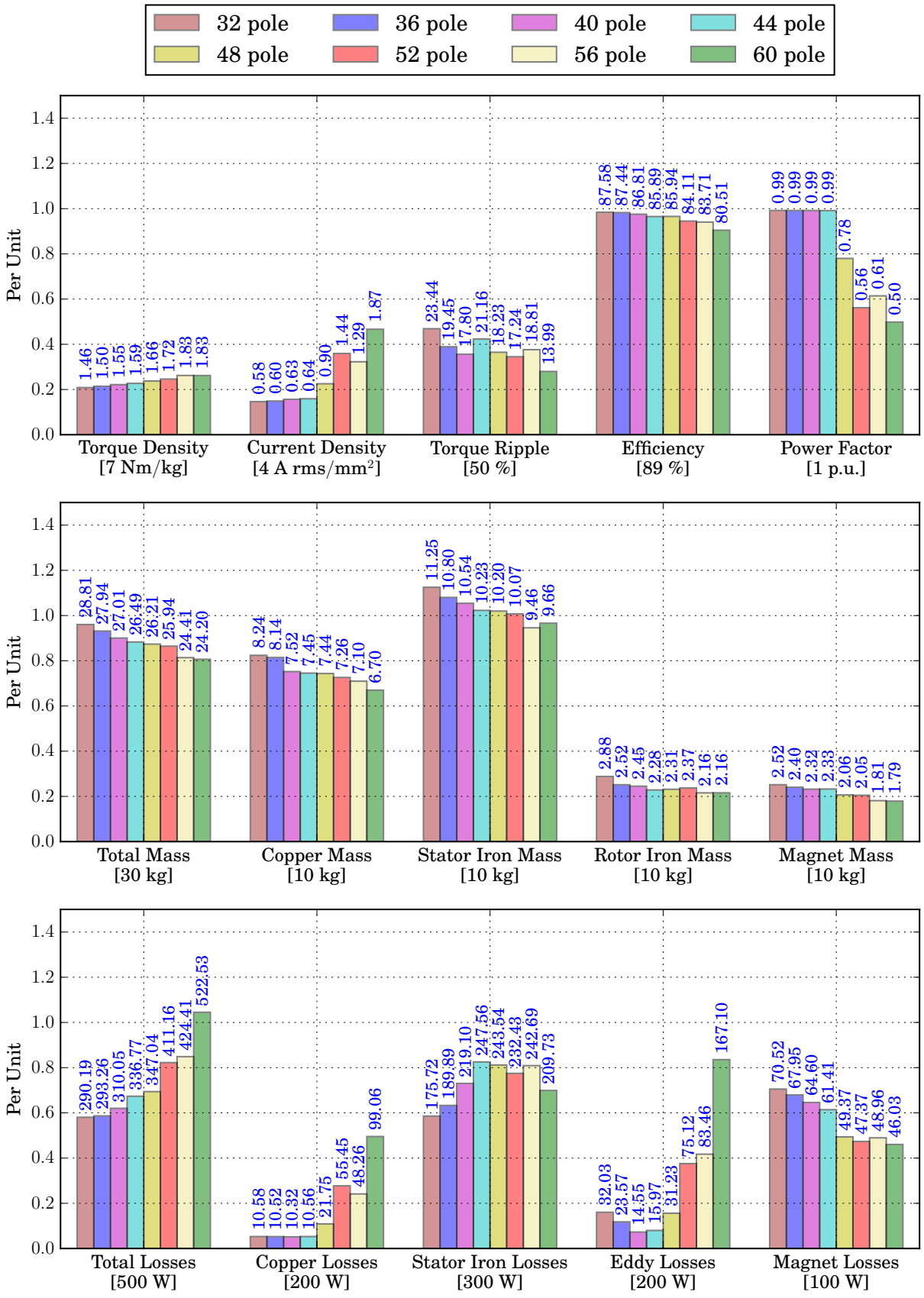

Figure 5.17: Performance comparison at 2 kW, 465 rpm, of the SORSPM machine for various pole numbers utilising solid copper bars.

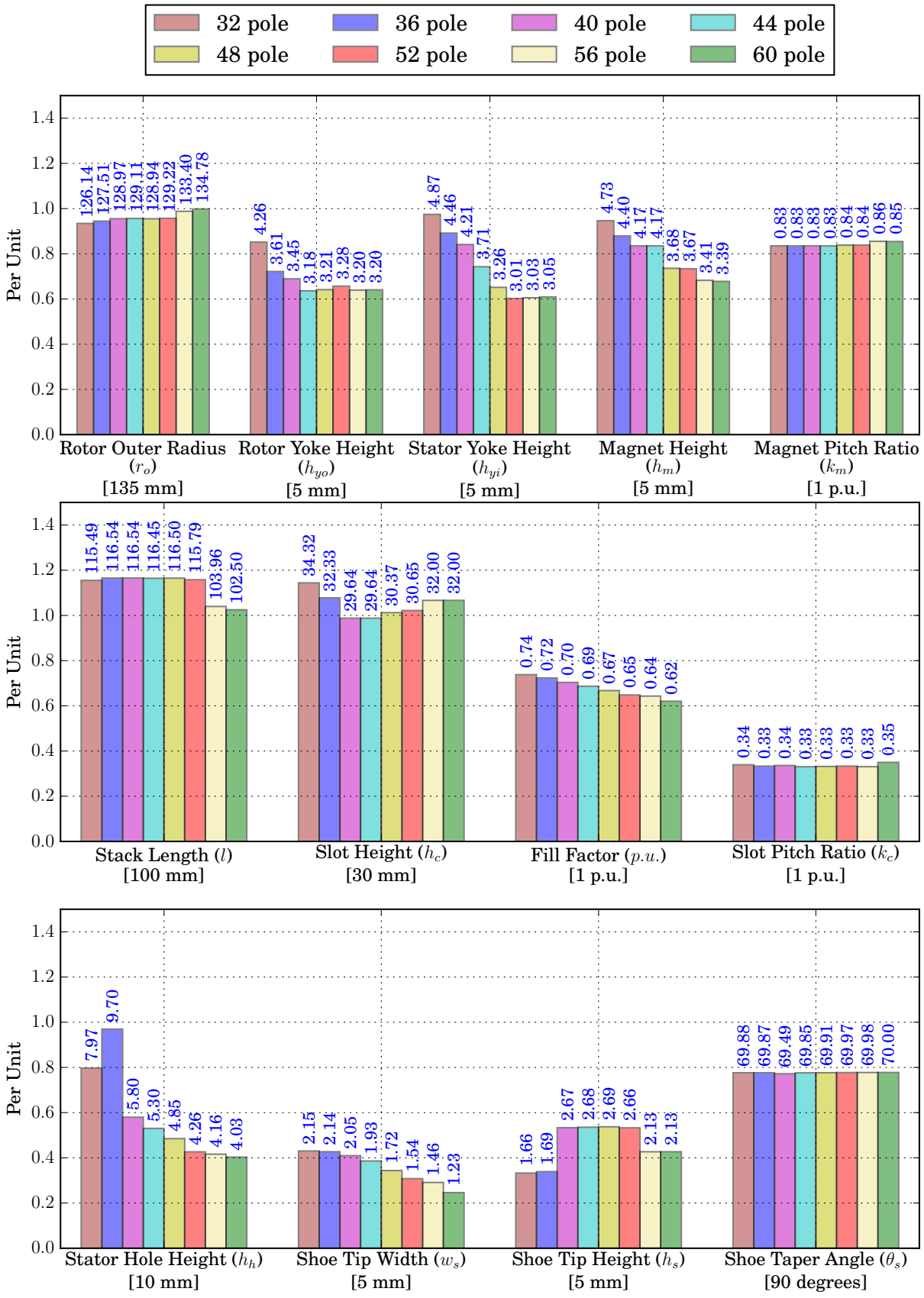

Figure 5.18: Input parameter comparison of the SORSPM machine for various pole numbers, utilising solid copper bars.

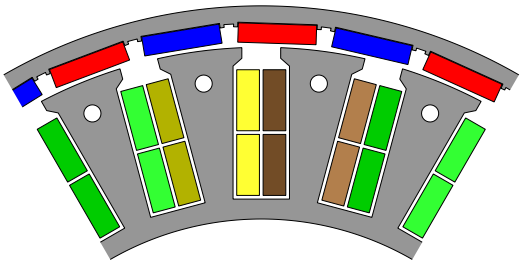

(a) 32 pole

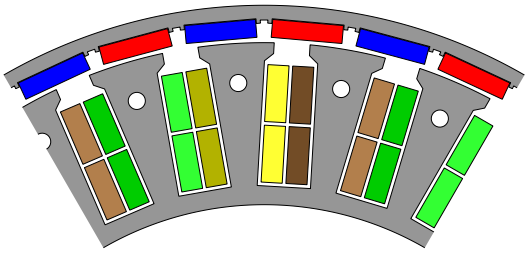

(b) 36 pole

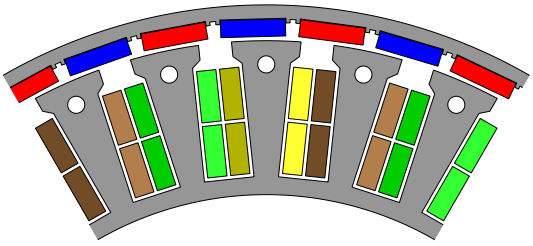

(c) 40 pole

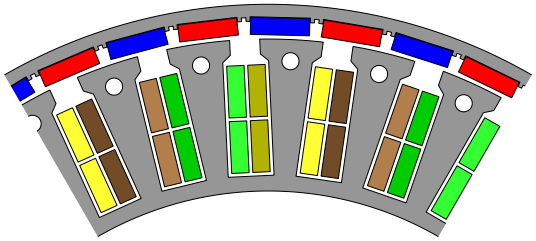

(d) 44 pole

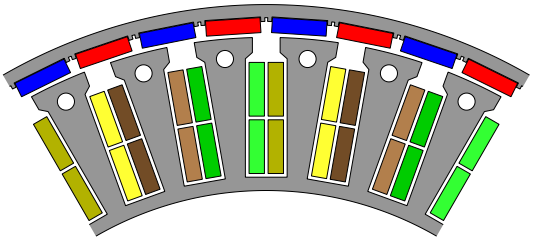

(e) 48 pole

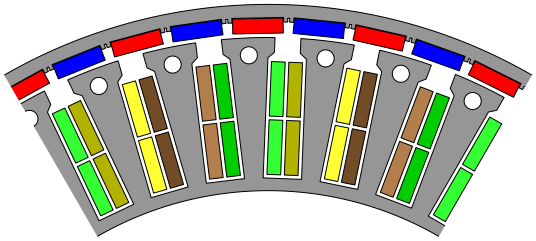

(f) 52 pole

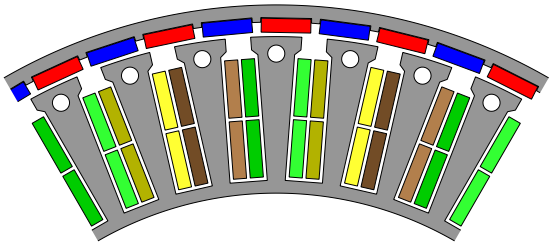

(g) 56 pole

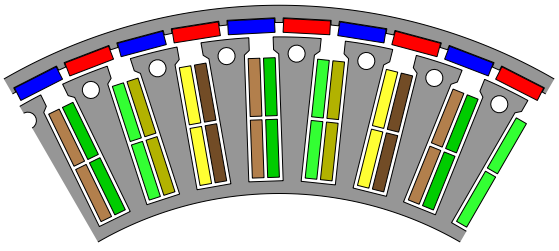

(h) 60 pole

Figure 5.19: Cross-section of the active components, focussed on $\frac{1}{6}^{\text{th}}$ of the SORSPM machine with solid copper bars. Each pole number is shown according to the same scale.

Chapter 6

Design Recommendation

6.1 Introduction

In Chapter 5, the optimisation of three different machine configurations for a range of pole numbers was done. That is, the IDRFPM machine utilising Litz wire, the SORSPM machine utilising Litz wire and the SORSPM machine utilising solid copper bars were optimised in Sections 5.8.2, 5.8.3 and 5.8.4 respectively. At the end of each section, a motivation was given for the most appealing pole number. In this chapter, the performance and machine parameters of the top candidate for each topology is compared and discussed. Thereafter, a single design will be recommended based on the aforementioned performance comparison and based on some practical considerations. To this end, an investigation into the construction of the the novel SORSPM machine utilising copper bars is done.

6.2 Design Comparison

The top candidates from each machine configuration is compared in this section. In Figure 6.1, the performance comparison at rated torque, rated power is shown. At first glance, the most noticeable differences are the torque density and magnet mass. The IDRFPM machine has a significantly lower torque density of 2.70 N·m/kg while the SORSPM design utilising Litz wire is at 7.17 N·m/kg, and the design utilising solid copper bars is at 7.29 N·m/kg. This vast difference in torque density between the IDRFPM and SORSPM designs, is largely attributed to the massive difference in magnet mass. The IDRFPM machine's large magnet mass of 50.79 kg was required in order to achieve the rated torque requirement, while adhering to the copper loss budget of 200 W. In this project it is especially important

to achieve a high torque density, or low total mass, as the machine's mass will add to the total vehicle mass, which will theoretically increase the torque requirement for a single motor initially calculated as 191 N·m. Since it is envisioned in this project to have both the rear wheels each propelled by its own motor, the machine mass added to the vehicle is at least double the value displayed in Figure 6.1. Thus for the IDRFPM machine, the total mass added to the vehicle will at the very least be a staggering 141.36 kg, which of course excludes other mechanical components such as the machine end-plates (back and front plates), shaft and ball bearings. In comparison, the SORSPM machine utilising solid copper bars, will add at least 52.42 kg to the total vehicle mass. The extremely large IDRFPM machine mass, would cause the vehicle's torque requirement to increase drastically, and in turn necessitate the IDRFPM machine's torque (and thus machine size) to increase yet again. This situation could very well lead to a runaway situation, in which the ever increasing vehicle mass and motor torque will prevent the vehicle's requirements to be met. To put these values into perspective, as mentioned in Section 2.4, the existing golf cart powertrain has a mass of 70 kg. To be fair, the 70 kg also includes drum breaks and an axle on which the chassis can be mounted. Therefore, if a practical powertrain with the SORSPM machine is employed, the actual total powertain mass is likely to be in the vicinity of 70 kg. The point is that the IDRFPM solution is very far from the aforementioned values.

Considering the rated torque, rated power operating point from Figure 6.1, the only performance metrics in which the IDRFPM machine excels in comparison to the other SORSPM designs, is that of the power factor, efficiency and torque ripple. While at this operating point, the IDRFPM machine's efficiency and torque ripple advantage is not as significant, the power factor is impressive as it is rounded up to unity. The almost perfect power factor is rather appealing, compared to the the power factors of 0.88 and 0.85 of the SORSPM designs. Recall that in Chapter 2, Table 2.3, it was stated that the desired efficiency and power factor at rated (base) speed is 89 % and 0.90 respectively. All the candidates considered here, adhere to the 89 % efficiency constraint. Unfortunately, the SORSPM designs do not satisfy the minimum power factor goal of 0.90.

The performance at the rated power, top speed operating point is shown in Figure 6.2. Again, the IDRFPM machine's power factor, efficiency and torque ripple trumps that of the SORSPM designs. The power factor of the IDRFPM machine remains at unity, however unlike at the rated torque operating point, here the SORSPM designs perform much worse, achieving only 0.62 and 0.78 respectively. This is because both SORSPM machines make use of flux weakening at the top speed operating point. Additionally, the

efficiency of the IDRFPM machine is astounding, almost reaching the 100 % mark. Keep in mind that the efficiency numbers reported in this project do not account for mechanical and friction losses. In comparison, the SORSPM designs exhibit a much lower efficiency, of only 87.38 % and 85.94 % for the Litz and solid bar configurations respectively. The reason for the noticeably lower efficiency of the SORSPM machine utilising solid bars, is because of the eddy losses within the copper bars during high speed operation. However, since efficiency was one of the objectives of the optimisation procedure, the optimisation process was able to protect the copper bars from excessive eddy current losses (as was the case in Table 4.4). This is quite clear when comparing the copper location in Figure 6.6 to that of the Litz variant in Figure 6.5. The copper bars are located much further from the airgap in order to avoid the alternating flux caused by the magnets.

The disadvantage of the aforementioned copper bar placement, is that it makes the machine susceptible to torque ripple at higher speeds (constant power operation) as the reluctance torque component becomes more pronounced. This can be seen when comparing the overall torque ripple results shown for the top speed in Figures 5.13 and 5.17. However, torque ripple was also an optimisation objective in Chapter 5, which means a compromise between efficiency and torque ripple for the copper bar topology had to be reached. Unfortunately, despite the compromise, for any given pole number both the efficiency and torque ripple is less desirable than that of the SORSPM machine utilising Litz wire. The torque ripple of the IDRFPM machine remains below 1 %, while the SORSPM machine utilising Litz wire is at 8.40 % and the SORSPM machine utilising solid bars is at 18.23 %.

Figure 6.3 shows the machine parameters and dimensions of each design, while Figures 6.4, 6.5 and 6.6 show the physical representations thereof, all according to the same scale. The fact that the optimisation procedure for the IDRFPM machine opted for a fairly long stack length of 290.12 mm, shows that the IDRFPM configuration struggles to provide the torque requirement within the constraints of this project. When comparing Figures 6.4, 6.5 and 6.6, the sheer size of the IDRFPM machine's magnets, compared to the SORSPM candidates, is particularly striking. The aforementioned, together with the IDRFPM machine's long stack length, results in the very large magnet mass. The IDRFPM machine's much larger aluminium mass is also as a result of the long stack length. The IDRFPM machine and the SORSPM machine utilising Litz wire were both optimised to the outer radius limit of 135 mm, while the SORSPM design utilising copper bars settled at a lower value of 128.94 mm. Therefore the most compact machine is the SORSPM machine utilising copper bars with a stack length of 116.50 mm, while the SORSPM machine utilising Litz wire is at second place with 120.32 mm and the IDRFPM last with 290.12 mm.

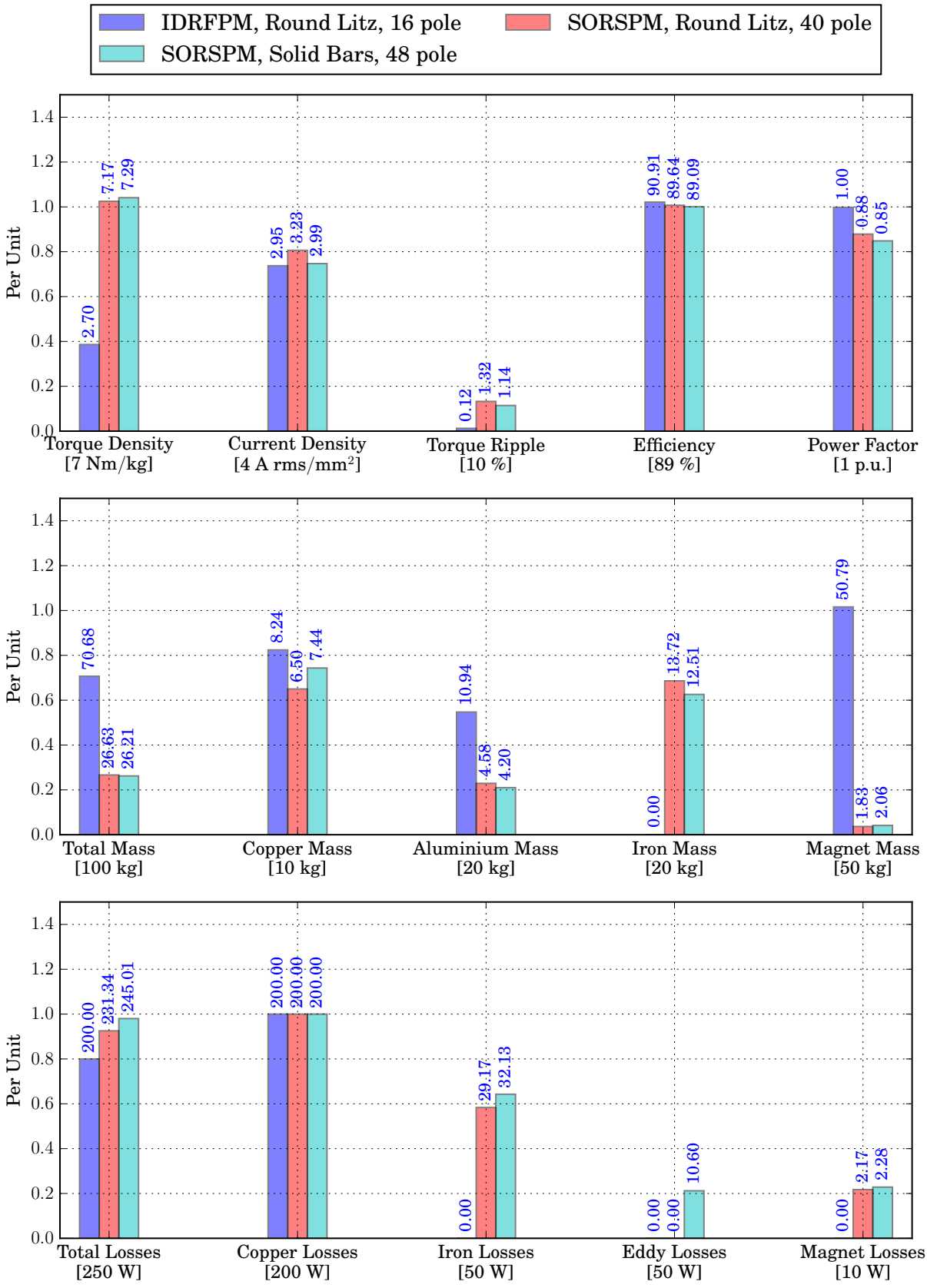

Figure 6.1: Performance comparison of the most appealing design of each machine configuration at 2 kW, 100 rpm.

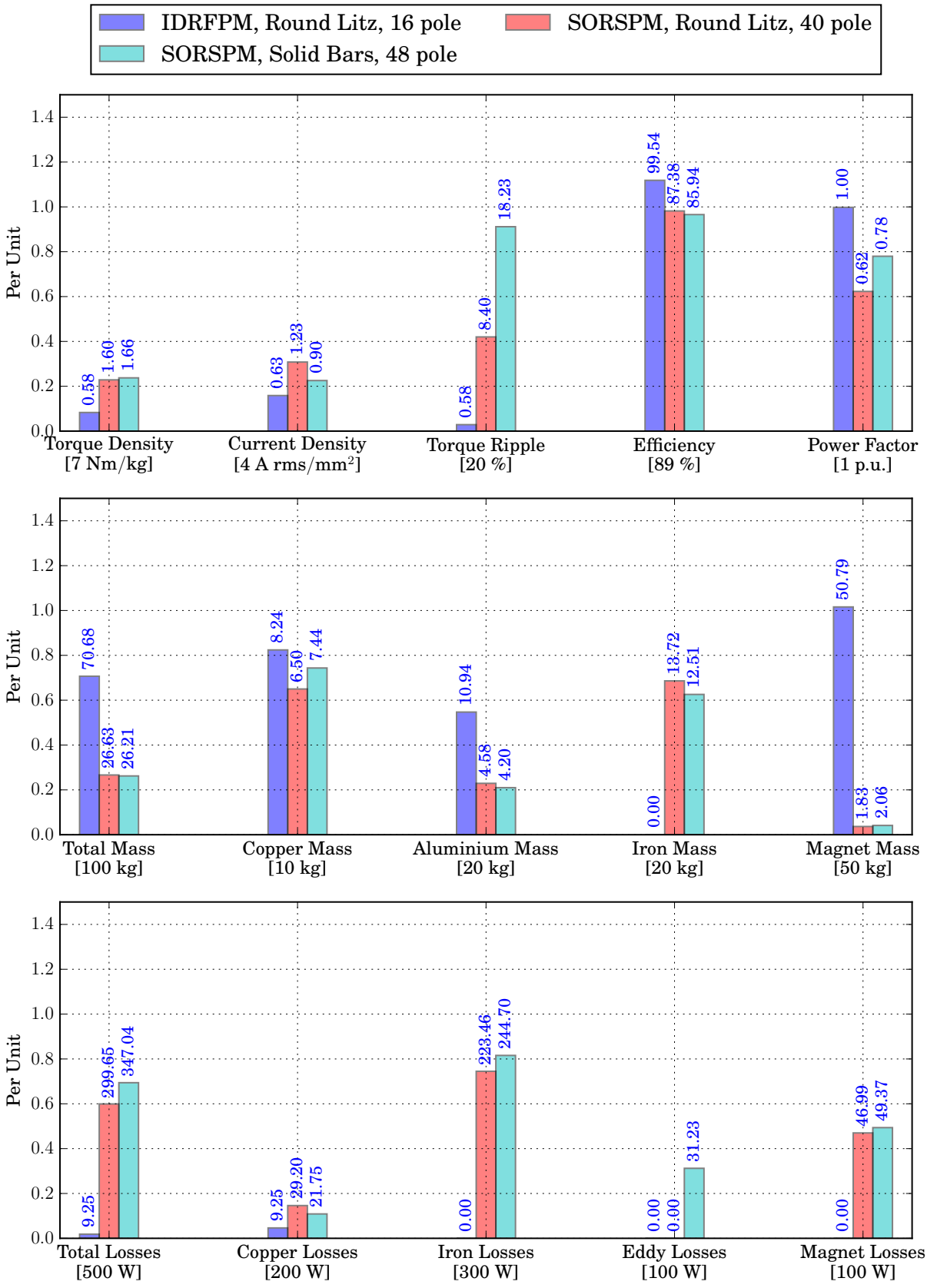

Figure 6.2: Performance comparison of the most appealing design of each machine configuration at 2 kW, 465 rpm.

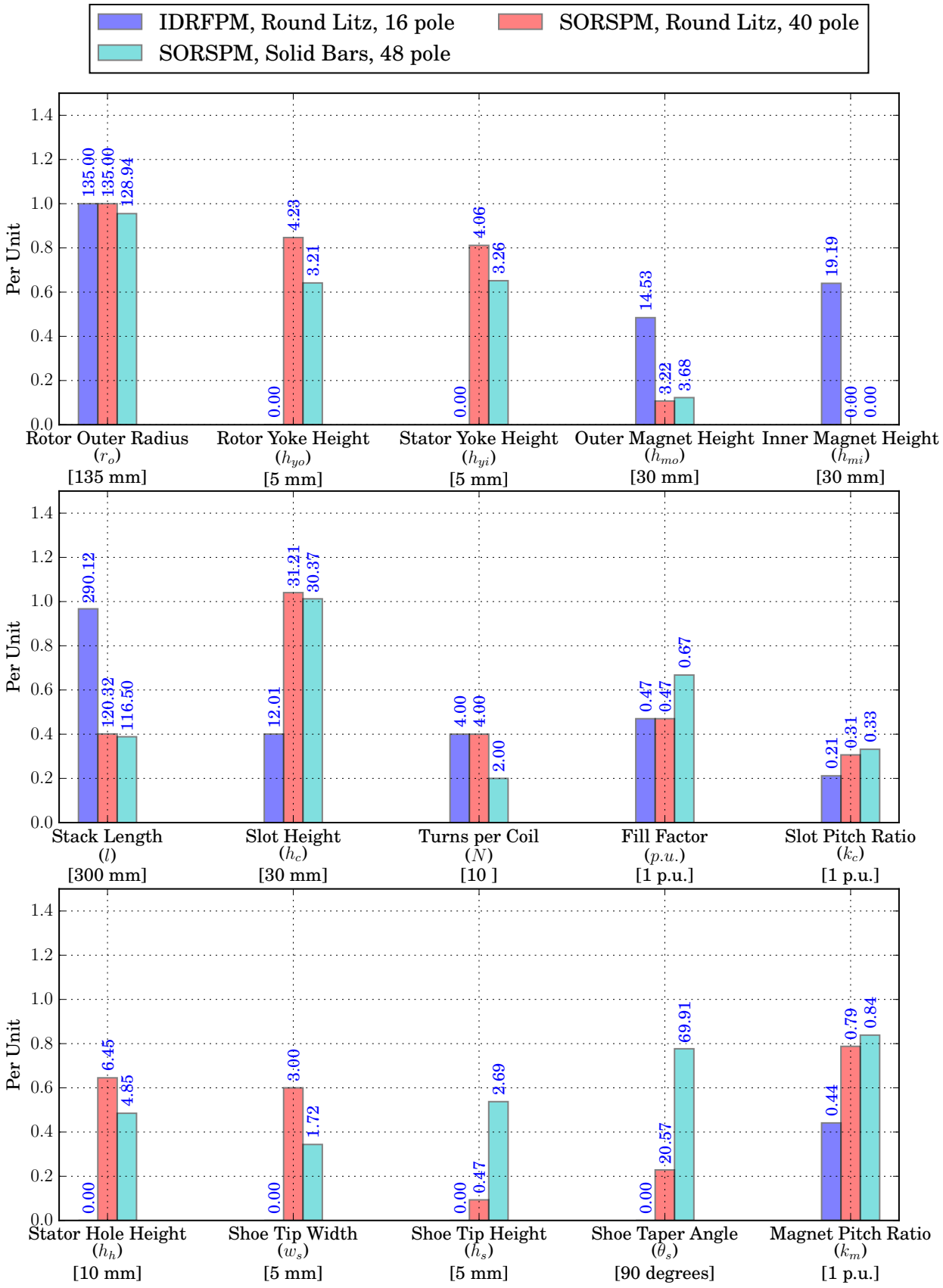

Figure 6.3: Input parameter comparison of the most appealing design of each machine configuration.

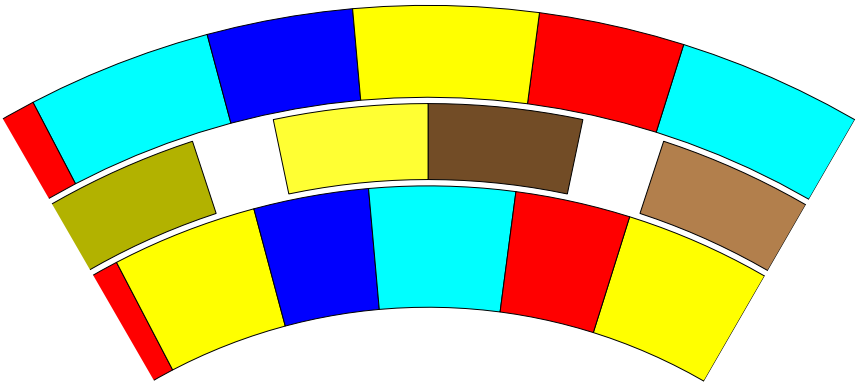

Figure 6.4: IDRFPM machine, utilising round Litz wire, 16 pole.

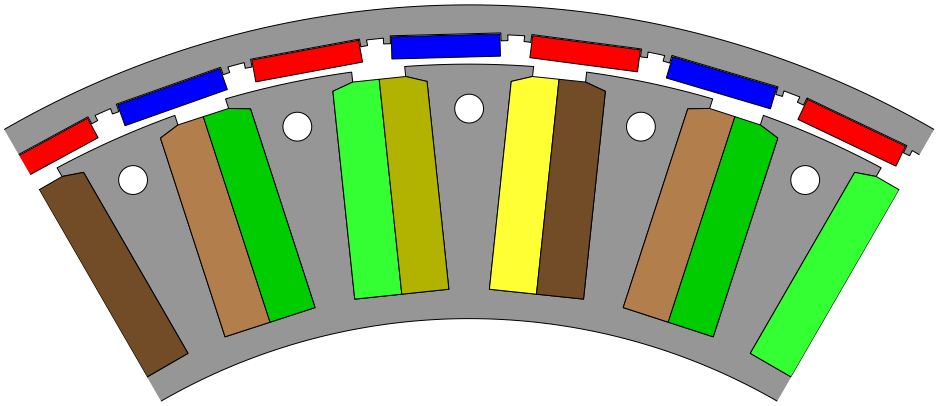

Figure 6.5: SORSPM machine, utilising round Litz wire, 40 pole.

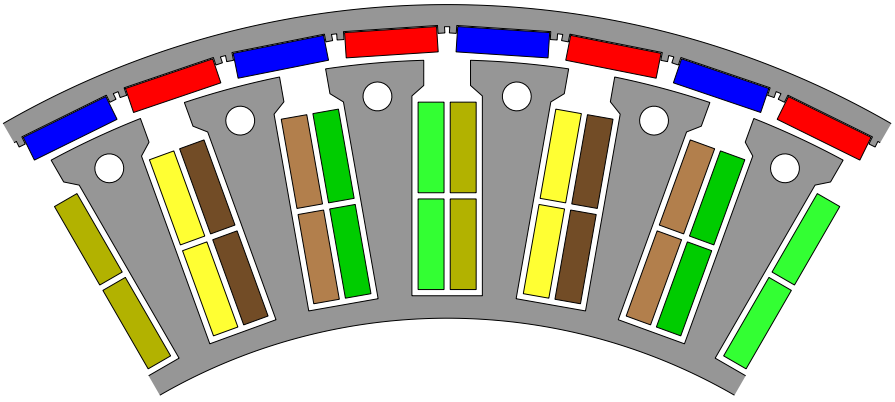

Figure 6.6: SORSPM machine, utilising solid copper bars, 48 pole.

6.3 Construction Investigation

6.3.1 Introduction

In Section 6.2, the designs were compared in terms of basic performance metrics and machine dimensions. However, a comprehensive comparison cannot be made without an investigation into the manufacturing feasibility of the SORSPM machine utilising copper bars. Working prototypes of the IDRFPM machine and the SORSPM machine utilising Litz wire already exist, so it is assumed that their manufacturability is reasonable.

In this section, a method to construct a prototype of the SORSPM machine utilising copper bars is investigated. The investigation serves as a first attempt, and is not necessarily the best or most efficient method to construct the machine. The purpose of this section is twofold: to determine if the optimised SORSPM designs utilising copper bars could be practically implemented, and two serve as a starting point for future projects which wish to continue an investigation into the mechanical aspects of the machine.

The 3D images that follow in this section were created using Autodesk Inventor® Professional 2016 (Student Version), and will be discussed according to a sequence of assembly steps. The figures were initially drawn for a 40 pole, 30 slot machine which was not optimised to consider the eddy losses within the copper bars. Nonetheless the proposed construction procedure remains the same. The detailed dimensions and performance metrics can be seen in Appendix B. As a reminder to the reader, the prototype presented here is not meant to be an in-hub (in-wheel) prototype, but rather a direct-drive motor. It is however envisioned that future projects with a focus on the mechanical aspects, will aim to build an in-hub machine for this light-vehicle application.

6.3.2 Stator

Figure 6.7 shows the copper bars connected to the copper end-turn pieces. The copper bars have different lengths, of which the reason will become clearer later in this discussion. The end-turn pieces, placed below the copper bars, are used to create two turns per coil. The pieces have pre-drilled holes so that screws (in this case M3 brass screws) can be used to attach the pieces onto the copper bars. A single lamination is also shown in order to better visualise the stator layout. Figure 6.8 shows the aluminium stator drum, which serves as the stator yoke and end-plate.

Consider Figure 6.9. In order to prevent eddy currents from flowing between stator laminations, transformer paper (or also commonly known as Nomex® paper) can be wrapped

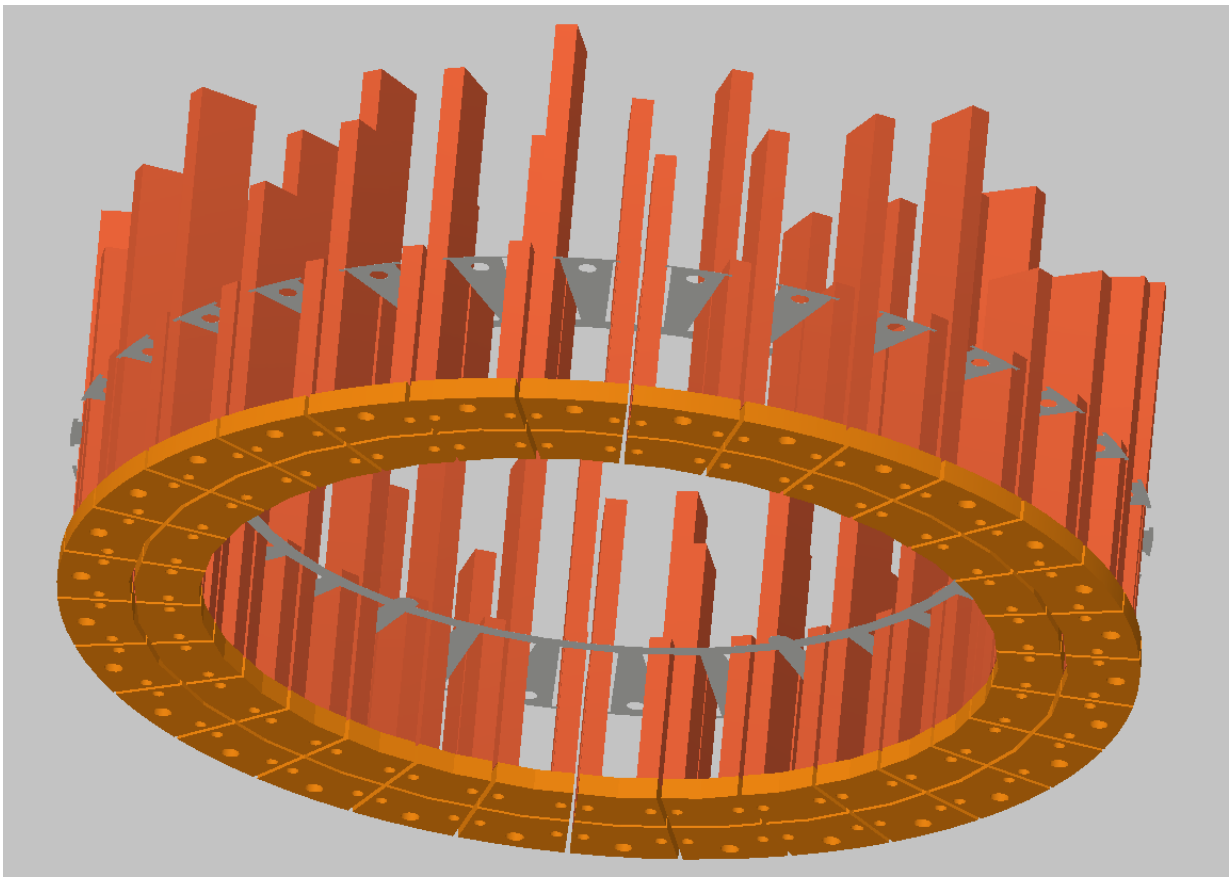

Figure 6.7: Copper bars, with end-turn pieces, and a single lamination shown of the machine specified in Appendix B.

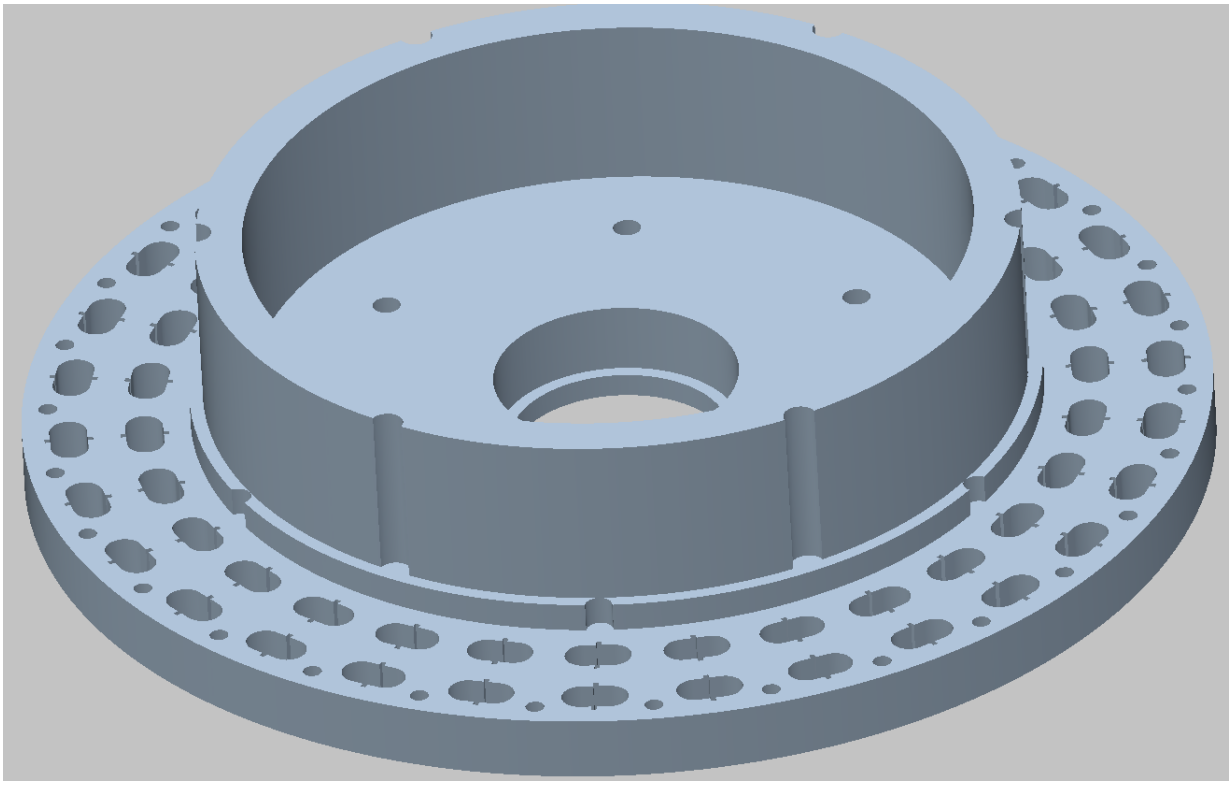

Figure 6.8: Aluminium stator drum of the machine described in Appendix B.

around the the stator yoke. The transformer paper is indicated as a coarse white coloured material. The green ring is made from a 0.8 mm thick FR4 sheet (also discussed in Section 4.2.4.2), and will insulate the end-turn pieces from the stator drum. The FR4 material can be purchased in sheets and then cut into shape using a Computer Numerical Control (CNC) machine. The M4 threaded nylon rods will help compress the stator lamination stack, and will also hold the copper bars and end-turn pieces in place. Nylon (specifically Nylon 66) rods are chosen, as it has a sufficiently high operating temperature and it pertains a similar magnetic permeability to air, thus not interfering with the electromagnetic features of the machine. Additionally, nylon does not conduct electrical current, which prevents potential eddy currents within the rods. At this stage, the nylon rods should be secured with nuts at the bottom of the stator drum. In Figure 6.10, the copper bars (with end-turn pieces pre-attached to the bars) are placed one by one on top of the stator drum, with the nylon rods protruding through the M4 holes in the center of the copper end-turn pieces. The copper bars are thus now held in place by the nylon rods. Then, another FR4 ring is dropped into place, guided by the nylon rods. This FR4 ring will rest on top of the end-turn pieces, and will insulate the lamination stack from these copper end-turn pieces.

In Figure 6.11, the laminations are all slid into place, guided by the nylon rods and the key openings on the stator drum. A final FR4 ring is added on top of the lamination stack, to once again provide insulation from the copper pieces which will be added on top. The copper bars in Figure 6.11 needs to be insulated from each other, and also insulated from the stator laminations. This insulation is provided by FR4 sheets which are inserted axially along the copper bars, as shown in Figure 6.12. The top view is shown in Figure 6.12b. As can be seen from the top view, seven individual FR4 pieces are required per slot. As an additional precaution or a complete alternative, the copper bars could also have been wrapped in transformer paper. At this stage the copper bars should fit tightly within the slots. The nylon rod ends protruding at the top of the stack can also now be tightened with nuts.

In Figure 6.13, the end-turn pieces which finally complete the two-turn coil is also mounted using M3 brass screws. It should be noted that all the end-turn pieces are designed in such a manner that the copper cross-section area remains constant throughout the current's path. Also, the bottom ball bearing is fitted into its locator. The locator can be seen in Figure 6.8. The shaft is then located into the bottom ball bearing. The top ball bearing is placed within the stator cap (ball bearing not explicitly shown). The ball bearings are identical and is sized 25 mm and 52 mm for the inner and outer diameter respectively. Finally, the stator cap is merged with the shaft and stator assembly, and is

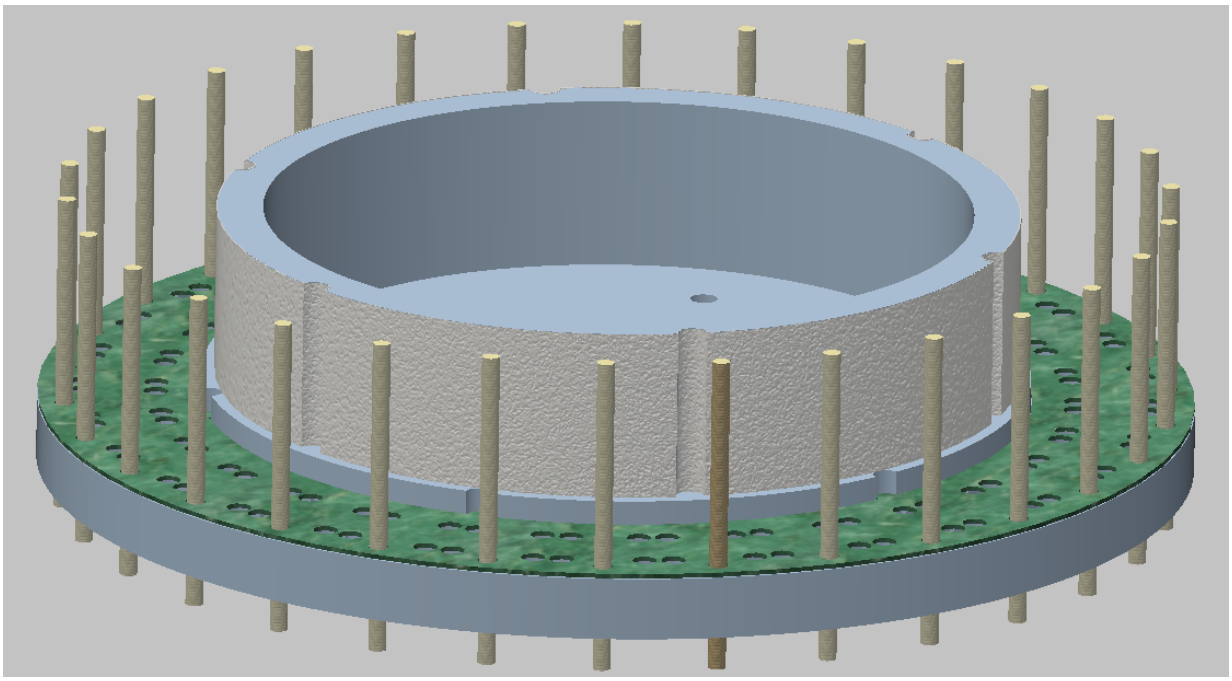

Figure 6.9: Aluminium stator drum, with FR4 ring, transformer paper and nylon rods. Machine dimensions as described in Appendix B.

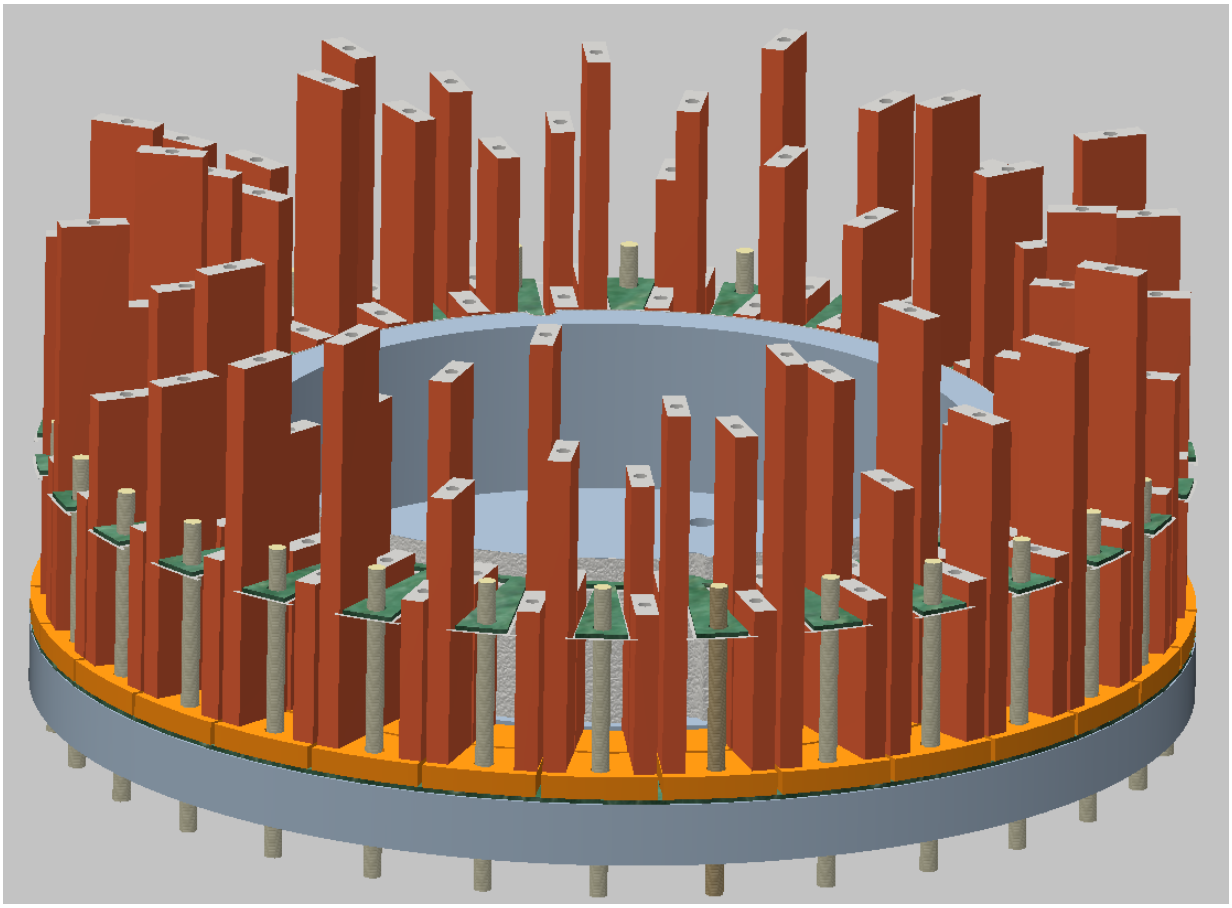

Figure 6.10: Same as Figure 6.9, but with copper bars placed into position. An additional FR4 ring is inserted, which will rest on top of the end-turn pieces. Machine dimensions as described in Appendix B.

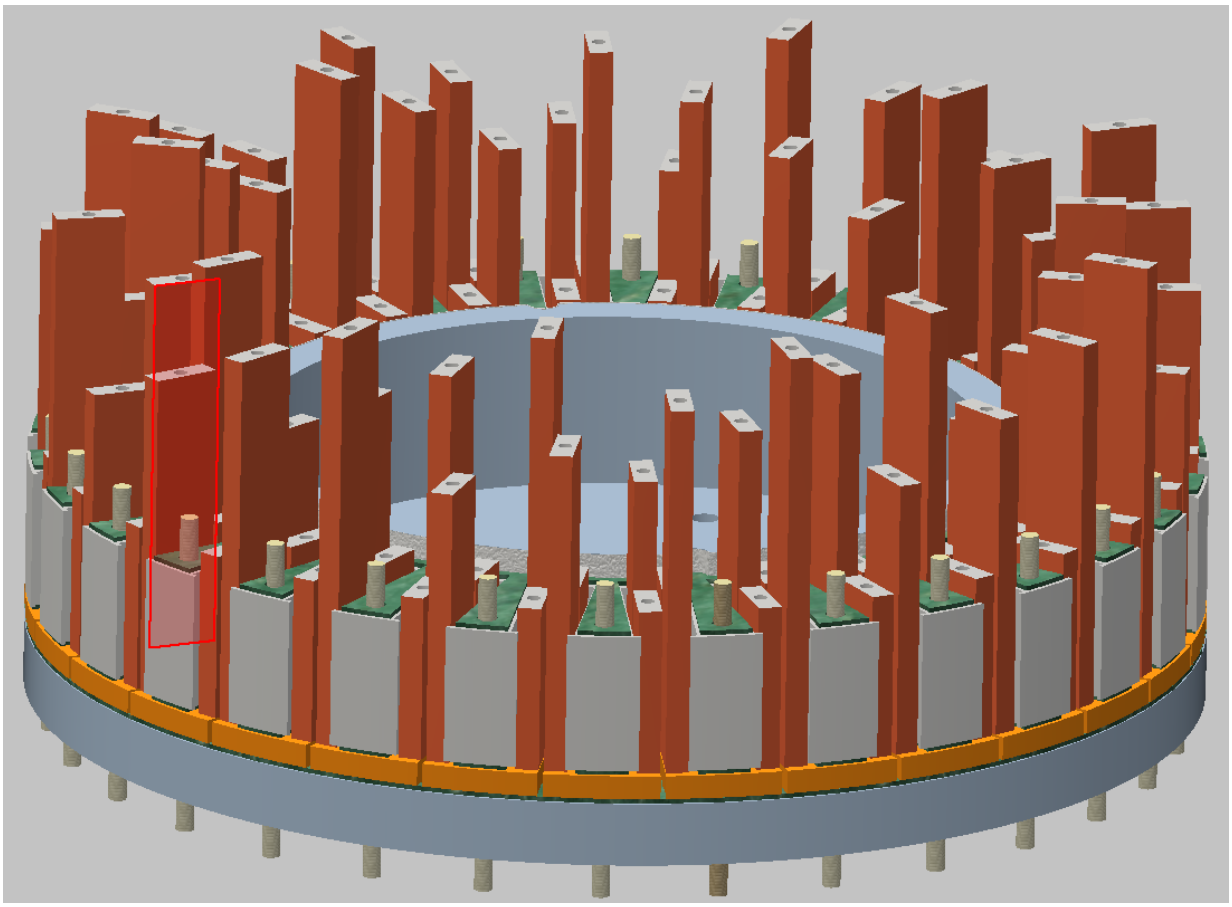

Figure 6.11: Aluminium stator drum, with the lamination stack in place, and a final FR4 ring on top. Machine dimensions as described in Appendix B.

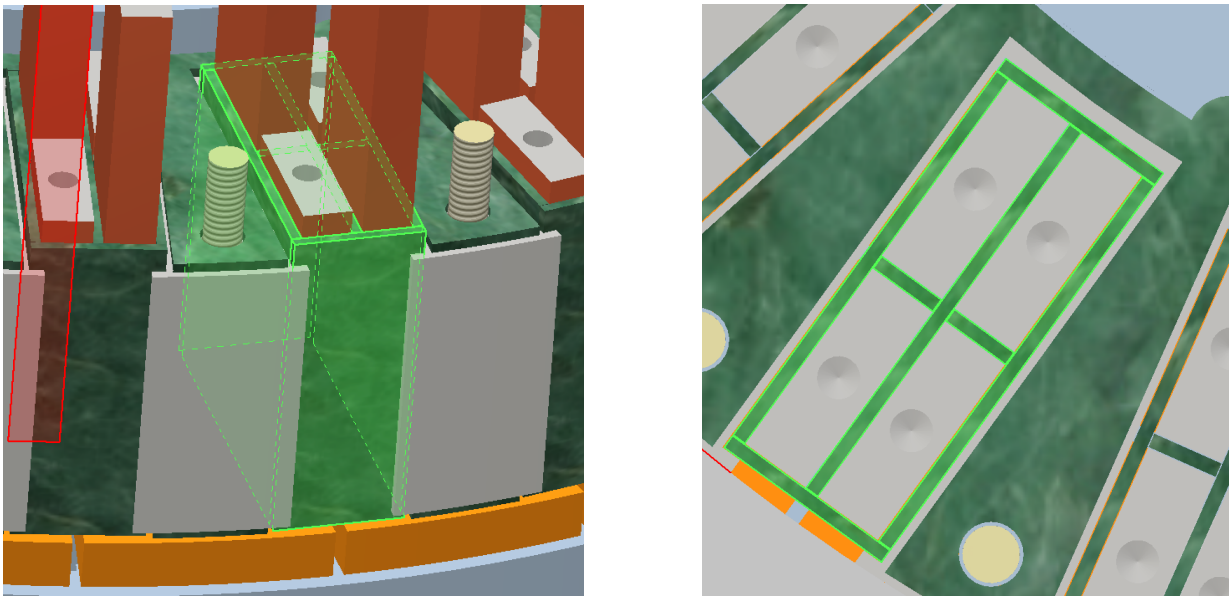

(a) (b)

Figure 6.12: FR4 sheets inserted along with copper bars. Machine dimensions as described in Appendix B.

married using six M6 steel threaded rods. The stator cap and stator drum now compress the laminations at the yoke region, while the laminations are also compressed at the stator shoes with the aid of the nylon rods. It is important to realise that the purpose of the M4 and M6 rods, is not only to compress the laminations, but also to hold the bottom end-turn pieces in a secure position against the stator drum. Since these end-turn pieces are also joined with the copper bars, the bars are also held in place as a result. If this were not the case, the bars would be free to move in the axial direction. Figure 6.14 shows the bottom side of the stator drum. These openings can also be seen in Figure 6.8. The purpose of the openings is to prevent the screw heads from making contact with the stator drum, as the M3 brass screws will also be conducting some current. Furthermore, the screw heads of neighbouring coils are very close to one another, thus the openings could perhaps be filled with epoxy resin in order to insulate the heads from each other, and also from the stator drum itself. In fact, it will probably be best to pour epoxy resin over the entire stator structure with the help of a mould. This would help to keep all the components firmly in place and also increase the insulation between neighbouring conductors.

In Figure 6.15, the series connections between each coil is added. Phase a coils are represented by yellow, phase b by green and phase c by red. As can be seen from the figure, the coil connections are transposed. This is the reason for the different copper bar lengths. To achieve this transposition, the connections interchange in four different heights. Due to the number of symmetric sections of the machine, the transposition is not perfect but it is probably better than not transposing at all. The three-phase terminals are coloured in blue. In these figures the terminals are connected for a delta (Δ) connection, but it was later on decided to implement a wye (Y) connection for this machine topology as discussed in Section 4.2.4.5.

It is thought, that the copper end-turn pieces and the copper series connectors of Figure 6.15 could be cut into shape also using a CNC machine. Alternatively, the series connectors could also be cut as regular straight bars, and then bent using a bending machine. Another option is to make use of flexible braided copper cables as shown in Figure 6.16. Of course, it would be necessary to insulate these cables.

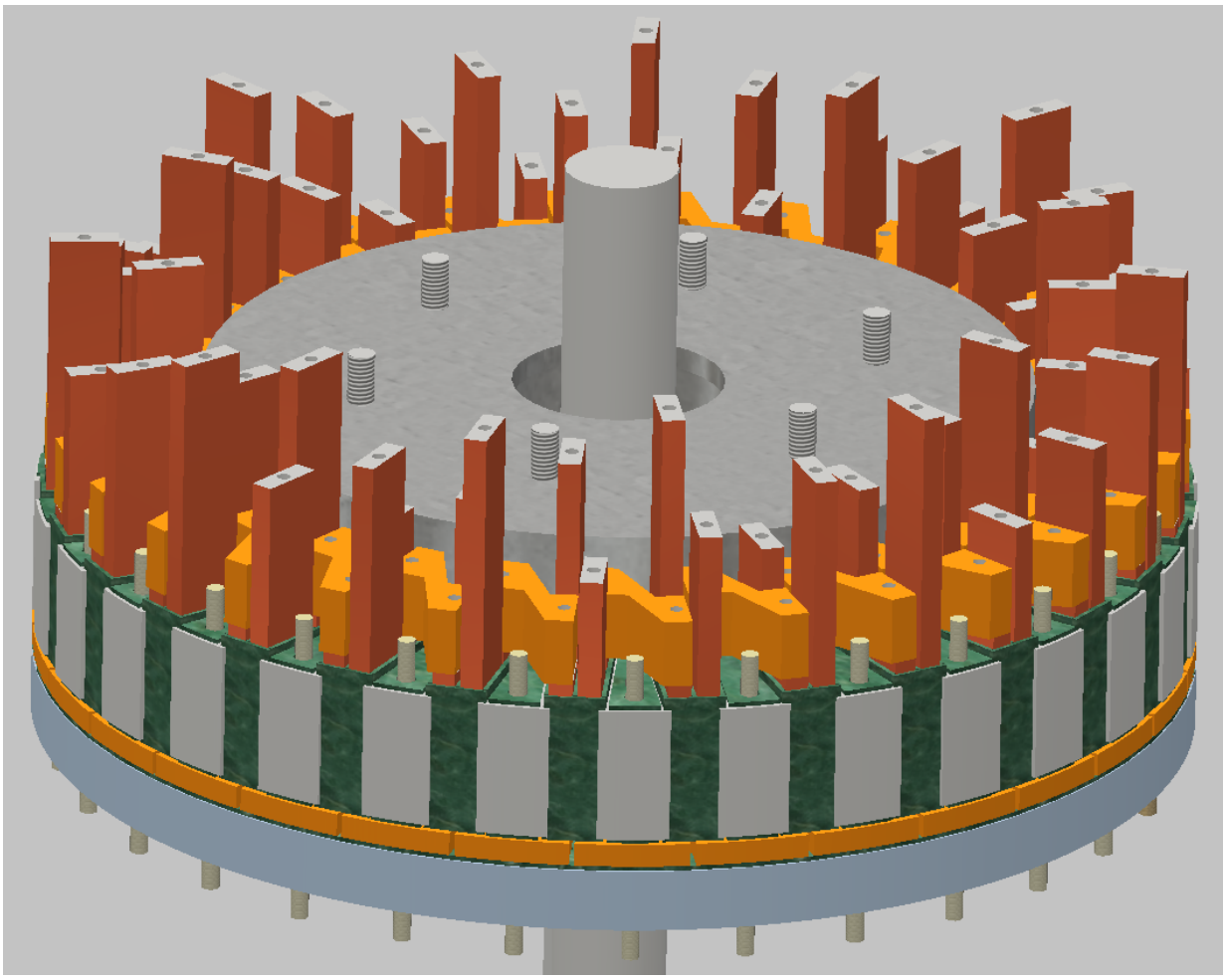

Figure 6.13: Majority of stator now assembled, with end-turn pieces, stator cap, shaft and ball bearings in place. Machine dimensions as described in Appendix B.

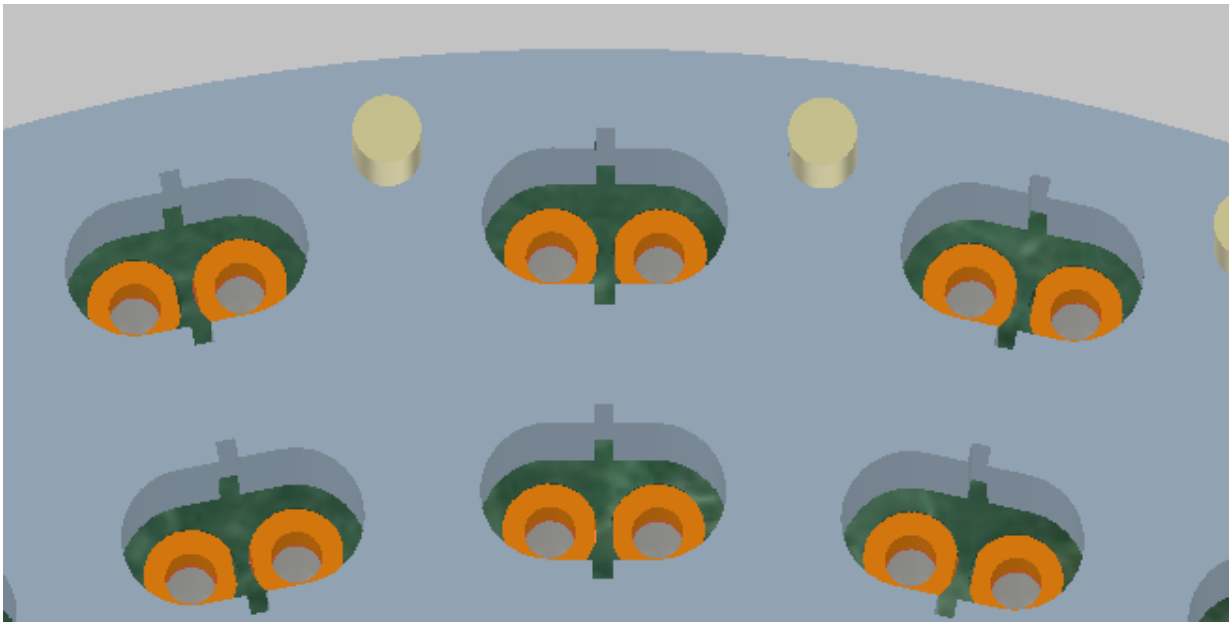

Figure 6.14: Stator openings in stator drum, in order to insulate the screw heads from the stator drum and neighbouring screw heads. Machine dimensions as described in Appendix B.

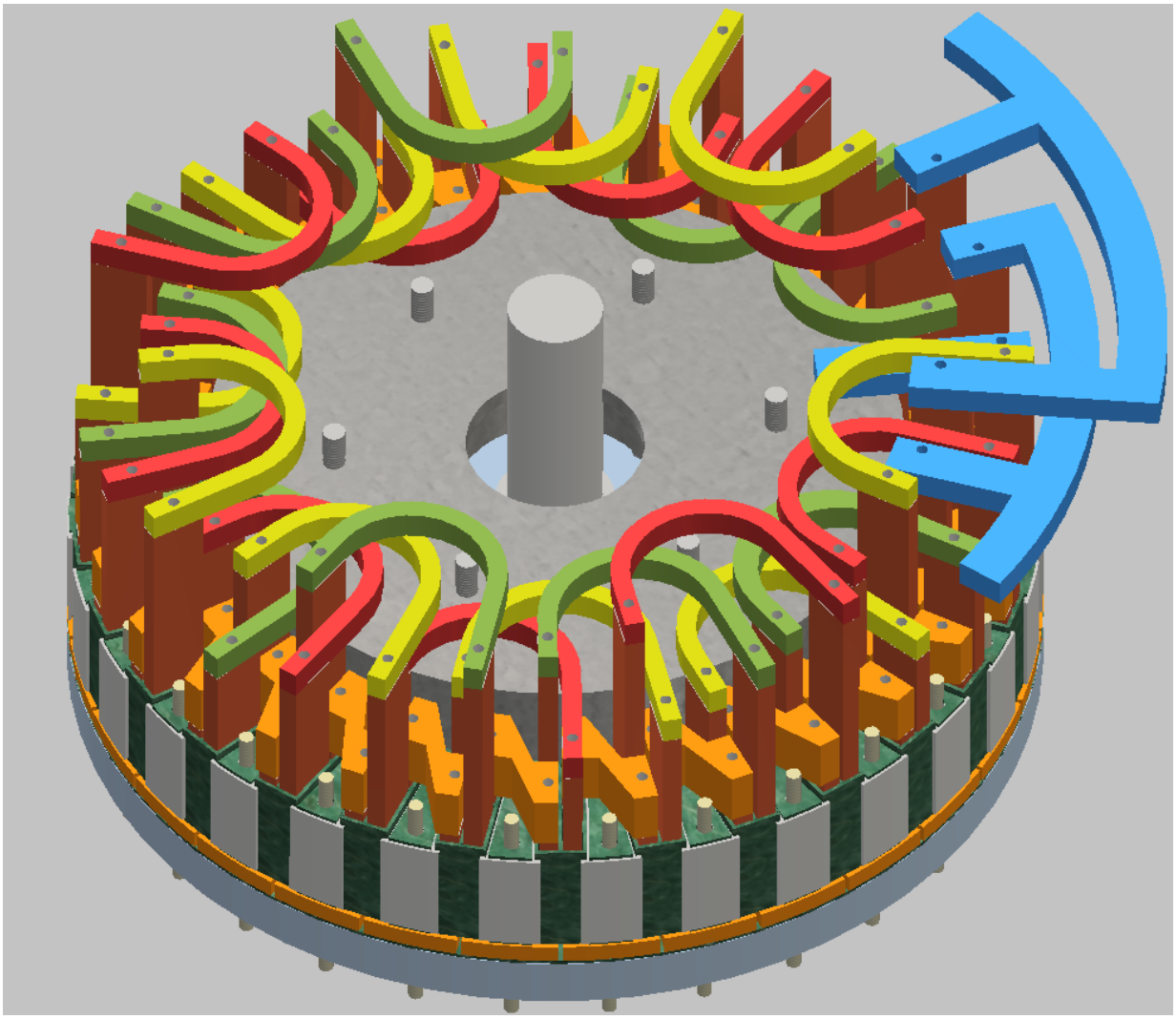

Figure 6.15: Complete stator assembly, with series connections between coils and three-phase terminals included. Machine dimensions as described in Appendix B.

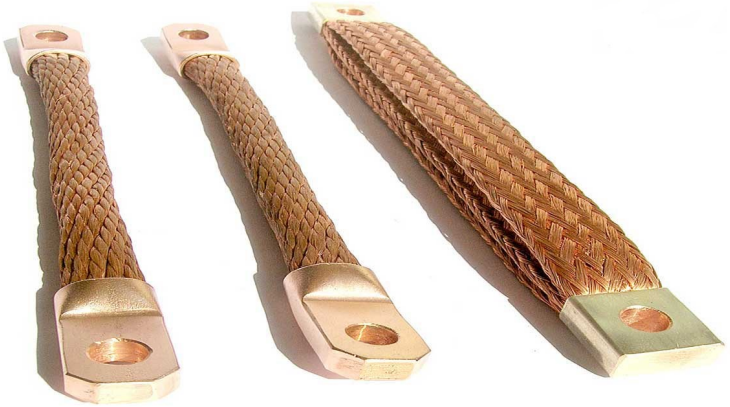

Figure 6.16: The external connections could perhaps be realised using flexible braided copper cables, commonly used as earthing conductors in buildings.

6.3.3 Rotor

In Figure 6.17, a cross-section view of the aluminium rotor drum is shown. The rotor drum is insulated from the rotor laminations, with the aid of transformer paper and a FR4 ring as shown in Figure 6.18. In Figure 6.19, the laminations and an additional FR4 ring is added. The magnets are glued into place. Finally, a rotor cap is placed on top to compress the rotor laminations. The rotor cap is married with the rotor drum using 16 M5 screws.

6.3.4 Complete Assembly

The rotor drum can now be merged with the stator assembly, as shown in Figure 6.20. A cross-section view of the complete assembly is given by Figure 6.21. Notice that the ball bearings are not explicitly shown. A closer look at the stator and rotor is given by the top view in Figure 6.22.

6.3.5 Conclusion

It is the author's opinion that the complexity of this machine topology is much more challenging than initially anticipated. Securing the copper pieces together will likely be a very time consuming and error-prone step. Perhaps alternatively, the copper connections could instead be brazed together, although this could also be just as time consuming. Furthermore, the parts required for the end-turns and for the series connections could be very expensive to order if they need to be cut with a CNC machine. Another concern is that, due to the high number of copper parts, it could be difficult to ensure that all the copper parts are properly insulated.

In this investigation it was assumed that transposition of the phase conductors is necessary. The various copper bar lengths required at specific slots will certainly be difficult to install without making any misplacements. However, it would be interesting to see if neglecting the transposition would be noticeably detrimental to the machine's performance. If the transposition is abandoned, the series connections could be simplified substantially.

All these uncertainties are probably best answered when such a prototype is actually built. Nevertheless, after consulting with the SED workshop, the author concludes that this topology is likely too cumbersome, time-consuming and expensive to build.

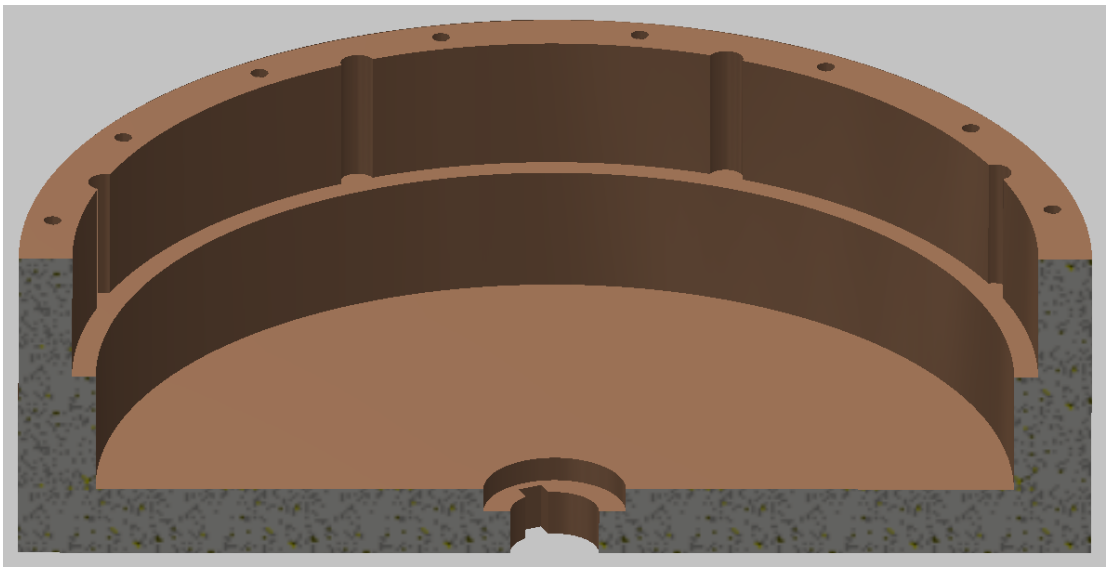

Figure 6.17: Aluminium rotor drum. Machine dimensions as described in Appendix B.

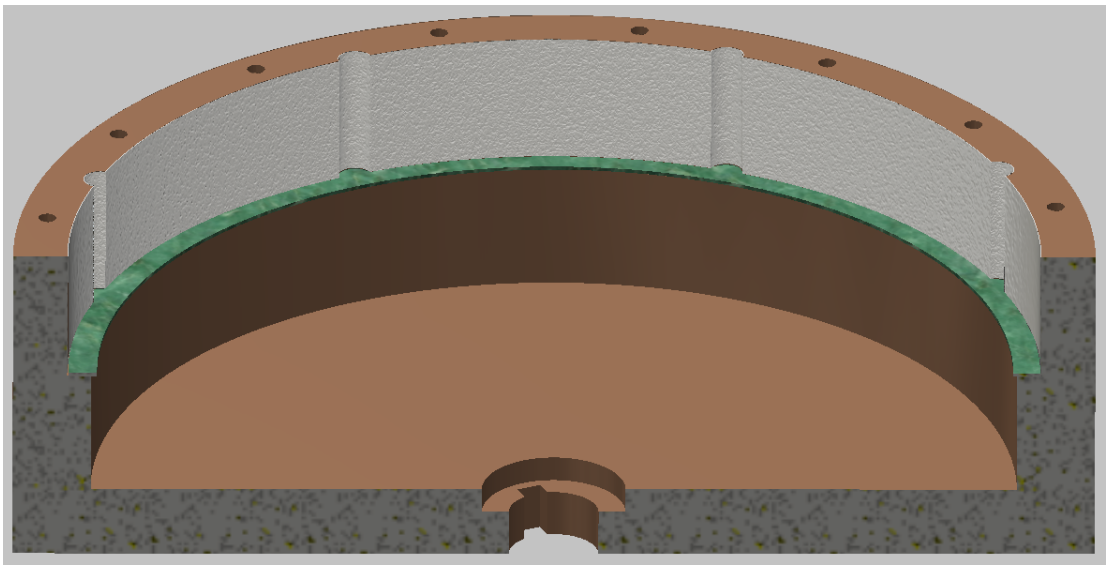

Figure 6.18: Rotor drum with insulating transformer paper and FR4 ring. Machine dimensions as described in Appendix B.

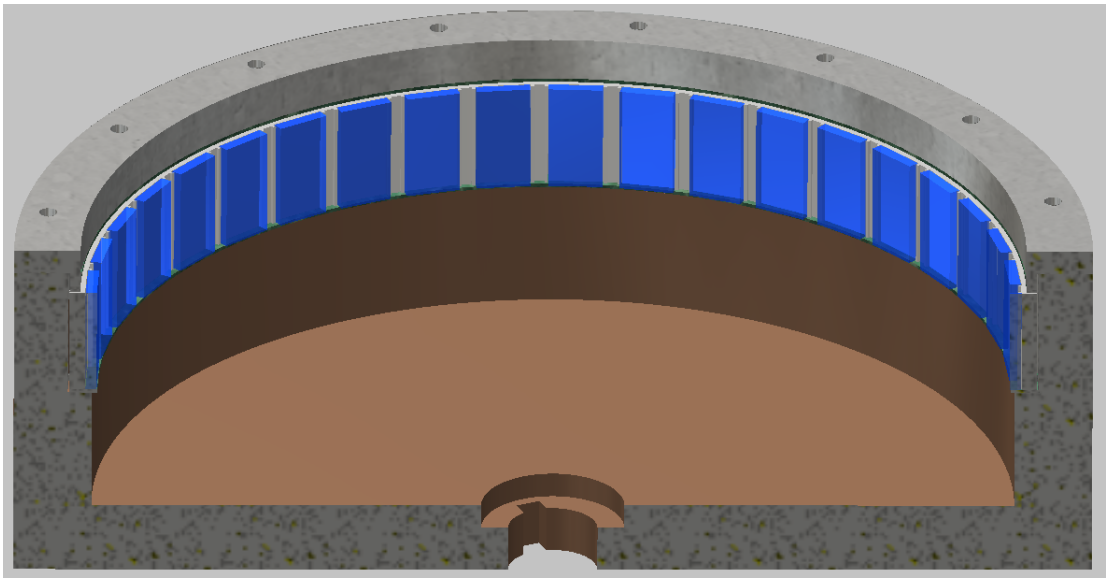

Figure 6.19: Complete rotor assembly of the machine in Appendix B.

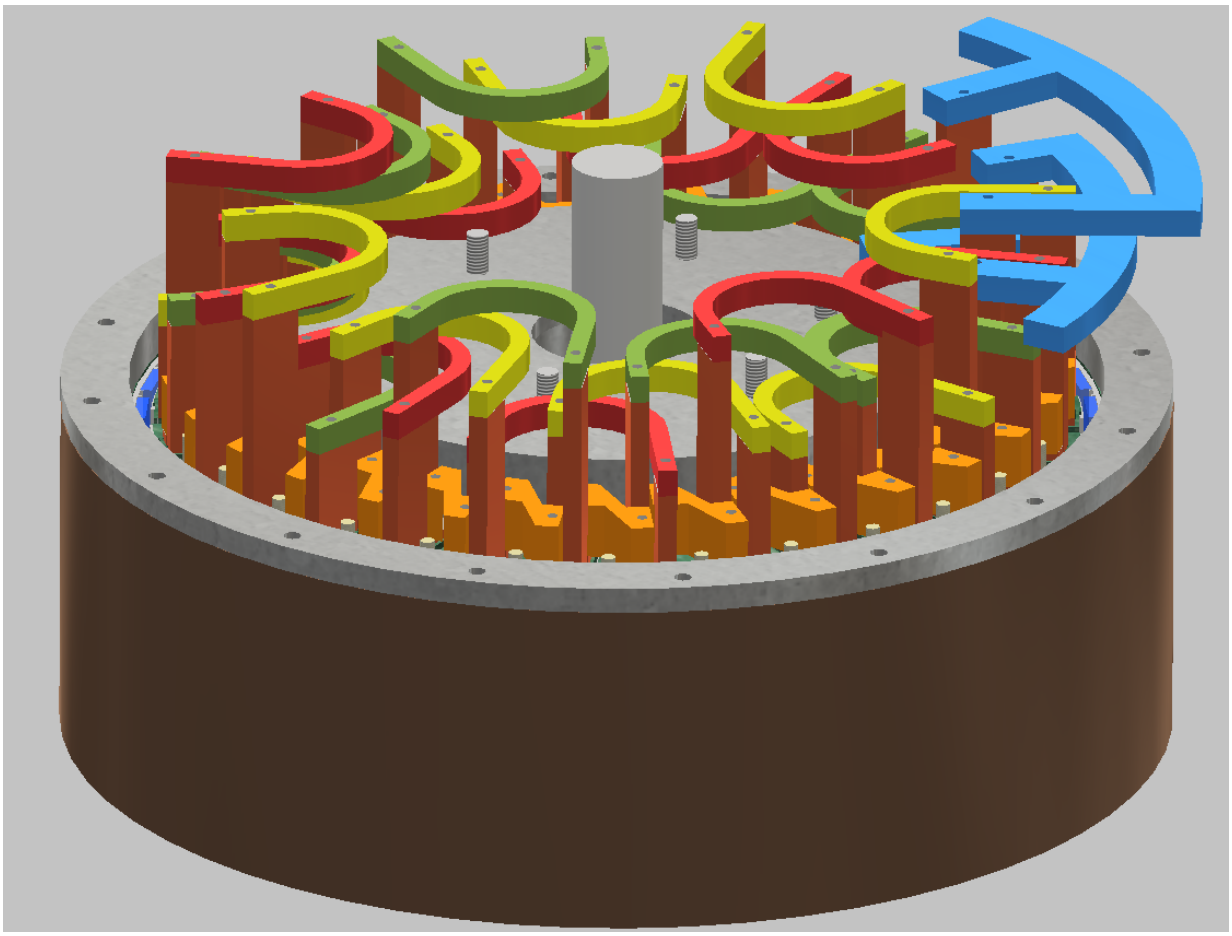

Figure 6.20: Complete machine assembly of the machine in Appendix B.

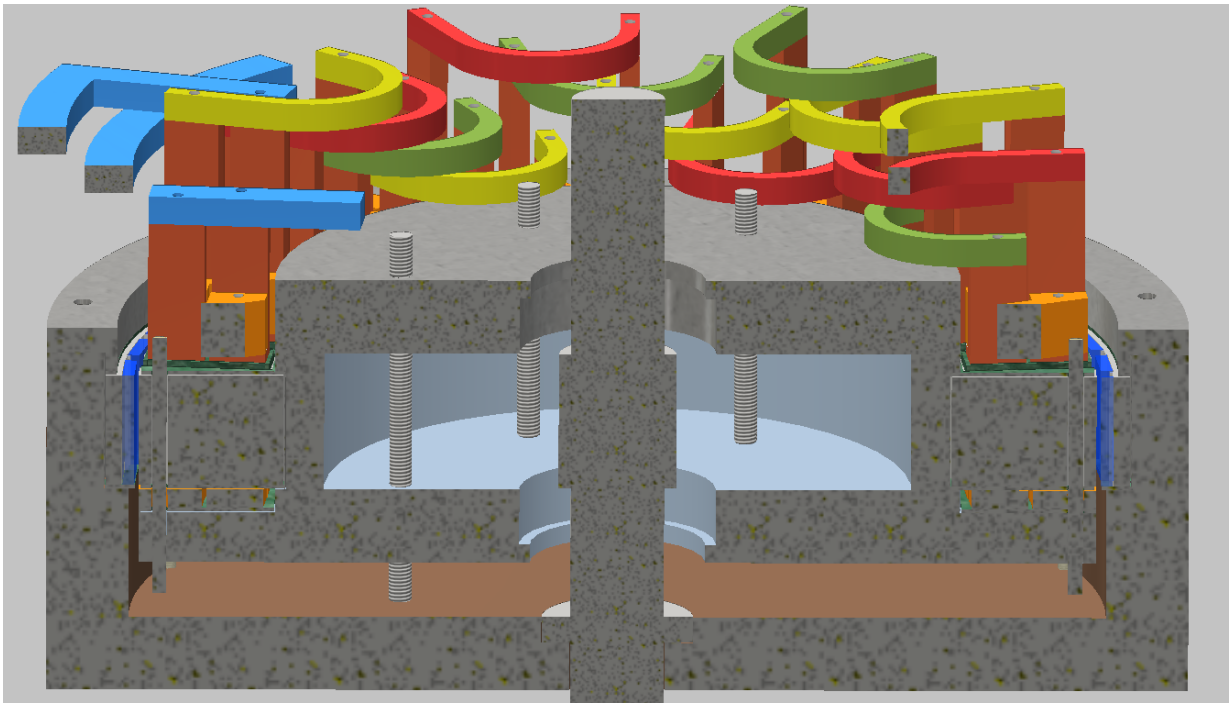

Figure 6.21: Cross-section view of the complete machine assembly. Machine dimensions as described in Appendix B.

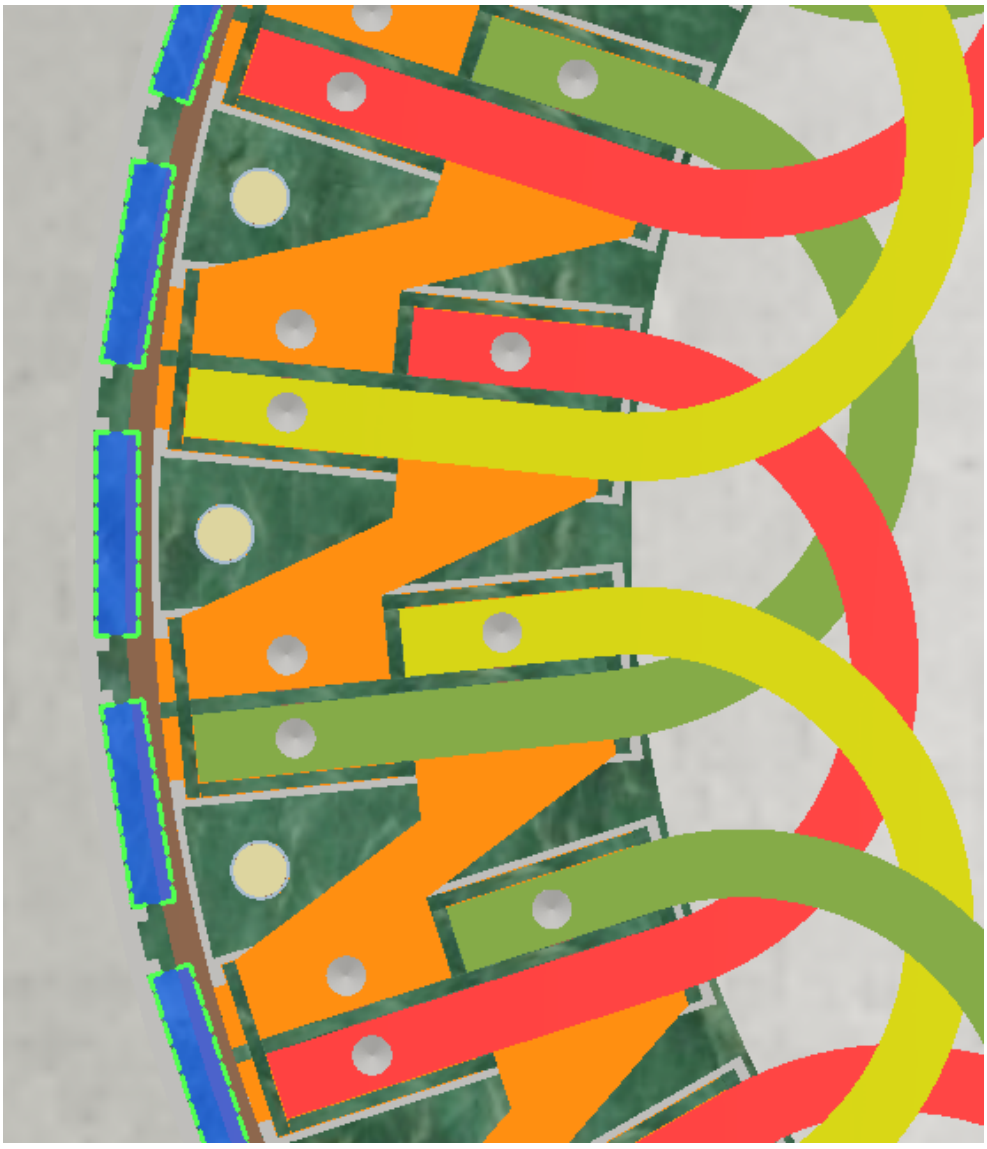

Figure 6.22: Top view of the stator and rotor. Machine dimensions as described in Appendix B.

6.4 Design Recommendation

In this section, the design comparison in Section 6.2 and the construction investigation in Section 6.3, are considered in order to make a final design recommendation.

The IDRFPM machine certainly exhibits some performance traits which are very desirable at both base and top speed operating points. These traits are, the outstanding efficiency, power factor and torque ripple. However, the major drawbacks are the massive magnet mass, much longer stack length, and consequently a much lower torque density. Needless to say, the IDRFPM machine's magnet mass would be very cost-inefficient. Unfortunately these drawbacks, especially the machine's large mass value, render the IDRFPM

machine infeasible for a direct-drive light vehicle application. As discussed in Section 6.2, the IDRFPM machine's large mass could cause a runaway situation in which the increasing vehicle mass would require an even larger IDRFPM machine. Therefore a more suitable design recommendation has to be made, with the remaining two SORSPM configurations in mind.

During the earlier stages of this project, it was initially expected that the SORSPM machine utilising solid copper bars would deliver the most promising all-round results. Although, at the time, the magnitude of the eddy current losses within the copper bars was not expected to be as severe. After more thorough research on the issue was done, as presented in Section 4.5.3, it became evident that the eddy current losses within the copper bars will play a major role in the machine's performance. In Section 6.2 it is discussed that in order to avoid these eddy losses, the copper bars were optimised so that their cross-section area became smaller, and that they are located further away from the airgap. This caused the torque ripple to increase, and also a decrease in the torque density (compared to if the eddy losses within the copper bars were ignored). Therefore, the performance gains that were initially pursued with this topology, could not be achieved. Instead, the SORSPM machine utilising solid copper bars promises only a marginal performance improvement in some aspects, but at the expense of a very difficult and expensive construction process.

Table 6.1 serves as a summary of all the key points for the comparison between the SORSPM machine utilising Litz wire and the SORSPM machine utilising solid copper bars.

SORSPM Litz Wire	SORSPM Solid Bars
• better all-round η	• slightly better $\tau_{density}$
• much better τ_{ripple} at top speed	• smaller outer radius and stack length
• better power factor at base speed	• better power factor at top speed
• easier construction	• Y-connection prevents triplen harmonics

Table 6.1: A summary of all the most important advantages of each configuration.

Finally in conclusion, of the topologies considered in this project, it is believed that the 40 pole SORSPM machine utilising round Litz wire is the best suited candidate for the direct-drive application of the Mellowcabs L2 class electrical vehicle.

Chapter 7

Conclusions and Recommendations

This project is a comparative study between two outrunner machine topologies - the IDRFPM machine and the SORSPM machine. The SORSPM machine was investigated for two conductor types, namely round Litz wire and solid rectangular copper bars. The application is for the direct-drive of the Mellowcabs L2 class electric vehicle. In this chapter, the key findings of the project is summarised and recommendations are made for future studies.

7.1 Conclusions

- The combined requirements of the Mellowcabs vehicle and the L2 class specification, makes designing a suitable direct-drive hub rather challenging. The mass of the vehicle, together with a 15° slope, requires a significant torque figure. Accordingly, this project proposes the use of two direct-drive motors, each coupled to a rear wheel. The subsequent torque requirement is 191 N·m per motor. The Mellowcabs vehicle imposes a 48 V system-wide restriction, and the BMS is able provide a continuous power output of 5 kW. At the same time, the L2 classification imposes a 4 kW traction power limit to the vehicle, thus 2 kW for each direct-drive motor. If a VSD with an efficiency of 90 % is assumed, the base speed efficiency of the motors needs to be 89 % in order to make full use of the BMS supply. With this in mind, the copper losses (excluding eddy losses) in this project were budgeted at 200 W. Therefore, the

machines in this project were constrained by a copper loss figure of 200 W, instead of a fixed current density.

- For the IDRFPM machine, a 2D subdomain analytical analysis was done in order to be used with an optimisation procedure. The results of the subdomain analysis proved to be in good agreement with that of 2D FEM packages and an existing machine prototype. An analytical analysis roughly took 0.6 seconds to compute, whereas the same machine took 16 minutes and 20 seconds to compute in a 2D SEMFEM simulation with a comparable accuracy.

- The SORSPM machine was analysed using the 2D SEMFEM package. However, the the copper losses (including eddy losses) and magnet losses were calculated analytically by extracting data of the magnetic fields from the simulation.

- Contrary to literature, it was shown that the copper losses are not constant when a constant current density and copper area is used, and it is noticeable especially when the number of turns per coil is small. This is due to the external wiring needed to connect the coils in series. The calculation of the phase resistance in this project thus took into account the number of turns used.

- The IDRFPM and SORSPM machines were both optimised, for a range of pole numbers, with priority given to torque density. In the case of the SORSPM machine, it was also necessary to prioritise efficiency and torque ripple. For the multi-objective optimisation, the weighted sum method was employed, and for the single-objective optimisation an open-source package called NLopt was used.

- The IDRFPM machine generally exhibited superior efficiency, power factor and torque ripple. Unfortunately, the magnet mass was about 25 times more and the stack length was almost 2.5 times more than that of the SORSPM contenders. Consequently, the IDRFPM machine was much larger in size and mass and thus suffered from low torque density. The IDRFPM machine's large mass could result in a runaway situation in which the vehicle weight would increase drastically, which in turn, would require an even larger IDRFPM machine to deliver sufficient hill-climbing torque. For these reasons, the IDRFPM machine was considered impractical for the application of this project. Nevertheless, it could be concluded that the IDRFPM machine would be suitable for applications where efficiency, power factor and torque ripple are prioritised, and where the size and weight of the machine are not as important.

- With the IDRFPM machine eliminated, the two SORSPM candidates were compared against each other. Before a performance comparison could ensue, it was decided to investigate how the SORSPM machine utilising copper bars could be constructed. The investigation serves as a first attempt, and is not necessarily the best approach in constructing a prototype. The investigation concludes that the machine would be too complex to build compared to a machine using Litz wire.

- The SORSPM machine utilising copper bars was initially expected to outperform the same machine using Litz wire, due to the increased fill factor of the copper bars. However, after research was done on the topic of eddy losses, it was identified that the eddy losses in the copper bars could be much more than anticipated. Nonetheless, the efficiency objective within the optimisation procedure was able to protect the copper bars from experiencing too much eddy losses. This was done by burying the bars deeper in the stator region, so as to avoid the alternating flux caused by the rotor poles. The subsequent side-effect is that the torque ripple is deteriorated. But as the torque ripple is also an optimisation objective, a compromise is achieved. Unfortunately, despite the compromise, for any given pole number, the efficiency and torque ripple was found to be less promising than that of the SORSPM machine utilising Litz wire.

- Generally, it was found that the SORSPM machine utilising copper bars only delivered marginal improvements in some aspects such as torque density and machine size, but performed slightly worse in terms of efficiency and far worse in terms of torque ripple. Considering the construction complexity of the SORSPM machine utilising copper bars, and the unconvincing performance metrics, it is concluded that the SORSPM machine utilising Litz wire is overall a better candidate for this application.

- The candidate for the SORSPM machine utilising copper bars is a 48 pole machine, promising an efficiency of 89.09 % and a torque ripple of 1.14 % at the base speed, rated torque operating point. The torque density and power factor at this operating point is 7.29 N·m/kg and 0.85 respectively. At the top speed, rated power operating point, the machine promises an efficiency and torque ripple of 85.94 % and 18.23 % respectively. At this operating point, the power factor of 0.78 is relatively low due to the flux weakening being implemented.

- The proposed machine for this applicaton, is a 40 pole SORSPM machine utilising Litz wire, promising an efficiency of 89.64 % and a torque ripple of 1.32 % at the base

speed, rated torque operating point. The torque density and power factor at this operating point is 7.17 N·m/kg and 0.88 respectively. At the top speed, rated power operating point, the machine promises an efficiency and torque ripple of 87.38 % and 8.40 % respectively. At this operating point, the power factor of 0.62 is relatively low due to the flux weakening being implemented.

7.2 Recommendations

- The IDRFPM utilising Litz wire is ideal for applications requiring a very high efficiency, power factor and low torque ripple. In this project, the torque density proved to be a huge disadvantage. This is mostly due to the large effective airgap between the two rotors, resulting in a weak airgap flux density. The airgap flux density could be increased by introducing soft magnetic composites (SMCs) within the coil blocks. However, the SMCs could increase the torque ripple substantially, and decrease the efficiency and power factor. A full investigation, which includes the optimisation of the performance trade-offs, could be done in the future.

- The design optimisation in this project was done for a single base speed operating point, and then a top speed operating point was observed as a result. A more comprehensive design optimisation could be implemented for a well-known driving cycle, such as the New European Driving Cycle (NEDC). This could result in a machine which is better suited for a whole range of operating points, rather than just one or two operating points. Subsequently, a comparison of various machines types optimised for a driving cycle should ensue.

- Although only synchronous PM machines were considered for the direct-drive application of this project, a future study could include other machine types, such as the reluctance synchronous machine (RSM). These machines could be beneficial when a low voltage system is required, as the absence of permanent magnets could result in lower back-EMF for a given stator construction. Furthermore, the RSM machine has other traits which could be ideal for this application, such as the simple, robust and low-cost construction. Therefore a cost analysis of all the most promising topologies could be done for the direct-drive application.

- In this project, the performance for only two conductor types for the SORSPM machine was investigated and optimised. In Section 4.2.4, two other conductor options were also listed. From a performance perspective, the enamelled rectangular cop-

per wire ("hair pins") could be quite promising as it is claimed that the fill factor could be as high as 0.85, which is even higher than the highest achieved fill factor for the solid copper bars in this project - 0.74. Furthermore these conductors can be inserted axially which allows the slot openings to be a minimum, if need be. A performance and optimisation investigation should however again consider the eddy currents which could exist in these conductors. Additionally, it is believed that the construction with this conductor type would be less complex than that of the solid copper bars.

- The scope of this project did not include the mechanical design and heat dissipation aspects of the machines. An in-depth investigation into the suitability of various machine types for an in-wheel (in-hub) versus a direct-drive powertrain could be very useful for other projects to follow. This could also include comparing the practical feasibility of inrunner versus outrunner machines.

- Mellowcabs should consider to abandon their 48 V system-wide restriction. A higher voltage BMS and VSD will allow for machines with a higher number of turns per coil, and thus greater design flexibility. This will reduce the conductor thickness and the associated eddy current losses within the conductors. Furthermore, a reduction in the diameter of all the external wiring could be realised. Also, Mellowcabs should revisit their decision to standardise their vehicle within the L2 specification. Other alternatives, such as the L5 specification, would remove the 4 kW traction power limit.

- Although a 15° inclination angle was chosen for the powertrain design specification, it is the author's opinion that Mellowcabs should cater for a greater inclination angle. If not, the vehicle would be limited to low sloped areas.

Appendices

Appendix A

Subdomain Analysis

A.1 Magnetisation

A medium becomes magnetised in the presence of a magnetic field. On a microscopic level, tiny dipoles create a net alignment on a macroscopic level [81]. The magnetisation vector $\vec{\mathbf{M}}$ is also known as the magnetic dipole moment per unit volume or the magnetic polarisation. Due to this magnetisation, bound volume currents $\vec{\mathbf{J}}_b = \nabla \times \vec{\mathbf{M}}$ and bound surface currents $\vec{\mathbf{K}}_b = \vec{\mathbf{M}} \times \hat{\mathbf{n}}$ exist in the material. These currents are the result of many microscopic currents summing together produced by the net magnetic field in the magnetised material [81].

Another symbolic current, the free current $\vec{\mathbf{J}}_f$, is introduced to represent the current that we usually have control over, whereas the bound currents represent the current which we do not. The free current could be the current flowing through embedded wires within the magnetised material, or through the material itself if the material is conductive [81]. The total current is subsequently,

$$\vec{\mathbf{J}} = \vec{\mathbf{J}}_b + \vec{\mathbf{J}}_f \ . \tag{A.1}$$

According to [81], it is important to note that (A.1) does not introduce any new fundamental laws; it is merely a helpful representation since the free current is the current which we introduce by means of a voltage source such as a battery, and the bound current results from the magnetisation caused by many aligned atomic dipoles. The bound current cannot be turned on or off independently as is the case with the free current.

Ampère's law can now be rewritten using (A.1) which gives

$$\frac{1}{\mu_0}(\nabla \times \vec{\mathbf{B}}) = \vec{\mathbf{J}} = \vec{\mathbf{J}}_b + \vec{\mathbf{J}}_f \ , \tag{A.2}$$

where $\vec{\mathbf{B}}$ denotes the magnetic flux density (also known as magnetic induction or just the magnetic field). The definition for the bound current $\vec{\mathbf{J}}_b = \nabla \times \vec{\mathbf{M}}$ can then be substituted into (A.2) and the curls can be grouped together to give

$$\nabla \times \left(\frac{1}{\mu_0}\vec{\mathbf{B}} - \vec{\mathbf{M}}\right) = \vec{\mathbf{J}}_f \ . \tag{A.3}$$

The quantity $\left(\frac{1}{\mu_0}\vec{\mathbf{B}} - \vec{\mathbf{M}}\right)$ is replaced with an auxiliary variable $\vec{\mathbf{H}}$, which results in

$$\vec{\mathbf{H}} = \frac{1}{\mu_0}\vec{\mathbf{B}} - \vec{\mathbf{M}} \ . \tag{A.4}$$

This $\vec{\mathbf{H}}$ vector is known by several names such as the auxiliary magnetic field, the magnetic field intensity, the magnetic field strength or just the "H"-field. The auxiliary field simplifies the representation of Ampère's law so that the value of $\vec{\mathbf{H}}$ is easily obtained by the known free current $\vec{\mathbf{J}}_f$.

The magnetisation $\vec{\mathbf{M}}$ together with the specific magnetic properties and magnetic history (hysteresis) of the material determine the strength of the magnetic field $\vec{\mathbf{B}}$ [81]. However, it is customary to write this relationship in terms of $\vec{\mathbf{H}}$ rather than $\vec{\mathbf{B}}$. For a linear homogeneous, isotropic and ferromagnetic medium, the relationship between the magnetisation vector $\vec{\mathbf{M}}$ and the auxiliary magnetic field vector $\vec{\mathbf{H}}$ is described by [81] and [82] as

$$\vec{\mathbf{M}} = \chi_m \vec{\mathbf{H}} \ , \tag{A.5}$$

where χ_m denotes the magnetic susceptibility. Typical values of χ_m for diamagnetic and paramagnetic materials are in the order of 10^{-5} (unitless). For a ferromagnetic material such as iron, χ_m is in the positive range of up to 5000 (depending on the purity of the iron) at a flux density of $B = 1\,\mathrm{T}$ [82].

The magnetic flux density $\vec{\mathbf{B}}$ is then calculated by changing the subject of (A.4) to get

$$\vec{\mathbf{B}} = \mu_0(\vec{\mathbf{H}} + \vec{\mathbf{M}}) \ , \tag{A.6}$$

and substituting (A.5) into (A.6) gives

$$\vec{\mathbf{B}} = \mu_0(1 + \chi_m)\vec{\mathbf{H}} \ . \tag{A.7}$$

The factor $(1+\chi_m)$ is usually replaced with a new variable, known as the relative magnetic permeability μ_r, so that we now have

$$\vec{\mathbf{B}} = \mu_0 \mu_r \vec{\mathbf{H}} \ , \tag{A.8}$$

which is the form frequently used in introductory electric machinery textbooks such as [67] and [83], instead of using equations with $\vec{\mathbf{M}}$ or χ_m.

If a material is already magnetised, we say that it has a residual magnetisation $\vec{\mathbf{M}}_0$ [12]. The magnetisation we add due to free current, is called induced magnetisation $\vec{\mathbf{M}}_i$. The total magnetisation is then described by

$$\vec{\mathbf{M}} = \vec{\mathbf{M}}_0 + \vec{\mathbf{M}}_i \ , \tag{A.9}$$

where $\vec{\mathbf{M}}_\mathbf{i}$ takes the definition as described by (A.5) which gives

$$\vec{\mathbf{M}} = \vec{\mathbf{M}}_0 + \chi_m \vec{\mathbf{H}} \ . \tag{A.10}$$

The resultant flux density in the material is subsequently determined by substituting (A.10) into (A.6),

$$\begin{aligned} \vec{\mathbf{B}} &= \mu_0 \vec{\mathbf{H}} + \mu_0 \chi_m \vec{\mathbf{H}} + \mu_0 \vec{\mathbf{M}}_0 \\ &= \mu_0 (1+\chi_m) \vec{\mathbf{H}} + \mu_0 \vec{\mathbf{M}}_0 \\ &= \mu_0 \mu_r \vec{\mathbf{H}} + \mu_0 \vec{\mathbf{M}}_0 \ , \end{aligned} \tag{A.11}$$

which looks similar to (A.8) but with an extra term for the residual (or remanent) [82] flux density $\vec{\mathbf{B}}_{rem}$,

$$\vec{\mathbf{B}}_{rem} = \mu_0 \vec{\mathbf{M}}_\mathbf{0} \ . \tag{A.12}$$

According to [12], it is helpful to accommodate for the quantity $\vec{\mathbf{B}}_{rem}$ since this quantity is normally supplied by the datasheets of permanent magnet manufacturers.

To conclude, the relationship between the magnetic field density, "H"-field and magnetisation is,

$\vec{\mathbf{B}} = \mu_0 \mu_r \vec{\mathbf{H}}$ for materials without residual magnetisation, such as air (A.13)

$\vec{\mathbf{B}} = \mu_0 \mu_r \vec{\mathbf{H}} + \mu_0 \vec{\mathbf{M}}_0$ and for materials such as permanent magnets. (A.14)

A.2 The Maxwell Equations

The equations which govern electromagnetic behaviour are known as the Maxwell equations,

$$\nabla \times \vec{\mathbf{E}} = -\frac{\partial \vec{\mathbf{B}}}{\partial t} \ , \tag{A.15}$$

$$\nabla \times \vec{\mathbf{H}} = \vec{\mathbf{J}}_f + \frac{\partial \vec{\mathbf{D}}}{\partial t} \ , \tag{A.16}$$

$$\nabla \cdot \vec{\mathbf{D}} = \rho_v \quad \text{and} \tag{A.17}$$

$$\nabla \cdot \vec{\mathbf{B}} = 0 \ . \tag{A.18}$$

A.3 Magnetic Vector Potential

The magnetic flux density vector $\vec{\mathbf{B}}$ as seen in (A.15), is a continuous (solenoidal) vector because (A.18) states that its divergence is zero [82]. This means that for a closed surface, the magnetic flux entering a surface is equal to the magnetic flux leaving the closed surface. Or otherwise put, magnetic field lines are always continuous, starting from a north pole and ending at a south pole, and within the magnetic source itself, the field lines continue from the south pole to the north pole. From vector calculus, the divergence of the curl is zero,

$$\nabla \cdot (\nabla \times \vec{\mathbf{A}}) = 0 \ . \tag{A.19}$$

Therefore the magnetic flux density in (A.18) can be expressed by 'n curl of another vector (an auxiliary vector) known as the magnetic vector potential $\vec{\mathbf{A}}$ such that,

$$\vec{\mathbf{B}} = \nabla \times \vec{\mathbf{A}} \ . \tag{A.20}$$

In the cylyndrical coordinate system, the magnetic vector potential can be written as,

$$\vec{\mathbf{A}} = A_r \vec{\mathbf{a}}_r + A_\phi \vec{\mathbf{a}}_\phi + A_z \vec{\mathbf{a}}_z \ . \tag{A.21}$$

Equation (A.20) can now be substituted into (A.11) which results in,

$$\vec{\mathbf{H}} = \frac{\nabla \times \vec{\mathbf{A}} - \mu_0 \vec{\mathbf{M}}_0}{\mu_0 \mu_r} \ , \tag{A.22}$$

when the subject is changed to $\vec{\mathbf{H}}$. If it is assumed that the wavelength of the time-varying electromagnetic field is much longer than the medium itself, then according to [12], the Equation (A.16) from Maxwell's laws can be reduced to

$$\nabla \times \vec{\mathbf{H}} = \vec{\mathbf{J}}_f \ . \tag{A.23}$$

Equation (A.22) can now be substituted into (A.23) resulting in,

$$\nabla \times \left(\frac{\nabla \times \vec{\mathbf{A}} - \mu_0 \vec{\mathbf{M}}_0}{\mu_0 \mu_r} \right) = \vec{\mathbf{J}}_f \ . \tag{A.24}$$

Vector calculus simplification (curl of the curl) of (A.24) deduces to

$$\nabla(\nabla \cdot \vec{\mathbf{A}}) - \nabla^2 \vec{\mathbf{A}} - \mu_0(\nabla \times \vec{\mathbf{M}}_0) = \mu_0 \mu_r \vec{\mathbf{J}}_f \ . \tag{A.25}$$

As explained in [82, p. 60], a constraint is introduced which will allow $\vec{\mathbf{A}}$ to be a unique vector field. The constraint, known as Coulomb's gauge, is defined by

$$\nabla \cdot \vec{\mathbf{A}} = 0 \ , \tag{A.26}$$

so that (A.25) becomes

$$\nabla^2 \vec{\mathbf{A}} = -\mu_0(\nabla \times \vec{\mathbf{M}}_0) - \mu_0 \mu_r \vec{\mathbf{J}}_f \ . \tag{A.27}$$

A.4 Subdomain Modelling

The basic idea around the subdomain modelling which will be performed here, is to solve for $\vec{\mathbf{A}}$ in (A.27) within a specific uniform region. Once $\vec{\mathbf{A}}$ is obtained, we can derive the values for $\vec{\mathbf{B}}$ and $\vec{\mathbf{H}}$ which is subsequently used to determine the flux linkage, inductance and torque of the machine. It will be shown, that the functions for $\vec{\mathbf{A}}$, $\vec{\mathbf{B}}$ and $\vec{\mathbf{H}}$ will consist of Fourier series functions. The Fourier coefficients are revealed by simultaneous equations involving the basic field theory boundary conditions.

The regions are chosen in such a manner so that a constant permeability is present and that a single governing equation such as (A.27) can be used in that region [12, p. 40]. This is achieved by dividing the machine into ring regions as was done in [12].

The overall strategy for analysis of the magnetic fields in the machine, will be to determine the magnetic fields only due to the permanent magnets (with the stator coils

"switched off" or deactivated). Thereafter, the magnetic fields due to the armature reaction (active stator), will be determined while the permanent magnets are ignored. The resultant magnetic fields are then realised by the superposition of the two active components. This is done so that more insight and knowledge may be gained from the machine's workings. In addition, the torque approximated by the Lorentz method requires information of the magnetic field density only due to the permanent magnets. And secondly, to determine the self and mutual inductances of the stator, the magnetic field density due to the armature reaction will be required. Nevertheless, it should also be possible to assume both stator and magnets active, and solve only a single subdomain modelled problem - which would directly deliver the total magnetic field due to both active components.

A.5 Finding the Poisson and Laplace Equations

Figure A.1 shows the regions that are used to execute subdomain modelling when only the permanent magnets are considered active. The roman numbers on the left of Figure A.1 indicate the manner in which the regions are divided.

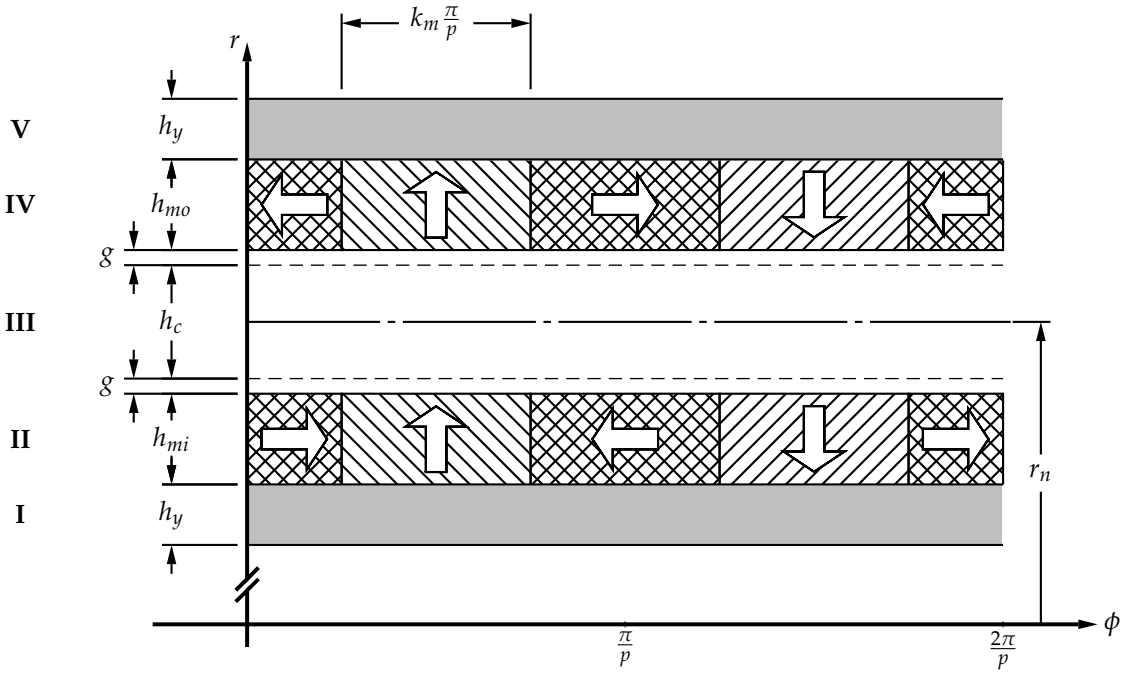

Figure A.1: A linear representation of the different regions of the RFAPM machine with only the permanent magnets active.

Because we consider the stator coils "switched off", no free current exist within them. Also, the copper coils do not have any meaningful residual magnetisation, so $\vec{\mathbf{M}}_0 = 0$. Thus (A.27) in Region III reduces to $\nabla^2 \vec{\mathbf{A}} = 0$. Within the permanent magnet regions, no

free current exists, thus in Regions II and IV (A.27) becomes $\nabla^2\vec{\mathbf{A}} = -\mu_0(\nabla \times \vec{\mathbf{M}}_0)$. The permeabilities of Regions I and V are given the values μ_{yi} and μ_{yo} respectively. This is to accommodate the possible use of other materials for the yokes, such as iron. However for this research, air-equivalent yokes will be used, so $\mu_{yi} = \mu_{yo} = 1$. These regions are also important because some leakage flux will exist on the outside of the permanent magnets. Table A.1 summarises the governing equations.

Region	Range for r	μ_r	Governing equation
V	$r_n + \frac{h_c}{2} + g + h_{mo} + h_y \geq r \geq r_n + \frac{h_c}{2} + g + h_{mo}$	μ_{yo}	$\nabla^2\vec{\mathbf{A}} = 0$
IV	$r_n + \frac{h_c}{2} + g + h_{mo} \geq r \geq r_n + \frac{h_c}{2} + g$	1	$\nabla^2\vec{\mathbf{A}} = -\mu_0(\nabla \times \vec{\mathbf{M}}_0)$
III	$r_n + \frac{h_c}{2} + g \geq r \geq r_n - \frac{h_c}{2} - g$	1	$\nabla^2\vec{\mathbf{A}} = 0$
II	$r_n - \frac{h_c}{2} - g \geq r \geq r_n - \frac{h_c}{2} - g - h_{mi}$	1	$\nabla^2\vec{\mathbf{A}} = -\mu_0(\nabla \times \vec{\mathbf{M}}_0)$
I	$r_n - \frac{h_c}{2} - g - h_{mi} \geq r \geq r_n - \frac{h_c}{2} - g - h_{mi} - h_y$	μ_{yi}	$\nabla^2\vec{\mathbf{A}} = 0$

Table A.1: The governing equations for solving the magnetic vector potential in the different regions of the RFAPM machine when employing permanent magnet excitation.

The governing equations are in the form of Laplace and Poisson equations. Specifically, regions I, III and V are Laplace equations, which will have general solutions. Regions II and IV are Poisson equations, and will deliver both general and unique solutions. Note that for regions II and IV, we require more information about the magnetisation vector $\vec{\mathbf{M}}_0$, or rather, more information of $\boldsymbol{\nabla} \times \vec{\mathbf{M}}_0$.

Both radial and azimuthal magnetised permanent magnets exist within a single region (Region II and IV). The magnetisation vector must then be described using both radial and azimuthal components,

$$\vec{\mathbf{M}}_0 = M_{0|r}\vec{\mathbf{a}}_r + M_{0|\phi}\vec{\mathbf{a}}_\phi \ . \tag{A.28}$$

In general, the curl becomes,

$$\begin{aligned}
\boldsymbol{\nabla} \times \vec{\mathbf{M}}_0 &= \frac{1}{r}\begin{vmatrix} \vec{\mathbf{a}}_r & r\vec{\mathbf{a}}_\phi & \vec{\mathbf{a}}_z \\ \frac{\partial}{\partial r} & \frac{\partial}{\partial \phi} & \frac{\partial}{\partial z} \\ M_{0|r} & rM_{0|\phi} & - \end{vmatrix} \\
&= \frac{1}{r}\left[\frac{\partial(rM_{0|\phi})}{\partial r} - \frac{\partial M_{0|r}}{\partial \phi}\right]\vec{\mathbf{a}}_z \\
&= \left[\frac{M_{0|\phi}}{r} + \frac{\partial M_{0|\phi}}{\partial r} - \frac{1}{r}\frac{\partial M_{0|r}}{\partial \phi}\right]\vec{\mathbf{a}}_z \ .
\end{aligned} \tag{A.29}$$

Because the radial and azimuthal magnetised magnets are equally strong magnetised (the same magnet grades are assumed) we have,

$$M_{0|_r} = M_{0|_\phi} = M_0 = \frac{B_{rem}}{\mu_0} \ . \tag{A.30}$$

It is intuitive that for a particular region (either Region II or IV), the residual magnetisation $M_{0|_\phi}$ is not a function of r. This is because the magnetic material (and thus residual magnetisation) is uniform for all r within that entire region. Or simply put, the magnetic material consumes the entire length of Regions II and IV in the r direction. Thus (A.29) reduces to,

$$\boldsymbol{\nabla} \times \vec{\mathbf{M}}_0 = \frac{1}{r}\left[M_{0|_\phi} - \frac{\partial M_{0|_r}}{\partial \phi}\right]\vec{\mathbf{a}}_z \ . \tag{A.31}$$

It is now clear that we need to determine the terms of (A.31). In particular, we need to determine $M^{II}_{0|\phi}$, $M^{IV}_{0|\phi}$, $\frac{\partial M^{II}_{0|r}}{\partial \phi}$ and $\frac{\partial M^{IV}_{0|r}}{\partial \phi}$. The aforementioned will be determined in the following sections.

A.6 Magnetisation Distribution Functions of Radial Magnetised Permanent Magnets

Figure A.2 shows the residual magnetisation distribution $M_{0|_r}(\phi)$ of the radial magnetised permanent magnets. Notice that from Figure A.1, the radially magnetised magnets on the inner and outer rotors are equally wide (in the azimuthal direction), and also have the same magnetisation polarity direction at the same azimuthal position, which means $M^{II}_{0|_r}(\phi) = M^{IV}_{0|_r}(\phi) = M_{0|_r}(\phi)$.

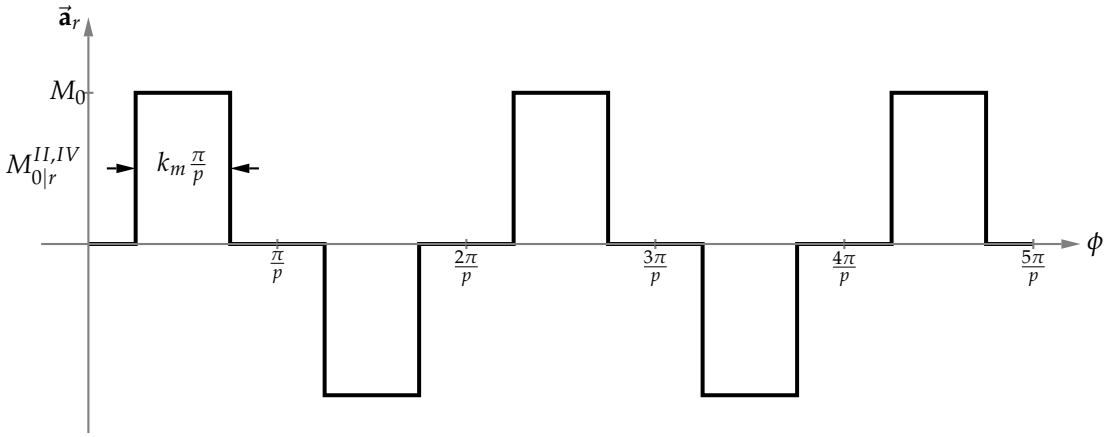

Figure A.2: The residual magnetisation distribution of the radially magnetised permanent magnets on the inner and outer rotor (i.e regions II and IV respectively) with respect to ϕ.

However, we only need to determine the partial derivative $\frac{\partial M_{0|r}^{II,IV}}{\partial \phi}$ which can be directly deduced from Figure A.2 as shown by Figure A.3. The derivatives will now be written in short hand as

$$\frac{\partial M_{0|r}^{II,IV}}{\partial \phi} = M_{0|r}^{II,IV\prime}(\phi) \ . \tag{A.32}$$

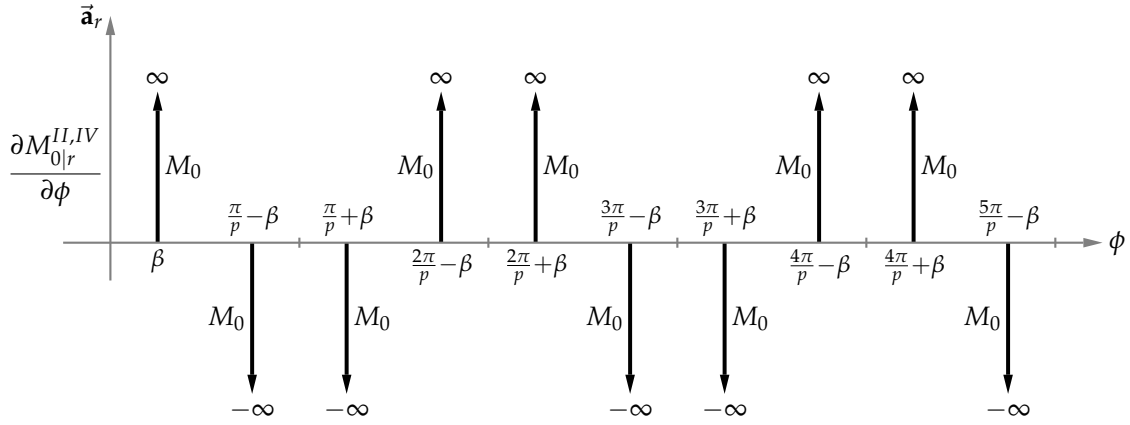

Figure A.3: The derivative of the residual magnetisation distribution of the radial magnetised permanent magnets on the inner and outer rotor (i.e regions II and IV respectively) with respect to ϕ.

To help describe the position of the impulse signals in Figure A.3 we use,

$$\beta = \left(\frac{1-k_m}{2}\right)\frac{\pi}{p} \ . \tag{A.33}$$

Because Figure A.2 and A.3 are periodic, the functions can be described using a Fourier series. The general form of a Fourier series representation is described as,

$$f(\phi) = a_0 + \sum_{m=1}^{\infty} a_m \cos(mp\phi) + b_m \sin(mp\phi) \ . \tag{A.34}$$

We now let $f(\phi) = M_{0|r}^{II,IV'}(\phi)$. Due to even quarter wave symmetry as seen in Figure A.3, only odd harmonics are considered ($m = 1, 3, 5...$) and the coefficients are defined as

$$a_{0|M_{0|r}^{II,VI'}} = 0 \tag{A.35}$$

$$b_{m|M_{0|r}^{II,VI'}} = 0 \tag{A.36}$$

$$\begin{aligned} a_{m|M_{0|r}^{II,VI'}} &= \frac{4p}{\pi} \int_0^{\frac{\pi}{2p}} M_{0|r}^{II,IV'}(\phi) \cos(mp\phi)\, d\phi \\ &= \frac{4p}{\pi} \int_0^{\frac{\pi}{2p}} [\delta(\phi - \beta) M_0] \cos(mp\phi)\, d\phi \\ &= \frac{4pM_0}{\pi} \cos(mp\beta) \ . \end{aligned} \tag{A.37}$$

Thus we have,

$$M_{0|r}^{II,IV'}(\phi) = \sum_{m=1,3,5...}^{\infty} \left[\frac{4pM_0}{\pi} \cos(mp\beta) \right] \cos(mp\phi) \ . \tag{A.38}$$

A.7 Magnetisation Distribution Functions of Azimuthal Magnetised Permanent Magnets

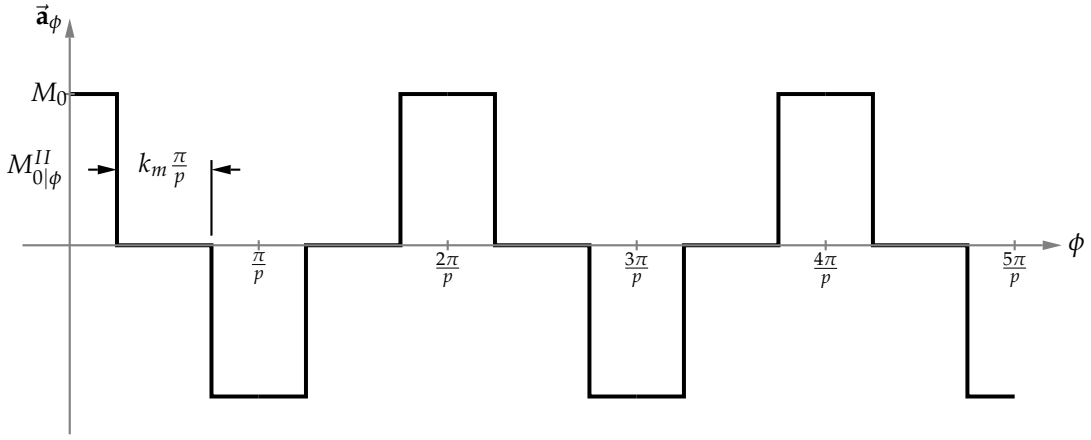

Figure A.4: The residual magnetisation distribution of the azimuthal magnetised permanent magnets on the inner rotor (i.e. region II) with respect to ϕ.

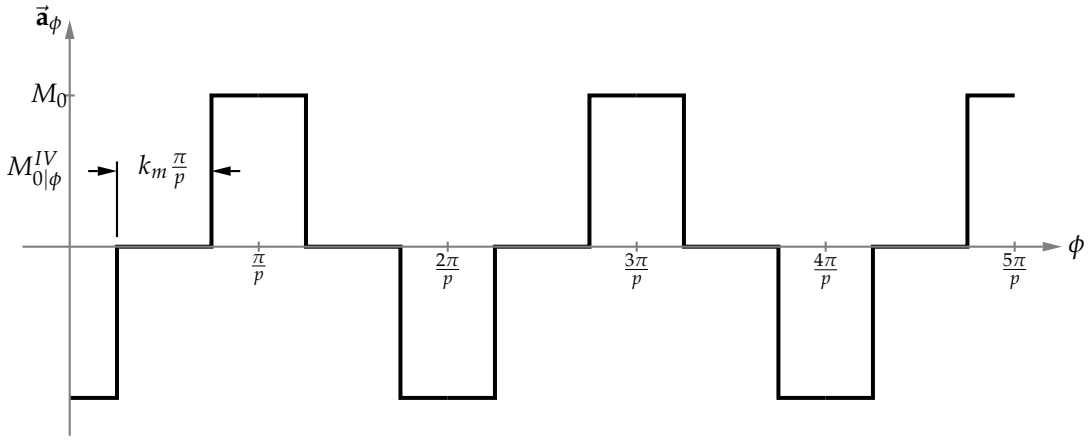

Figure A.5: The residual magnetisation distribution of the azimuthal magnetised permanent magnets on the outer rotor (i.e. region IV) with respect to ϕ.

Figure A.4 and Figure A.5 show the residual magnetisation distribution of the inner and outer azimuthal magnetised permanent magnets respectively. Notice that from Figure A.1, the inner azimuthal magnetised magnets are polarised in the opposite direction of the outer azimuthal magnetised magnets at any given azimuthal position, therefore

$$M^{II}_{0|\phi}(\phi) = -M^{IV}_{0|\phi}(\phi) \ . \tag{A.39}$$

Also notice that due to (A.31), the partial derivatives of the azimuthal magnetisation do not need to be determined. From Figure A.4, we have even quarter wave symmetry so the coefficients become,

$$a_{0|M^{II}_{0|\phi}} = 0 \tag{A.40}$$

$$b_{m|M^{II}_{0|\phi}} = 0 \tag{A.41}$$

$$\begin{aligned} a_{m|M^{II}_{0|\phi}} &= \frac{4p}{\pi} \int_0^{\frac{\pi}{2p}} M^{II}_{0|r}(\phi) \cos(mp\phi)\, d\phi \\ &= \frac{4}{m\pi} M_0 \sin(mp\phi)\Big|_0^{\beta} \\ &= \frac{4M_0}{m\pi} \sin(mp\beta) \ . \end{aligned} \tag{A.42}$$

Thus we have,

$$M^{II}_{0|\phi}(\phi) = \sum_{m=1,3,5\ldots}^{\infty} \left[\frac{4M_0}{m\pi} \sin(mp\beta)\right] \cos(mp\phi) \ , \tag{A.43}$$

and due to (A.39) we also have

$$M_{0|\phi}^{IV}(\phi) = -\sum_{m=1,3,5...}^{\infty}\left[\frac{4M_0}{m\pi}\sin(mp\beta)\right]\cos(mp\phi)\ . \tag{A.44}$$

For the inner rotor (region II) the Poisson equation becomes,

$$\begin{aligned}\boldsymbol{\nabla}^2\vec{\mathbf{A}} &= -\mu_0\left(\boldsymbol{\nabla}\times\vec{\mathbf{M}}_0\right)\\ &= -\frac{\mu_0}{r}\left[\frac{4M_0}{\pi}\sum_{m=1,3,5,...}^{\infty}\frac{\sin(mp\beta)}{m}\cos(mp\phi) - \frac{4pM_0}{\pi}\sum_{m=1,3,5,...}^{\infty}\cos(mp\beta)\cos(mp\phi)\right]\\ &= \frac{4\mu_0 M_0}{\pi r}\sum_{m=1,3,5,...}^{\infty}\left[p\cos(mp\beta) - \frac{\sin(mp\beta)}{m}\right]\cos(mp\phi)\\ &= \frac{4B_{rem}}{\pi r}\sum_{m=1,3,5,...}^{\infty}\left[\frac{mp\cos(mp\beta) - \sin(mp\beta)}{m}\right]\cos(mp\phi)\ ,\end{aligned} \tag{A.45}$$

and for the outer rotor (region IV)

$$\boldsymbol{\nabla}^2\vec{\mathbf{A}} = \frac{4B_{rem}}{\pi r}\sum_{m=1,3,5,...}^{\infty}\left[\frac{mp\cos(mp\beta) + \sin(mp\beta)}{mp}\right]\cos(m\phi)\ . \tag{A.46}$$

The remaining regions are all governed by Laplace equations, namely $\boldsymbol{\nabla}^2\vec{\mathbf{A}} = 0$.

A.8 Finding the Format of the General Solution

Recall that the aim is to find $\vec{\mathbf{A}}_{PM}$, so that the flux density $\vec{\mathbf{B}}_{PM}$ and other important quantities can be determined. Poisson equations are non-homogeneous partial differential equations. The solutions thereof, consist of both general and particular solutions. The general solution, is achieved by solving the homogeneous version of the Poisson equation, namely the Laplace equation. Consequently, the format of the general solution for regions II and IV, will also be the format of the final solution for regions I, III and V.

The solution of $A_{z|PM}(r,\phi)$ for a Poisson equation (regions II and IV) will consist of a general solution and a particular solution, thus,

$$A_{z|PM}^{II,IV}(r,\phi) = A_{z|PM,gen}^{II,IV}(r,\phi) + A_{z|PM,part}^{II,IV}(r,\phi)\ . \tag{A.47}$$

The solution of $A_{z|PM}(r,\phi)$ for a Laplace equation (regions I, III and IV) will consist only of a general solution, thus,

$$A_{z|PM}^{I,III,V}(r,\phi) = A_{z|PM,gen}^{I,III,V}(r,\phi)\ . \tag{A.48}$$

According to [12], if the current density exists only in the z direction, then it can be shown that the vector potential will also only exist in the z direction. Also due to the uniformity of the IDRFPM machine in the z direction, $\vec{\mathbf{A}}$ is only a function of r and ϕ. Subsequently, the left-hand-side of the Laplace equation $\boldsymbol{\nabla}^2\vec{\mathbf{A}}$ can be written in the partial differential format (in cylindrical coordinates), which results in the following two-dimensional homogeneous partial differential equation,

$$\boldsymbol{\nabla}^2\vec{\mathbf{A}} = \frac{\partial^2 A_{z|PM}}{\partial r^2} + \frac{1}{r}\frac{\partial A_{z|PM}}{\partial r} + \frac{1}{r^2}\frac{\partial^2 A_{z|PM}}{\partial \phi^2} = 0 \ . \tag{A.49}$$

The methodology in finding a solution of a homogeneous partial differential Laplace equation of an annulus is explained by [84, pp. 366-371]. Specifically, the Dirichlet boundary-type problem is discussed and it is assumed that the boundary functions (the functions which help describe the value of $A_{z|PM,gen}$ on the boundaries of each region) are continuous and periodic, meaning

$$A_{z|PM,gen}(r_{bound}, \phi) = A_{z|PM,gen}(r_{bound}, 2n\pi + \phi) \quad \text{for all integers of n,} \tag{A.50}$$

where the subscript *bound* refers to the position r at some boundary of a region. Furthermore, the Dirichlet problem requires a harmonic function as the solution, which simply means that the solution function $A_{z|PM,gen}$ is valid for all (r, ϕ) within the specific region. This also implies that the solution should extend continuously toward the boundary value of the region.

In short, [84, pp. 366-371] shows that "product solutions" can be used to determine the form of the solution for (A.49). Thus, the solution is assumed to be a product of two separate solutions,

$$A_{z|PM,gen}(r, \phi) = R(r)\,T(\phi) \ . \tag{A.51}$$

Equation (A.51) is then substituted (partial differentiation will occur) into (A.49) and separation of variables are utilised. By considering $R(r)$ constant, the solution for $T(\phi)$ will be in the form of,

$$T_m(\phi) = a_{m|PM}\cos(m\phi) + b_{m|PM}\sin(m\phi) \ , \text{ and } m = 0, 1, 2, ..., \tag{A.52}$$

By considering $T(\phi)$ constant, the solution for $R(r)$ will be in the form of,

$$R_m(r) = c_{m|PM}r^m + d_{m|PM}r^{-m} \ , \text{ and } m = 0, 1, 2, ..., \tag{A.53}$$

The final solution of (A.49) is then achieved by multiplying the solutions (A.52) and (A.53) with each other. The format of the solution is then described as,

$$A_{z|PM,gen} = c_{0|PM} + d_{0|PM}\ln(r) \qquad \text{for } m = 0\ , \tag{A.54}$$

$$A_{z|PM,gen} = (c_{m|PM}r^{m} + d_{m|PM}r^{-m})(a_{m|PM}cosm\phi + b_{m|PM}sinm\phi) \qquad \text{for } m \geq 1\ . \tag{A.55}$$

Notice that the solutions (A.52), (A.53) and thus (A.55) are in the form of harmonic functions. This implies that we will have unique constants for each harmonic of $A_{z|PM,gen}$, consequently each harmonic of $A_{z|PM,gen}$ will have its own magnitude.

Because we know that the flux density is calculated by derivatives of the vector potential ($\vec{\mathbf{B}} = \boldsymbol{\nabla} \times \vec{\mathbf{A}}$), we do not need to determine the value of $c_{0|PM}$ so we can therefore set it to 0 for convenience. Additionally, there should be no DC component of the vector potential, thus we can say $d_{0|PM} = 0$. To summarise,

$$c_{0|PM} = 0 \tag{A.56}$$

$$d_{0|PM} = 0 \tag{A.57}$$

$$\text{therefore} \quad A_{z|PM,gen} = 0 \quad \text{for } m = 0\ . \tag{A.58}$$

Furthermore we know that the magnetisation distribution and its derivatives, as described by (A.38), (A.43) and (A.44), only consist of odd numbered harmonics. It is for this reason intuitive that the solution for the vector potential will also only consist of odd numbered harmonics. In [29], [30] and [12], the general solution

$$A_{z|PM,gen}(r,\phi) = \sum_{m=1,3,5,\ldots}^{\infty}(C_{m|PM}r^{mp} + D_{m|PM}r^{-mp})\cos(mp\phi)\ , \tag{A.59}$$

is successfully implemented. Notice that from (A.55), $a_{m|PM}$ is multiplied with $c_{m|PM}$ and $d_{m|PM}$ to create new constants, namely $C_{m|PM}$ and $D_{m|PM}$.

A.9 Finding the Format of the Particular Solution

The Poisson equations for regions II and IV can also be put in the two-dimensional homogeneous partial differential equation format, as was done in (A.49). Of course, for regions II and IV, equations (A.45) and (A.46) are now included into the right-hand-side of the

non-homogeneous PDE. The Poisson equation for Region II becomes,

$$\frac{\partial^2 A_{z|PM}}{\partial r^2}+\frac{1}{r}\frac{\partial A_{z|PM}}{\partial}+\frac{1}{r^2}\frac{\partial^2 A_{z|PM}}{\partial \phi^2}=\frac{4B_{rem}}{\pi r}\sum_{m=1,3,5,...}^{\infty}\left[\frac{mp\cos(mp\beta)-\sin(mp\beta)}{m}\right]\cos(mp\phi)\ , \tag{A.60}$$

and for Region IV,

$$\frac{\partial^2 A_{z|PM}}{\partial r^2}+\frac{1}{r}\frac{\partial A_{z|PM}}{\partial}+\frac{1}{r^2}\frac{\partial^2 A_{z|PM}}{\partial \phi^2}=\frac{4B_{rem}}{\pi r}\sum_{m=1,3,5,...}^{\infty}\left[\frac{mp\cos(mp\beta)+\sin(mp\beta)}{mp}\right]\cos(m\phi)\ . \tag{A.61}$$

In general when attempting to solve of Poisson equations, an intuitive guess of the shape of the particular solution is done. Previous subdomain analysis studies on electrical machines with both radial and azimuthal magnetised magnets, such as [12] and [30], successfully uses the particular solution,

$$A_{z|PM,part}(r,\phi)=\sum_{m=1,3,5,...}^{\infty}G^{II,IV}_{m|PM}\,r\cos(mp\phi)\ . \tag{A.62}$$

A quick check can be done to verify the solution. To test the solution for Region II, we can substitute (A.62) into (A.60) to get,

$$\frac{\partial A_{z|PM}}{\partial r}=\sum_{m=1,3,5,...}^{\infty}G^{II}_{m|PM}\cos(mp\phi)\ , \tag{A.63}$$

$$\frac{\partial^2 A_{z|PM}}{\partial r^2}=0\ , \tag{A.64}$$

$$\frac{\partial A_{z|PM}}{\partial \phi}=-\sum_{m=1,3,5,...}^{\infty}mpG^{II}_{m|PM}\,r\sin(mp\phi)\ \text{and} \tag{A.65}$$

$$\frac{\partial^2 A_{z|PM}}{\partial \phi^2}=-\sum_{m=1,3,5,...}^{\infty}(mp)^2\,G^{II}_{m|PM}\,r\cos(mp\phi)\ , \tag{A.66}$$

which results in,

$$\begin{aligned}\frac{\partial^2 A_{z|PM}}{\partial r^2}+\frac{1}{r}\frac{\partial A_{z|PM}}{\partial}+\frac{1}{r^2}\frac{\partial^2 A_{z|PM}}{\partial \phi^2}&=\frac{1}{r}\sum_{m=1,3,5,...}^{\infty}G^{II}_{m|PM}\cos(mp\phi)-\frac{1}{r^2}\sum_{m=1,3,5,...}^{\infty}(mp)^2\,G^{II}_{m|PM}\,r\cos(mp\phi)\\&=\frac{1}{r}\sum_{m=1,3,5,...}^{\infty}G^{II}_{m|PM}\left(1-(mp)^2\right)\cos(mp\phi)\ .\end{aligned} \tag{A.67}$$

The right-hand-side of (A.60) and right-hand-side of (A.67) can now be compared in order to find the value of $G^{II}_{m|PM}$,

$$G^{II}_{m|PM}=\frac{4B_{rem}}{\pi m}\left(\frac{mp\cos(mp\beta)-\sin(mp\beta)}{1-(mp)^2}\right)\ . \tag{A.68}$$

The same process can be done for Region IV,

$$G^{IV}_{m|PM} = \frac{4B_{rem}}{\pi m}\left(\frac{mp\cos(mp\beta)+\sin(mp\beta)}{1-(mp)^2}\right) . \tag{A.69}$$

As can be seen from (A.68) and (A.69), the expressions do not hold for $mp = 1$. In [12] it is shown that a slightly different definition for the remanent flux density can be used to achieve values for $G^{II}_{m|PM}$ and $G^{IV}_{m|PM}$ which would hold for all mp. However, in practical and optimised electrical machines, the number of pole pairs p will surely be more than 1. Thus (A.68) and (A.69) are sufficient for practical purposes.

A.10 Boundary Conditions

We have already determined $G^{II}_{m|PM}$ and $G^{IV}_{m|PM}$, but we still need to solve for $C_{m|PM}$ and $D_{m|PM}$ for each of the regions. In order to reveal the aforementioned unknowns and to ensure that the solutions are continuous from one region to another, we need extra information. This information can be obtained by considering the boundaries of each region. The boundary conditions are defined using the magnetic vector potential, magnetic flux density and "H"-field. We obtain the latter two quantities by using (A.20),

$$\begin{aligned}\vec{\mathbf{B}} &= \boldsymbol{\nabla}\times\vec{\mathbf{A}}\\ &= \frac{1}{r}\begin{vmatrix}\vec{\mathbf{a}}_r & r\vec{\mathbf{a}}_\phi & \vec{\mathbf{a}}_z\\ \frac{\partial}{\partial r} & \frac{\partial}{\partial\phi} & \frac{\partial}{\partial z}\\ A_r & rA_\phi & A_z\end{vmatrix}\\ &= \frac{1}{r}\left(\frac{\partial A_z}{\partial\phi}-r\frac{\partial A_\phi}{\partial z}\right)\vec{\mathbf{a}}_r+\left(\frac{\partial A_r}{\partial z}-\frac{\partial A_z}{\partial r}\right)\vec{\mathbf{a}}_\phi+\frac{1}{r}\left(\frac{\partial(rA_\phi)}{\partial r}-\frac{\partial A_r}{\partial\phi}\right)\vec{\mathbf{a}}_z .\end{aligned} \tag{A.70}$$

We can simplify (A.70) due to the fact that the vector potential is only a function of r and ϕ, thus we have

$$\begin{aligned}\vec{\mathbf{B}} &= \frac{1}{r}\frac{\partial A_z}{\partial\phi}\vec{\mathbf{a}}_r-\frac{\partial A_z}{\partial r}\vec{\mathbf{a}}_\phi\\ &= B_r\vec{\mathbf{a}}_r+B_\phi\vec{\mathbf{a}}_\phi ,\end{aligned} \tag{A.71}$$

where

$$B_r = \frac{1}{r}\frac{\partial A_z}{\partial\phi} \tag{A.72}$$

$$B_\phi = -\frac{\partial A_z}{\partial r} . \tag{A.73}$$

Regarding the "H"-field, in regions I, III and V we have the relationship from (A.13),

$$H_\phi = \frac{B_\phi}{\mu_0\mu_r} \tag{A.74}$$

and in regions II and IV we have the relationship from (A.14)

$$H_\phi = \frac{B_\phi - B_{rem}}{\mu_0 \mu_r} \ . \tag{A.75}$$

A.10.1 Boundary Definitions

The following radii definitions are used to describe the boundary positions between regions,

$$r_i = r_n - \frac{h_c}{2} - g - h_{mi} - h_y \tag{A.76}$$

$$r_{ii} = r_n - \frac{h_c}{2} - g - h_{mi} \tag{A.77}$$

$$r_{iii} = r_n - \frac{h_c}{2} - g \tag{A.78}$$

$$r_{iv} = r_n + \frac{h_c}{2} + g \tag{A.79}$$

$$r_v = r_n + \frac{h_c}{2} + g + h_{mo} \tag{A.80}$$

$$r_{vi} = r_n + \frac{h_c}{2} + g + h_{mo} + h_y \ . \tag{A.81}$$

A.10.2 Conditions from the Vector Potential

We assume that no magnetic flux leaves the outer boundary of Region V and that no flux leaves the inner boundary of Region I. This assumption should be fairly good if we choose regions I and V large enough so that minimal leakage flux will exist outside of regions I and V (and of course outside of regions II, III and IV). By this assumption, the vector potential at these boundaries are,

$$A^I_{z|r=r_i} = 0 \tag{A.82}$$

$$A^V_{z|r=r_{vi}} = 0 \ . \tag{A.83}$$

We know from (A.59) that the vector potential in regions I and V is defined as,

$$A^I_z(r,\phi) = \sum_{m=1,3,5,\ldots}^{\infty} (C^I_m r^{mp} + D^I_m r^{-mp}) \cos(mp\phi) \tag{A.84}$$

$$A^V_z(r,\phi) = \sum_{m=1,3,5,\ldots}^{\infty} (C^V_m r^{mp} + D^V_m r^{-mp}) \cos(mp\phi) \ . \tag{A.85}$$

Thus, it follows that on the boundaries of $r = r_i$ and $r = r_{vi}$, for any value of ϕ,

$$C^I_m r_i^{mp} + D^I_m r_i^{-mp} = 0 \tag{A.86}$$

$$C^V_m r_{vi}^{mp} + D^V_m r_{vi}^{-mp} = 0 \ . \tag{A.87}$$

A.10.3 Conditions from the Radial Flux Density

From fundamental electromagnetic field theory [82, p. 212], [85, p. 101] and [86, p. 262] we know that the normal components of the flux density between two regions are equal at the boundary. Therefore in this application, the radial components between each ring region will be equal. Thus,

$$B^{I}_{r|r=r_{ii}} = B^{II}_{r|r=r_{ii}} \tag{A.88}$$

$$B^{II}_{r|r=r_{iii}} = B^{III}_{r|r=r_{iii}} \tag{A.89}$$

$$B^{III}_{r|r=r_{iv}} = B^{IV}_{r|r=r_{iv}} \tag{A.90}$$

$$B^{IV}_{r|r=r_{v}} = B^{V}_{r|r=r_{v}} \tag{A.91}$$

The radial flux density as described by (A.72) can now be determined for every region. In Region I this is

$$\begin{aligned} B^{I}_{r}(r,\phi) &= \frac{1}{r}\frac{\partial A^{I}_{z}}{\partial \phi} \\ &= -\frac{1}{r}\sum_{m=1,3,5,\ldots}^{\infty} mp(C^{I}_{m}r^{mp} + D^{I}_{m}r^{-mp})\sin(mp\phi) \\ &= -\sum_{m=1,3,5,\ldots}^{\infty} mp(C^{I}_{m}r^{mp-1} + D^{I}_{m}r^{-mp-1})\sin(mp\phi)\ . \end{aligned} \tag{A.92}$$

For region II we have,

$$\begin{aligned} B^{II}_{r}(r,\phi) &= \frac{1}{r}\frac{\partial A^{II}_{z}}{\partial \phi} \\ &= -\frac{1}{r}\sum_{m=1,3,5,\ldots}^{\infty} mp(C^{II}_{m}r^{mp} + D^{II}_{m}r^{-mp} + G^{II}_{m}r)\sin(mp\phi) \\ &= -\sum_{m=1,3,5,\ldots}^{\infty} mp(C^{II}_{m}r^{mp-1} + D^{II}_{m}r^{-mp-1} + G^{II}_{m})\sin(mp\phi)\ . \end{aligned} \tag{A.93}$$

And for regions III, IV and V we have,

$$B^{III}_{r}(r,\phi) = -\sum_{m=1,3,5,\ldots}^{\infty} mp(C^{III}_{m}r^{mp-1} + D^{III}_{m}r^{-mp-1})\sin(mp\phi) \tag{A.94}$$

$$B^{IV}_{r}(r,\phi) = -\sum_{m=1,3,5,\ldots}^{\infty} mp(C^{IV}_{m}r^{mp-1} + D^{IV}_{m}r^{-mp-1} + G^{IV}_{m})\sin(mp\phi) \tag{A.95}$$

$$B^{V}_{r}(r,\phi) = -\sum_{m=1,3,5,\ldots}^{\infty} mp(C^{V}_{m}r^{mp-1} + D^{V}_{m}r^{-mp-1})\sin(mp\phi) \tag{A.96}$$

Now all these expressions can be equated according to the boundary conditions stated in Equations (A.88) to (A.91). Thus, on the boundaries of $r = r_{ii}$, r_{iii}, r_{iv} and $r = r_v$, for any value of ϕ we have,

$$C_m^I r_{ii}^{mp-1} + D_m^I r_{ii}^{-mp-1} = C_m^{II} r_{ii}^{mp-1} + D_m^{II} r_{ii}^{-mp-1} + G_m^{II} \tag{A.97}$$

$$C_m^{II} r_{iii}^{mp-1} + D_m^{II} r_{iii}^{-mp-1} + G_m^{II} = C_m^{III} r_{iii}^{mp-1} + D_m^{III} r_{iii}^{-mp-1} \tag{A.98}$$

$$C_m^{III} r_{iv}^{mp-1} + D_m^{III} r_{iv}^{-mp-1} = C_m^{IV} r_{iv}^{mp-1} + D_m^{IV} r_{iv}^{-mp-1} + G_m^{IV} \tag{A.99}$$

$$C_m^{IV} r_v^{mp-1} + D_m^{IV} r_v^{-mp-1} + G_m^{IV} = C_m^{V} r_v^{mp-1} + D_m^{V} r_v^{-mp-1} \ . \tag{A.100}$$

A.10.4 Conditions from the Azimuthal "H"-field

Again, from fundamental electromagnetic field theory [82, p. 213], [85, p. 102] and [86, p. 263] we know that the tangential components of the "H"-field between two regions are equal at the boundary when there is no *free* surface current present on the boundary. In this application, we will assume that there are no *free* currents present on the surfaces of the permanent magnets. To alleviate any confusion, recall from Section A.1 that permanent magnets can be represented using *bound* surface currents and *bound* volume currents, which are not the same as *free* surface currents. Furthermore, according to [85, p. 102], *free* surface currents only really come in to play when perfect electrical conductors are considered, or when the skin effect of conductors are investigated. Thus the boundary conditions are,

$$H_{\phi|r=r_{ii}}^I = H_{\phi|r=r_{ii}}^{II} \tag{A.101}$$

$$\therefore \quad \frac{B_{\phi|r=r_{ii}}^I}{\mu_0 \mu_r^I} = \frac{B_{\phi|r=r_{ii}}^{II} - \mu_0 M_{0|\phi}^{II}}{\mu_0 \mu_r^{II}} \tag{A.102}$$

$$H_{\phi|r=r_{iii}}^{II} = H_{\phi|r=r_{iii}}^{III} \tag{A.103}$$

$$\therefore \quad \frac{B_{\phi|r=r_{iii}}^{II} - \mu_0 M_{0|\phi}^{II}}{\mu_0 \mu_r^{II}} = \frac{B_{\phi|r=r_{iii}}^{III}}{\mu_0 \mu_r^{III}} \tag{A.104}$$

$$H_{\phi|r=r_{iv}}^{III} = H_{\phi|r=r_{iv}}^{IV} \tag{A.105}$$

$$\therefore \quad \frac{B_{\phi|r=r_{iv}}^{III}}{\mu_0 \mu_r^{III}} = \frac{B_{\phi|r=r_{iv}}^{IV} - \mu_0 M_{0|\phi}^{IV}}{\mu_0 \mu_r^{IV}} \tag{A.106}$$

$$H_{\phi|r=r_v}^{IV} = H_{\phi|r=r_v}^{V} \tag{A.107}$$

$$\therefore \quad \frac{B_{\phi|r=r_v}^{IV} - \mu_0 M_{0|\phi}^{IV}}{\mu_0 \mu_r^{IV}} = \frac{B_{\phi|r=r_v}^{V}}{\mu_0 \mu_r^{V}} \ . \tag{A.108}$$

By using (A.13), the solution for the azimuthal "H"-field in region I is,

$$\begin{aligned} H_{\phi}^{I}(r,\phi) &= \frac{B_{\phi}^{I}(r,\phi)}{\mu_0\mu_r^{I}} \\ &= -\frac{1}{\mu_0\mu_r^{I}}\frac{\partial A_z^{I}}{\partial r} \\ &= -\frac{1}{\mu_0\mu_r^{I}}\sum_{m=1,3,5,\ldots}^{\infty} mp(C_m^{I} r^{mp-1} - D_m^{I} r^{-mp-1})\cos(mp\phi)\ . \end{aligned} \tag{A.109}$$

For region II we use (A.14) which gives,

$$\begin{aligned} H_{\phi}^{II}(r,\phi) &= \frac{B_{\phi}^{II}(r,\phi) - \mu_0 M_{0|\phi}^{II}}{\mu_0\mu_r^{II}} \\ &= \frac{1}{\mu_0\mu_r^{II}}\left[-\frac{\partial A_z^{II}}{\partial r} - \mu_0 M_{0|\phi}^{II}\right] \\ &= -\frac{1}{\mu_0\mu_r^{II}}\left[\sum_{m=1,3,5,\ldots}^{\infty}(mpC_m^{II} r^{mp-1} - mpD_m^{II} r^{-mp-1} + G_m^{II})\cos(mp\phi)\right. \\ &\qquad \left. +\mu_0\frac{4M_0}{\pi}\sum_{m=1,3,5,\ldots}^{\infty}\frac{\sin(mp\beta)}{m}\cos(mp\phi)\right] \\ &= -\frac{1}{\mu_0\mu_r^{II}}\sum_{m=1,3,5,\ldots}^{\infty}\left[mpC_m^{II} r^{mp-1} - mpD_m^{II} r^{-mp-1}\right. \\ &\qquad \left. +\frac{4B_{rem}}{\pi m}\left(\frac{mp\cos(mp\beta) - \sin(mp\beta)}{1-(mp)^2} + \sin(mp\beta)\right)\right]\cos(mp\phi) \\ &= -\frac{1}{\mu_0\mu_r^{II}}\sum_{m=1,3,5,\ldots}^{\infty}\left[mpC_m^{II} r^{mp-1} - mpD_m^{II} r^{-mp-1}\right. \\ &\qquad \left. +\frac{4B_{rem}}{\pi m}\left(\frac{mp\cos(mp\beta) - (mp)^2\sin(mp\beta)}{1-(mp)^2}\right)\right]\cos(mp\phi) \\ &= -\frac{1}{\mu_0\mu_r^{II}}\sum_{m=1,3,5,\ldots}^{\infty} mp\left[C_m^{II} r^{mp-1} - D_m^{II} r^{-mp-1} + U_m^{II}\right]\cos(mp\phi)\ , \end{aligned} \tag{A.110}$$

where

$$U_m^{II} = \frac{4B_{rem}}{\pi m}\left(\frac{\cos(mp\beta) - mp\sin(mp\beta)}{1-(mp)^2}\right)\ . \tag{A.111}$$

The remaining solutions for the azimuthal magnetic field intensity in regions III, IV and

V are

$$H_\phi^{III}(r,\phi) = -\frac{1}{\mu_0\mu_r^{III}}\sum_{m=1,3,5,\ldots}^{\infty} mp(C_m^{III}r^{mp-1} - D_m^{III}r^{-mp-1})\cos(mp\phi) \tag{A.112}$$

$$H_\phi^{IV}(r,\phi) = -\frac{1}{\mu_0\mu_r^{IV}}\sum_{m=1,3,5,\ldots}^{\infty} mp\left[C_m^{IV}r^{mp-1} - D_m^{IV}r^{-mp-1} + U_m^{IV}\right]\cos(mp\phi) \tag{A.113}$$

$$H_\phi^{V}(r,\phi) = -\frac{1}{\mu_0\mu_r^{V}}\sum_{m=1,3,5,\ldots}^{\infty} mp(C_m^{V}r^{mp-1} - D_m^{V}r^{-mp-1})\cos(mp\phi)\ , \tag{A.114}$$

where

$$U_m^{IV} = \frac{4B_{rem}}{\pi m}\left(\frac{\cos(mp\beta) + mp\sin(mp\beta)}{1-(mp)^2}\right)\ . \tag{A.115}$$

Finally all these expressions can be equated according to the boundary conditions stated in Equations (A.101) to (A.107). Thus, on the boundaries of $r = r_{ii}$, r_{iii}, r_{iv} and $r = r_v$, for any value of ϕ we have,

$$\mu_r^{II}\left(C_m^I r_{ii}^{mp-1} - D_m^I r_{ii}^{-mp-1}\right) = \mu_r^I\left(C_m^{II}r_{ii}^{mp-1} - D_m^{II}r_{ii}^{-mp-1} + U_m^{II}\right) \tag{A.116}$$

$$\mu_r^{III}\left(C_m^{II} r_{iii}^{mp-1} - D_m^{II} r_{iii}^{-mp-1} + U_m^{II}\right) = \mu_r^{II}\left(C_m^{III} r_{iii}^{mp-1} - D_m^{III} r_{iii}^{-mp-1}\right) \tag{A.117}$$

$$\mu_r^{IV}\left(C_m^{III} r_{iv}^{mp-1} - D_m^{III} r_{iv}^{-mp-1}\right) = \mu_r^{III}\left(C_m^{IV} r_{iv}^{mp-1} - D_m^{IV} r_{iv}^{-mp-1} + U_m^{IV}\right) \tag{A.118}$$

$$\mu_r^{V}\left(C_m^{IV} r_v^{mp-1} - D_m^{IV} r_v^{-mp-1} + U_m^{IV}\right) = \mu_r^{IV}\left(C_m^{V} r_v^{mp-1} - D_m^{V} r_v^{-mp-1}\right)\ . \tag{A.119}$$

A.11 Solving the Coefficients

The 10 simultaneous equations from (A.86), (A.87), (A.97), (A.98), (A.99), (A.100), (A.116), (A.117), (A.118) and (A.119) are summarised here,

$$C_m^I r_i^{mp} + D_m^I r_i^{-mp} = 0 \tag{A.120}$$

$$C_m^I r_{ii}^{mp-1} + D_m^I r_{ii}^{-mp-1} - C_m^{II} r_{ii}^{mp-1} - D_m^{II} r_{ii}^{-mp-1} = G_m^{II} \tag{A.121}$$

$$\mu_r^{II} C_m^I r_{ii}^{mp-1} - \mu_r^{II} D_m^I r_{ii}^{-mp-1} - \mu_r^I C_m^{II} r_{ii}^{mp-1} + \mu_r^I D_m^{II} r_{ii}^{-mp-1} = \mu_r^I U_m^{II} \tag{A.122}$$

$$C_m^{II} r_{iii}^{mp-1} + D_m^{II} r_{iii}^{-mp-1} - C_m^{III} r_{iii}^{mp-1} - D_m^{III} r_{iii}^{-mp-1} = -G_m^{II} \tag{A.123}$$

$$\mu_r^{III} C_m^{II} r_{iii}^{mp-1} - \mu_r^{III} D_m^{II} r_{iii}^{-mp-1} - \mu_r^{II} C_m^{III} r_{iii}^{mp-1} + \mu_r^{II} D_m^{III} r_{iii}^{-mp-1} = -\mu_r^{III} U_m^{II} \tag{A.124}$$

$$C_m^{III} r_{iv}^{mp-1} + D_m^{III} r_{iv}^{-mp-1} - C_m^{IV} r_{iv}^{mp-1} - D_m^{IV} r_{iv}^{-mp-1} = G_m^{IV} \tag{A.125}$$

$$\mu_r^{IV} C_m^{III} r_{iv}^{mp-1} - \mu_r^{IV} D_m^{III} r_{iv}^{-mp-1} - \mu_r^{III} C_m^{IV} r_{iv}^{mp-1} + \mu_r^{III} D_m^{IV} r_{iv}^{-mp-1} = \mu_r^{III} U_m^{IV} \tag{A.126}$$

$$C_m^{IV} r_v^{mp-1} + D_m^{IV} r_v^{-mp-1} - C_m^{V} r_v^{mp-1} - D_m^{V} r_v^{-mp-1} = -G_m^{IV} \tag{A.127}$$

$$\mu_r^{V} C_m^{IV} r_v^{mp-1} - \mu_r^{V} D_m^{IV} r_v^{-mp-1} - \mu_r^{IV} C_m^{V} r_v^{mp-1} + \mu_r^{IV} D_m^{V} r_v^{-mp-1} = -\mu_r^{V} U_m^{IV} \tag{A.128}$$

$$C_m^V r_{vi}^{mp} + D_m^V r_{vi}^{-mp} = 0\ . \tag{A.129}$$

$$
\begin{bmatrix}
r_i^{mp} & -r_i^{mp} & & & & & & & & & & & & & & & \\
r_{ii}^{mp-1} & -r_{ii}^{mp-1} & -r_{ii}^{mp-1} & & & & & & & & & & & & & & \\
\mu_r^{II} r_{ii}^{mp-1} & -\mu_r^{II} r_{ii}^{mp-1} & \mu_r^{I} r_{ii}^{mp-1} & & & & & & & & & & & & & & \\
 & & & r_{iii}^{mp-1} & -r_{iii}^{mp-1} & -r_{iii}^{mp-1} & & & & & & & & & & & \\
 & & & \mu_r^{III} r_{iii}^{mp-1} & \mu_r^{II} r_{iii}^{mp-1} & -\mu_r^{II} r_{iii}^{mp-1} & & & & & & & & & & & \\
 & & & & & & r_{iv}^{mp-1} & -r_{iv}^{mp-1} & -r_{iv}^{mp-1} & & & & & & & & \\
 & & & & & & \mu_r^{IV} r_{iv}^{mp-1} & -\mu_r^{IV} r_{iv}^{mp-1} & \mu_r^{III} r_{iv}^{mp-1} & & & & & & & & \\
 & & & & & & & & & r_v^{mp-1} & -r_v^{mp-1} & & & & & & \\
 & & & & & & & & & \mu_r^{V} r_v^{mp-1} & -\mu_r^{V} r_v^{mp-1} & -r_v^{mp-1} & & & & & \\
 & & & & & & & & & & & \mu_r^{IV} r_v^{mp-1} & -r_v^{mp-1} & & & & \\
 & & & & & & & & & & & & r_{vi}^{mp} & -r_{vi}^{mp} & & & \\
 & & & & & & & & & & & & & & C_m^I & & \\
 & & & & & & & & & & & & & & D_m^I & & \\
 & & & & & & & & & & & & & & C_m^{II} & & \\
 & & & & & & & & & & & & & & D_m^{II} & & \\
 & & & & & & & & & & & & & & C_m^{III} & & \\
 & & & & & & & & & & & & & & D_m^{III} & & \\
 & & & & & & & & & & & & & & C_m^{IV} & & \\
 & & & & & & & & & & & & & & D_m^{IV} & & \\
 & & & & & & & & & & & & & & C_m^{V} & & \\
 & & & & & & & & & & & & & & D_m^{V} &
\end{bmatrix}
$$

$$
=
\begin{bmatrix}
0 \\
G_m^{II} \\
\mu_r^{I} U_m^{II} \\
-G_m^{II} \\
-\mu_r^{III} U_m^{II} \\
G_m^{IV} \\
\mu_r^{III} U_m^{IV} \\
-G_m^{IV} \\
-\mu_r^{V} U_m^{IV} \\
0
\end{bmatrix}
\tag{A.130}
$$

Appendix B

Initial Design of the SORSPM Machine

This appendix lists the dimensions and performance metrics, of the initial attempt at the design of the SORSPM machine utilising solid copper bars. The dimensions listed in Table B.1 is that which were used in the construction investigation of Section 6.3. Furthermore, in Chapter 4 as an example, many of the loss components were computed for this exact machine. The purpose of the dimensions and performance characteristics shown here is merely to serve as reference to those loss calculations.

Variable	Value	Unit
Number of poles (P)	40	poles
Number of slots (Q)	30	slots
Number of turns per coil (N)	2	turns
Number of parallel circuits per phase (a)	1	
Three-phase connection	Y	
PM type	NdFeB N48	
PM remnant flux Density (B_{rem})	1.4	T
Stack length (ℓ)	100	mm
Outer radius (r_o)	134.79	mm
Inner radius (r_i)	87.05	mm
Rotor yoke height (h_{yo})	4.61	mm
Magnet height (h_m)	3.15	mm
Magnet width	15.16	mm
Shoe tip height (h_s)	0.91	mm
Slot height (h_c)	34.38	mm
Slot width	13.61	mm
Stator yoke height (h_{yi})	3.57	mm
Hole height (h_h)	5.49	mm
Hole diameter	4.20	mm
Magnet pitch ratio (k_m)	0.76	p.u.
Slot pitch ratio (k_c)	0.29	p.u.
Shoe tip width (w_s)	1.5	mm
Shoe taper angle (θ_s)	0	$^\circ$
Airgap (g)	1	mm
Copper bar height	15.46	mm
Copper bar width	5.08	mm
Insulation spacing between bars	1.15	mm
Effective fill factor	0.67	p.u.
Iron mass	11.45	kg
Copper mass	8.44	kg
Magnet mass	1.43	kg
Aluminium mass	3.76	kg
Total mass	25.09	kg

Table B.1: Design parameters of an early attempt of the SORSPM machine utilising solid copper bars.

Variable	Value	Unit
Average developed torque (τ_{mech})	194.53	N·m
Torque ripple (τ_{ripple})	6.70	%
Torque density ($\tau_{density}$)	7.75	N·m/kg
Rated power (p_{mech})	2.04	kW
Rated efficiency (η)	89.11	%
Rated power factor (PF)	0.85	p.u.
Base speed (n_{rpm})	100	rpm
Rotor iron losses (P_{rotor})	2.20	W
Stator iron losses (P_{stator})	22.45	W
Copper losses (P_{copper})	200	W
Eddy current losses (P_{eddy})	22.10	W
Magnet losses (P_{magnet})	2.26	W
Total losses (P_{total})	249	W
Electrical frequency (f_e)	33.33	Hz
RMS current density (J_q)	2.68	A/mm^2
RMS phase current (I_a)	210.28	A
Peak induced phase voltage ($\hat{E}_a$)	5.08	V
Peak terminal phase voltage ($\hat{V}_a$)	5.53	V
Phase resistance (AC) (R_a)	1.51	mΩ
Synchronous inductance (L_s)	22.73	µH
Peak terminal line-line voltage ($\hat{V}_{LL}$)	10.10	V

Table B.2: Performance metrics of an early attempt of the SORSPM machine utilising solid copper bars, at the rated base speed (100 rpm) operating point.

Variable	Value	Unit
Average developed torque (τ_{mech})	42.70	N·m
Torque ripple (τ_{ripple})	56.40	%
Torque density ($\tau_{density}$)	1.70	N·m/kg
Rated power (p_{mech})	2.08	kW
Efficiency (η)	82.11	%
Power factor (PF)	0.99	p.u.
Top speed (n_{rpm})	465	rpm
Rotor iron losses (P_{rotor})	15.11	W
Stator iron losses (P_{stator})	194.94	W
Copper losses (P_{copper})	11.20	W
Eddy current losses (P_{eddy})	182.87	W
Magnet losses (P_{magnet})	48.80	W
Total losses (P_{total})	452.92	W
Electrical frequency (f_e)	155.0	Hz
RMS current density (J_q)	0.57	A/mm^2
RMS phase current (I_a)	44.40	A
Peak induced phase voltage ($\hat{E}_a$)	21.36	V
Peak terminal phase voltage ($\hat{V}_a$)	21.48	V
Phase resistance (AC) (R_a)	1.90	mΩ
Synchronous inductance (L_s)	22.73	µH
Peak terminal line-line voltage ($\hat{V}_{LL}$)	40.36	V

Table B.3: Performance metrics of an early attempt of the SORSPM machine utilising solid copper bars, at the top speed (465 rpm) operating point.

Bibliography

[1] G. Oosthuizen and P. J. Randewijk, "Design of an Ironless Double-Rotor Radial Flux Permanent Magnet Machine", Master's Thesis, Stellenbosch University, 2015, ISBN: 9781479979400.

[2] A Joss and P. J. Randewijk, "Design and Optimisation of an Ironless Double-Rotor Radial Flux Permanent Magnet Machine", *SAUPEC*, p. 7, 2016.

[3] A. Joss and P. J. Randewijk, "Design of an Ironless Double-Rotor Radial Flux Permanent Magnet machine", *Proceedings - 22nd International Conference on Electrical Machines, ICEM 2016*, p. 7, 2016. DOI: 10.1109/IEMDC.2015.7409133.

[4] C. W. Vorster, "Design of a Reluctance Synchronous Machine for an Electric Vehicle with a Multi Speed Gearbox", Master's Thesis, Stellenbosch University, 2014.

[5] McCue TJ, *Global Electric Bike Market Is Still Moving Fast*. [Online]. Available: https://www.forbes.com/sites/tjmccue/2018/04/12/the-global-electric-bike-market-is-still-moving-fast-sondors-e-bike-offers-glimpse/{\#}55e5329b31ff (visited on 08/28/2018).

[6] *GEM In-Wheel Motors 4 KW & 6 KW In Production*. [Online]. Available: http://gemmotors.si/news/gem-in-wheel-motors-4-kw-6-kw-in-production-2018-08-27 (visited on 08/28/2018).

[7] "Economic and Social Council", United Nations: Economic and Social Council, Tech. Rep. Revision 2, 2011.

[8] B. V. W. Horn, "The Development of a 48V, 10kWh LiFePO4 Battery Management System for Low Voltage Battery Storage Applications", Master's Thesis, Stellenbosch University, 2017.

[9] E. Schaltz, "Electrical Vehicle Design and Modeling", *Electric Vehicles - Modelling and Simulations*, pp. 1–24, 2011.

[10] A. J. Rix, "Design , Comparison and Experimental Evaluation of Non-Overlap Winding Radial Flux Permanent Magnet Hub Drives for Electric Vehicles by", PhD thesis, Stellenbosch University, 2011.

[11] J. H. J. Potgieter, "Design and Analysis of Gearless Direct-Grid Permanent Magnet Induction Wind Generator", Master's Thesis, Stellenbosch University, 2011.

[12] P.-J. Randewijk, "Analysis of a radial flux-air-cored permanent magnet machine with a double-sided rotor and non overlapping windings", PhD thesis, Stellenbosch University, 2012. [Online]. Available: http://scholar.sun.ac.za/handle/10019.1/20246.

[13] J. A. Stegmann, "Design and Analysis Aspects of Radial Flux Air- cored Permanent Magnet Wind Generator System for Direct Battery Charging Applications by", Master's Thesis, Stellenbosch University, 2010, p. 114.

[14] D. Martínez, "Design of a Permanent-Magnet Synchronous Machine with Non-Overlapping Concentrated Windings Design of a Permanent-Magnet Synchronous Machine with Non-Overlapping Concentrated Windings for the Shell Eco Marathon Urban Prototype", Master's Thesis, Royal Institute of Technology, 2012.

[15] D. C. Hanselman, *Brushless Permanent Magnet Motor Design*, Second Edi. Lebenon, Ohio: Magna Physics Publishing, 2006, p. 392, ISBN: ISBN-10: 1-881855-15-5.

[16] J. Pyrhönen, T. Jokinen, and V. Hrabovcova, *Design of Rotating Electrical Machines*, First Edit. John Wiley & Sons, 2008, p. 512, ISBN: 9780470695166.

[17] D. J. Groenewald, "Evaluation of a radial flux air-cored permanent magnet machine drive with manual transmission drivetrain for electric vehicles", Master's Thesis, Stellenbosch University, 2011.

[18] O. Cote, A. Chebak, and J.-f. Methot, "Design and Optimization of a high torque in-wheel surface-mounted PM synchronous motor using concentrated winding", *IEEE*, pp. 863–870, 2013.

[19] M Kimiabeigi, J. D. Widmer, R. S. Sheridan, A Walton, and R Harris, "Design of high performance traction motors using cheaper grade of materials", pp. 1–7,

[20] J. R. Hendershot, *Permanent Magnet Synchronous Motor (PMSM) Introduction*.

[21] Y. L. Karnavas and C. D. Korkas, "Optimization methods evaluation for the design of radial flux surface PMSM", *Proceedings - 2014 International Conference on Electrical Machines, ICEM 2014*, pp. 1348–1355, 2014. DOI: 10.1109/ICELMACH.2014.6960357.

[22] L. Xiao-hai, Z. Li, Z. Ji-min, and J. Shu-zhong, "Permanent Magnet Synchronous Motor for Screw Pump", *Power Electronics and Motion Control Conference, 2009. IPEMC '09. IEEE 6th International*, vol. 3, pp. 1858–1862, 1858.

[23] Y. B. Deshpande, H. A. Toliyat, S. S. Nair, and S. J. Dhinagar, "High-Torque-Density Single Tooth-Wound Bar Conductor Permanent-Magnet Motor for Electric Two Wheeler Application", *IEEE Transactions on Industry Applications*, vol. 51, no. 3, pp. 2123–2135, 2015.

[24] J. A. Stegmann and M. J. Kamper, "Design Aspects of Double-Sided Rotor Radial Flux Air-Cored Permanent-Magnet Wind Generator", *IEEE Transactions on Industry Applications*, vol. 47, no. 2, pp. 767–778, 2011. [Online]. Available: `http://ieeexplore.ieee.org/stamp/stamp.jsp?arnumber=5680607`.

[25] P. J. Randewijk and M. J. Kamper, "Analytical analysis of a Radial Flux Air-cored Permanent Magnet machine with a double-sided rotor and non-overlapping double-layer windings", in *2012 XXth International Conference on Electrical Machines*, IEEE, 2012, pp. 1178–1184, ISBN: 978-1-4673-0142-8. DOI: `10.1109/ICElMach.2012.6350025`. [Online]. Available: `http://ieeexplore.ieee.org/stamp/stamp.jsp?arnumber=6350025`.

[26] G. I. Oosthuizen and P. J. Randewijk, "Double-rotor Ironless Radial Flux Permanent Magnet Machine", *2014 XXIIth International Conference on Electrical Machines*, pp. 1–6, 2014. [Online]. Available: `http://ieeexplore.ieee.org/stamp/stamp.jsp?arnumber=6960226`.

[27] M. J. Kamper, R. J. Wang, and F. G. Rossouw, "Analysis and performance of axial flux permanent-magnet machine with air-cored nonoverlapping concentrated stator windings", *IEEE Transactions on Industry Applications*, vol. 44, no. 5, pp. 1495–1504, 2008.

[28] S. Gerber, "A finite element based optimisation tool for electrical machines", Master's Thesis, Stellenbosch University, 2011. [Online]. Available: `http://ir1.sun.ac.za/handle/10019.1/6635`.

[29] Q Zhu, "Instantaneous Magnetic Field Distribution in Permanent Magnet Brushless dc Motors, Part IV: Magnetic Field on Load", *IEEE Transactions on Magnetics*, vol. 29, no. 1, pp. 152–158, 1993. [Online]. Available: `http://www.ewp.rpi.edu/hartford/~ernesto/Su2013/EP/MaterialsforStudents/Fellegara/Zhu1993-MagneticFieldDistributions-P1.pdf`.

[30] Q Zhu, D. Howe, and C. Chan, "Improved analytical model for predicting the magnetic field distribution in high-speed slotless permanent-magnet machines", *IEEE Transactions on Magnetics*, vol. 38, no. 1, pp. 229–238, 2002, ISSN: 00189464. DOI: 10.1109/TMAG.2014.2350508. [Online]. Available: http://eprints.whiterose.ac.uk/874/1/zhuzq16.pdf.

[31] R. J. Wang and M. J. Kamper, "Calculation of Eddy Current Loss in Axial Field Permanent-Magnet MachineWith Coreless Stator", *IEEE Transactions on Energy Conversion*, vol. 19, no. 3, pp. 532–538, 2004.

[32] A. Van den Bossche and V. C. Valchev, "Eddy Currents in Conductors", in *Inductors and Transformers for Power Electronics*, First Edit, Taylor & Francis Group, 2005, ch. 5.

[33] A. Van den Bossche, V. C. Valchev, and S. T. Barudov, "Practical Wide Frequency Approach for Calculating Eddy Current Losses in Transformer Windings", *IEEE ISIE*, no. 1, pp. 1070–1074, 2006.

[34] G. W. Carter, *Electromagnetic Field in its Engineering Aspects*, White Plains, NY, 1954.

[35] X. Wang, D. Liu, D. Lahaye, H. Polinder, and J. A. Ferreira, "Finite Element Analysis and Experimental Validation of Eddy Current Losses in Permanent Magnet Machines with Fractional-Slot Concentrated Windings", *Proceedings - 19th International Conference on Electrical Machines and Systems, ICEMS 2016*, 2016.

[36] C. Huynh, L. Zheng, and D. Acharya, "Losses in High Speed Permanent Magnet Machines Used in Microturbine Applications", *Journal of Engineering for Gas Turbines and Power*, vol. 131, no. 2, p. 022 301, 2009, ISSN: 07424795. DOI: 10.1115/1.2982151. [Online]. Available: http://gasturbinespower.asmedigitalcollection.asme.org/article.aspx?articleid=1474573.

[37] L. J. Wu, Z. Q. Zhu, D. Staton, M. Popescu, and D. Hawkins, "Analytical model for predicting magnet loss of surface-mounted permanent magnet machines accounting for slotting effect and load", *IEEE Transactions on Magnetics*, vol. 48, no. 1, pp. 107–117, 2012, ISSN: 00189464. DOI: 10.1109/TMAG.2011.2165321.

[38] P. Krause, O. Wasynczuk, S. Sudhoff, and S. Pekarek, *Analysis of Electric Machinery and Drive Systems*, Third Edit, J. Anderson, Ed. Piscataway, NJ: John Wiley & Sons, 2013, p. 659.

[39] F. Meier, "Permanent-Magnet Synchronous Machines with Non-Overlapping Concentrated Windings for Low-Speed Direct-Drive Applications", PhD thesis, Royal Institute of Technology, 2008, pp. 1–177, ISBN: 9789174150896. DOI: 10.1109/60.103641. [Online]. Available: http://www.ee.kth.se/php/modules/publications/reports/2008/TRITA-EE_2008_041.pdf.

[40] J. H. Van Wijk, "Analysis and Design of a Double-sided Rotor Iron-Cored Radial Flux Permanent Magnet Synchronous Wind Turbine Generator by", Master's Thesis, Stellenbosch University, 2012.

[41] S Zurek, *Encyclopedia Magnetica*. [Online]. Available: http://www.encyclopedia-magnetica.com/ (visited on 11/20/2017).

[42] *Fr4 G10 Epoxy Glass Fiber Laminate Sheets*. [Online]. Available: https://www.gaatech.com/fr4-g10-sheet-laminates-epoxyglass/ (visited on 11/21/2017).

[43] *FR4 Plain Laminate Base Material*. [Online]. Available: http://www.fortex.co.uk/product/fr4-plain-laminate-base-material/ (visited on 11/21/2017).

[44] *IT Tech*. [Online]. Available: https://it-tech-uk.com/products/glassfibre-sheet-grp-epoxy-glass-g10-fr4-fibreglass-sheet-12x6 (visited on 11/21/2017).

[45] *Epoxy FR-4*. [Online]. Available: http://www.dcwort.co.za/epoxy-fr-4 (visited on 11/21/2017).

[46] *Bikar Metalle*. [Online]. Available: http://www.bikar.com/copper-flat-bars.html (visited on 11/21/2017).

[47] D. Rey, "Tooth coils with litz wire: Advantages for e-drives", Von Roll Schweiz AG, Breitenbach, Switzerland, Tech. Rep., 2016.

[48] D. Sherman, *We Build the Chevy Spark EV's AC Permanent-Magnet Motor*, 2011. [Online]. Available: https://blog.caranddriver.com/we-build-the-chevy-spark-evs-ac-permanent-magnet-motor/ (visited on 11/20/2017).

[49] *Winding Wires and Litz Wires*. [Online]. Available: http://www.vonroll.com/en/products/electrical-conductors/litz-wires/ (visited on 11/20/2017).

[50] C. Mi, G. R. Slemon, and R. Bonert, "Minimization of iron losses of permanent magnet synchronous machines", *ICEMS 2001 - Proceedings of the 5th International Conference on Electrical Machines and Systems*, vol. 2, no. 1, pp. 818–823, 2001, ISSN: 08858969. DOI: 10.1109/ICEMS.2001.971802.

[51] J. R. Hendershot, "Pole & Slot Number Selection Procedure for PM Synchronous Machines", in *CWIEME*, Berlin: MotorSolver, 2016, pp. 1–18, ISBN: 7065420965.

[52] S. Gerber, J. Strauss, and P. Randewijk, "Evaluation of a hybrid finite element analysis package featuring dual air-gap elements", in *The XIX International Conference on Electrical Machines - ICEM 2010*, IEEE, 2010, pp. 1–6, ISBN: 978-1-4244-4174-7. DOI: 10.1109/ICELMACH.2010.5608074. [Online]. Available: http://ieeexplore.ieee.org/lpdocs/epic03/wrapper.htm?arnumber=5608074.

[53] P. N. Murgatroyd, "Some General Results for Low-Frequency Eddy Currents", *IEEE Transactions on Education*, vol. E-22, no. 4, pp. 178–180, 1979.

[54] K. V. Namjoshi and P. P. Biringer, "Low-Frequency Eddy-Current Loss Estimation in Long Conductors by Using the Moment of Inertia of Cross Sections", *IEEE Transactions on Magnetics*, vol. 24, no. 5, pp. 2181–2185, 1988, ISSN: 19410069. DOI: 10.1109/20.3426.

[55] J. Reinert, A. Brockmeyer, and R. W.A. A. De Doncker, "Calculation of losses in ferro- and ferrimagnetic materials based on the modified Steinmetz equation", *IEEE Transactions on Industry Applications*, vol. 37, no. 4, pp. 1055–1061, 2001, ISSN: 00939994. DOI: 10.1109/28.936396.

[56] Y. Chen and P. Pillay, "An improved formula for lamination core loss calculations in machines operating with high frequency and high flux density excitation", *Conference Record - IAS Annual Meeting (IEEE Industry Applications Society)*, vol. 2, no. C, pp. 759–766, 2002, ISSN: 01972618. DOI: 10.1109/IAS.2002.1042645.

[57] J. Soulard, "Modeling of iron losses in permanent magnet synchronous motors with field-weakening capability for electric vehicles", *International Journal of Automotive Technology*, vol. 4, no. 2, pp. 87–94, 2003, ISSN: 1229-9138.

[58] D. M. Ionel, M. Popescu, M. I. McGilp, T. J. E. Miller, S. J. Dellinger, and R. J. Heideman, "Computation of core losses in electrical machines using improved models for laminated steel", *IEEE Transactions on Industry Applications*, vol. 43, no. 6, pp. 1554–1564, 2007, ISSN: 00939994. DOI: 10.1109/TIA.2007.908159.

[59] H. Polinder and M. Hoeijmakers, "Eddy-current losses in the segmented surface-mounted magnets of a PM machine", *IEE Proceedings - Electric Power Applications*, vol. 146, p. 261, 1999, ISSN: 13502352. DOI: 10.1049/ip-epa:19990091.

[60] H. Toda, Z. Xia, J. Wang, K. Atallah, and D. Howe, "Rotor eddy-current loss in permanent magnet brushless machines", *IEEE Transactions on Magnetics*, vol. 40, no. 4 II, pp. 2104–2106, 2004, ISSN: 00189464. DOI: 10.1109/TMAG.2004.832481.

[61] Z. X. Fang, Z. Q. Zhu, L. J. Wu, and Z. P. Xia, "Simple and accurate analytical estimation of slotting effect on magnet loss in fractional-slot surface-mounted PM machines", *Proceedings - 2012 20th International Conference on Electrical Machines, ICEM 2012*, pp. 464–470, 2012. DOI: 10.1109/ICElMach.2012.6349910.

[62] D. A. Wills and M. J. Kamper, "Reducing PM eddy current rotor losses by partial magnet and rotor yoke segmentation", *19th International Conference on Electrical Machines, ICEM 2010*, 2010. DOI: 10.1109/ICELMACH.2010.5607993.

[63] J. Wang, K. Atallah, R. Chin, W. M. Arshad, and H. Lendenmann, "Rotor eddy-current loss in permanent-magnet brushless AC machines", *IEEE Transactions on Magnetics*, vol. 46, no. 7, pp. 2701–2707, 2010, ISSN: 00189464. DOI: 10.1109/TMAG.2010.2042963. arXiv: 5.

[64] Eclipse Magnetics, *Neodymium Iron Boron Magnets Datasheet*, 2017. [Online]. Available: https://www.eclipsemagnetics.com/media/wysiwyg/datasheets/magnet_materials_and_assemblies/ndfeb_neodymium_iron_boron-standard_ndfeb_range_datasheet_rev1.pdf (visited on 11/01/2017).

[65] M Markovic and Y Perriard, "A simplified determination of the permanent magnet (PM) eddy current losses due to slotting in a PM rotating motor", in *Electrical Machines and Systems Conference*, 2008, pp. 309–313.

[66] Z. Zhu and D. Howe, "Instantaneous magnetic field distribution in brushless permanent magnet DC motors, Part III. Effect of stator slotting", *IEEE Transactions on Magnetics*, vol. 29, no. 1, pp. 143–151, 1993, ISSN: 0018-9464. DOI: 10.1109/20.195559.

[67] S. D. Umans, *Fitzgerald and Kingsley's Electric Machinery*, Seventh Ed. New York: McGraw-Hill, 2014, p. 706.

[68] S. Gerber and R. J. Wang, "Statistical analysis of cogging torque considering various manufacturing imperfections", *Proceedings - 2016 22nd International Conference on Electrical Machines, ICEM 2016*, pp. 2066–2072, 2016. DOI: 10.1109/ICELMACH.2016.7732807.

[69] S. Skaar, O. Krovel, and R. Nilssen, "Distribution, coil-span and winding factors for PM machines with concentrated windings", *XVII International Conference on Electrical Machines, ICEM 2006*, p. 346, 2006. [Online]. Available: http://www.elkraft.ntnu.no/eno/Papers2006/icem-skaar-krovel-nilssen06.pdf.

[70] H. Lovatt, V. Ramsden, and B. Mecrow, "Design of an in-wheel motor for a solar-powered electric vehicle", *IEE Proceedings - Electric Power Applications*, vol. 145, no. 5, p. 402, 1998, ISSN: 13502352. DOI: 10.1049/ip-epa:19982167. [Online]. Available: http://digital-library.theiet.org/content/journals/10.1049/ip-epa_19982167.

[71] J. a. Snyman, *Practical Mathematical Optimization*. 2005, ISBN: 0387243488. DOI: 10.1007/b105200.

[72] R. Marler and J. Arora, "Survey of multi-objective optimization methods for engineering", *Structural and Multidisciplinary Optimization*, vol. 26, no. 6, pp. 369–395, 2004, ISSN: 1615-147X. DOI: 10.1007/s00158-003-0368-6. [Online]. Available: http://link.springer.com/10.1007/s00158-003-0368-6.

[73] L. S. de Oliveira and S. F. P. Saramago, "Multiobjective Optimization Techniques Applied to Engineering Problems", *Journal of the Brazilian Society of Mechanical Sciences and Engineering*, vol. 32, no. 1, pp. 94–105, 2010.

[74] I. Das and J. Dennis, "Normal-Boundary Intersection: An alternate method for generating pareto optimal points in multicriteria optimization problems", *Society for Industrial and Applied Mathematics Journal on Optimization*, no. 8, pp. 631–657, 1998. DOI: http://dx.doi.org/10.1137/S1052623496307510. [Online]. Available: http://hdl.handle.net/2060/19970005647.

[75] R. T. Marler and J. S. Arora, "The weighted sum method for multi-objective optimization: New insights", *Structural and Multidisciplinary Optimization*, vol. 41, no. 6, pp. 853–862, 2010, ISSN: 1615147X. DOI: 10.1007/s00158-009-0460-7.

[76] I. Y. Kim, "Adaptive Weighted Sum Method for Multiobjective Optimization", *Structural and Multidisciplinary Optimization*, pp. 1–13,

[77] R. E. Perez, P. W. Jansen, and J. R.R. A. Martins, "PyOpt: A Python-based object-oriented framework for nonlinear constrained optimization", *Structures and Multidisciplinary Optimization*, vol. 45, no. 1, pp. 101–118, 2012. DOI: 10.1007/s00158-011-0666-3.

[78] S. Johnson, *The NLopt nonlinear-optimization package*. [Online]. Available: http://ab-initio.mit.edu/nlopt.

[79] D. R. Jones, C. D. Pertunnen, and B. Stuckmann, "Lipschitzian optimization without the lipschitz constant", *Optimization Theory and Applications*, vol. 79, p. 157, 1993.

[80] T Rowan, "Functional Stability Analysis of Numerical Algorithms", PhD thesis, University of Texas at Austin, 1990.

[81] D. J. Griffiths, *Introduction to Electrodynamics*, Third Edit, A. Reeves and K. Dellas, Eds. Upper Saddle River, New Jersey: Prentice-Hall, 1999.

[82] B. Guru and H. Hiziroglu, *Electromagnetic Field Theory Fundamentals*, Second Edi. New York: Cambridge University Press, 2004, p. 681.

[83] S. J. Chapman, *Electric Machinery Fundamentals*, Fifth Edit. New York: McGraw-Hill Education, 2012.

[84] D. D. Bleecker and G. Csordas, *Basic Partial Differential Equations*, 1st. New York: Van Nostrand Reinhold, 1992, p. 735, ISBN: 9781571460363. [Online]. Available: `http://www.amazon.com/Partial-Differential-Equations-Bleecker-University/dp/1571460365/ref=sr_1_1?s=books&ie=UTF8&qid=1398197715&sr=1-1`.

[85] S. Ramo, J. R. Whinnery, and T. Van Duzer, *Field and Waves in Communication Electronics*, Third Edit, S. Elliot and S. Elbe, Eds. John Wiley & Sons, 1994, p. 844.

[86] D. K. Cheng, *Field and Wave Electromagnetics*, Second Edi, T. Robbins and M. Sorotskin, Eds. Addison-Wesley, 1989, p. 719.